ISSN 2500-316X (Online)

RUSSIAN TECHNOLOGICAL JOURNAL

РОССИЙСКИЙ ТЕХНОЛОГИЧЕСКИЙ ЖУРНАЛ

Information systems.
Computer sciences.
Issues of information security

Multiple robots (robotic centers) and systems.
Remote sensing and nondestructive testing

Modern radio engineering and telecommunication systems

Micro- and nanoelectronics.
Condensed matter physics

Analytical instrument engineering and technology

Mathematical modeling

Economics of knowledge-intensive and high-tech enterprises and industries.
Management in organizational systems

Product quality management. Standardization

Philosophical foundations of technology and society

12+
www.rtj-mirea.ru

13(6) 2025

ISSN 2500-316X (Online)

RUSSIAN TECHNOLOGICAL JOURNAL

РОССИЙСКИЙ ТЕХНОЛОГИЧЕСКИЙ ЖУРНАЛ

- Information systems. Computer sciences. Issues of information security
- Multiple robots (robotic centers) and systems. Remote sensing and nondestructive testing
- Modern radio engineering and telecommunication systems
- Micro- and nanoelectronics. Condensed matter physics
- Analytical instrument engineering and technology
- Mathematical modeling
- Economics of knowledge-intensive and high-tech enterprises and industries. Management in organizational systems
- Product quality management. Standardization
- Philosophical foundations of technology and society

- Информационные системы. Информатика. Проблемы информационной безопасности
- Роботизированные комплексы и системы. Технологии дистанционного зондирования и неразрушающего контроля
- Современные радиотехнические и телекоммуникационные системы
- Микро- и наноэлектроника. Физика конденсированного состояния
- Аналитическое приборостроение и технологии
- Математическое моделирование
- Экономика наукоемких и высокотехнологичных предприятий и производств. Управление в организационных системах
- Управление качеством продукции. Стандартизация
- Мировоззренческие основы технологии и общества

Russian Technological Journal
2025, Vol. 13, No. 6

Russian Technological Journal
2025, том 13, № 6

https://www.rtj-mirea.ru

https://doi.org/10.32362/2500-316X

ISSN 2500-316X (Online)

Russian Technological Journal
2025, Vol. 13, No. 6

Publication date November 28, 2025.

The peer-reviewed scientific and technical journal highlights the issues of complex development of radio engineering, telecommunication and information systems, electronics and informatics, as well as the results of fundamental and applied interdisciplinary researches, technological and economical developments aimed at the development and improvement of the modern technological base.

Periodicity: six times a year.
The journal was founded in December 2013. The titles were «Herald of MSTU MIREA» until 2016 (ISSN 2313-5026) and «Rossiiskii tekhnologicheskii zhurnal» from January 2016 until July 2021 (ISSN 2500-316X).

Founder and Publisher:
Federal State Budget
Educational Institution of Higher Education
«MIREA – Russian Technological University»
78, Vernadskogo pr., Moscow, 119454 Russia.

The journal is included into the List of peer-reviewed science press of the State Commission for Academic Degrees and Titles of Russian Federation. The Journal is included in Russian Science Citation Index (RSCI), Russian State Library (RSL), Science Index, eLibrary, Directory of Open Access Journals (DOAJ), Directory of Open Access Scholarly Resources (ROAD), Google Scholar, Ulrich's International Periodicals Directory.

The registration number ПИ № ФС 77 - 81733 was issued in August 19, 2021 by the Federal Service for Supervision of Communications, Information Technology, and Mass Media of Russia.

The subscription index of *Pressa Rossii*: **79641**.

Russian Technological Journal
2025, том 13, № 6

Дата опубликования 28 ноября 2025 г.

Научно-технический рецензируемый журнал освещает вопросы комплексного развития радиотехнических, телекоммуникационных и информационных систем, электроники и информатики, а также результаты фундаментальных и прикладных междисциплинарных исследований, технологических и организационно-экономических разработок, направленных на развитие и совершенствование современной технологической базы.

Периодичность: 6 раз в год.
Журнал основан в декабре 2013 года. До 2016 г. издавался под названием «Вестник МГТУ МИРЭА» (ISSN 2313-5026), а с января 2016 г. по июль 2021 г. под названием «Российский технологический журнал» (ISSN 2500-316X).

Учредитель и издатель:
федеральное государственное бюджетное образовательное учреждение высшего образования «МИРЭА – Российский технологический университет»
119454, РФ, г. Москва, пр-т Вернадского, д. 78.

Журнал входит в Перечень ведущих рецензируемых научных журналов ВАК РФ, в которых должны быть опубликованы основные научные результаты диссертаций на соискание ученой степени кандидата наук и доктора наук, входит в RSCI, РГБ, РИНЦ, eLibrary, Directory of Open Access Journals (DOAJ), Directory of Open Access Scholarly Resources (ROAD), Google Scholar, Ulrich's International Periodicals Directory.

Регистрационный номер и дата принятия решения о регистрации СМИ ПИ № ФС 77 - 81733 от 19.08.2021 г. СМИ зарегистрировано Федеральной службой по надзору в сфере связи, информационных технологий и массовых коммуникаций (Роскомнадзор).

Индекс по объединенному каталогу «Пресса России» **79641**.

https://www.rtj-mirea.ru

Editorial Board

Редакционная коллегия

Contents

Содержание

Information systems. Computer sciences. Issues of information security
Информационные системы. Информатика. Проблемы информационной безопасности

UDC 004.9:681.3
https://doi.org/10.32362/2500-316X-2025-13-6-7-24
EDN WGZAHH

RESEARCH ARTICLE

Organization and study of cluster computing systems with functional architecture determined by executable models. Automata executable models of information processing

Grigory V. Petushkov @

MIREA – Russian Technological University, Moscow, 119454 Russia
@ *Corresponding author, e-mail: petushkov@mirea.ru*

• **Submitted:** 04.08.2025 • **Revised:** 12.09.2025 • **Accepted:** 06.10.2025

Abstract

Objectives. An urgent task is to improve the functional architecture of cluster computing systems by introducing methodologies for creating software at the applied and intermediate levels based on formalized specifications. One such methodology is based on the use of automatic specifications for computer systems software. The complexity of resolving the problem is caused by the branching of the algorithms built, as well as the presence of cyclic sections. The execution time of the branched sections of the program and the number of cycles run depends on the type of conditions entered. In practice it can be determined using a detailed simulation model and analysis of the control program created on its basis. The aim of the work is to find approaches to the definition of functional architecture which can be applied practically at the main levels of the subject orientation of cluster computing systems.

Methods. The methods proposed and used are based on the concept of organization and research of cluster-type computing systems with a functional architecture as defined by executable automatic models.

Results. The paper proposes methods of constructing automatic and logical-probabilistic models of cluster computing systems and creating software tools based on them. The concept of the logical-probabilistic model "temporal probabilistic system of canonical equations (CES)" is introduced. This enables a visual formalization to be obtained, as well as implementation of automatic models and work programs typical for cluster and other applications. It also significantly reduced the number of "incremental" additions when enumerating discrete time moments. The main feature of the new logical-probabilistic model is the preservation of the original CES in its basis.

Conclusions. The work concludes that the choice of the system and functional architecture of a computing cluster should be determined not so much by the peak characteristics of the communication equipment specified by the manufacturer, as by the actual indicators achieved at the level of user applications and cluster usage modes. It is also shown that executable automatic models can be applied at almost all levels of cluster computing systems subject orientation.

Keywords: cluster computing system, intermediate level application, functional architecture, finite automaton models, logical-probabilistic model, logical-algebraic model, query processing modes, simulation results

For citation: Petushkov G.V. Organization and study of cluster computing systems with functional architecture determined by executable models. Automata executable models of information processing. *Russian Technological Journal.* 2025;13(6):7–24. https://doi.org/10.32362/2500-316X-2025-13-6-7-24, https://www.elibrary.ru/WGZAHH

Financial disclosure: The author has no financial or proprietary interest in any material or method mentioned.

The author declares no conflicts of interest.

НАУЧНАЯ СТАТЬЯ

Организация и исследование кластерных вычислительных систем с функциональной архитектурой, определяемой исполнимыми моделями. Автоматные исполнимые модели обработки информации

Г.В. Петушков [@]

МИРЭА – Российский технологический университет, Москва, 119454 Россия
[@] *Автор для переписки, e-mail: petushkov@mirea.ru*

• **Поступила:** 04.08.2025 • **Доработана:** 12.09.2025 • **Принята к опубликованию:** 06.10.2025

Резюме

Цели. Актуальной является задача совершенствования функциональной архитектуры кластерных вычислительных систем за счет внедрения методологий создания программного обеспечения прикладного и промежуточного уровней на основе формализованных спецификаций. Одна из таких методологий основана на использовании автоматных спецификаций программного обеспечения вычислительных систем. Сложность решения задачи вызвана разветвленностью построенных алгоритмов, а также наличием циклических участков. Время выполнения разветвленных участков программы и число проходимых циклов зависят от вида вводимых условий и на практике могут быть определены при помощи детальной имитационной модели и анализа созданной на ее основе управляющей программы. Цель работы – нахождение подходов к определению функциональной архитектуры, которые возможно применять практически на основных уровнях предметной ориентации кластерных вычислительных систем.

Методы. Предлагаемые и использованные методы основаны на концепции организации и исследования вычислительных систем кластерного типа с функциональной архитектурой, определяемой исполнимыми автоматными моделями.

Результаты. Предложены методы построения автоматных и логико-вероятностных моделей кластерных вычислительных систем и создания на этой основе программных средств. Вводится понятие логико-вероятностной модели «темпоральная вероятностная система канонических уравнений», которая позволит получить наглядную формализацию и реализацию автоматных моделей и рабочих программ, характерных для кластерных и других приложений, и в существенной степени сократить число «инкрементных» сложений при перечислении моментов дискретного времени. Главной особенностью новой логико-вероятностной модели является сохранение в ее основе исходной системы канонических уравнений.

Выводы. Сделан вывод о том, что выбор системной и функциональной архитектуры вычислительного кластера должен определяться не столько указанными производителем пиковыми характеристиками коммуникационной аппаратуры, сколько реальными показателями, достигаемыми на уровне приложений пользователей и режимов использования кластера. Показано, что исполнимые автоматные модели могут применяться практически на всех уровнях предметной ориентации кластерных вычислительных систем.

Ключевые слова: вычислительная система кластерного типа, приложение промежуточного уровня, функциональная архитектура, логико-вероятностная модель, логико-алгебраическая модель, режимы обработки запросов, результаты моделирования

Для цитирования: Петушков Г.В. Организация и исследование кластерных вычислительных систем с функциональной архитектурой, определяемой исполнимыми моделями. Автоматные исполнимые модели обработки информации. *Russian Technological Journal*. 2025;13(6):7–24. https://doi.org/10.32362/2500-316X-2025-13-6-7-24, https://www.elibrary.ru/WGZAHH

Прозрачность финансовой деятельности: Автор не имеет финансовой заинтересованности в представленных материалах или методах.

Автор заявляет об отсутствии конфликта интересов.

INTRODUCTION

Clustering is one of the most modern trends in the field of computing systems development. The emergence of cluster computing systems is due to advances in network technologies, most often local ones. When connecting machines into a cluster, computers are combined using network technologies based on bus architecture or a switch. This has led to an increase in the number of computing clusters purchased or leased as cloud services [1]. According to forecasts by a number of marketing companies, the cluster computing market is expected to grow to USD102.4 bn by 2032.[1]

The scope of application of clusters in the organization of information and subject-oriented systems used for the collection, processing, and subsequent analysis of information is constantly expanding. At the same time, the limitations of simple homogeneous cluster systems complicate the creation of systems which provide a high level of structural and functional dynamics and effective problem orientation based on the development of the *middleware* level software.

The rapid development of applications based on machine learning and artificial intelligence has created a need to train a large number of models. At the current time, one of the most powerful supercomputers in the world is the Colossus supercomputer cluster based on Nvidia graphics processing units (Nvidia Corporation, USA). This cluster can theoretically achieve a performance of about 497.9 exaflops (497900000 teraflops), setting new standards in supercomputing power. The goal of xAI (USA) is to increase the number of graphics processing units (GPUs) in Colossus to 1 million in the coming years.[2] Currently, the xAI supercluster has begun training a large language model (LLM) artificial intelligence system using more than 200000 Nvidia H100, H200, and GB200 graphics processing units optimized for deep learning neural network tasks. The cluster network is based on a high-speed Nvidia Spectrum-X Ethernet switch with a bandwidth of up to 800 Gb/s.[3]

The functional architecture of computing clusters is based on the coordinated operation of the following components: workflow management system; cluster monitoring system; libraries for parallel processing; cluster management tools; global process space connecting all cluster nodes; resource management system; network (possibly parallel) file system; and network services, including cloud services, providing access to the cluster for many users [1]. It is assumed that current issues in the field of high-performance computing will remain relevant in the future: the need for further significant increases in parallelism and data transfer speeds; the development of high-performance computing architecture and technology; the trend towards workflows and use cases extending beyond data centers; the existence of many powerful scientific and industrial drivers; and the transition from high-performance computing as isolated systems to high-performance infrastructures [2].

An important step in the development of science and industry is linked to the development and

[1] Cluster Computing Market Overview. https://www.marketresearchfuture.com/reports/cluster-computing-market-1746. Accessed June 02, 2025.

[2] Tyson M. Elon Musk fires up ‘the most powerful AI cluster in the world’ to create the ‘world’s most powerful AI’ by December – system uses 100000 Nvidia H100 GPUs on a single fabric. Published July 22, 2024. https://www.tomshardware.com/pc-components/gpus/elon-musk-fires-up-the-most-powerful-ai-training-cluster-in-the-world-uses-100000-nvidia-h100-gpus-on-a-single-fabric. Accessed June 02, 2025.

[3] Half a million GPUs in four months: how Musk is building the world’s most powerful cluster. https://www.braintools.ru/article/18041. Accessed June 02, 2025 (in Russ.).

implementation of the ELBJUWEL supercomputer with artificial intelligence (AI) capabilities.[4] The efforts of the developers are focused on creating a unique innovative platform which will combine expertise in the field of AI and high-performance computing. The works [3–5] are devoted to describing the needs for high-performance computing when solving machine learning problems.

The next problem faced by supercomputing centers is the inefficient use of resources for high-performance computing when resolving certain computational tasks. Such tasks can block valuable computing resources and slow down calculations for other users. In order to address this issue, the National Research University Higher School of Economics has developed a task monitoring system for the cHARISMa high-performance computing cluster which automatically generates conclusions about their performance [6]. This university has accumulated extensive experience in using the supercomputer complex based on the cHARISMa cluster to resolve tasks for various categories of users. These tasks include: searching, analyzing, and forecasting data on social networks [7]; researching machine learning models for predicting the risks of major cardiovascular events in patients with myocardial infarction and different genotypes [8]; and many others.

Additional information on existing software packages in cluster systems is provided in [9–11].

Russian cluster projects include the MVS-100K supercomputer installed at the Interdepartmental Supercomputer Center of the Russian Academy of Sciences and the Lomonosov supercomputer installed at the Research Computing Center of Lomonosov Moscow State University as part of the SKIF project[5]. The "Chervonenkis," "Galushkin," and "Lyapunov" supercomputers, created by Yandex, also have a cluster architecture[6]. They run on Nvidia A100 graphics accelerators (Nvidia A100 GPUs with tensor cores) with an InfiniBand communication system based on Mellanox switches (Israel)[7].

Many issues related to the computing resources required by ordinary users and organizations arise in connection with the organization and use of computing clusters. Therefore, the review of literature must be supplemented with an analysis of some characteristic foreign sources. Articles [12, 13] note the shortcomings of cluster computing systems. Some of these shortcomings contradict the advantages which can be explained by the specifics of enterprises and users. Clusters are difficult to manage without experience and given a large cluster size, it will be difficult to detect a malfunction.

The problem with troubleshooting arises because the user is dealing with a single entity, and when a malfunction is detected, it is unclear which component is causing the problem.

The following circumstance can also be attributed to the disadvantages of cluster computing systems [14]. Clusters are not suitable for commercial and business use by all consumers, as they require special programming skills, knowledge of systems and programming languages that are not widely used for commercial purposes. Personnel are required to have special technical skills for operation and administration.

A large number of the medium-cost and low-cost computing clusters considered are based on various types of switches, including Infiniband and Ethernet switches. In the example of the computing cluster and its infrastructure as shown in Fig. 1, traffic from different local networks can intersect if this does not interfere with the main function of the cluster nodes. Cluster nodes N_1–N_{16} process user load; U_1 and U_2 are control nodes which monitor the status of the cluster's hardware and software and take action to reconfigure it in response to any event occurring in the cluster; M_1 and M_2 are shared backup storage devices. They store information accessible to all cluster nodes and used by them to access shared data, including data about a failed node, which can be used by a backup node. S_1 and S_2 are servers accessible via public and client networks. The private network L_2 level switch exchanges data between cluster nodes using hardware MAC[8] addresses. Command messages used by nodes to check the cluster's operability, reconfigure it, and synchronize it are transmitted over the private network.

The L_3 level switch of the public network exchanges data using IP[9] or hardware MAC addresses. At the public network level, access to the cluster is virtualized as a single system. A local network built on the basis of an L_{2+} level switch with added features provides client access to the cluster. The presence of several network switches in the computing cluster infrastructure enables the use of three main types of networks: communication, transport, and service [15].

[4] *ParTec AG*: *A More Efficient Supercomputer for the AI Revolution*. Frankfurt, Bloomberg; 2024. 43 p.

[5] Center for Collective Use of Ultra-High-Performance Computing Resources at Lomonosov Moscow State University. https://parallel.ru/cluster. Accessed June 02, 2025 (in Russ.).

[6] Chernyavtseva V. *Yandex has created three of Russia's most powerful supercomputers*. https://nplus1.ru/news/2021/11/15/chervonenkis. Accessed June 02, 2025 (in Russ.).

[7] Russia suddenly burst into the world's top most powerful supercomputers. https://www.cnews.ru/news/top/2021-11-16_rossijskie_superkompyutery. Accessed June 02, 2025 (in Russ.).

[8] Media Access Control.

[9] Internet Protocol Address is a unique numerical device identifier.

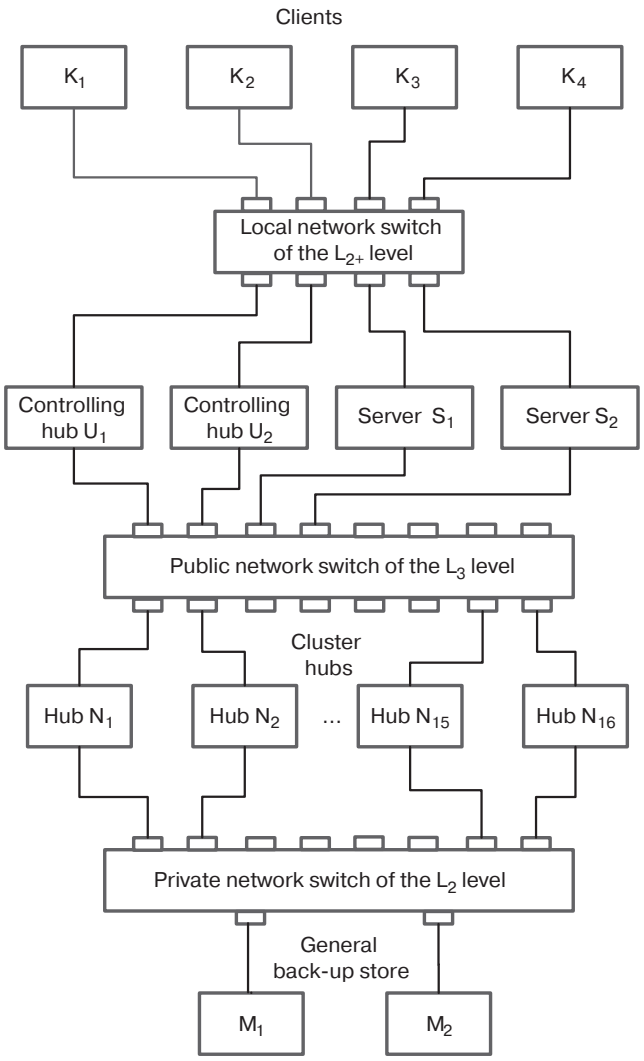

Fig. 1. Option for organizing a computing cluster and its infrastructure

In order to solve the pressing tasks set out in this paper—organizing an effective functional architecture for clusters by creating new application-class and *middleware*-class software—it is important to focus on existing, well-developed software: message processing services—*message-oriented middleware*, services that provide big data analytics and connection to data storage—*data warehousing and big data analytics* data warehousing and big data analytics, and protocols and products that provide *interprocess communications* [15].

1. AUTOMATIC MODELS OF INTERMEDIATE-LEVEL CLUSTER APPLICATIONS

A computing system in operation [1] is defined at an abstract level as a set of functional devices operating in time. When assessing the quality of operation, it is proposed that the content of the operations performed be abstracted and the operation of functional devices in the time reference system be considered. Therefore, it will be useful to construct formal models for analyzing the functioning of computing clusters. In addition, as follows from the "Computing and Cluster Systems" course [15], "in practice, the peak characteristics of communication equipment specified by the manufacturer are not as important as the actual performance achieved at the user application level." This statement implies that the choice of the system and functional architecture of a computing cluster should be determined mainly by the applications and modes of use of the cluster, including those implemented at the *middleware* level. Therefore, part of the application software and middleware can be conditionally considered as system software that determines the functionality of the entire computer cluster.

The main effect of interpreting the models proposed is the possibility that they can be used as formalized specifications when describing parallel processes in cluster computing systems and networks at the level of tasks, data, algorithms, and machine instructions, i.e., at the basic levels of abstraction—from conceptual representation to implementation details. The selection of the following model examples based on program diagrams is based on compliance with a high level of generality. The algorithms must contain all basic algorithmic constructs which enable the implementation of sequences, branches, and cycles. It must be possible to reinterpret types of parallelization—at the task level, at the data level, at the algorithm level, and at the machine-level command level, with the possibility of alternating sequential single-threaded parts of the program with multi-threaded parallel sections.

However, it is only possible to investigate the actual operation of applications on a working cluster. The problem can be resolved at the preliminary stages with less effort and expense by using executable formal models, on the basis of which simulation models of the cluster's operation should be constructed. These models may include characteristic or simplified fragments of real applications.

At this stage of model construction, the semantics of data and operations are not considered, i.e., preserving the generality of the models, the meanings of variables and operation symbols are not interpreted. It is assumed that the methods for creating and interpreting models can be further used in the creation of working interpreted applications when the cluster is put into operation. In this case, formal models can play the role of formalized specifications.

Convenient models for subsequent use for these purposes are: graph-scheme algorithm language (GSA), finite automata, and logic-algebraic models based on

first-order predicate logic. This subsection proposes using Moore's finite partial automaton model[10] [16]. This model is also well known from works in the field of microprogramming [17, 18]. Figures 2 and 3 show examples of GSA selected to illustrate the creation of application models: GSA_1 and GSA_2. The main criteria for selection are the usual requirements for GSA correctness and the presence of sequences of operators and branches. GSA_1 (Fig. 2) contains operator vertices (hereinafter simply operators) $A_0, A_1, A_2, \ldots, A_{16}, A_{27}, A_K$. In addition, GSA_1 contains parallel fragments represented by structured operators C_1, C_2, …, C_8, each of which corresponds to an "internal" copy of GSA_2 (Fig. 3); each copy, or clone, contains local operators $A_{17}, A_{18}, A_{19}, \ldots, A_{25}, A_{26}$.

Both GSAs contain conditional vertices (hereinafter referred to as logical conditions) $x_1, x_2, \ldots, x_5$ (GSA_1) and $x_6, x_7, \ldots, x_{10}$ (GSA_2). Condition symbols are treated as names of unary predicates. The values of logical conditions—0 (true) or 1 (false)—are calculated after the execution of operators, including operators for entering input conditions (input signals, input symbols, or partial automata).

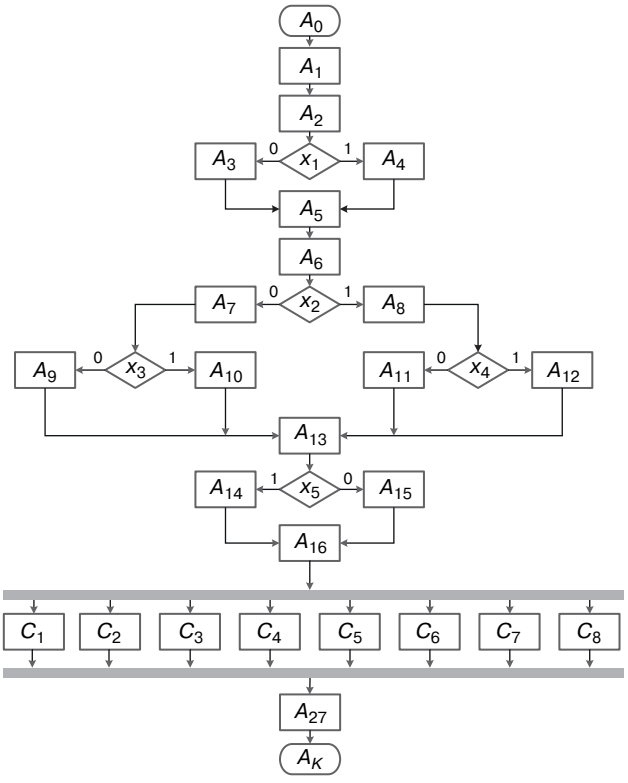

Fig. 2. Flowchart of the GSA_1 algorithm for cluster application operation

The construction and study of automata models will be carried out for the case of SPMD (Single Program, Multiple Data) methods. In the following subsections, other executable models will be constructed based on a logical-algebraic approach: MPMD (Multiple Programs, Multiple Data) and MPSD (Multiple Programs, Single Data) [1]. The latter method is most suitable for pipeline data processing. All these methods are used to achieve parallelism. There are a number of implementation options for these methods used in computing clusters.

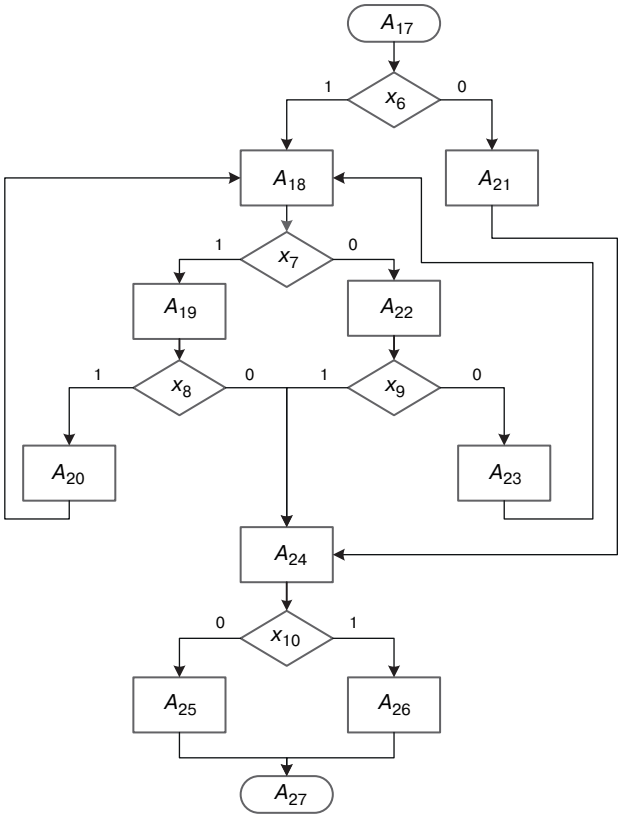

Fig. 3. Block diagram of the GSA_2 algorithm for a single copy of a parallel application section for a cluster

Canonical equation systems (CES) [18, 19], which describe transitions from one state to another, were chosen as the initial language for specifying partial automata. Permissible parallel transitions correspond, for example, to the representation of parallel sections in modified logical diagrams of algorithms, known from works on microprogramming [20]. In these diagrams, parallel sections are considered to be private logical diagrams of algorithms and enable for simple reinterpretation into the graphical form of GSA. Parallel GSA languages were also used in works [21, 22]. The structuring of hierarchical automata states was proposed earlier in a number of works [23–25].

The following concepts are used in the proposed CES models. Operators are assigned a one-to-one

[10] Gurenko V.V. *Introduction to Automata Theory*. Moscow: Bauman Moscow State Technical University; 2013. https://rusist.info/book/10028635?ysclid=mf5p2z07v616437010. Accessed June 02, 2025 (in Russ.).

correspondence with so-called private events, represented by unary predicates of the form $A_i(t)$, defined on the set of discrete time values t. Partial input variables, or input conditions, are represented by unary predicates of the form $x_j(t)$, also defined on the set of discrete time values t. Unary predicates of the form $z_k(t)$, are also introduced to take true values only after the corresponding events of the form $A_k(t)$ have already occurred. This corresponds to the fact that the operator A_k has completed its work. Thus, when $z_k(t) = 0$ (false), the event $A_k(t)$ is preserved, and when $z_k(t) = 1$ (true), it is not preserved. The first condition for the event $A_k(t)$ enables its execution to be extended, and when the second, opposite condition is fulfilled, the event $A_k(t)$ is completed. The condition for the onset of an event corresponds to the transition from the preceding event. The remaining features of the CES construction can be conveniently explained using examples of the transition from GSA to CES.

Figure 4 shows the state transition graph of the sequential application's automaton model, constructed by transitioning from GSA_1 and GSA_2. Section C_0 is highlighted, intended for subsequent cloning when transitioning to the application simulation corresponding to the SPMD cluster operating mode. This graph, as will be required later, can also be viewed as a sequential composition of two partial automata: the first automaton corresponds to states 1–16, and the second to states 17–27.

Figures 2 and 3 use standard GSA notation for logical conditions: $x_1, x_2, \ldots, x_{10}$, which are also considered in the CES entry-level language for specifying partial finite automata as names of unary predicates. In Fig. 4 and further in Fig. 5, other names are used for the three input variables. These are also convenient for further testing of applications using partial automaton analysis: x (value x = true after the end of any operator without calculation or without entering a condition value); nx (value nx = true if, after the end of the operator, a false condition value is calculated or entered, otherwise nx = false); and yx (value yx = true if, after the end of the operator, a true condition value is calculated or entered, otherwise yx = false). The locations for calculating and checking these variables are uniquely determined by the location of the operator. If necessary, this can be used for the usual numbering of logical conditions $x_1, x_2, \ldots, x_{10}$ and used further in the compilation of CES and logic-algebraic expressions. In Fig. 4, the first state is designated as the initial, starting (Start) state, and the 28th as the final, ending (End).

A system of canonical equations can be considered as a system of production rules designed to represent knowledge in automata models. Productions can be used to represent knowledge that can take the form of rules such as "*premise* → *conclusion*, *condition* → *action*." The left side of the rule is called the antecedent, and

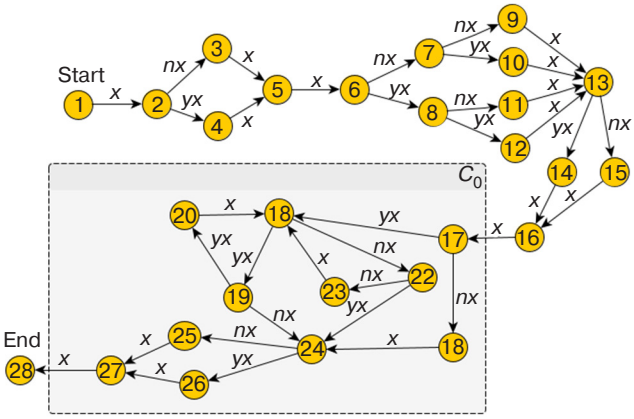

Fig. 4. State transition graph of the sequential application automaton model; section C_0, is highlighted, intended for subsequent cloning when transitioning to SPMD mode

the right side is called the consequent. The antecedent is the premise of the rule (the conditional part) and consists of elementary statements using the logical symbols AND, OR, NOT. The consequent (conclusion) includes one or more statements which express either a certain fact or an indication of a specific action to be performed [26–28]. A set of productions forms a production system for which special procedures are specified for selecting productions and executing one or another production from among those selected.

A distinctive feature of CES, considered as a type of production system, is the placement of the conditional part (antecedent) on the right, and the action or conclusion (consequent) on the left. Therefore, the direction of the conclusion is from right to left. This is largely due to the theory and practice of microprogrammed automata synthesis and the representation, along with canonical equations, of excitation functions of elementary automata (D-triggers, or delay elements) in the unitary encoding of the states of a finite partial automaton [17, 18, 29]. In the future, the concept of "product" will also be used in the construction of logical-algebraic models of cluster-type systems.

2. AUTOMATIC CES MODEL OF THE SEQUENTIAL PART OF THE APPLICATION

Figure 4 shows the state transition graph of the sequential application's automaton model. Some of the states $a_1, a_2, \ldots, a_{16}, a_{28}$ were obtained by marking the states of the Moore automaton on GSA_1, shown in Fig. 2. The rest of the states $a_{17}, a_{18}, \ldots, a_{27}$ belong to the subgraph C_0, which was constructed by marking the states of the Moore automaton on GSA_2.

At this stage, the recurrent predicate equations of the $\boldsymbol{SP}_{\mathbf{Seq}}$ CES for GSA_1 are compiled without taking

into account the structured operators C_1, C_2, …, C_8 and, accordingly, without the structured states a_{17}, a_{18}, …, a_{27} of the automaton, i.e., the model currently covers only operators A_0, A_1, …, A_{16}:

$$A_0(t+1) = A_0(t)\ \&\ \neg x_0(t) \vee x_{begin}(t);$$
$$A_1(t+1) = A_0(t)\ \&\ x_0(t) \vee A_1(t)\ \&\ \neg z_1(t);$$
$$A_2(t+1) = A_1(t)\ \&\ z_1(t) \vee A_2(t)\ \&\ \neg z_2(t);$$
$$A_3(t+1) = A_2(t)\ \&\ z_2(t)\ \&\ \neg x_1(t) \vee A_3(t)\ \&\ \neg z_3(t);$$
$$A_4(t+1) = A_2(t)\ \&\ z_2(t)\ \&\ x_1(t) \vee A_4(t)\ \&\ \neg z_4(t);$$
$$A_5(t+1) = A_3(t)\ \&\ z_3(t) \vee A_4(t)\ \&\ z_4(t) \vee A_5(t)\ \&\ \neg z_5(t);$$
$$A_6(t+1) = A_5(t)\ \&\ z_4(t) \vee A_6(t)\ \&\ \neg z_6(t);$$
$$A_7(t+1) = A_6(t)\ \&\ z_6(t)\ \&\ \neg x_2(t) \vee A_7(t)\ \&\ \neg z_7(t);$$
$$A_8(t+1) = A_6(t)\ \&\ z_6(t)\ \&\ x_2(t) \vee A_8(t)\ \&\ \neg z_8(t);$$
$$A_9(t+1) = A_7(t)\ \&\ z_7(t)\ \&\ \neg x_3(t) \vee A_9(t)\ \&\ \neg z_9(t);$$
$$A_{10}(t+1) = A_7(t)\ \&\ z_7(t)\ \&\ x_3(t) \vee A_{10}(t)\ \&\ \neg z_{10}(t);$$
$$A_{11}(t+1) = A_8(t)\ \&\ z_8(t)\ \&\ \neg x_4(t) \vee A_{11}(t)\ \&\ \neg z_{11}(t);$$
$$A_{12}(t+1) = A_8(t)\ \&\ z_8(t)\ \&\ x_4(t) \vee A_{12}(t)\ \&\ \neg z_{12}(t);$$
$$A_{13}(t+1) = A_9(t)\ \&\ z_9(t) \vee A_{10}(t)\ \&\ z_{10}(t) \vee A_{11}(t)\ \& \& z_{11}(t) \vee A_{12}(t)\ \&\ z_{12}(t) \vee A_{13}(t)\ \&\ \neg z_{13}(t);$$
$$A_{14}(t+1) = A_{13}(t)\ \&\ z_{13}(t)\ \&\ x_5(t) \vee A_{14}(t)\ \&\ \neg z_{14}(t);$$
$$A_{15}(t+1) = A_{13}(t)\ \&\ z_{13}(t)\ \&\ \neg x_5(t) \vee A_{15}(t)\ \&\ \neg z_{15}(t);$$
$$A_{16}(t+1) = A_{14}(t)\ \&\ z_{14}(t) \vee A_{15}(t)\ \&\ z_{15}(t) \vee A_{16}(t)\ \& \& \neg z_{16}(t),$$

where $x_{begin}(t)$ is the input variable ("signal").

Copies (or clones) of the application module compiled according to the $\boldsymbol{SP}_{\mathbf{Seq}}$ CES for GSA_1 are loaded onto all computing nodes of the cluster and executed in parallel mode, processing the same data or entering data of the same type. The automatic model assumes different execution times for events corresponding to application operators. In the further description of the CES equations, for the sake of brevity the terms "event" and "state" will be considered synonymous.

Below are descriptions of some key equations from the given CES. The initial equation has the following form:

$$A_0(t+1) = A_0(t)\ \&\ \neg x_0(t) \vee x_{begin}(t).$$

According to this equation, when the true value of the input variable $x_{begin}(t)$ = true appears in the automaton, the initial event $A_0(t+1)$ = true is set in the next cycle, which corresponds to its inception. This event is retained as long as the condition for its retention $A_0(t)\ \&\ \neg x_0(t)$ at $A_0(t+1)$ = true and $x_0(t)$ = false. Further, when the input signal $x_0(t)$ = true is received, the true condition $A_0(t)\ \&\ x_0(t)$ for the initiation of a new event $A_1(t+1)$ is formed in the automaton:

$$A_1(t+1) = A_0(t)\ \&\ x_0(t) \vee A_1(t)\ \&\ \neg z_1(t).$$

This event persists as long as the condition $A_1(t)\ \&\ \neg z_1(t)$ for its persistence is true. It will end with ($A_1(t+1)$ = false, i.e., this statement will become false) when operator A_1 generates the sign $z_1(t)$ = true indicating the end of its work. As can be seen from the recursive predicate equations of this $\boldsymbol{SP}_{\mathbf{Seq}}$ CES, the event of establishing the truth of the antecedent (right statement) occurs at a fixed moment in time t, and the event of establishing the truth of the consequent (left statement) occurs at the next moment in time ($t+1$).

3. AUTOMATIC CES MODEL OF ONE OF THE PARALLEL SECTIONS (CLONES) OF THE APPLICATION

Figure 4 shows the state transition graph of the sequential application's automaton model; section C_0 is highlighted. This is intended for subsequent cloning when transitioning to SPMD mode.

Recursive predicate equations of CES $\boldsymbol{MD}_{\mathbf{Clon}}$ for GSA_2:

$$A_{17}(t+1) = A_{16}(t)\ \&\ z_{16}(t) \vee A_{17}(t)\ \&\ \neg z_{17}(t);$$
$$A_{18}(t+1) = A_{17}(t)\ \&\ z_{17}(t)\ \&\ x_6(t) \vee A_{20}(t)\ \&\ z_{20}(t) \vee \vee A_{23}(t)\ \&\ z_{23}(t) \vee A_{18}(t)\ \&\ \neg z_{18}(t);$$
$$A_{19}(t+1) = A_{18}(t)\ \&\ z_{18}(t)\ \&\ x_7(t) \vee A_{19}(t)\ \&\ \neg z_{19}(t);$$
$$A_{20}(t+1) = A_{19}(t)\ \&\ z_{19}(t)\ \&\ x_8(t) \vee A_{20}(t)\ \&\ \neg z_{20}(t);$$
$$A_{21}(t+1) = A_{17}(t)\ \&\ z_{17}(t)\ \&\ \neg x_6(t) \vee A_{21}(t)\ \&\ \neg z_{21}(t);$$
$$A_{22}(t+1) = A_{18}(t)\ \&\ z_{18}(t)\ \&\ \neg x_7(t) \vee A_{22}(t)\ \&\ \neg z_{22}(t);$$
$$A_{23}(t+1) = A_{22}(t)\ \&\ z_{22}(t)\ \&\ \neg x_9(t) \vee A_{23}(t)\ \&\ \neg z_{23}(t);$$
$$A_{24}(t+1) = A_{19}(t)\ \&\ z_{19}(t)\ \&\ \neg x_8(t) \vee A_{22}(t)\ \&\ z_{22}(t)\ \& \& x_9(t) \vee A_{21}(t)\ \&\ \neg z_{21}(t) \vee A_{24}(t)\ \&\ \neg z_{24}(t);$$
$$A_{25}(t+1) = A_{24}(t)\ \&\ z_{24}(t)\ \&\ \neg x_{10}(t) \vee A_{25}(t)\ \&\ \neg z_{25}(t);$$
$$A_{26}(t+1) = A_{24}(t)\ \&\ z_{24}(t)\ \&\ x_{10}(t) \vee A_{26}(t)\ \&\ \neg z_{26}(t);$$
$$A_{27}(t+1) = A_{25}(t)\ \&\ z_{25}(t) \vee A_{26}(t)\ \&\ z_{26}(t) \vee A_{27}(t)\ \& \& \neg z_{27}(t).$$

The shared $\boldsymbol{SP}_{\mathbf{Seq}}$ CES model and a single copy of the $\boldsymbol{MD}_{\mathbf{Clon}}$, CES model, taken together, define a single CES model designated $\boldsymbol{SP}_{\mathbf{Seq}} * \boldsymbol{MD}_{\mathbf{Clon}}$, where the symbol "*" denotes the operation of combining two CESs into one common CES. The state transition graph for this model is shown in Fig. 4. Another interpretation, as mentioned earlier, allows the state transition graph $\boldsymbol{SP}_{\mathbf{Seq}} * \boldsymbol{MD}_{\mathbf{Clon}}$ to be considered as a sequential composition of partial automata.

4. SEQUENTIALLY-PARALLEL COMPOSITION OF AUTOMATONS DETERMINING THE OPERATION OF CLUSTER COMPUTERS

The flowchart of the GSA_1 algorithm in Fig. 2 contains parallel sections, abbreviated as structured operators C_1, C_2, …, C_8. In a complete

single-level representation, each of these operators is replaced by GSA_2 in Fig. 3 while, in the program implementation, it is executed independently of the others on its "own" cluster computer. The complete network CES model of a sequential-parallel network of automata is represented by the following expression:

$$\boldsymbol{SP}_{\mathbf{Seq}} * (\boldsymbol{ParReplicate}(\mathbf{1..8})\boldsymbol{MD}_{\mathbf{Clon}}),$$

wherein ***Replicate*(1..8)** is the inclusion of the CES into the general system 8 times in a row. ***Par*** is the indication that these replicas must be executed in parallel.

The state transition graph for this network of partial automata with structured states C_1–C_8 is shown in Fig. 5. When constructing a network CES model, equations need to be compiled to include structured events. Each structured event represents a nested partial automaton. The use of hierarchical finite automata is a fundamentally important method of software design, and corresponds to the concept of a "subroutine".

The advantage of the method of formalizing algorithms using CESs is the compact logical description of transition functions [16, 17]. Structured events with the same names are introduced in a manner analogous to structured states C_1–C_8. Each structured event is "embedded" in already compiled $\boldsymbol{MD}_{\mathbf{Clon}}$.

The initiation and continuation of events C_1–C_8 (initiation and parallel operation of independent software modules) are described by the following CES $\boldsymbol{S}_{\mathbf{C}}$:

$$\begin{aligned}
C_1(t+1) &= A_{16}(t)\ \&\ z_{16}(t) \vee C_1(t)\ \&\ \neg w_1(t);\\
C_2(t+1) &= A_{16}(t)\ \&\ z_{16}(t) \vee C_2(t)\ \&\ \neg w_2(t);\\
C_3(t+1) &= A_{16}(t)\ \&\ z_{16}(t) \vee C_3(t)\ \&\ \neg w_3(t);\\
C_4(t+1) &= A_{16}(t)\ \&\ z_{16}(t) \vee C_4(t)\ \&\ \neg w_4(t);\\
C_5(t+1) &= A_{16}(t)\ \&\ z_{16}(t) \vee C_5(t)\ \&\ \neg w_5(t);\\
C_6(t+1) &= A_{16}(t)\ \&\ z_{16}(t) \vee C_6(t)\ \&\ \neg w_6(t);\\
C_7(t+1) &= A_{16}(t)\ \&\ z_{16}(t) \vee C_7(t)\ \&\ \neg w_7(t);\\
C_8(t+1) &= A_{16}(t)\ \&\ z_{16}(t) \vee C_8(\mathrm{t})\ \&\ \neg w_8(t).
\end{aligned}$$

Each of the events C_1–C_8 originates when the compound statement $A_{16}(t)$ & $z_{16}(t)$ is true, i.e., it is a consequence of the successful completion of the event A_{16}. Each of these events C_i persists until the termination condition $w_i(t)$, i = 1, 2, …, 8 is satisfied. Events C_1–C_8 start simultaneously, but do not necessarily end simultaneously, since the termination conditions may not depend on each other. However, the transition to event A_{28} should only occur after all events C_1–C_8 have been completed. Therefore, the CES model should be followed by events which determine barrier synchronization and consist of waiting for the completion of the events C_1–C_8 in each of the branches, as well as the subsequent initiation and retention of indicator events D_1–D_8 for the termination of all branches.

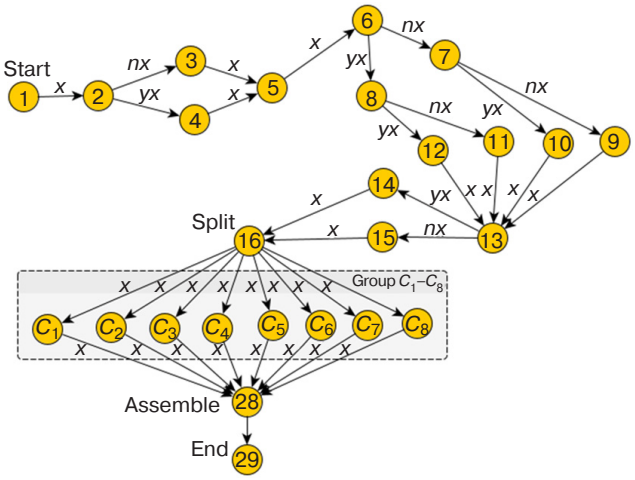

Fig. 5. Sequential-parallel network of automata with nested states of application execution in a cluster in SPMD mode

The system of canonical $\boldsymbol{S}_{\mathbf{D}}$ equations describing the origin and conservation of these events has the following form:

$$\begin{aligned}
D_1(t+1) &= C_1(t)\ \&\ w_1(t) \vee D_1(t)\ \&\ \neg D_9(t);\\
D_2(t+1) &= C_2(t)\ \&\ w_2(t) \vee D_2(t)\ \&\ \neg D_9(t);\\
D_3(t+1) &= C_3(t)\ \&\ w_3(t) \vee D_3(t)\ \&\ \neg D_9(t);\\
D_4(t+1) &= C_4(t)\ \&\ w_4(t) \vee D_4(t)\ \&\ \neg D_9(t);\\
D_5(t+1) &= C_5(t)\ \&\ w_5(t) \vee D_5(t)\ \&\ \neg D_9(t);\\
D_6(t+1) &= C_6(t)\ \&\ w_6(t) \vee D_6(t)\ \&\ \neg D_9(t);\\
D_7(t+1) &= C_7(t)\ \&\ w_7(t) \vee D_7(t)\ \&\ \neg D_9(t);\\
D_8(t+1) &= C_8(t)\ \&\ w_8(t) \vee D_8(t)\ \&\ \neg D_9(t).
\end{aligned}$$

The following single equation, additionally designated as the CES $\boldsymbol{D}_{\mathbf{9}}$, system, describes the expectation of the occurrence of all indicator events D_1–D_8 for the completion of parallel work on all branches:

$$\begin{aligned}
D_9(t+1) = D_1(t)\ \&\ D_2(t)\ \&\ D_3(t)\ \&\ D_4(t)\ \&\ D_5(t)\ \&\\
\&\ D_6(t)\ \&\ D_7(t)\ \&\ D_8(t) \vee D_9(t)\ \&\ \neg v_9(t).
\end{aligned}$$

The equations describing the transition to the final events A_{28}, A_{29} and further to event A_1 of the control module are as follows:

$$\begin{aligned}
A_{28}(t+1) &= D_9(t)\ \&\ v_9(t) \vee A_{28}(t)\ \&\ \neg z_{28}(t);\\
A_{29}(t+1) &= A_{28}(t)\ \&\ z_{28}(t) \vee A_{29}(t)\ \&\ \neg z_{29}(t);\\
A_1(t+1) &= A_{29}(t)\ \&\ z_{29}(t) \vee A_1(t)\ \&\ \neg z_1(t).
\end{aligned}$$

In order to use the equations for the events A_{28} and A_{29} in a combined expression for a network of partial automata, they are designated as separate CESs $\boldsymbol{A_{28}}$ and $\boldsymbol{A_{29}}$, respectively.

In order to implement a detailed network CES model for executing an application in a cluster in sequential-parallel processing (SPMD) mode, all equations must be combined in the following sequence:

$$\text{SPMD: } \boldsymbol{SP_{Seq}} * \boldsymbol{S_C} * \boldsymbol{S_D} * \boldsymbol{D_9} * \boldsymbol{A_{28}} * \boldsymbol{A_{29}},$$

moreover, the initiation of the previously described parallel replicas $\boldsymbol{ParReplicate(1..8)MD_{Clon}}$ is performed upon the occurrence of the events C_1–C_8, determined by the CES $\boldsymbol{S_C}$ subsystem. The completion of these replicas occurs upon the occurrence of the events D_1–D_8, determined by the CES $\boldsymbol{S_D}$ subsystem. When the replicas are running, the range of variation of the variable t, which counts system time, is expanded.

The resulting general CES model of the network of application execution machines in a cluster in SPMD sequential-parallel processing mode belongs to the class of executable models. It is easily programmable in algorithmic languages containing message passing operators, as well as in assembly language for microcontrollers and microprogramming language. A simulation model is built on its basis, enabling the functioning of the cluster system to be studied at the micro level.

The networks of partial finite automata considered in this work consist of automata which simulate application of software modules of a computing cluster connected by a message passing interface at the inputs and outputs. Each module can receive a message at the input which transmits control with data, process it, and transmit a control message with data to the next module. Other types of inter-module interaction in the cluster are not considered. Therefore, issues of automata composition and other methods of constructing complex automata from simple ones are not taken into account here [30].

Automatic programming is currently considered one of the technologies to significantly reduce the time required to write programs and simplify their testing [31]. Systems of canonical equations also enable the creation of application, intermediate, and system-level programs based on them.

As is well known, mutual blocking, ambiguity, and deadlock and other configurations lead to violations of GSA correctness. Therefore, the work proposes to resolve the problem of checking the graph scheme for correctness on an abstract model of algorithm interactions—on Petri nets [32, 33]. Methods for transitioning from a parallel GSA to a Petri net are given, for example, in [21, 22].

5. FORMALIZATION OF LOGICAL-PROBABILISTIC MODELS OF PARTIAL AUTOMATON NETWORKS CREATED BASED ON THE CES LANGUAGE

The concept of a logical-probabilistic model such as "temporal probabilistic CES" (TPCES) will enable the visual formalization and implementation of automatic models and working programs characteristic of cluster and other applications, for example, with pipeline parallelism. This will also significantly reduce the number of "incremental" additions when listing discrete time moments:

$$\text{TPCES} = (\text{CES}_0, \text{S}, \text{X}, \text{T}_\text{X}, \text{W}_\text{TX}, \text{T}_\text{Z}, \text{W}_\text{TZ}),$$

wherein network CES_0 is the initial language adopted for describing the CES finite state machine network, limited by the description of partial machines and characterized by cluster and pipeline computing systems, mainly by the sequential execution of events in time. Furthermore, only simple parallelism of events is enabled without interaction between copies of CES_0 branches, ending with barrier synchronization of branches. S is a finite set of events $\{S_0(t), S_1(t), \ldots, S_n(t)\}$ specified by unary predicates. X is a finite set of input events specified by unary predicates $\{X_0(t), X_1(t), \ldots, X_m(t)\}$. T_X is a finite set of random time intervals $\{t_{x0}, t_{x1}, \ldots, t_{xm}\}$ from the current moments to the moments of occurrence of input events X. W_TX is a finite set of probability distribution functions of the form $P\{t_{xk} = i\} = p_{ki}$, $i = 0, 1, \ldots, i_k$, of random time intervals from the set T_X. T_Z is a finite set of random time intervals $\{t_{z0}, t_{z1}, \ldots, t_{zn}\}$ of preservation. Thus, the occurrence of events from the set S; W_TZ is a finite set of probability distribution functions of the form $P\{t_{zr} = j\} = p_{rj}, j = 0, 1, \ldots, j_r$, of random time intervals from the set T_Z.

Random variables (pseudorandom variables in software implementations) t_x and t_z only take non-negative integer values. Only finite probability distributions of integer random variables are considered. It is also possible to use integer constants as values for t_{Xk}, $k = 0, 1, \ldots, m$ and t_{zr}, $r = 0, 1, \ldots, n$.

The structure of an application containing sequential and independent parallel sections forming a network of automata may enable for a deeper level of nesting, which is characteristic of most cluster computing systems.

The initial non-interpretability of the TPCES model enables it to be applied at the level of programs, program modules, operators, down to the level of machine commands and microprograms.

The general approach to developing a statistically executable model of a cluster application is as follows. The method of organizing a sequence of events is

used, in which periods of event generation alternate with periods of event preservation. Let us assume, for example, that for a sequential section of an application formalized, for example, by the CES $\boldsymbol{SP}_{\mathbf{Seq}}$ system, the actions specified by the following three equations are performed:

$$A_2(t+1) = A_1(t)\ \&\ z_1(t) \vee A_2(t)\ \&\ \neg z_2(t);$$
$$A_3(t+1) = A_2(t)\ \&\ z_2(t)\ \&\ \neg x_1(t) \vee A_3(t)\ \&\ \neg z_3(t);$$
$$A_4(t+1) = A_2(t)\ \&\ z_2(t)\ \&\ x_1(t) \vee A_4(t)\ \&\ \neg z_4(t).$$

As determined when constructing any equation, the onset of the next event, for example, event $A_2(t + 1)$, occurs at time $(t + 1)$. For this event to occur at the specified moment in time then at the previous moment in time t the statements $A_1(t)$ and $z_1(t)$ need to be true—i.e., event $A_1(t)$ would have occurred for the last time at this moment, which would be indicated by the appearance of the true value of the statement $z_1(t)$—the end of the action of the event $A_1(t)$. From the moment of time $(t + 1)$, event $A_2(t + 1)$ begins and continues until statement $z_2(t)$ is false. The appearance of the true value of the statement $z_2(t)$ will lead the compound statement $A_2(t)\ \&\ \neg z_2(t)$ being become false, and the condition for the continuation of event $A_2(t)$ not to be fulfilled. At the next moment in time, the event $A_2(t)$ will occur for the last time, and if the statement $A_2(t)\ \&\ z_2(t)\ \&\ \neg x_1(t)$ is true, then the event $A_2(t)$ will begin to occur (will originate) at the next moment in time $(t + 1$". The preservation of the event $A_2(t)$ can be "extended" by moving to the time mark $t = t + t_{z2}$ of its end, where the value of the time interval t_{z2} is determined using a pseudo-random number generator with a given distribution law. Acting in a similar way, the inception of the event $A_3(t + 1)$ can be delayed by delaying the action of input variable $x_1(t)$ by the amount of the time interval t_{x1}. This is achieved by moving to the time mark of the event $t = t + t_{x1}$ corresponding to the activation of the variable $x_1(t)$. The value of the variable t_{x1} is set by a pseudo-random number generator. The compound statement $A_2(t)\ \&\ z_2(t)\ \&\ \neg x_1(t)$ will become true, and then event $A_3(t + 1)$ will occur at the next moment in time $(t + 1)$. The preservation of the event A_3 and the initiation and preservation of the event A_4 occur in a similar manner. Thus, by transitioning from event to event, the logical-probabilistic model of the cluster application is implemented.

Figure 5 shows a network automaton model of application execution in a cluster in SPMD sequential-parallel mode. With the accepted mode of operation of independent parallel programs in the parallel section of the SPMD mode, independent $\boldsymbol{MD}_{\mathbf{Clon}}$-type CES models can be used to represent structured events C_1–C_8.

6. RESULTS OF STATISTICAL EXPERIMENTS WITH CLUSTER SYSTEM MODELS IN PARALLEL-SERIAL SPMD

Simulation statistical models of application execution were constructed on the basis of automatic probabilistic CES models. The table shows the numerical values of the acceleration coefficient of the application executed in SPMD mode on a computing cluster, obtained from the constructed simulation model. Following [1], acceleration is taken as the ratio of the application execution time on one node $(t_{seq} + Nt_N)$ to the sum $(t_{seq} + t_N)$ of the execution time of the same application in parallel mode on all N nodes of the cluster t_N, and the time t_{seq} of a single execution of a sequential section of the application:

$$k = (t_{seq} + Nt_N) / (t_{seq} + t_N).$$

It was assumed that parallel sections are executed independently of each other. Since the execution times of sequential and parallelized sections are unknown in advance, their statistical characteristics are determined by performing a statistical experiment. Therefore, in the given formula, t_{seq} and t_N are estimates of the mathematical expectations of these time intervals. In the simulation, it was assumed that the execution time of each operator was uniformly distributed from 1 to 9 ms. Transitions between conditions are equally probable (0.5 each).

The results are summarized in the table. The entries in the column headers indicate that the acceleration coefficient k is calculated at the specified time value $T = t_{seq}$, expressed in units of model time (here in milliseconds, ms).

Table. Estimates of the calculation acceleration coefficient k determined using statistical models

N	$T = 0$	$T = 10$	$T = 20$	$T = 30$	$T = 40$	$T = 50$
1	1	1	1	1	1	1
2	2	1.98	1.96	1.94	1.92	1.9
4	4	3.88	3.77	3.67	3.57	3.48
8	8	7.46	7.0	6.6	6.25	5.93
16	16	13.8	12.25	11.0	10.0	9.25
32	32	24.2	19.6	16.5	14.3	12.6

Examples of dependencies of the acceleration coefficient k on the number of nodes in the cluster are illustrated in Fig. 6.

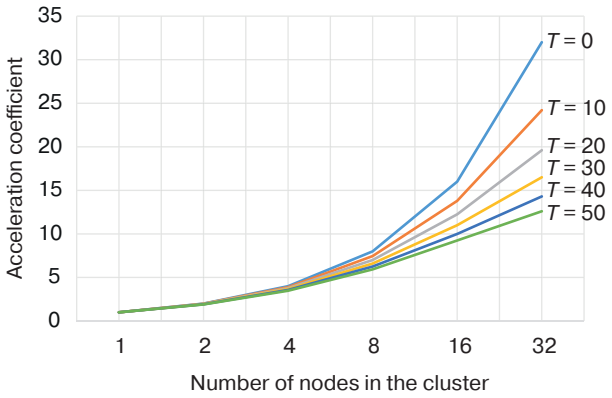

Fig. 6. Results of statistical experiments with cluster models running a sequential-parallel application $L_{Seq} * ParReplicate(i = 1..8)C_i$

At $T = 0$, there is no sequential section, so the acceleration factor values are equal to the number of nodes involved. As values of T increase, the effect of parallelization becomes less pronounced, since the execution time of the sequential section has a greater impact on the result of the acceleration factor calculation.

The complexity of the problem is caused by the branching nature of the selected algorithm, as well as the presence of cycles. The execution time of the branched sections of the program and the number of cycles passed depend on the type of conditions entered and, in practice, can be determined using a detailed simulation model. Both automaton CES models and models based on logical algebraic expressions are executable models, since in order to study the properties and dynamic behavior of the modeled object, the model must be "executed," i.e., run on a computer and the processes of event change must be studied.

The acceleration coefficient k was calculated based on the results of statistical modeling. For example, Fig. 7 shows a histogram of the distribution of the execution time $t_{ex} = t_{seq} + Nt_N$ of the application without parallelization at $N = 1$.

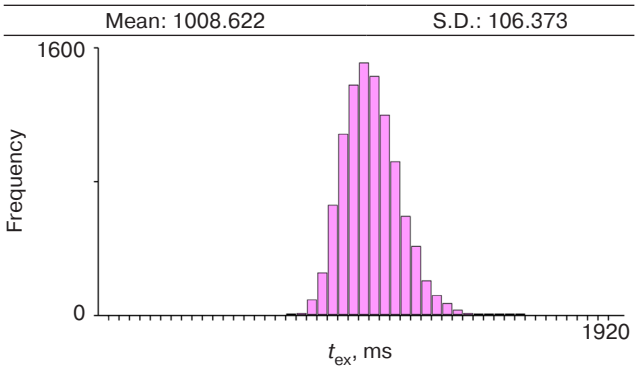

Fig. 7. Histogram of the execution time distribution $t_{ex} = t_{seq} + 32t_{32}$ of the application at $N = 1$ without parallelization; the abscissa axis shows the frequency class boundaries for the histogram, the histogram step is 40 ms; the ordinate axis shows the number of hits in each frequency class with a sample size of 10000

Here, $Mean1 = t_{seq} + 32t_{32} = 1008.622$ ms is the estimate of the mathematical expectation of the application execution time without parallelization.

Figure 8 shows a histogram of the application execution time distribution for $N = 32$ with a sequential section and parallelization. Here, $Mean2 = t_{seq} + t_{32} = 80.266$ ms is the estimate of the mathematical expectation of the application execution time with a sequential section and parallelization of the rest. The execution time of the sequential section was determined in the same experiment and is equal to $t_{seq} = 49.991$ ms.

Then $k = (t_{seq} + 32t_{32})/(t_{seq} + t_{32}) = 12.58$. The same result is obtained by calculating the acceleration coefficient using the known formula for Amdahl's second law [1]:

$$k = N / [\beta N + (1 - \beta)] = 12.61$$

at $N = 32$ with a proportion of sequential calculations

$$\beta = t_{seq} / (t_{seq} + 32t_{32}) = 49.991 / 1008.622 = 0.04957.$$

A small error is caused by the use of the static modeling method when evaluating time parameters in the computing cluster model.

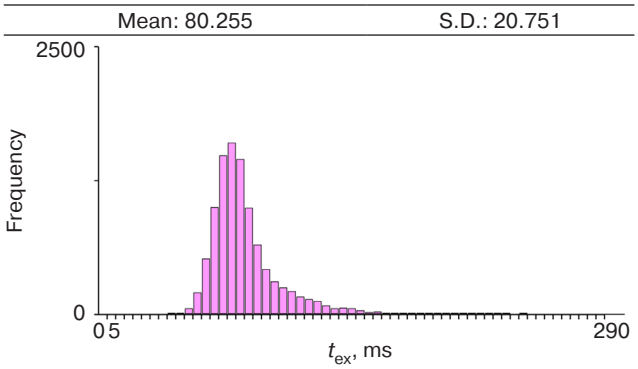

Fig. 8. Histogram of the execution time distribution $t_{ex} = t_{seq} + t_{32}$ of the application at $N = 32$, with a sequential section and parallelization of the rest; the abscissa axis shows the frequency class boundaries for the histogram, the histogram step is 5 ms; the *y*-axis shows the number of hits in each frequency class for a sample size of 10000

7. TRANSITION FROM AUTOMATIC MODELS TO ASYNCHRONOUS LOGICAL-ALGEBRAIC MODELS OF CLUSTER COMPUTING SYSTEMS AT THE *MIDDLEWARE* LEVEL

Logical-algebraic models are based on logical calculi and algebraic systems. Logical calculi include propositional calculus and predicate calculus.

The logical-algebraic operational expression (LAOE) apparatus, based on the integration of a number of models, is described from the perspective of various

applications. It is substantiated in works [34, 35]. However, in the final stages of testing the models by means of studying their dynamics, the direct use of Petri nets is recommended, in this way replacing or removing "innovations" related to the additional use of first-order predicate logic. In order to maintain continuity in the names of the cluster application modules, the names of the operator vertices in GSA_1 (Fig. 2) and GSA_2 (Fig. 3) were chosen for the names of the positions. Double indices were chosen for the indexing of the transitions of the Petri net.

Figure 9 shows examples which illustrate transitions from GSA to the CES model of a partial automaton and further to the initial logical algebraic expressions for a Petri net. Canonical equations have been compiled for the fragments in Figs. 9a and 9b, and logical algebraic expressions have been compiled for the fragment in Fig. 9c.

The system of canonical equations for the examples in Figs. 9a and 9b is as follows:

$$A_3(t+1) = A_2(t)\ \&\ z_2(t) \vee A_3(t)\ \&\ \neg z_3(t);$$
$$A_4(t+1) = A_3(t)\ \&\ z_3(t)\ \&\ \neg x_1(t) \vee A_4(t)\ \&\ \neg z_4(t);$$
$$A_5(t+1) = A_3(t)\ \&\ z_3(t)\ \&\ x_1(t) \vee A_4(t)\ \&\ \neg z_4(t).$$

The CES model is synchronous, and during simulation, the current time of event execution must be counted. This slows down the simulation program. According to the previously introduced designations for input variables in partial automata in Fig. 4 and Fig. 9b, x = true, $nx = \neg x_1$ and $yx = x_1$.

The asynchronous LAOE system shown in Fig. 9c is represented as follows:

$$T_{2,3}: [M(A_2)\&\neg M(A_3)](\{M(A_2) \neg \text{false}, M(A_3) \neg \text{true}\} \vee \vee Ret);$$

$$T_{3,4}: [M(A_3)\ \&\ \neg M(A_4)\ \&\ \neg X(A_3)](\{X(A_3) \neg \text{undef}, M(A_3) \neg \text{false}, M(A_4) \neg \text{true}\} \vee Ret);$$

$$T_{3,5}: [M(A_3)\ \&\ \neg M(A_5)\ \&\ X(A_3)](\{X(A_3) \neg \text{undef}, M(A_3) \neg \text{false}, M(A_5) \neg \text{true}\} \vee Ret),$$

wherein undef is an undefined value of a logical condition.

The LAOE expressions given in this case are interpreted as rules for triggering transitions in a Petri net. Here, M is a unary predicate, or a function for marking positions, with the same name as the operators of the original GSA; $M(A_i)$ is a statement, the truth of which corresponds to the presence of one label in position A_i, while falsity corresponds to the absence of a label. X is a unary predicate which defines the conditions in the original GSA. $X(A_i)$ is a statement which takes true, false, or undefined values, determined by the result of executing the operator A_i. The *Ret* operator enhances the procedural component of the LAOE and transitions to its repeated execution when the condition enclosed in square brackets is false.

A logical-algebraic operational model can obviously be constructed using a state transition graph (Fig. 9b), which served as the basis for constructing a Petri net (Fig. 9c). For this purpose, compliance is required with the rule of forming conditions by operators, including condition input operators.

The rules for triggering transitions can be further modified or supplemented in accordance with the requirements of the subject area. Additional events—message transmission, message reception, transmission acknowledgment, event duration determination, represented by binary or ternary predicate modification operations—may not correspond to the generally accepted concepts of Petri nets. Therefore, transition

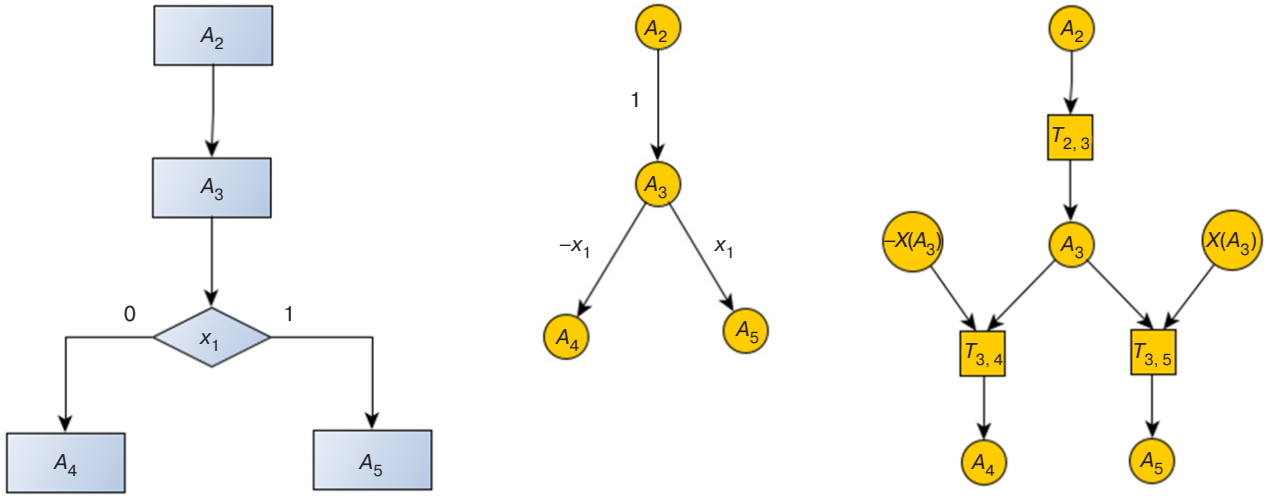

(a) (b) (c)

Fig. 9. Fragments of the GSA (a), the transition graph of a partial automaton (b), and a Petri net (c)

rules can take the form of more general LAOEs, for which other apparatus is used: apparatus of algorithmic algebra systems [36, 37]; abstract machine networks [38]; relational calculus and algebras [39].

CONCLUSIONS

1. The relevance of the tasks addressed in this article arises from the limitations of simple homogeneous cluster systems which complicate the creation of systems providing a high level of structural and functional dynamics. New approaches to designing the system and functional architecture of computing clusters can be based on organizing the effective use and management of cluster operations, by means of enhanced problem orientation by creating *middleware* applications and software.
2. The method proposed and used in this work is based on the concept of architecture design defined by executable models. This is a type of object-oriented design.
3. A distinctive feature of the methods proposed in this work is the use of automatic, network automata. In the future, logical-algebraic approaches may be implemented, in order to define the system and functional architecture, applied at virtually all levels of subject orientation of cluster computing systems. These will ensure the implementation of the architectural concept formed when creating a cluster system model at various levels of abstraction—from conceptual representation to implementation details.
4. The work shows that the main effect of interpreting the proposed automata models and methods is the possibility of their use as formalized specifications when describing parallel processes in cluster computing systems at the level of tasks, data, algorithms, and machine instructions.
5. The results of statistical experiments show the correctness of constructing probabilistic-automata CES models and logical-probabilistic models, as well as the possibility of using them as formalized specifications.

REFERENCES

1. Voevodin V.V., Voevodin Vl.V. *Parallel'nye vychisleniya* (*Parallel Computing)*. St. Petersburg: BHV-Petersburg; 2002. 608 p. (in Russ.).
2. Pleiter D. Supercomputer Architectures: Current State and Future Trends. *The AQTIVATE Project, European Union's HORIZON MSCA Doctoral Networks Programmer, Grant Agreement No. 101072344.* September 2023. 38 p.
3. Boldyrev A., Ratnikov F., Shevelev A. Approach to Finding a Robust Deep Learning Model. *IEEE Access*. 2025;13: 102390–102406. https://doi.org/10.1109/ACCESS.2025.3578926, https://doi.org/10.48550/arXiv.2505.17254
4. Mishenin R.M., Kostenetskii P.S. Modeling the task flow of the HSE computing cluster using SLURM Simulator. In: *Parallel Computing Technologies* (*PCT'2025*): Proceedings of the 19th All-Russian Scientific Conference with International Participation. Moscow; 2025. P. 324 (in Russ.).
5. Promyslov G., Efremov A., Ilyasov Y., Pisarev V., Timofeev A. Efficiency of Machine Learning Tasks on HPC Devices. In: *Parallel Computing Technologies* (*PCT'2025*): Proceedings of the 19th All-Russian Scientific Conference with International Participation. Moscow; 2025. P. 56–81 (in Russ.).
6. Kostenetskiy P.S., Kozyrev V.I., Chulkevich R.A., Raimova A.A. Enhancement of the Data Analysis Subsystem in the Task-Efficiency Monitoring System HPC TaskMaster for the cHARISMa Supercomputer Complex at HSE University. In: Sokolinsky L., Zymbler M., Voevodin V., Dongarra J. (Eds.). *Parallel Computational Technologies* (*PCT'2024*). *Communications in Computer and Information Science*. Springer; 2024. V. 2241. P. 49–64. https://doi.org/10.1007/978-3-031-73372-7_4
7. Slastnikov S.A., Zhukova L.F., Semichasnov I.V. Application for data retrieval, analysis, and forecasting in social networks. *Informatsionnye tekhnologii i vychislitel'nye sistemy = Journal of Information Technologies and Computing Systems.* 2024;1:97–108 (in Russ.). https://doi.org/10.14357/20718632240110
8. Kirdeev A., Burkin K., Vorobev A., Zbirovskaya E., Lifshits G., Nikolaev K., Zelenskaya E., Donnikov M., Kovalenko L., Urvantseva I., Poptsova M. Machine learning models for predicting risks of MACEs for myocardial infarction patients with different VEGFR2 genotypes. *Front. Med.* 2024;11:1452239. https://doi.org/10.3389/fmed.2024.1452239
9. Al-Khulaidi A., Sadovoy N. Analysis of existing software packages in the cluster systems. *Vestnik Donskogo gosudarstvennogo tekhnicheskogo universiteta = Vestnik of Don State Technical University*. 2010;10(3):303–310 (in Russ.). https://elibrary.ru/mvsqql
10. Ladygin I.I., Loginov A.V., Filatov A.V., Yankov S.G. *Klastery na mnogoyadernykh protsessorakh* (*Clusters on Multi-Core Processors*). Moscow: MPEI Publ.; 2008. 112 p. (in Russ.). ISBN 978-5-383-00142-4. https://elibrary.ru/qmsnap
11. Kokots A.V. Development of a software model of an effective cluster computing system *Vychislitel'nye seti. Teoriya i praktika = Network Journal. Theory and Practice.* 2016;2(29):6.1. Available from URL: https://network-journal.mpei.ac.ru/ (in Russ.). Accessed June 02, 2025.

12. Kaur K., Rai A.K. A Comparative Analysis: Grid, Cluster and Cloud Computing. *Int. J. Adv. Res. Computer Commun. Eng*. 2014;3(3):5730–5734.
13. Omer S.M.I., Mustafa A.B.A., Alghali F.A.E. Comparative study between Cluster, Grid, Utility, Cloud and Autonomic computing. *IOSR Journal of Electrical and Electronics Engineering* (*IOSR-JEEE*). 2014;9(6):61–67. http://doi.org/10.9790/1676-09636167
14. Kumar R. Comparison between Cloud Computing, Grid Computing, Cluster Computing and Virtualization. *Int. J. Mod. Computer Sci. Appl*. (*IJMCSA*). 2015;3(1):42–47. http://doi.org/10.13140/2.1.1759.7765
15. Voevodin Vl.V., Zhumatii S.A. *Vychislitel'noe delo i klasternye sistemy* (*Computing and Cluster Systems*). Moscow: MSU Press; 2007. 150 p. (in Russ.). ISBN 978-5-211-05440-0
16. Hopcroft J.D., Motwani R., Ulman J.D. *Vvedenie v teoriyu avtomatov, yazykov i vychislenii* (*Introduction to Automata Theory, Languages, and Computations*): transl. from Engl. Moscow: Vil'yams; 2015. 528 p. (in Russ.). ISBN 978-5-8459-1969-4
[Hopcroft J.E., Motwani R., Ulman J.D. *Introduction to Automata Theory, Languages and Computation*. Boston, etc.: Addison-Wesley Publ. Comp.; 2001. 521 p.]
17. Baranov S.I. *Sintez mikroprogrammnykh avtomatov* (*Graf-skhemy i avtomaty*) (*Synthesis of Microprogrammed Automata* (*Graph-Schemes and Automata*)). Leningrad: Energiya; 1979. 231 p. (in Russ.).
18. Vashkevich N.P. *Sintez mikroprogrammnykh upravlyayushchikh avtomatov* (*Synthesis of Microprogram Control Automata*). Penza; 1990. 115 c. (in Russ.).
19. Vashkevich N.P., Sibiryakov M.A. The formal automatic models of algorithms of processing of cached data. *Sovremennye naukoemkie tekhnologii = Modern High Technologies*. 2016;(8-2):205–213 (in Russ.). https://elibrary.ru/whksst
20. Lazarev V.G., Piil' E.I., Turuta E.N. *Postroenie programmiruemykh upravlyayushchikh ustroistv* (*Construction of Programmable Control Devices*). Moscow: Energoatomizdat; 1984. 264 p. (in Russ.).
21. Anishev P.A., Achasova S.M., Bandman O.L. *Metody parallel'nogo programmirovaniya* (*Methods of Parallel Programming*). Novosibirsk: Nauka; 1981. 180 p. (in Russ.).
22. Yuditskii S.A., Magergut V.Z. *Logicheskoe upravlenie diskretnymi protsessami. Modeli, analiz, sintez* (*Logical Control of Discrete Processes. Models, Analysis, Synthesis*). Moscow: Mashinostroenie; 1987. 176 p. (in Russ.).
23. Girault A., Lee E.A. Hierarchical finite state machines with multiple concurrency models. *IEEE Trans. Comput.-Aided Design Integr. Circuits Syst*. 1999;18(6):742–760. https://doi.org/10.1109/43.766725
24. Stefansson E., Johansson K.H. Hierarchical finite state machines for efficient optimal planning in large-scale systems. In: *2023 European Control Conference* (*ECC*). June, Bucharest, Romania. IEEE; 2023. https://doi.org/10.23919/ECC57647.2023.10178139
25. Alur R., Yannakakis M. Model checking of hierarchical state machines. *ACM SIGSOFT Software Engineering Notes*. 1998;23(6):175–188. http://doi.org/10.1145/503502.503503
26. Bolotova L.S. *Sistemy iskusstvennogo intellekta. Modeli i tekhnologii, osnovannye na znaniyakh* (*Artificial Intelligence Systems. Models and Technologies Based on Knowledge*). Moscow: Finansy i statistika; 2012. 664 p. (in Russ.). ISBN 978-5-279-03530-4
27. Thayse A., Gribomont P., Louis J. *Logicheskii podkhod k iskusstvennomu intellektu: ot klassicheskoi logiki k logicheskomu programmirovaniyu* (*Logical Approach to Artificial Intelligence: From Classical Logic to Logical Programming*): transl. from French. Moscow: Mir; 1990. 429 p. (in Russ.). ISBN 5-03-001636-8
28. Ueno H., Ishizuka M. (Eds.). *Predstavlenie i ispol'zovanie znanii* (*Representation and Use of Knowledge*): transl. from. Japan. Moscow: Mir; 1989. 220 p. (in Russ.). ISBN 5-03-000685-0
29. Evreinov E.V., Kosarev Yu.G. *Odnorodnye universal'nye sistemy vysokoi proizvoditel'nosti* (*Homogeneous Universal Systems of High Productivity*). Novosibirsk: Nauka; 1966. 308 p. (in Russ.).
30. Belov V.V., Vorob'ev E.M., Shatalov V.E. *Teoriya grafov* (*Graph Theory*). Moscow: Vysshaya shkola; 1976. 392 p. (in Russ.).
31. Polikarpova N.I., Shalyto A.A. *Avtomatnoe programmirovanie* (*Automata Programming*): 2nd ed. St. Petersburg: Piter; 2011. 176 p. (in Russ.). ISBN 987-5-4237-0075-1
32. Peterson J. *Teoriya setei Petri i modelirovanie system* (*Petri Net Theory and the Modeling of Systems*): transl. from Engl. Moscow: Mir; 1984. 368 p. (in Russ.).
[Peterson J.L. *Petri Net Theory and the Modeling of Systems.* NY: Prentice-Hall; 1981. 310 p.]
33. Kotov V.E. *Seti Petri* (*Petri Nets*). Moscow: Nauka; 1984. 160 p. (in Russ.).
34. Volchikhin V.I., Zinkin S.A. Logic and algebraic models and methods in designing functional architecture of distributed data storage and processing systems. *Izvestiya vuzov. Povolzhskii region. Tekhnicheskie nauki = University Proceedings. Volga Region. Technical Sciences*. 2012;2:3–16 (in Russ.). https://elibrary.ru/pfpgml
35. Zinkin S.A. Elements of a new object-oriented technology for modeling and implementing systems and networks for storing and processing data. *Informatsionnye tekhnologii = Information Technologies*. 2008;10:20–27 (in Russ.).
36. Andon F.I., Doroshenko A.E., Tseitlin G.E., Yatsenko E.A. *Algebroalgoritmicheskie modeli i metody parallel'nogo programmirovaniya* (*Algebraic Algorithmic Models and Methods of Parallel Programming*). Kiev: Akademperiodika; 2007. 634 p. (in Russ.).
37. Yushchenko E.L., Tseitlin G.E, Gritsai V.P., Terzyan T.K. *Mnogourovnevoe strukturnoe proektirovanie programm. Teoreticheskie osnovy, instrumentarii* (*Multilevel structural design of programs. Theoretical foundations, tools*). Moscow: Finansy i statistika; 1989. 208 p. (in Russ.). ISBN 5-279-00233-X
38. Gurevich Y. Abstract State Machines: An Overview of the Project. In: Seipel D., Turull-Torres J.M. (Eds.). *Foundations of Information and Knowledge Systems. Lecture Notes in Computer Science.* Springer; 2004. V. 2942. P. 6–13. https://doi.org/10.1007/978-3-540-24627-5_2

39. Maier D. *Teoriya relyatsionnykh baz dannykh* (*The Theory of Relational databases*): transl. from Engl. Moscow: Mir; 1987. 608 p. (in Russ.).
[Maier D. *The Theory of Relational databases:* 1st ed. Computer Sci. Press; 1983. 656 p.]

СПИСОК ЛИТЕРАТУРЫ

1. Воеводин В.В., Воеводин Вл.В. *Параллельные вычисления*. СПб.: БХВ-Петербург; 2002. 608 с.
2. Pleiter D. Supercomputer Architectures: Current State and Future Trends. *The AQTIVATE Project, European Union's HORIZON MSCA Doctoral Networks Programmer, Grant Agreement No. 101072344.* September 2023. 38 p.
3. Boldyrev A., Ratnikov F., Shevelev A. Approach to Finding a Robust Deep Learning Model. *IEEE Access*. 2025;13: 102390–102406. https://doi.org/10.1109/ACCESS.2025.3578926, https://doi.org/10.48550/arXiv.2505.17254
4. Мишенин Р.М., Костенецкий П.С. Моделирование потока задач вычислительного кластера НИУ ВШЭ с использованием SLURM Simulator. В сб.: *Параллельные вычислительные технологии* (*ПаВТ'2025*): сборник трудов XIX Всероссийской научной конференции с международным участием. М.: 2025. С. 324.
5. Promyslov G., Efremov A., Ilyasov Y., Pisarev V., Timofeev A. Efficiency of Machine Learning Tasks on HPC Devices. В сб.: *Параллельные вычислительные технологии* (*ПаВТ'2025*): сборник трудов XIX Всероссийской научной конференции с международным участием. М.; 2025. С. 56–81.
6. Kostenetskiy P.S., Kozyrev V.I., Chulkevich R.A., Raimova A.A. Enhancement of the Data Analysis Subsystem in the Task-Efficiency Monitoring System HPC TaskMaster for the cHARISMa Supercomputer Complex at HSE University. In: Sokolinsky L., Zymbler M., Voevodin V., Dongarra J. (Eds.). *Parallel Computational Technologies* (*PCT'2024*). *Communications in Computer and Information Science*. Springer; 2024. V. 2241. P. 49–64. https://doi.org/10.1007/978-3-031-73372-7_4
7. Сластников С.А., Жукова Л.Ф., Семичаснов И.В. Приложение поиска, анализа и прогнозирования данных в социальных сетях. *Информационные технологии и вычислительные системы.* 2024;1:97–108. https://doi.org/10.14357/20718632240110
8. Kirdeev A., Burkin K., Vorobev A., Zbirovskaya E., Lifshits G., Nikolaev K., Zelenskaya E., Donnikov M., Kovalenko L., Urvantseva I., Poptsova M. Machine learning models for predicting risks of MACEs for myocardial infarction patients with different VEGFR2 genotypes. *Front. Med.* 2024;11:1452239. https://doi.org/10.3389/fmed.2024.1452239
9. Аль-Хулайди А.А., Садовой Н.Н. Анализ существующих программных пакетов в кластерных системах. *Вестник Донского государственного технического университета* (*Вестник ДГТУ*). 2010;10(3-46):303–310. https://elibrary.ru/mvsqql
10. Ладыгин И.И., Логинов А.В., Филатов А.В., Яньков С.Г. *Кластеры на многоядерных процессорах.* М.: Издательский дом МЭИ; 2008. 112 с. ISBN 978-5-383-00142-4. https://elibrary.ru/qmsnap
11. Кокоц А.В. Разработка программной модели функционирования кластерной вычислительной системы. *Вычислительные сети. Теория и практика*. 2016;2(29):6.1. URL: https://network-journal.mpei.ac.ru/. Дата обращения 02.06.2025.
12. Kaur K., Rai A.K. A Comparative Analysis: Grid, Cluster and Cloud Computing. *Int. J. Adv. Res. Computer Commun. Eng*. 2014;3(3):5730–5734.
13. Omer S.M.I., Mustafa A.B.A., Alghali F.A.E. Comparative study between Cluster, Grid, Utility, Cloud and Autonomic computing. *IOSR Journal of Electrical and Electronics Engineering* (*IOSR-JEEE*). 2014;9(6):61–67. http://doi.org/10.9790/1676-09636167
14. Kumar R. Comparison between Cloud Computing, Grid Computing, Cluster Computing and Virtualization. *Int. J. Mod. Computer Sci. Appl*. (*IJMCSA*). 2015;3(1):42–47. http://doi.org/10.13140/2.1.1759.7765
15. Воеводин Вл.В., Жуматий С.А. *Вычислительное дело и кластерные системы*. М.: Изд-во МГУ; 2007. 150 с. ISBN 978-5-211-05440-0
16. Хопкрофт Д., Мотвани Р., Ульман Д. *Введение в теорию автоматов, языков и вычислений*: пер. с англ. М.: Вильямс; 2015. 528 с. ISBN 978-5-8459-1969-4
17. Баранов С.И. *Синтез микропрограммных автоматов* (*Граф-схемы и автоматы*). Л.: Энергия; 1979. 231 с.
18. Вашкевич Н.П. *Синтез микропрограммных управляющих автоматов*. Пенза: Изд-во Пенз. политехн. ин-та; 1990. 115 с.
19. Вашкевич Н.П., Сибиряков М.А. Формальные автоматные модели алгоритмов обработки кэшируемой информации. *Современные наукоемкие технологии*. 2016;(8-2):205–213. https://elibrary.ru/whksst
20. Лазарев В.Г., Пийль Е.И., Турута Е.Н. *Построение программируемых управляющих устройств*. М.: Энергоатомиздат; 1984. 264 с.
21. Анишев П.А., Ачасова С.М., Бандман О.Л. *Методы параллельного программирования*. Новосибирск: Наука; 1981. 180 с.
22. Юдицкий С.А., Магергут В.З. *Логическое управление дискретными процессами. Модели, анализ, синтез*. М.: Машиностроение; 1987. 176 с.
23. Girault A., Lee E.A. Hierarchical finite state machines with multiple concurrency models. *IEEE Trans. Comput.-Aided Design Integr. Circuits Syst*. 1999;18(6):742–760. https://doi.org/10.1109/43.766725
24. Stefansson E., Johansson K.H. Hierarchical finite state machines for efficient optimal planning in large-scale systems. In: *2023 European Control Conference* (*ECC*). June, Bucharest, Romania. IEEE; 2023. https://doi.org/10.23919/ECC57647.2023.10178139

25. Alur R., Yannakakis M. Model checking of hierarchical state machines. *ACM SIGSOFT Software Engineering Notes*. 1998;23(6):175–188. http://doi.org/10.1145/503502.503503
26. Болотова Л.С. *Системы искусственного интеллекта. Модели и технологии, основанные на знаниях*. М.: Финансы и статистика; 2012. 664 с. ISBN 978-5-279-03530-4
27. Тейз А., Грибомон П., Луи Ж. *Логический подход к искусственному интеллекту: от классической логики к логическому программированию*: пер. с франц. М.: Мир; 1990. 429 с. ISBN 5-03-001636-8
28. *Представление и использование знаний*; под ред. Х. Уэно, М. Исидзука. М.: Мир; 1989. 220 с. ISBN 5-03-000685-0
29. Евреинов Э.В., Косарев Ю.Г. *Однородные универсальные системы высокой производительности*. Новосибирск: Наука, Сибирское отд.; 1966. 308 с.
30. Белов В.В., Воробьев Е.М., Шаталов В.Е. *Теория графов*. М.: Высшая школа; 1976. 392 с.
31. Поликарпова Н.И., Шалыто А.А. *Автоматное программирование*: 2-е изд. СПб.: Питер; 2011. 176 с. ISBN 987-5-4237-0075-1
32. Питерсон Дж. *Теория сетей Петри и моделирование систем*: пер. с англ. М.: Мир; 1984. 368 с.
33. Котов В.Е. *Сети Петри*. М.: Наука; 1984. 160 с.
34. Волчихин В.И., Зинкин С.А. Логико-алгебраические модели и методы в проектировании функциональной архитектуры распределенных систем хранения и обработки данных. *Известия вузов. Поволжский регион. Технические науки.* 2012;2:3–16. https://elibrary.ru/pfpgml
35. Зинкин С.А. Элементы новой объектно-ориентированной технологии для моделирования и реализации систем и сетей хранения и обработки данных. *Информационные технологии*. 2008;10:20–27.
36. Андон Ф.И., Дорошенко А.Е., Цейтлин Г.Е., Яценко Е.А. *Алгеброалгоритмические модели и методы параллельного программирования*. Киев: Академпериодика; 2007. 634 с.
37. Ющенко Е.Л., Цейтлин Г.Е, Грицай В.П., Терзян Т.К. *Многоуровневое структурное проектирование программ. Теоретические основы, инструментарий*. М.: Финансы и статистика; 1989. 208 с. ISBN 5-279-00233-X
38. Gurevich Y. Abstract State Machines: An Overview of the Project. In: Seipel D., Turull-Torres J.M. (Eds.). *Foundations of Information and Knowledge Systems. Lecture Notes in Computer Science.* Springer; 2004. V. 2942. P. 6–13. https://doi.org/10.1007/978-3-540-24627-5_2
39. Мейер Д. *Теория реляционных баз данных*: пер. с англ. М.: Мир; 1987. 608 с.

About the Author

Grigory V. Petushkov, Vice-Rector, MIREA – Russian Technological University (78, Vernadskogo pr., Moscow, 119454 Russia). E-mail: petushkov@mirea.ru. RSCI SPIN-code 4985-4344, https://orcid.org/0009-0006-0801-429X

Об авторе

Петушков Григорий Валерьевич, проректор, ФГБОУ ВО «МИРЭА – Российский технологический университет» (119454, Россия, Москва, пр-т Вернадского, д. 78). E-mail: petushkov@mirea.ru. SPIN-код РИНЦ 4985-4344, https://orcid.org/0009-0006-0801-429X

Translated from Russian into English by Lyudmila O. Bychkova
Edited for English language and spelling by Dr. David Mossop

Information systems. Computer sciences. Issues of information security
Информационные системы. Информатика. Проблемы информационной безопасности

UDC 004.387
https://doi.org/10.32362/2500-316X-2025-13-6-25-46
EDN XEUFSE

RESEARCH ARTICLE

Approach for identifying the optimal set of qubits of quantum computing devices based on a model for generating binary random sequences

Andrey V. Korolkov, Andrey A. Kryuchkov @

MIREA – Russian Technological University, Moscow, 119454 Russia
@ *Corresponding author, e-mail: kryuchkov_a@mirea.ru*

• **Submitted:** 23.12.2024 • **Revised:** 15.05.2025 • **Accepted:** 06.10.2025

Abstract

Objectives. The absence of error-resistant quantum computers, coupled with the challenges associated with providing unrestricted and fully operational physical access to cloud quantum computing systems, prompts a critical examination of the necessity to develop universal and independent methods for evaluating and verifying cloud quantum computers. A promising approach involves evaluating the capabilities of a quantum computer in relation to its effectiveness in addressing specific challenges encountered in the assessment of information security systems. A potential test for ascertaining the performance and computational quality of a quantum computing device (QCD) is based on a model designed to generate a random binary sequence. By analyzing this sequence, insights can be obtained into the accuracy and reliability of the quantum register under study. The paper presents a software program developed for simulating the operation of a quantum random number generator.

Methods. The software implementation for interacting with cloud quantum computers was performed using the Qiskit open-source software kit. The graphical user interface of the software package was developed using a Qt5 cross-platform set of tools and widgets for creating applications. The analysis of the generated binary sequence was performed using a set of statistical tests NIST STS[1].

Results. The developed software package provides users with a graphical interface for conducting an analysis of a cloud QCD to identify the optimal and most error-resistant set of qubits. The findings from experiments conducted on three cloud quantum computing devices are reported.

Conclusions. The proposed approach, which is constrained by limitations of computing power and duration of access to cloud-based QCD, imposes minimal demands on the productive capabilities of the quantum system. It offers clear and unequivocally interpretable insights into the technical characteristics of a cloud quantum computer, while also being reproducible, easily scalable, and universally applicable.

Keywords: quantum computer, quantum computer device, random number generator, benchmarking

[1] The National Institute of Standards and Technology, Statistical Test Suite.

For citation: Korolkov A.V., Kryuchkov A.A. Approach for identifying the optimal set of qubits of quantum computing devices based on a model for generating binary random sequences. *Russian Technological Journal.* 2025;13(6):25–46. https://doi.org/10.32362/2500-316X-2025-13-6-25-46, https://www.elibrary.ru/XEUFSE

Financial disclosure: The authors have no financial or proprietary interest in any material or method mentioned.

The authors declare no conflicts of interest.

НАУЧНАЯ СТАТЬЯ

Подход к выявлению оптимального набора кубит квантовых вычислительных устройств на примере модели генерации случайных двоичных последовательностей

А.В. Корольков, А.А. Крючков @

МИРЭА – Российский технологический университет, Москва, 119454 Россия
@ *Автор для переписки, e-mail: kryuchkov_a@mirea.ru*

• **Поступила:** 23.12.2024 • **Доработана:** 15.05.2025 • **Принята к опубликованию:** 06.10.2025

Резюме

Цели. Отсутствие квантовых компьютеров, устойчивых к ошибкам, а также невозможность обеспечить беспрепятственный и полнофункциональный физический доступ к облачным квантовым системам поднимает актуальный вопрос о необходимости разработки методов оценки и верификации облачных квантовых компьютеров. Авторам видится перспективным использование подхода к анализу возможностей квантового процессора в контексте его применимости для решения некоторых задач, возникающих при оценке систем защиты информации. Одним из примеров теста квантового вычислительного устройства (КВУ) на предмет выявления уровня производительности и качества вычислений может послужить модель генерации случайной двоичной последовательности, анализ которой предоставляет информацию о корректности и надежности исследуемого квантового регистра. Цель работы заключается в разработке программного комплекса, с помощью которого представляется возможным моделирование работы КВУ в режиме квантового генератора случайных чисел.

Методы. Программная реализация по взаимодействию с облачными квантовыми компьютерами выполнена с использованием библиотеки Qiskit. Интерфейс программного комплекса реализован средствами Qt5, кроссплатформенного набора инструментов и виджетов для создания графических приложений. Анализ генерируемой двоичной последовательности выполнен статистическими тестами NIST STS[2].

Результаты. Разработан программный комплекс, предоставляющий пользователю в графическом режиме возможность выполнения опционального исследования некоторых облачных квантовых компьютеров на предмет выявления оптимального и наиболее устойчивого к ошибкам набора кубит. Приведены результаты экспериментов на трех облачных КВУ.

Выводы. В условиях накладываемых ограничений на вычислительные мощности и время использования облачных КВУ предложенный подход отличается минимальными требованиями к производительности устройства, предоставляет наглядные и однозначно-интерпретируемые сведения об исследуемых технических характеристиках квантового компьютера, является воспроизводимым, легко масштабируемым и универсальным.

[2] The National Institute of Standards and Technology, Statistical Test Suite – Национальный институт стандартов и технологий США, набор статистических тестов.

Ключевые слова: квантовый компьютер, квантовое вычислительное устройство, генератор случайных чисел, оценка производительности

Для цитирования: Корольков А.В., Крючков А.А. Подход к выявлению оптимального набора кубит квантовых вычислительных устройств на примере модели генерации случайных двоичных последовательностей. *Russian Technological Journal*. 2025;13(6):25–46. https://doi.org/10.32362/2500-316X-2025-13-6-25-46, https://www.elibrary.ru/XEUFSE

Прозрачность финансовой деятельности: Авторы не имеют финансовой заинтересованности в представленных материалах или методах.

Авторы заявляют об отсутствии конфликта интересов.

INTRODUCTION

In recent years, quantum processors have consistently demonstrated improvements in their computational and technological capabilities. This progress necessitates a straightforward and efficient method for tracking and recording the evolution of quantum computing technology, from intermediate stages to its final form. Such a mechanism, whether used alone or as part of a broader testing suite, offers a way to leverage quantum computing devices (QCD) for solving random number generation (RNG) problems. This approach provides a dependable and straightforward method for benchmarking the performance and reliability of the device under study.

QCD BENCHMARKING

Currently, there is no globally accepted standard for evaluating QCD computing power within the international scientific community. Nevertheless, the Institute of Engineers and Electrical Engineering (IEEE)[3], along with the United States Defense Advanced Research Projects Agency (DARPA)[4], are actively working on establishing such a framework. These projects, which were both initiated in 2021, anticipate releasing preliminary findings in the near future.

The absence of a standardized framework in quantum computing is primarily due to the early developmental phase of the industry; the first conceptualization of a 1-qubit cloud quantum computer occurred only in 2016. However, results that hold practical significance are continuously advancing, with QCD testing methodologies being refined, broadened, and updated each year to keep pace with current innovations and the technological viability of specific metrics. The previously established metric known as quantum volume is an unreliable indicator for modern quantum devices due to its failure to accurately reflect the true capabilities of various quantum processors. As a result, it has been replaced by newer metrics that provide a more effective evaluation of the quality and performance of these processors. For further insights into these technologies and the progression of QCD assessment methods, please refer to [1–4].

To confirm the significance of the issue and to ascertain the applicability of the RNG model in analyzing the QCD capabilities, we will outline several key aspects of widely recognized methods for evaluating their computational potential.

Quantum computers are categorized into four epochs of technological advancement, the most recent of which is referred to as a noisy intermediate-scale quantum (NISQ) system. This stage, which represents the foundational level in the hierarchy, pertains to devices featuring a limited number of qubits within the processor. However, NISQ systems lack error correction codes and exhibit a high vulnerability to disturbances resulting from environmental interactions.

The second essential aspect of quantum computer analysis pertains to the execution technology. Contemporary quantum processors can be developed using photons, ions, superconductors, or neutral atoms. When comparing devices based on various physical principles, the foundational components of a quantum computer play a critical role. For instance, superconducting QCDs typically operate at significantly higher speeds than their ionic counterparts, which can render performance comparisons between these types of devices regarding quantum circuit speed less meaningful. Nevertheless, when assessing speed characteristics within a single physical implementation, even across different versions, such evaluations remain valuable. They demonstrate the extent to which changes to QCD affect the processing speed of a quantum circuit (Fig. 1).

The methods for studying QCD can differ based on the specific application. This may involve examining the overall system such as the circuit layer operation per second (CLOPS) [6], which measures the number of layers processed in a quantum circuit each second, or focusing on particular functional aspects, like the error per layer gate (EPLG) [7]. Analysis can additionally, be conducted at the device level by investigating independent components, such as specific gates used in conjunction with designated qubits [8]. This approach entails applying a certain set of gates to quantum states to evaluate the quality of the quantum chain nodes.

[3] P7131. Standard for Quantum Computing Performance Metrics & Performance Benchmarking. IEEE. 2021. https://sagroups.ieee.org/7131/. Accessed October 06, 2025.

[4] Quantifying Utility of QC, DARPA. 2021. https://www.darpa.mil/news-events/2021-04-02. Accessed October 06, 2025.

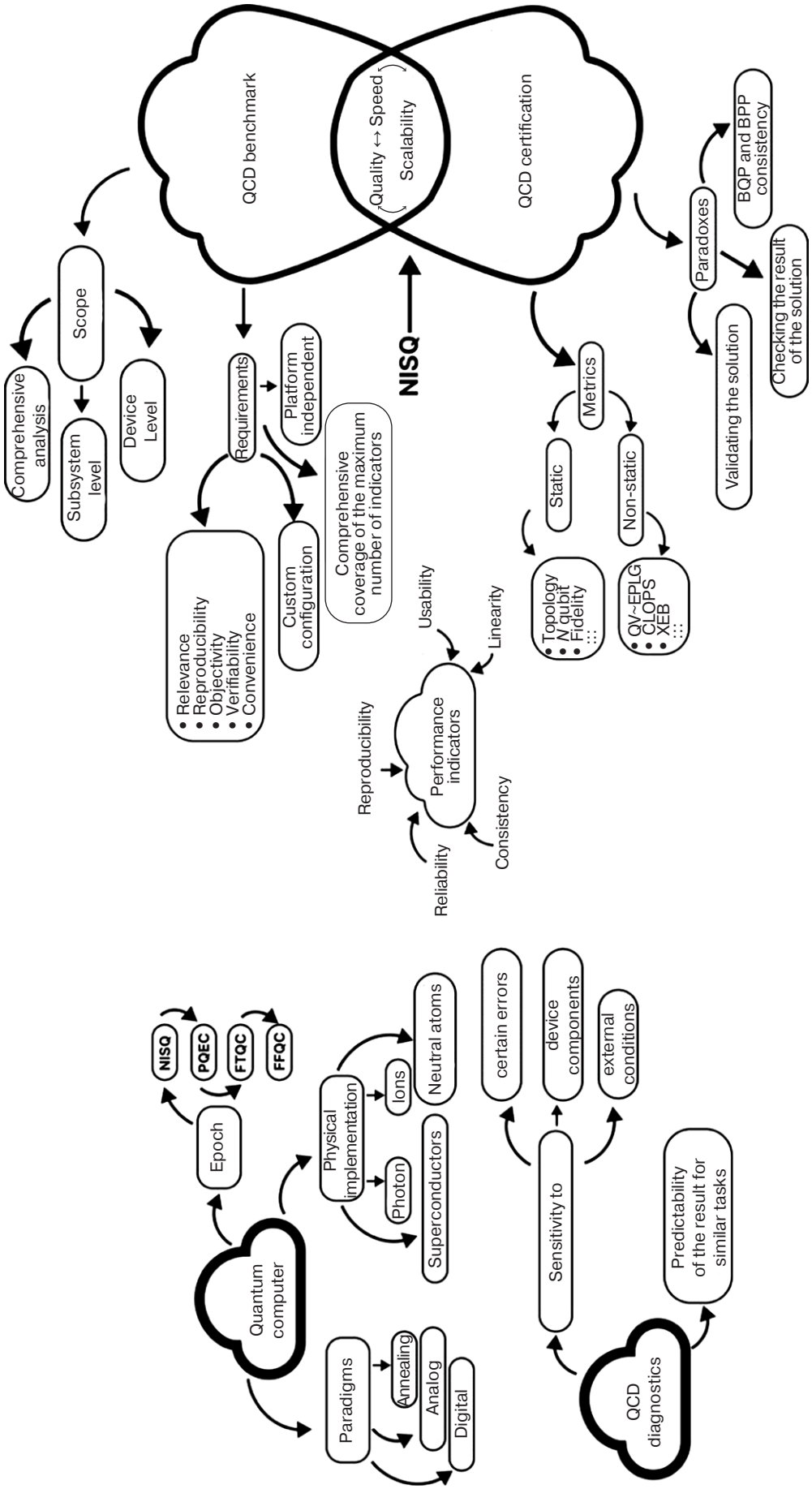

Fig. 1. Flow diagram of QCD performance tools [5]. PQEC—Partially Quantum Error Corrected, i.e., partial correction of errors that occur on the QCD; FTQC—fault tolerant quantum computers; FFQC—fully functional quantum computers; XEB—cross-entropy benchmarking

It is essential to focus on the issue of certifying quantum computers or verifying the accuracy of their computed results. The central paradox lies in the fact that, while operating within the classical realm (where Bounded-Error Probabilistic Polynomial Time denotes polynomial time with a constraint on error probability), assessing the reliability of a quantum algorithm (represented by Bounded-Error Quantum Polynomial Time) presents a complex challenge. Here the main issue involves verifying that the program executed on the quantum computer has been solved correctly by the quantum device. In other words, what methods can be employed to validate the classical results obtained through quantum computation? In certain instances, such as with the Shor algorithm [9], the expected result may be predetermined to eliminate the potential for multiple interpretations of the final outcome. However, the approach to verification becomes less straightforward in cases where the results are unique and cannot be classically simulated for comparison with expected results.

The benchmark and validation of quantum computers in the NISQ era must adhere to three interrelated imperatives: quality, speed, and scalability. For instance, the quantum volume metric has become less relevant due to the challenges involved in meeting scalability requirements. As a result, manufacturers of quantum devices no longer include it in the essential list of metrics that indicate the computational capabilities of quantum computing devices.

The final and essential aspect of analyzing quantum computers involves viewing a quantum processor as a unified device. In its canonical form, the execution of a quantum algorithm is segmented into three stages: initializing the quantum register, executing the quantum algorithm, and analyzing the results, which are presented as classical information in binary format.

Current QCDs are made accessible to regular users via cloud services. This presents a crucial challenge, since individual researchers, who are limited to observing the output of a distant quantum computer (functioning as a “black box”), cannot be certain that a classical QCD simulator is not being disguised as a cloud-based quantum system.

Upon initial observation, it appears reasonable to conclude that no conventional computing device or complex of such devices possesses the capability to effectively simulate the execution of a multi-bit quantum program featuring a substantial depth of quantum circuit operations. Nevertheless, it is important to remember that this is a working assumption rather than a definitive rule. Additionally, the absence of physical access to cloud-based QCD and the current challenges in verifying classical information generated by quantum computers create limitations and opportunities for speculation, sometimes bordering on unfounded assumptions, regarding the characteristics and capabilities of devices marketed as quantum computers.

Given these considerations, the present authors propose a study focused on modeling the creation of binary random sequences (RSs) using cloud-based quantum computers. This study aims to provide fundamental and practical insights into the performance and technological capabilities of these devices.

METHOD FOR SIMULATING RNG ON A QUANTUM COMPUTER

Along with inherent errors stemming from hardware limitations, the accuracy and dependability of solutions derived from modern QCD applied to real-world problems are currently hampered by external factors. These hardware limitations arise from the current technological imperfections and the intricate process of tuning the entire quantum system. However, even with the current limitations of modern quantum computers, it may be worthwhile to explore the potential for analyzing the computational capabilities and quantum characteristics of QCD within the context of modeling RS generation.

The creation of binary RSs and evaluation of the technical capabilities of a quantum computer have additional practical significance due to the need to safeguard information obtained through cryptography. For this reason, the use of sequences generated on any cloud device, regardless of its type, is strictly forbidden. At the present time, the results generated by cloud quantum computers within RNGs are primarily suitable for research purposes such as simulating random processes. Nevertheless, exploring the potential of QCD in RNG applications can lay the groundwork for future research when technological advancements allow for more precise localization of quantum systems.

Contemporary RNGs are categorized into three primary types distinguished by their technical execution and implementation methods: software, physical, and combined. Software RNGs, considered the least reliable, are susceptible to vulnerabilities such as predictable output patterns (periods) in pseudo-RSs (PRS) and weaknesses stemming from the initialization vector, which, if compromised, could jeopardize the security of binary data. The randomness of output from physical and RNGs is often lacking in robust mathematical justification. Furthermore, such generators can be susceptible to external factors such as temperature fluctuations, magnetic radiation, or radio wave interference.

Although quantum random number generators (QRNG) are categorized as physical RNGs, they stand apart due to their robust mathematical

foundation for ensuring the randomness of the generated RSs. Examples of QRNG devices are described in [10–12].

When comparing a portable QRNG to a quantum computer used as an RNG, several factors come into play. An independent quantum RS generation device offers a clear advantage in terms of the security of the generated sequence, particularly when employed within a "controlled zone." However, it remains susceptible to environmental factors, which could degrade the randomness quality of the output bit string. On the other hand, a cloud-based quantum computer operates within an ideally isolated environment to minimize the risk of external noise and interference while preserving the intrinsic properties of quantum computation. Yet, due to its remote nature, concerns about security are inevitable in such scenarios.

We will now consider the process of simulating the generation of a random bit of classical information on a quantum computer according to the assumption that there are no adverse effects on QCD caused by the hardware or the physical environment of the device. Several studies exploring this topic are referenced in works [13–16].

At the heart of any quantum processor is the qubit, which is the fundamental unit. A qubit can be represented as a unit vector in a two-dimensional complex vector space, with the basis being defined by the orthogonal vectors $|\mathbf{0}\rangle$ and $|\mathbf{1}\rangle$.

$$|\psi\rangle = c_1|\mathbf{0}\rangle + c_2|\mathbf{1}\rangle, \quad (1)$$

where c_1, c_2 are arbitrary complex numbers, the probabilities of the quantum states are given by:

$$|c_1|^2 + |c_2|^2 = 1. \quad (2)$$

To generate a random bit using a single qubit on a quantum processor, it is both necessary and sufficient to prepare the qubit in a superposition state. In this state, the probabilities of measuring either "0" or "1" will both be equal to 0.5. Achieving this requires applying the Walsh–Hadamard transform to the quantum state, which is represented by the following matrix:

$$\mathbf{H} = \frac{1}{\sqrt{2}}\begin{pmatrix} 1 & 1 \\ 1 & -1 \end{pmatrix}. \quad (3)$$

Applying the Hadamard gate to a single qubit results in a quantum state superposition given by the following expression:

$$\begin{aligned} \mathbf{H}:|\mathbf{0}\rangle &\to \frac{1}{\sqrt{2}}\left(|\mathbf{0}\rangle + |\mathbf{1}\rangle\right), \\ \mathbf{H}:|\mathbf{1}\rangle &\to \frac{1}{\sqrt{2}}\left(|\mathbf{0}\rangle - |\mathbf{1}\rangle\right). \end{aligned} \quad (4)$$

As seen from (4), the initial state of the RNG simulation is irrelevant irrespective of whether the qubit begins in state $|0\rangle$ or $|1\rangle$. This ensures the effective creation of a superposition state to produce equal probabilities for the quantum bit to collapse into a classical state of "0" or "1" upon measurement. To generate an RS of a specific length, operation (4) should be executed iteratively for the desired number of cycles and the results stored as a single binary string.

The proposed QRNG model represents a theoretical process for generating RS under optimal conditions with the aim of producing an RS with a balanced distribution of "0" and "1." However, achieving these ideal conditions is currently unfeasible due to the limitations of current quantum equipment, which have inherent technological imperfections. These limitations are particularly evident in the era of NISQ devices used by manufacturers of quantum processors.

Contemporary developers of quantum computers are closely focused on addressing the technical limitations arising from hardware imperfections and external environmental influences. In order to enhance the performance of quantum algorithms, it is recommended that error correction codes be implemented. These codes consolidate multiple physical qubits into a single logical qubit to ensure greater reliability and accuracy.

When working with a logical qubit constructed from three physical qubits, such as when transmitting the quantum state $|\mathbf{0}\rangle$, the receiver should receive the encoded state $|\mathbf{000}\rangle$ (referred to as the codeword). If one of the bits is flipped (bit-flip)—for example, the first one resulting in $|\mathbf{100}\rangle$—an error can be detected by the system. However, if more than two bits are flipped, it becomes impossible to identify any discrepancy in the final state. For this reason, it is essential in such scenarios to carefully determine the code distance $d = 2t + 1$, where d represents the maximum number of errors that cannot be detected, and t corresponds to the number of errors that can be identified.

The most widely recognized quantum error correction codes today include[5] repetition-, Shor-, surface-, Steane-, and Hastings—Haah codes.

However, for the specific task at hand, employing error correction codes proves to be impractical; in order to generate a genuinely RS, direct interaction with quantum states at the physical level is required.

Contemporary quantum computers possess various parameters that enable preliminary assessment of their computational capabilities and technical attributes. The information presented in Table 1, which highlights the key characteristics specific to quantum processors

[5] Introduction to quantum error correction. Microsoft Quantum Azure. 2024. https://learn.microsoft.com/en-us/azure/quantum/concepts-error-correction. Accessed October 06, 2025.

Table 1. Impact of superconducting QCD parameters on the performance of quantum circuit execution steps

Quantum circuit execution step	QCD Parameter											
	T_1	T_2	Frequency	Anharmonicity	Readout length	Readout error	meas0 prep1	meas1 prep0	(ID) error	(Pauli-X) error	(sx) error	ECR error
Qubit initialization	–	–	–	–	–	–	+	+	–	–	–	–
Quantum scheme implementation	+	+	+	+	–	–	–	–	+	+	+	+
Register measurement	–	–	–	–	+	+	–	–	–	–	–	–

Note: T_1 and T_2 represent the relaxation and dephasing times of quantum states; Frequency and Anharmonicity denote the qubit's frequency and anharmonicity (the difference in energy between the first and second excited states, expressed in Hertz); Readout error/length refers to error/time for reading the qubit state; (ID) error, (Pauli-X) error, and (sx) error represent errors in initialization, inversion, and qubit superposition, respectively. ECR error stands for a two-qubit gate error.

built using superconducting technology, serves as a foundational reference for upcoming experiments involving IBM quantum processors based on superconductors.[6]

The values presented in Table 1, which are not fully applicable to all three stages of program execution on a quantum computer, only influence specific periods of operation within the quantum circuit on a remote device. Furthermore, not all of these values need to be considered during the initial assessment of the test qubit's quality. To determine which parameters can be disregarded, it is necessary to construct a quantum scheme that clearly highlights the relevant characteristics of the selected qubits.

The RS generator on the quantum computer can be implemented as illustrated in Fig. 2. In Fig. 2a, the original quantum circuit designed by the user is presented, while Fig. 2b shows the same circuit after it has been compiled and decomposed into a version compatible with the native gates of the quantum computer executing the program. These native gates represent the fundamental operations specific to the hardware's architecture. Notably, the same circuit implemented on a QCD with a different underlying physical design and native gate set may differ substantially from the intended configuration.

Considering the quantum scheme post-compilation (Fig. 2b) alongside the available QCD parameters outlined in Table 1, the key factors to be addressed include T_1, T_2, Readout error, and (sx) error.

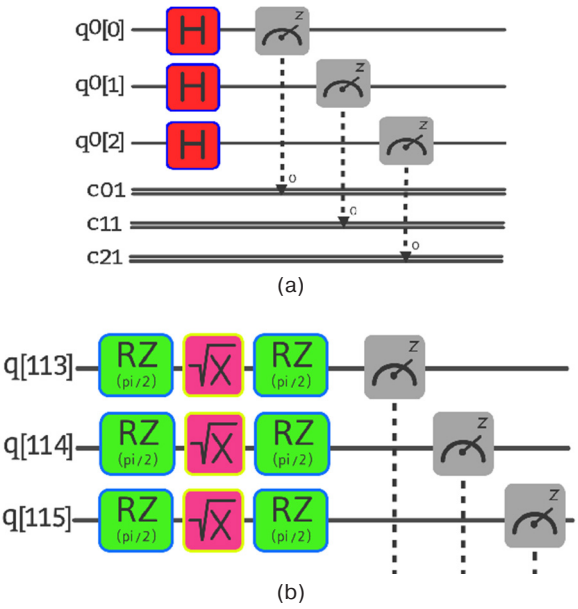

Fig. 2. Three-qubit QRNG circuit for superconducting QCD: (a) High-level representation; (b) Base gate decomposition of QCD (low-level representation). q0[0], q0[1], q0[2], q[113], q[114], and q[115] represent qubits while c11, c12, and c21 are classic bits. H are Hadamard gates; "speedometer"—qubit measurement operation; RZ—quantum state rotation at an angle of π/2; $\sqrt{X}$ —one of the Hadamard operation components [17]

Since their minimal variance across all qubits utilized in the experimental research renders them insignificant, the properties of Frequency, Anharmonicity, and Readout length are intentionally

[6] IBM Quantum Platform. https://quantum.ibm.com/. Accessed May 15, 2025.

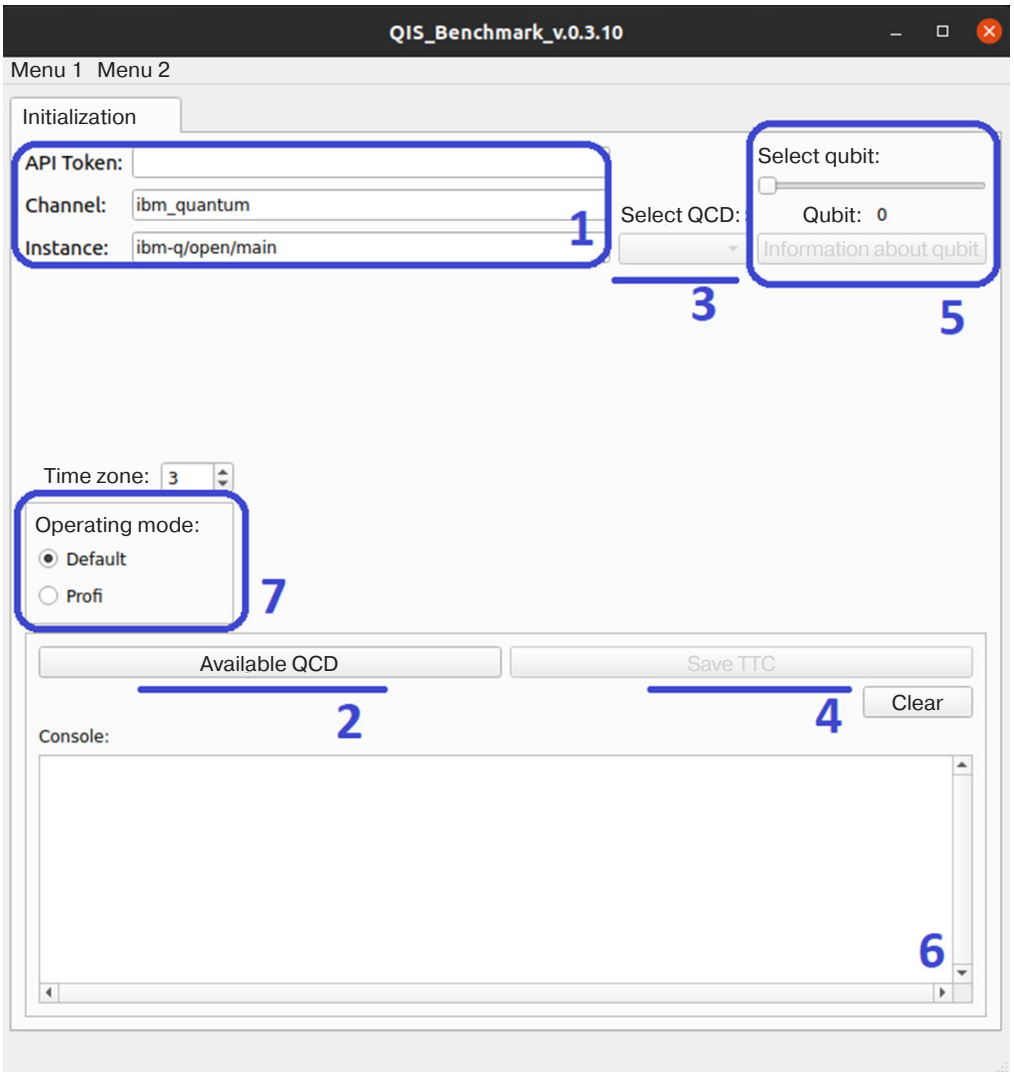

Fig. 3. *QISs* main window. TTC—tactical and technical characteristics

excluded. Similarly, the parameters meas0 prep1 and meas1 prep0 are irrelevant in this context, given that the "H" gate is applied to qubits in an idle state without prior initialization. Furthermore, as stated in Eq. (4), the operational output of the programmable circuit can be assumed to be independent of the qubit's initial state.[7] Among the remaining error sources affecting the relevant qubits, only (sx) error remains significant, as indicated by the diagram in Fig. 2b. According to the specifications provided by the cloud QCD manufacturer, the gate responsible for RZ quantum state rotation has a zero-error value and is can thus be omitted from consideration.

Having developed the RS generation model and identified the key parameters of the cloud QCD that require consideration when analyzing the results, we will proceed with a practical series of QRNG experiments on a cloud-based quantum computer.

EXPERIMENTAL QRNG IMPLEMENTATION ON A CLOUD-BASED QCD

In order to conduct permit the conducting of various experiments, IBM quantum computers are made accessible to users via the company's cloud-based services in the public domain.

To enhance the efficiency, autonomy, adaptability, and ease of use when working with these quantum devices, the present authors have developed an application leveraging the open-source library Qiskit. This application is designed with the graphical interface of the Qt5 framework. The main window of the program, named *Quantum Information Security* (*QISs*) [18], is illustrated in Fig. 3.

To initiate the program for establishing a remote connection with the cloud QCD in Area 1, the operator needs to input the initialization data,

[7] As a rule, the quantum register is "reset" to the state $|00...0\rangle$ by default.

including a personal API[8]-token that is uniquely tied to each user. Following this, the operator can proceed to retrieve details about the accessible cloud QCD in Area 2. Currently, IBM provides the capability to run quantum circuits on 12 devices, 9 of which cater to commercial usage. However, users without a paid subscription are limited to conducting research on only three cloud systems. Once information about the user's accessible QCD is obtained, the drop-down menu in Area 3 will populate to enable access to both general information in Area 4 and more specific details in Area 5 about the chosen QCD or individual qubits.

The text window serves to display the program's progress (Area 6). For less experienced users, the operating mode selection (Area 7) is tailored to simplify interaction with both the application and the cloud-based quantum computer.

Upon switching to Profi mode, the program unveils additional windows, as illustrated in Fig. 4.

The INIT–IDLE mode[9] (Fig. 4, left) is designed to permit the effective configuration of study qubits. Once the QCD is selected (Area 3), the user specifies the qubits to utilize (Area 4) and configures the initialization gate (Area 5) along with the Hadamard gate settings (Area 6). Subsequently, instructions are set for the quantum computer, and the circuit is submitted for execution (Area 7). If it is not feasible to wait for the QCD to complete its online computations, users can download the program results using the JobID (Area 8). A text window provides real-time updates on the program progress (Area 9).

The QRNG mode (Fig. 4) offers multiple functionalities (Area 1). Among these, the cloud QCD selection is only required for the configuration unit responsible for QRNG operations (Area 3). As part of the training process, users can generate quantum circuits and analyze corresponding data by executing a QRNG simulation on a quantum computer simulator (Area 4). Area 5 focuses on testing the generated RS and PRS to detect any statistical dependencies within their binary strings. Additionally, the QRNG tab allows results to be stored offline (Area 7). Each step of the application workflow is detailed within the text box located in Area 6.

A key parameter is Alpha, the significance level. Within the RNG process, the sequence produced by each qubit undergoes analysis to verify its adherence to a uniform distribution of "0" and "1." To achieve this, the frequency bit test, representing a component of the NIST STS[10] suite of statistical tests designed for evaluating binary sequences[11], is employed. After testing, a P_{value} is provided, calculated using statistical methods. This value ranges from 0 (indicating a strong bias) to 1 (suggesting an evenly probable distribution between "0" and "1"). It should be noted that P_{value} does not always fall at the extremes, meaning the user's judgment plays a role in determining randomness or uniformity. The user independently selects the significance level Alpha, which serves as a benchmark when comparing statistical metrics.

The NIST STS test documentation suggests setting Alpha within a range of 0.001 to 0.01. When P_{value} exceeds the chosen significance level ($P_{\text{value}} > \alpha$), the sequence is considered random with confidence levels of 99.9% and 99%, respectively. The selected Alpha value directly affects type I errors, leading to false positives and the incorrect rejection of the null hypothesis. For instance, with $\alpha = 0.01$, approximately one in every 100 RSs will be mistakenly rejected.

In the *QISs* application, a frequency bit test serves as a method for filtering quantum states into two categories: "bad" and "good" qubits. This classification is based on a threshold value, termed "Alpha," which is specified by the user to evaluate the suitability of quantum states. While the separation of qubits is subject to conditional constraints, in certain scenarios, it becomes both evident and essential.

To conduct a bitwise frequency test on a binary sequence $\{x\}_{i=1}^{n}$, the statistical distribution of "0" and "1" values is determined according to the following rule:

$$s_{\text{obs}} = \frac{|S_n|}{\sqrt{n}}, \tag{5}$$

where at $X_i = 2x_i - 1$:

$$S_n = \sum_{i=1}^{n} X_i. \tag{6}$$

Based on the results obtained, an additional error function is used to calculate the P_{value}. The error function has the following form:

$$\operatorname{erfc}(x) = \frac{2}{\sqrt{\pi}} \int_x^{\infty} e^{-t^2} dt. \tag{7}$$

[8] Application Programming Interface.

[9] INIT is initialization; IDLE stands for on "idle" (initialization). The "INIT–IDLE" mode is not considered in the paper.

[10] The National Institute of Standards and Technology, Statistical Test Suite.

[11] NIST SP 800-22. https://csrc.nist.gov/projects/random-bit-generation/documentation-and-software. Accessed May 15, 2025.

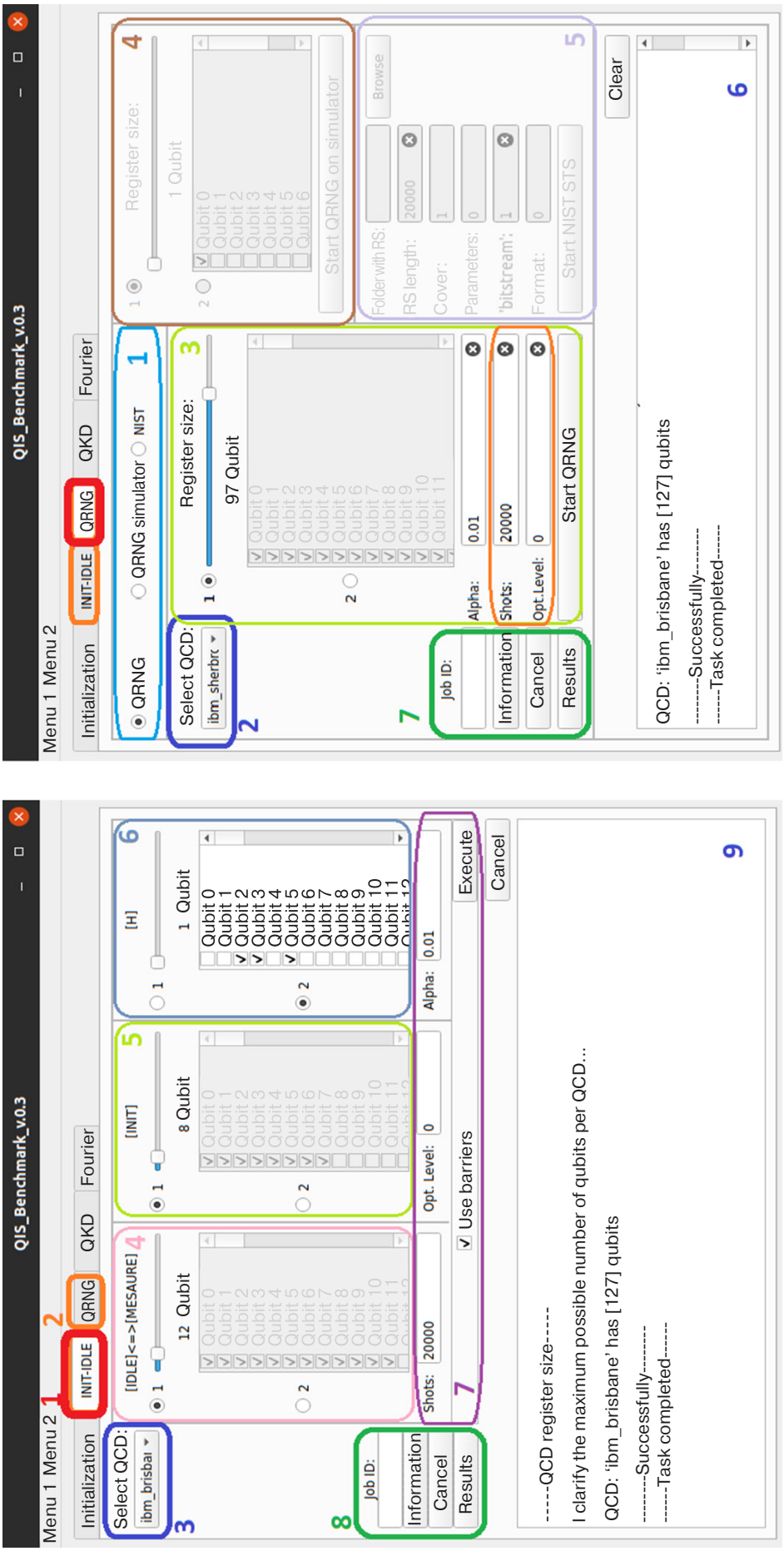

Fig. 4. Interface of the INIT-IDLE and *QISs* tabs. QKD—quantum key distribution

P_{value} is then calculated using the following equation:

$$P_{value} = \text{erfc}\left(\frac{s_{obs}}{\sqrt{2}}\right). \quad (8)$$

When the calculated P_{value} is smaller than the chosen significance level alpha, the RS fails to meet the randomness criteria.[12] Conversely, if P_{value} exceeds the significance level, the RS is deemed to be of good quality, indicating that the qubit is stable and well-suited for use in RNG tasks.

After outlining the description and fundamental operations of the *QIS* software and establishing the method for identifying stable and reliable qubits among the quantum states of the QCD register, we will proceed to generate RS on a cloud-based quantum computer. To achieve this, the following steps are carried out:

1. Navigate to the QRNG tab, select QCD ibm_brisbane from the drop-down list, and wait for the connection to be established with the cloud device.
2. Using the slider interface element, note the entire quantum register of QCD. The ibm_brisbane has 127 qubits, so select all 127 quantum states for the QRNG.
3. Set the significance level "Alpha" to 0.01.
4. The quantum scheme is set to repeat 20,000 times, representing the maximum available during the research period. Consequently, each qubit will generate an RS measuring $2 \cdot 10^4$ bits in length. Considering a total of 127 qubits per QCD, with the same maximum repetition count, the final length of the potential key will reach $254 \cdot 10^4$ bits—equivalent to approximately 0.3 MB.
5. The optimization level of the quantum scheme is deemed irrelevant for the task under consideration, so its parameter remains fixed at 0.
6. With all configurations finalized, the QRNG process can now commence.

ANALYSIS AND INTERPRETATION OF RESULTS

Step 1. Statistics Collection

Once the quantum computer has finished processing, the results will be stored in the user's home folder (Fig. 5).

Directories labeled "1" and "2" are designated to store RS files generated from each qubit, which are categorized into "good" and "bad" quantum states following the filtering process. Directories "3" and "4" hold files resulting from the concatenation of all RS files in directories "1" and "2," respectively. The authors aim to derive the final random binary key using qubits identified as stable and appropriate for the QRNG process. Additionally, a final "bad" key is created to enable comparison and assessment of the generated

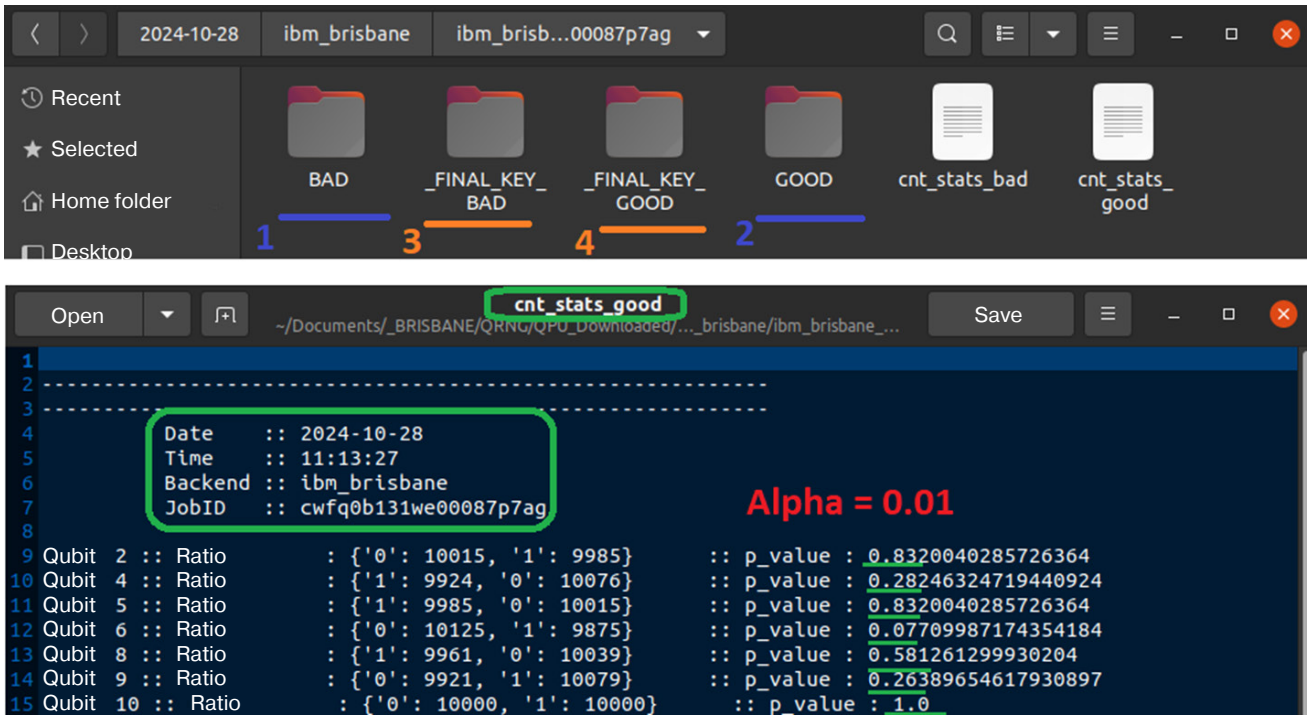

Fig. 5. *QISs* results (QRNG mode)

[12] The frequency test is clearly an essential step in assessing the randomness of the RS, though on its own, it remains insufficient to fully establish randomness.

keys along with their corresponding qubits against each other. Figure 5 below illustrates the contents of a file containing the final statistics of a single experiment, derived from the "good" qubits in the QCD.

Due to the probabilistic nature of the computing processes in quantum computers, it becomes evident that a single execution may not always suffice. To address this, the *QISs* software incorporates mechanisms for accumulating statistical data from prior completed projects. Figure 6 illustrates the information gathered from executing the QRNG on two IBM QCD systems.

This method is intended to enable users to visually monitor variations in both the quantity and quality of qubits within the quantum register of a cloud-based device. However, caution is necessary when interpreting the results. Minor fluctuations in the ratio of "0" and "1" may mistakenly classify a qubit as "unreliable" (false positive), even when the actual distribution of zeros and ones remains nearly unchanged. Therefore, it is essential to clarify the specific objective the user aims to achieve:

1. Generating a random binary key with optimal properties, leveraging the capabilities of the QCD. This involves strict criteria for the Alpha parameter and improving its value based on the quality of the resulting RS.
2. Evaluating the QCD quantum register to identify the most stable qubits in order to ensure the selection of an optimal set of quantum states for future experiments. Given Alpha's requirements, it may be acceptable to reduce the stability parameters to a necessary level.

Based on the above, it can be concluded that careful consideration should be given to selecting an appropriate level of significance when filtering qubits by frequency. Additionally, it is essential to verify the final statistical results of individual experiments, as illustrated in Fig. 5, which records all the "0" and "1" values for each qubit. In certain scenarios, adjustments may be required to relax the Alpha parameter. However, caution is advised, as overly lenient modifications might compromise the reliability of the RS by amplifying minor deviations from individual qubits into significant discrepancies between "0" and "1" values in the concatenated final key derived from the processed files.

Step 2. Correlation analysis

Performing a preliminary correlation analysis on the obtained results is crucial before taking any further steps. Even with the use of "good" qubits, concatenating generated files containing binary sequences without such analysis is not recommended.

Essentially, submitting a QRNG implementation scheme to a quantum computer implies that the QCD is not a standalone RNG. In our case, the quantum computer itself is divided into numerous smaller RS generators, which correspond to individual qubits in the cloud-based device.

A natural question then arises: can each qubit in this context be considered an independent source of random data? The answer has a direct impact on whether there are valid justifications for combining small RSs to form a single final key consisting of two or more qubits.

The RS correlation test aims to establish if chosen qubits act as independent sources of random numbers, both in terms of their own states and when compared to other states in the quantum register.

The correlation between two randomly generated binary sequences $\{x\}_{i=1}^{n}$, $\{z\}_{i=1}^{n}$ of length $n \in \mathbb{N}$ is described by the following function:

$$F_{\mathrm{corr}(i)} = \frac{1}{n}\sum_{j=1}^{n} s_j,\ i = (0,n), \tag{9}$$

where $s_j = 1$ for $\overline{x \oplus z(i)} = 1$ and $s_j = -1$ for $\overline{x \oplus z(i)} = 0$.

In other words, s_j performs a bitwise addition modulo 2 operation on the two sequences. However, when it comes to binary string comparison, this analysis is done with a cyclic shift. The results of the comparison are visually represented using inversion, with "1" being displayed when the two sequences are identical.

Although the current version of the *QISs* application does not include an automatic preliminary analysis of received RS for correlation, the results of this analysis were presented at the RADIOINFOCOM conference held in November 2024 [19]. The results of the preliminary studies show that the correlation between "good" qubits does not exceed a value of 10^{-3}, while qubits producing less stable and reliable sequences have a certain offset in the correlation function, ranging up to $4 \cdot 10^{-2}$.

Step 3. Verification of statistical independence

The final step in verifying the generated RS is to test them for statistical independence. One possible tool for this verification is the NIST Statistical Test Suite (STS), which is included in the *QISs* software for automated and user-defined RS verification (Fig. 4, on the right, Area 5).

Here, the focus lies in analyzing the final RS produced when merging binary strings with "good" qubits. However, since examining a single sequence may not always be revealing, a comparison of the final sequences generated over a defined timeframe enables us to observe the characteristics of the quantum device over time (such as the length of the final key, the number of successful and unsuccessful tests, etc.).

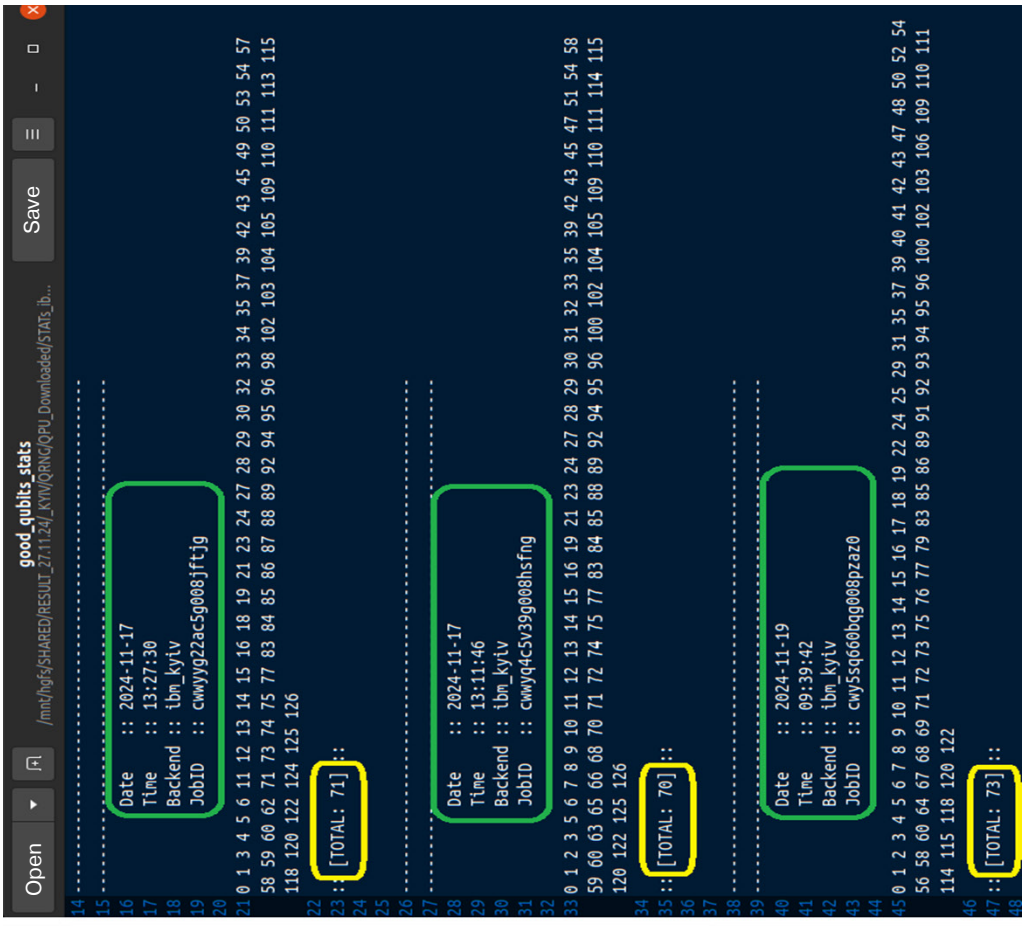

Fig. 6. Statistics on qubits of three-cloud QCD in QRNG tasks

The data presented in Fig. 7 is derived from the analysis of RS measurements conducted on the ibm_brisbane quantum computer, with a one-month time interval between data points.

Although the number of stable qubits varies slightly over the course of the experiments, it consistently starts and ends each month at 79. Notably, the results of the tests are largely consistent, except for the test measuring the length of consecutive "1" strings, which demonstrates success on the second attempt.

Similar studies are conducted on the ibm_kyvi QCD, with a two-week interval between each (Fig. 8a) and on the ibm_sherbrooke QCD, with a seven-day gap (Fig. 8b).

The nature of passing the tests for two QCD shown in Fig. 8 deserves special attention. When separately RS is applied to each "good" qubit in the selected QCD, with a length of $2 \cdot 10^4$ bits, the bit test passes successfully. However, when these strings are concatenated into final RSs (slightly larger than 0.1 MB), identical tests related to the search for "0" and "1" fail. The reason for this phenomenon is the "run-in" difference between the levels of zeros and ones in the final binary string due to the low requirements for the significance level of the primary filtering of qubits (Alpha = 0.01). Meanwhile, the ibm_brisbane QCD, which has similar significance levels, shows better results.

The experimental results are presented in Table 2.

The minimum and maximum ratios of stable qubits observed over the research period, with a significance level of 0.01 applied to each QCD, are as follows: ibm_brisbane at 65/81, ibm_kyvi at 59/73, and ibm_sherbrooke at 52/62, respectively.

While these findings are not exhaustive and do not offer full comprehension of the computational capabilities of the investigated quantum devices, the results serve as a specific case study to confirm the possibility of utilizing quantum computers as RNGs to unveil crucial aspects of a computing system. The described approach, which offers valuable starting points for initial QCD evaluations, is of value in assessing the strengths of a selected computer and in identifying the most desirable features of quantum states for effectively handling user-defined applications.

Table 2. Results of the QRNG process on cloud-based QCD

Date	QCD	Number of "good" qubits / RS length	Failed NIST STS tests[13]	Circuit operation time, s	Best / Worst "0" to "1" ratio across entire QCD register
28.10.2024	ibm_brisbane	79 / $158 \cdot 10^4$	1 "Runs" test 8 "RandomExcursions" tests 18 "RandomExcursionsVariant" tests	7	10.000–10.000 / 12.684–7.316
26.11.2024	ibm_brisbane	79 / $158 \cdot 10^4$	8 "RandomExcursions" tests 18 "RandomExcursionsVariant" tests	8	9.999–10.001 / 7.498–12.502
05.11.2024	ibm_kyvi	59 / $118 \cdot 10^4$	1 "Frequency" test 2 "CumulativeSums" tests	13	9.998–10.002 / 13.029–6.971
24.11.2024	ibm_kyvi	64 / $128 \cdot 10^4$	1 "Frequency" test 2 "CumulativeSums" tests 8 "RandomExcursions" tests 18 "RandomExcursionsVariant" tests	14	9.999–10.001 / 15.143–4.857
06.11.2024	ibm_sherbrooke	52 / $104 \cdot 10^4$	1 "Frequency" test 2 "CumulativeSums" tests 8 "RandomExcursions" tests 18 "RandomExcursionsVariant" tests	9	9.997–10.003 / 13.404–6.596
12.11.2024	ibm_sherbrooke	52 / $104 \cdot 10^4$	1 "Frequency" test 2 "CumulativeSums" tests 8 "RandomExcursions" tests 18 "RandomExcursionsVariant" tests	8	9.984–10.016 / 12.596–7.404

[13] Maurer's universal test is not taken into account due to a lack of adequate information.

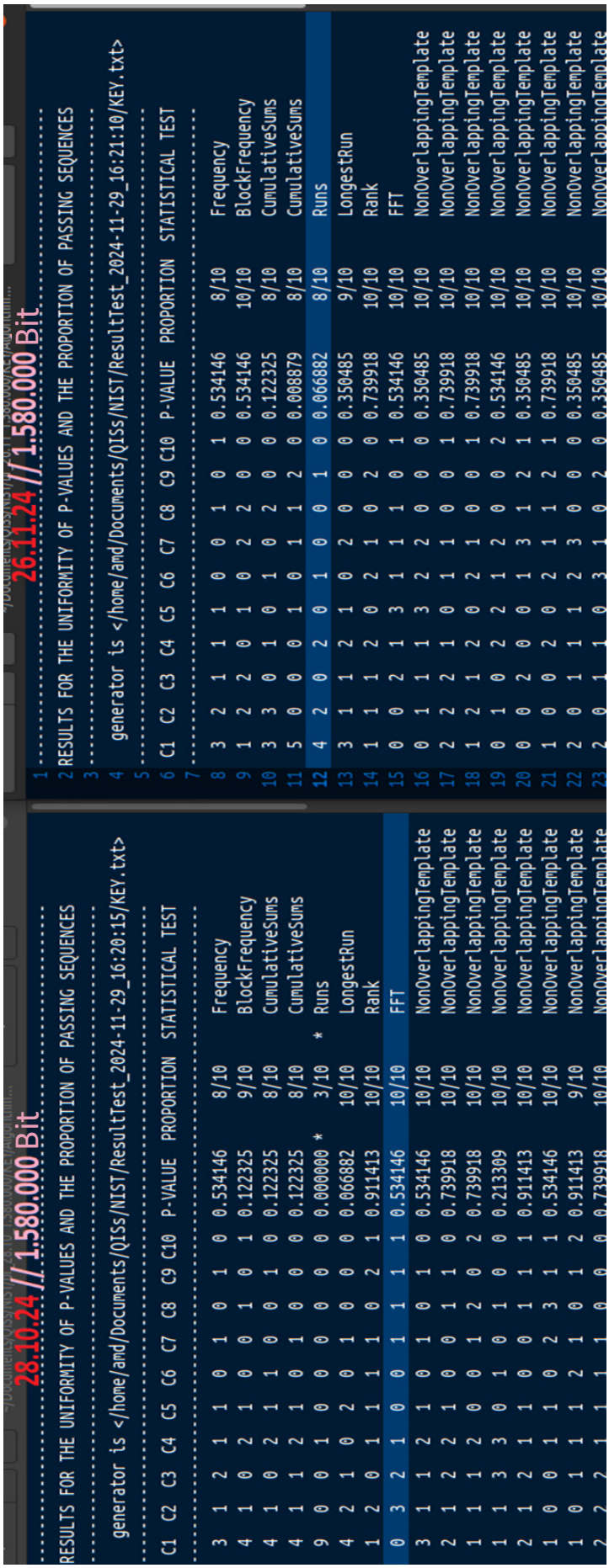

Fig. 7. Results of verifying the final RS using the ibm_brisbane QCD

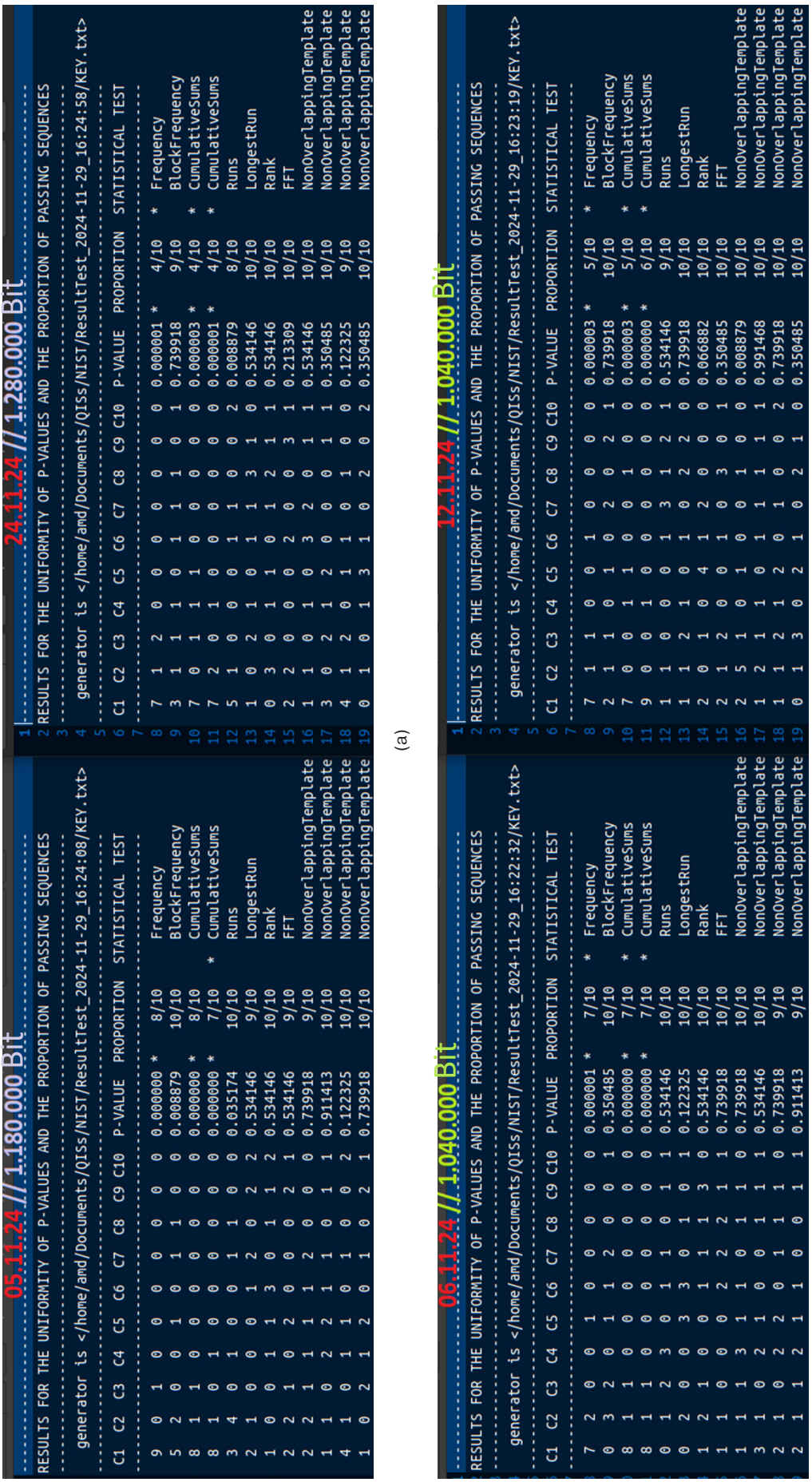

Fig. 8. Verification results of the final RS with QCD: (a) ibm_kyvi, (b) ibm_sherbrooke

RESULTS AND DISCUSSION

Based on the findings of the study, the following observations, which may serve as a basis for future research, can be made.

1. Given the QCD technical specifications that influence the quantum state and consequent RS generation outcome, there is a need to determine a formal mathematical approach to the degree of correlation between the current calibration parameters of the quantum processor and the expected outcomes of the QRNG process. For instance, the characteristics of the best and the worst qubits within the entire quantum register for each experiment detailed in Table 2 are presented in Table 3.

Although some results are not immediately apparent, it is proposed that a portion of the qubit may produce suboptimal outcomes, including when neighboring quantum states are engaged, which has a secondary effect on the targeted qubit. Verification of this hypothesis, as well as the development of a mathematical model for the correlation between the tactical and technical properties of the QCD and the outcomes of the QRNG system, are potential areas for future investigation.

2. Using the entire quantum processor, the maximum RS length can be 254 · 104 bits, which results in a sample size of approximately 0.3 MB with a bit depth of 127 qubits and max_shots = 20.000 (the number of times the quantum circuit is run). In this scenario, given the processing time of the quantum circuit, the ibm_brisbane (7 seconds) is the fastest QCD, which ideally provides an RNG speed of approximately 44 kbit/s. Obviously, this speed places limitations on the application of QCD as an RNG. Furthermore, experiments have shown that approximately half of the qubits may not be suitable for obtaining a stable RS. However, by scaling up the bit depth of quantum processors and addressing existing equipment errors and interferences, the current limitations can be overcome, opening up new opportunities for using QCD in information security applications.

3. Introduced in 2010, NIST STS tests represent an older approach to verifying the RS quality. The present authors believe it is crucial to further investigate RS generated by contemporary methods, as these can not only be used to assess the statistical independence of the data but also to delve into the inherent characteristics and nature of the RNG itself, ultimately determining how well it mimics the properties of a truly physical QRNG.

4. The proposed method could be incorporated into the expanded suite of tests and programs used to evaluate the technical capabilities of a given QCD. Using this approach, preliminary insights into the execution speed of quantum circuits on the chosen QCD

Table 3. Characteristics of IBM's "extreme" cloud QCD qubits

Date	QCD/qubit	«0» to «1» Ratio	T_1, μs	T_2, μs	Readout, err	(sx), err
28.10.2024	brisbane/10	10.000–10.000	290.18	276.91	0.018	$1 \cdot 10^{-4}$
	brisbane/86	12.684–7.316	90.85	115.17	0.113	$1.45 \cdot 10^{-2}$
26.11.2024	brisbane/55	9.999–10.001	243.83	120.25	0.01	$2 \cdot 10^{-4}$
	brisbane/24	7.498–12.502	226.79	98.47	0.14	$2 \cdot 10^{-4}$
05.11.2024	kyvi/5	9.998–10.002	347.03	331.96	0.008	$2 \cdot 10^{-4}$
	kyvi/90	13.029–6.971	43.91	22.84	0.114	$3.3 \cdot 10^{-3}$
24.11.2024	kyvi/122	9.999–10.001	211.81	173.1	0.002	$2 \cdot 10^{-4}$
	kyvi/65	15.143–4.857	201.52	126.32	0.092	$2 \cdot 10^{-3}$
06.11.2024	sherbr-ke/23	9.997–10.003	220.73	24.85	0.009	$4 \cdot 10^{-4}$
	sherbr-ke/56	13.404–6.596	173.46	16.9	0.033	$3 \cdot 10^{-4}$
12.11.2024	sherbr-ke/63	9.984–10.016	217.35	133.31	0.035	$2 \cdot 10^{-4}$
	sherbr-ke/9	12.596–7.404	469.69	70.2	0.035	$2 \cdot 10^{-4}$

can be rapidly obtained. Additionally, the QRNG output offers valuable information regarding the most efficient qubit configuration, which users can then leverage when designing more intricate and resource-intensive quantum circuits.

5. Many researchers are actively exploring ways to address the decoherence challenge faced by quantum states [20–22]. The prevailing strategies often involve implementing error correction techniques and utilizing a conceptual entity known as a logical qubit. A logical qubit can be conceptualized as a group of physical qubits that, when considered together, effectively represent the behavior of a single quantum state. Nevertheless, employing correction codes or shifting to logical qubits within the framework of the QRNG task proves unsuitable since the rationale behind generating an RS on a quantum computer hinges solely on utilizing qubits functioning as independent physical RNGs.

The authors plan to incorporate a QRNG task within cloud-based QCD as part of a suite of tests designed to evaluate the computational capabilities of quantum computers for cybersecurity experts. This software package will encompass three core tests: QRNG, a simulation of the QKD protocol, and the execution of a quantum Fourier transform. The developed algorithm should be characterized by its speed, simplicity, accessibility, reliance on QCD principles, reproducibility, scalability, and unambiguous interpretability.

Both the latest version of the *QISs* program code and the associated research findings are accessible within the project repository on GitHub.[14]

CONCLUSIONS

Within this research, the authors have developed an application enabling the design and remote execution of quantum circuits leveraging RNG on the cloud-based QCD platform. In order to assess any potential unintended connections between quantum states functioning as independent QRNGs, the application also provides tools for analyzing correlations within the generated RSs.

Utilizing a frequency bit test and the user-defined significance level, the application delivers insights into the most and least reliable qubits, assessing their stability and suitability for quantum Walsh–Hadamard state applications.

To assess the randomness of the binary patterns (zeros and ones) produced in the generated sequences, the program offers the functionality for the RS evaluation using a suite of statistical tests from the NIST STS.

The approach proposed in the present paper can serve as a useful tool for researchers in solving several problems, such as identifying the optimal set of qubits in a quantum processor, generating binary RSs on quantum computers, and assessing some technical capabilities of studied quantum devices.

ACKNOWLEDGMENTS

The authors thank K.E. Komogorov, a student at RTU MIREA, for his prompt assistance in preparing the bash script, initial testing of the *QISs* application software capabilities, and providing his own GitHub repository for hosting the developed program in the public domain.

Authors' contribution

All authors contributed equally to the research work.

[14] GitHub / QISs. https://github.com/cyberravenman/QISs. Accessed May 15, 2025.

REFERENCES

1. Proctor T., Young K., Baczewski A.D., Blume-Kohout R. Benchmarking quantum computers. *arXiv*. 2024. arXiv:2407.08828. https://doi.org/10.48550/arXiv.2407.08828
2. Amico M., Zhang H., Jurcevic P., et al. Defining Standard Strategies for Quantum Benchmarks. *IBM Publications*. 2023. Available from URL: https://research.ibm.com/publications/defining-standard-strategies-for-quantum-benchmarks. Accessed May 15, 2025.
3. Acuaviva A., Aguirre D., Pena R., Sanz M. Benchmarking Quantum Computers: Towards a Standard Performance Evaluation Approach. *arXiv*. 2024. arXiv:2407.10941. https://doi.org/10.48550/arXiv.2407.10941
4. Eisert J., Hangleiter D., Walk N., et al. Quantum certification and benchmarking. *Nat. Rev. Phys.* 2020;2:382–390. https://doi.org/10.1038/s42254-020-0186-4
5. Kryuchkov A.A. On the need to adopt a single standard for evaluating the performance and certification of quantum computers. *Informatsionno-ehkonomicheskie aspekty standartizatsii i tekhnicheskogo regulirovaniya = Information and Economic Aspects of Standardization and Technical Regulation.* 2024;6(81):43–49 (in Russ.).
6. Wack A., Paik H., Javadi-Abhari A., Jurcevic P., Faro I., Gambetta J.M., Johnson B.R. Scale, Quality, and Speed: three key attributes to measure the performance of near-term quantum computers. *arXiv*. 2021. arXiv:2110.14108. https://doi.org/10.48550/arXiv.2110.14108
7. McKay D.C., Hincks I., Pritchett E.J., Carroll M., Govia L.C.G., Merkel S.T. Benchmarking Quantum Processor Performance at Scale. *arXiv*. 2023. arXiv:2311.05933. https://doi.org/10.48550/arXiv.2311.05933
8. Amico M., Zhang H., Jurcevic P., Bishop L.S., Nation P., Wack A., McKay D.C. Defining Standard Strategies for Quantum Benchmarks. *arXiv*. 2023. arXiv:2303.02108 https://doi.org/10.48550/arXiv.2303.02108
9. Shor P.W. Algorithms for quantum computation: discrete logarithms and factoring. In: *Proceedings 35th Annual Symposium on Foundations of Computer Science*. IEEE; 1994. P. 124–134. https://doi.org/10.1109/SFCS.1994.365700
10. Balygin K.A., Kulik S.P., Molotkov S.N. Implementation of a Quantum Generator of Random Numbers: Extraction of Provably Random Bit Sequences from Correlated Markov Chains. *Jetp. Lett.* 2024;119(7):538–548. https://doi.org/10.1134/S0021364024600575
[Original Russian Text: Balygin K.A., Kulik S.P., Molotkov S.N. Implementation of a Quantum Generator of Random Numbers: Extraction of Provably Random Bit Sequences from Correlated Markov Chains. *Pis'ma v Zhurnal ehksperimental'noi i teoreticheskoi fiziki* (*Pis'ma v ZHEHTF*). 2024;119(7):533–544 (in Russ.). https://doi.org/10.31857/S1234567824070115]
11. Gaidash A.A., Goncharov R.K., Kozubov A.V., Yakovlev P.V. Mathematical model of random number generator based on vacuum fluctuations. *Vestnik Sankt-Peterburgskogo universiteta. Prikladnaya matematika. Informatika. Protsessy upravleniya = Vestnik of Saint Petersburg University. Applied Mathematics. Computer Science. Control Processes.* 2024;20(2):136–153 (in Russ.). https://doi.org/10.21638/spbu10.2024.202
12. Petrenko A.A., Kovalev A.V., Bougrov V.E. Random number generation with arrays of coupled quantum-dot micropillar lasers. *Nauchno-tekhnicheskii vestnik informatsionnykh tekhnologii, mekhaniki i optiki = Scientific and Technical Journal of Information Technologies, Mechanics and Optics*. 2021;21(6):962–968 (in Russ.). https://doi.org/10.17586/2226-1494-2021-21-6-962-968
13. Orlov M.A., Nechaev K.A., Reznichenko S.A. Evaluation of statistical properties and cryptographic strength of random sequences obtained by an IBM quantum computer. *Bezopasnost' informatsionnykh tekhnologii = IT Security* (Russia). 2023;30(1):14–26 (in Russ.). http://doi.org/10.26583/bit.2023.1.01
14. Li Y., Fei Y., Wang W., et al. Quantum random number generator using a cloud superconducting quantum computer based on source-independent protocol. *Sci Rep.* 2021;11:23873. https://doi.org/10.1038/s41598-021-03286-9
15. Salehi R., Razaghi M., Fotouhi B. Hybrid Hadamard and Controlled-Hadamard Based Quantum Random Number Generators in IBM QX. *Physica Scripta*. 2022;97(6):065101. https://doi.org/10.1088/1402-4896/ac698b
16. Yadav A., Mishra S., Pathak A. Partial loopholes free device-independent quantum random number generator using IBM's quantum computers. *Physica Scripta*. 2024;99(11):115103. https://doi.org/10.1088/1402-4896/ad7c02
17. Feynman R.P. Quantum Mechanical Computers. *Optics News*. 1985;11(2):11–20. Available from URL: https://www.optica-opn.org/home/articles/on/volume_11/issue_2/features/quantum_mechanical_computers/. Accessed May 15, 2025.
18. Kryuchkov A.A. *QISs_v.0.3.9*: Computer Program RU2025613655 RF. Publ. 13.02.2025 (in Russ.).
19. Kryuchkov A.A., Komogorov K.E. Simulation of the random number generation process on quantum computing devices. In: *Proceedings of the 8th Scientific and Practical Conference "Actual Problems and Prospects of Radio Engineering and Infocommunication Systems."* Moscow: RTU MIREA; 2024. P. 501–506 (in Russ.).
20. Acharya R., Abanin D.A., Aghababaie-Beni L., et al. Quantum error correction below the surface code threshold. *Nature*. 2025;638:920–926. https://doi.org/10.1038/s41586-024-08449-y

21. Verma S., Kumari S.S., Kumar R.S. Topological quantum error correction with semions. *Int. J. Phys. Math*. 2024:6(2):44–47. https://doi.org/10.33545/26648636.2024.v6.i2a.95
22. Webster M., Browne D. Engineering Quantum Error Correction Codes Using Evolutionary Algorithms. *IEEE Trans. Quantum Eng*. 2025;6:3100514. https://doi.org/10.1109/TQE.2025.3538934

СПИСОК ЛИТЕРАТУРЫ

1. Proctor T., Young K., Baczewski A.D., Blume-Kohout R. Benchmarking quantum computers: *arXiv*. 2024. arXiv:2407.08828. https://doi.org/10.48550/arXiv.2407.08828
2. Amico M., Zhang H., Jurcevic P., et al. Defining Standard Strategies for Quantum Benchmarks. *IBM Publications*. 2023. URL: https://research.ibm.com/publications/defining-standard-strategies-for-quantum-benchmarks. Дата обращения 15.05.2025.
3. Acuaviva A., Aguirre D., Pena R., Sanz M. Benchmarking Quantum Computers: Towards a Standard Performance Evaluation Approach: *arXiv*. 2024. arXiv:2407.10941. https://doi.org/10.48550/arXiv.2407.10941
4. Eisert J., Hangleiter D., Walk N., et al. Quantum certification and benchmarking. *Nat. Rev. Phys.* 2020;2:382–390. https://doi.org/10.1038/s42254-020-0186-4
5. Крючков А.А. О необходимости принятия единого стандарта по оценке производительности и сертификации квантовых вычислительных устройств. *Информационно-экономические аспекты стандартизации и технического регулирования. Сборник научных трудов участников I Научно-практической конференции «Стандартизация: траектория науки», посвященной 100-летию деятельности ФГБУ «Институт стандартизации»*. 2024;6(81):43–49.
6. Wack A., Paik H., Javadi-Abhari A., Jurcevic P., Faro I., Gambetta J.M., Johnson B.R. Scale, Quality, and Speed: three key attributes to measure the performance of near-term quantum computers. *arXiv*. 2021. arXiv:2110.14108. https://doi.org/10.48550/arXiv.2110.14108
7. McKay D.C., Hincks I., Pritchett E.J., Carroll M., Govia L.C.G., Merkel S.T. Benchmarking Quantum Processor Performance at Scale. *arXiv*. 2023. arXiv:2311.05933. https://doi.org/10.48550/arXiv.2311.05933
8. Amico M., Zhang H., Jurcevic P., Bishop L.S., Nation P., Wack A., McKay D.C. Defining Standard Strategies for Quantum Benchmarks. *arXiv*. 2023. arXiv:2303.02108 https://doi.org/10.48550/arXiv.2303.02108
9. Shor P.W. Algorithms for quantum computation: discrete logarithms and factoring. In: *Proceedings 35th Annual Symposium on Foundations of Computer Science*. IEEE; 1994. P. 124–134. https://doi.org/10.1109/SFCS.1994.365700
10. Балыгин К.А., Кулик С.П., Молотков С.Н. Реализация квантового генератора случайных чисел: экстракция доказуемо случайных битовых последовательностей из коррелированных марковских цепочек. *Письма в ЖЭТФ*. 2024;119(7):533–544. https://doi.org/10.31857/S1234567824070115
11. Гайдаш А.А., Гончаров Р.К., Козубов А.В., Яковлев П.В. Математическая модель квантового генератора случайных чисел на основе флуктуации вакуума. *Вестник Санкт-Петербургского университета. Прикладная математика. Информатика. Процессы управления*. 2024;20(2):136–153. https://doi.org/10.21638/spbu10.2024.202
12. Петренко А.А., Ковалев А.В., Бугров В.Е. Генерация случайных чисел с использованием массива связанных лазеров на основе микростолбиков с квантовыми точками. *Научно-технический вестник информационных технологий, механики и оптики.* 2021;21(6):962–968. https://doi.org/10.17586/2226-1494-2021-21-6-962-968
13. Орлов М.А., Нечаев К.А., Резниченко С.А. Оценка статистических свойств и криптографической стойкости случайных последовательностей, полученных квантовым компьютером IBM. *Безопасность информационных технологий*. 2023;30(1):14–26. http://doi.org/10.26583/bit.2023.1.01
14. Li Y., Fei Y., Wang W., et al. Quantum random number generator using a cloud superconducting quantum computer based on source-independent protocol. *Sci Rep.* 2021;11:23873. https://doi.org/10.1038/s41598-021-03286-9
15. Salehi R., Razaghi M., Fotouhi B. Hybrid Hadamard and Controlled-Hadamard Based Quantum Random Number Generators in IBM QX. *Physica Scripta*. 2022;97(6):065101. https://doi.org/10.1088/1402-4896/ac698b
16. Yadav A., Mishra S., Pathak A. Partial loopholes free device-independent quantum random number generator using IBM's quantum computers. *Physica Scripta*. 2024;99(11):115103. https://doi.org/10.1088/1402-4896/ad7c02
17. Feynman R.P. Quantum Mechanical Computers. *Optics News*. 1985;11(2):11–20. URL: https://www.optica-opn.org/home/articles/on/volume_11/issue_2/features/quantum_mechanical_computers/. Дата обращения 15.05.2025. Accessed May 15, 2025.
18. Крючков А.А. *QISs_v.0.3.9*: свидетельство о государственной регистрации Программы для ЭВМ RU 2025613655 РФ. Заявка № 2025611456; заявл. 28.01.2025; опубл. 13.02.2025. Бюл. № 2.
19. Крючков А.А., Комогоров К.Е. Моделирование процесса генерации случайных чисел на квантовых вычислительных устройствах. В сб.: *Материалы VIII НПК «Актуальные проблемы и перспективы радиотехнических и инфокоммуникационных систем»* (18–22 ноября 2024 г., Москва). М.: РТУ МИРЭА; 2024. С. 501–506.

20. Acharya R., Abanin D.A., Aghababaie-Beni L., et al. Quantum error correction below the surface code threshold. *Nature*. 2025;638:920–926. https://doi.org/10.1038/s41586-024-08449-y
21. Verma S., Kumari S.S., Kumar R.S. Topological quantum error correction with semions. *Int. J. Phys. Math*. 2024:6(2):44–47. https://doi.org/10.33545/26648636.2024.v6.i2a.95
22. Webster M., Browne D. Engineering Quantum Error Correction Codes Using Evolutionary Algorithms. *IEEE Trans. Quantum Eng*. 2025;6:3100514. https://doi.org/10.1109/TQE.2025.3538934

About the Authors

Andrey V. Korolkov, Cand. Sci. (Eng.), Corresponding Member of the Academy of Cryptography of the Russian Federation, Corresponding Member of the A.M. Prokhorov Academy of Engineering Sciences of the Russian Federation, Head of the Department of Information Security, Institute of Artificial Intelligence, MIREA – Russian Technological University (78, Vernadskogo pr., Moscow, 119454 Russia). E-mail: korolkov@mirea.ru. RSCI SPIN-code 3849-6868, https://orcid.org/0009-0003-4862-4816

Andrey A. Kryuchkov, Senior Lecturer, Department of Information Security, Institute of Artificial Intelligence, MIREA – Russian Technological University (78, Vernadskogo pr., Moscow, 119454 Russia). E-mail: kryuchkov_a@mirea.ru. RSCI SPIN-code 7117-7238, https://orcid.org/0009-0002-4750-6204

Об авторах

Корольков Андрей Вячеславович, к.т.н., член-корреспондент Академии криптографии Российской Федерации, член-корреспондент Академии Инженерных наук им. А.М. Прохорова Российской Федерации, заведующий кафедрой информационной безопасности, Институт искусственного интеллекта, ФГБОУ ВО «МИРЭА – Российский технологический университет», (119454, Россия, Москва, пр-т Вернадского, д. 78). E-mail: korolkov@mirea.ru. SPIN-код РИНЦ 3849-6868, https://orcid.org/0009-0003-4862-4816

Крючков Андрей Андреевич, старший преподаватель, кафедра информационной безопасности, Институт искусственного интеллекта, ФГБОУ ВО «МИРЭА – Российский технологический университет» (119454, Россия, Москва, пр-т Вернадского, д. 78). E-mail: kryuchkov_a@mirea.ru. SPIN-код РИНЦ 7117-7238, https://orcid.org/0009-0002-4750-6204

Translated from Russian into English by K. Nazarov
Edited for English language and spelling by Thomas A. Beavitt

Modern radio engineering and telecommunication systems

Современные радиотехнические и телекоммуникационные системы

UDC 654.1
https://doi.org/10.32362/2500-316X-2025-13-6-47-62
EDN EYOGWG

RESEARCH ARTICLE

Maximum likelihood estimates of the angle-of-arrival of deterministic and random signals in multielement antenna arrays of various configurations

Olesya V. Bolkhovskaya @

National Research Lobachevsky State University of Nizhny Novgorod, Nizhny Novgorod, 603950 Russia
@ *Corresponding author, e-mail: obol@rf.unn.ru*

• **Submitted:** 02.04.2025 • **Revised:** 23.05.2025 • **Accepted:** 02.10.2025

Abstract

Objectives. The purpose of this work is to study in detail the properties of maximum likelihood (ML) estimates of the angles-of-arrival of deterministic and random signals in multielement antenna arrays, to develop effective algorithms for finding ML estimates and to determine the exact values of threshold signal-to-noise ratios (SNR), below which abnormally large errors occur significantly in excess of the theoretically minimum values determined by the Cramér–Rao bounds.

Methods. The methods used include: the theory of optimal signal detection; intensive numerical simulation of the signal processing system in multielement antenna arrays based on the developed algorithms for finding ML estimates; and comparison of the standard errors of the estimates obtained by means of the theoretically minimal analytically established Cramér–Rao bounds.

Results. Numerical study of the characteristics of ML estimates of the direction of arrival for deterministic and random signals was performed over a wide range of SNRs in multielement linear and circular antenna arrays. The study proposes a method for high-precision determination of threshold SNR values, below which anomalously large measurement errors occur. Numerical simulations demonstrate that coherent and incoherent signal processing yield the same ultimately achievable accuracy at the same SNR values above the threshold. At the same time, the threshold value is significantly influenced by the type of signal and the processing method. The general relationships between these threshold values, antenna array configurations, the type of signal processed, and the estimation algorithm used were identified.

Conclusions. The numerical and analytical results obtained allow recommendations to be developed relating to the choice of multielement antenna arrays configurations and the main parameters of systems for high-precision bearing of radiation sources of various signals. These enable abnormally large measurement errors to be avoided. The results can be directly utilized in the calculation of characteristics of systems under design.

Keywords: multielement antennas, estimation of the signal arrival angle, estimation accuracy, Cramér–Rao lower bound, CRLB, thresholds of signal-to-noise ratio

For citation: Bolkhovskaya O.V. Maximum likelihood estimates of the angle-of-arrival of deterministic and random signals in multielement antenna arrays of various configurations. *Russian Technological Journal.* 2025;13(6):47–62. https://doi.org/10.32362/2500-316X-2025-13-6-47-62, https://www.elibrary.ru/EYOGWG

Financial disclosure: The author has no financial or proprietary interest in any material or method mentioned.

The author declares no conflicts of interest.

НАУЧНАЯ СТАТЬЯ

Максимально правдоподобные оценки угла прихода детерминированных и случайных сигналов в многоэлементных антенных решетках различной конфигурации

О.В. Болховская @

Национальный исследовательский Нижегородский государственный университет им. Н.И. Лобачевского, Нижний Новгород, 603950 Россия
@ *Автор для переписки, e-mail: obol@rf.unn.ru*

• **Поступила:** 02.04.2025 • **Доработана:** 23.05.2025 • **Принята к опубликованию:** 02.10.2025

Резюме

Цели. Целью работы является исследование свойств максимально правдоподобных (МП) оценок углов прихода детерминированных и случайных сигналов в многоэлементных антенных решетках, разработка эффективных алгоритмов нахождения МП-оценок и определение точных значений пороговых отношений сигнал/шум, ниже которых возникают аномально большие ошибки, существенно превышающие теоретически минимальные значения, определяемые границами Крамера – Рао.

Методы. Теория оптимального приема сигналов, численное моделирование системы обработки сигналов в многоэлементных антенных решетках на основе разработанных алгоритмов нахождения МП-оценок, сравнение среднеквадратичных ошибок полученных оценок с теоретически минимальными границами Крамера – Рао, найденными аналитически.

Результаты. В широком интервале значений отношений сигнал/шум выполнено численное исследование характеристик МП-оценок угла прихода детерминированных и случайных сигналов в многоэлементных линейных и круговых антенных решетках. Предложена методика определения с высокой точностью пороговых значений отношений сигнал/шум, ниже которых возникают аномально большие ошибки измерений. С помощью численного моделирования показано, что когерентная и некогерентная обработка сигналов дают одинаковые предельно достижимые точности при одинаковых отношениях сигнал/шум, превышающих пороговые значения. В то же время, на величину порога существенно влияют вид полезного сигнала и метод его обработки. Выявлены общие закономерности между этими пороговыми значениями, конфигурациями антенных решеток, типом обрабатываемого сигнала и используемым алгоритмом оценивания.

Выводы. Полученные численные и аналитические результаты позволяют выработать позволяющие избегать возникновения аномально больших ошибок измерений рекомендации по выбору конфигураций многоэлементных антенных решеток и основных параметров систем высокоточного пеленгования источников излучения различных сигналов. Результаты могут быть использованы непосредственно при расчете характеристик проектируемых систем.

Ключевые слова: многоэлементные антенны, оценка угла прихода сигнала, точность оценивания, граница Крамера – Рао, пороговые значения отношений сигнал/шум

Для цитирования: Болховская О.В. Максимально правдоподобные оценки угла прихода детерминированных и случайных сигналов в многоэлементных антенных решетках различной конфигурации. *Russian Technological Journal*. 2025;13(6):47–62. https://doi.org/10.32362/2500-316X-2025-13-6-47-62, https://www.elibrary.ru/EYOGWG

Прозрачность финансовой деятельности: Автор не имеет финансовой заинтересованности в представленных материалах или методах.

Автор заявляет об отсутствии конфликта интересов.

INTRODUCTION

The problem of optimal detection and estimation of the direction to a signal source located in the far field of a multielement antenna array (AA) arises in many fields, such as radar, radio communication, sonar, hydro acoustics, navigation, seismology, and radio astronomy. Due to its significant practical importance, a very large number of publications have been devoted to resolving this problem. They consider various assumptions about the temporal structure of the signal, the geometry of the AA, signal wavefront parameters, the number of radiation sources, and others (see, for example, [1–8]). Among the existing research in this area, a number of rigorous mathematical studies can also be highlighted. Under certain assumptions, they have enabled theoretical limits for angle-of-arrival (AoA) estimates of the useful signal to be derived based on the maximum likelihood (ML) approach [9–16].

The main reason for the widespread usage of ML method in the general theory of optimal signal parameter estimation lies in the fact that, under defined regularity conditions of the likelihood function, high SNRs, and large sample sizes, ML estimates are asymptotically unbiased. Their variances reach the theoretically minimal value determined by the Cramér–Rao Lower Bound (CRLB or CRB) [17, 18].

At the same time, when the ML method of signal parameters estimation is used in the region of low SNR, below a certain threshold value, anomalously large errors are observed, significantly in excess of the CRB.

The threshold effect in ML estimation theory was discovered quite some time ago. The description and initial investigation of this effect were carried out in a number of classical monographs devoted to the theory of optimal signal parameter estimation, for example, in [19, 20].

Attempts to develop an analytical tool for analyzing the accuracy of ML estimates at low SNR region were made in a number of well-known mathematical works [21–23], where more accurate lower bounds for the variances of ML estimates in the low SNR region were derived and investigated. The most comprehensive review of the approaches used in the works cited and the results obtained there can be found in [13, 14, 24]. Unfortunately, these studies did not lead to major breakthroughs in this field due to the high complexity of an analytical description of the significantly nonlinear problems which arise. They are specific to each scenario of constructing an estimation system and implementing the algorithm for finding ML estimates.

Nevertheless, due to the significant practical importance of the general task of improving the accuracy of signal parameter estimation, the study of threshold effects and methods for reducing the SNR threshold values at which anomalous large errors (outliers) begin to occur remains relevant. This is evidenced by a number of scientific articles by foreign and Russian authors published in recent years on this topic [25–32].

One of the promising methods for investigating the behavior of ML estimates in the region of low and threshold SNR values is the direct numerical modeling of signal processing systems [14]. Modern computing technology allows for a sufficiently large number of numerical experiments on signal processing at different SNR values. This also enables the precise measurement of the SNR threshold values themselves and the achievable accuracies of ML AoA estimates in the low SNR region for various configurations of multielement AAs and types of received signals [15, 16, 33–40].

The present article offers a detailed numerical study of the accuracy of ML AoA estimates for deterministic and random signals in multielement AAs. Analysis is performed for the most common configurations of equidistant AAs—linear (uniform linear array, ULA) and circular (uniform circular array, UCA)—with varying numbers of elements.

1. GENERAL FORMULATION OF THE WAVEFRONT PARAMETER ESTIMATION PROBLEM R DETERMINISTIC AND RANDOM SIGNALS

Let us consider the problem of estimating the AoA θ of a signal with a plane wavefront from a source located in the far field of multielement AAs with linear and circular configurations. We can assume that the distance d between the antenna elements in all cases is half the wavelength ($\lambda/2$). Figure 1 shows the signal reception schemes for the AAs considered and their corresponding radiation patterns.

Let us assume that the AAs consist of M elements and satisfy the narrowband condition. This means that the signal propagation time across the array aperture is much shorter than the correlation time of the signal's complex amplitude. Then, the complex vector of observed signal samples $\mathbf{x}[n] = (x_1[n], \ldots, x_M[n])^T$ of dimension M can be written as:

$$\mathbf{x}[n] = a[n]\mathbf{s} + \boldsymbol{\xi}[n], \quad (1)$$

wherein $a[n]$ is the complex amplitude of the useful signal (emitted by the source). This is the same across all elements of the AA: $\mathbf{s} = (s_1, \ldots, s_M)^T$ is the unknown plane wavefront vector (phasor vector) of the received useful signal, depending on the AoA of the signal relative to the antenna aperture normal θ. The symbol T denotes transposition, and $\boldsymbol{\xi}[n] = (\xi_1[n], \ldots, \xi_M[n])^T$ is the complex Gaussian vector of independent internal noises in the antenna elements with zero mean and variance σ^2; $\boldsymbol{\xi}[n] \sim CN(\mathbf{0}, \sigma^2\mathbf{I})$. Here n is the discrete time instants of sampling, CN denotes complex normal distribution, and $\mathbf{I}$ is the identity matrix. It can be assumed that the estimation of the AoA is performed based on the processing of N samples of the observed vector $\mathbf{x}[n]$, $n = 1 - N$. Next, we will consider the two most commonly used models of the signal $a[n]$ emitted by the source:

Deterministic known signal. In this case, it is assumed that $a[n]$ is the function of time *a priori* known at the receiver and expressing the modulation law of the useful signal at time instant n. This model adequately describes the case on base station estimating the AoA of a signal from a mobile device transmitting standard-defined preambles in cellular communication systems or wireless broadband Internet access (Wi-Fi) [10, 41, 42].

Random unknown signal. In this case, it is assumed that $a[n]$ is a stationary complex Gaussian process with uncorrelated samples, having zero mean $\langle a[n] \rangle = 0$, where $\langle \cdot \rangle$ denotes ensemble averaging, and unknown

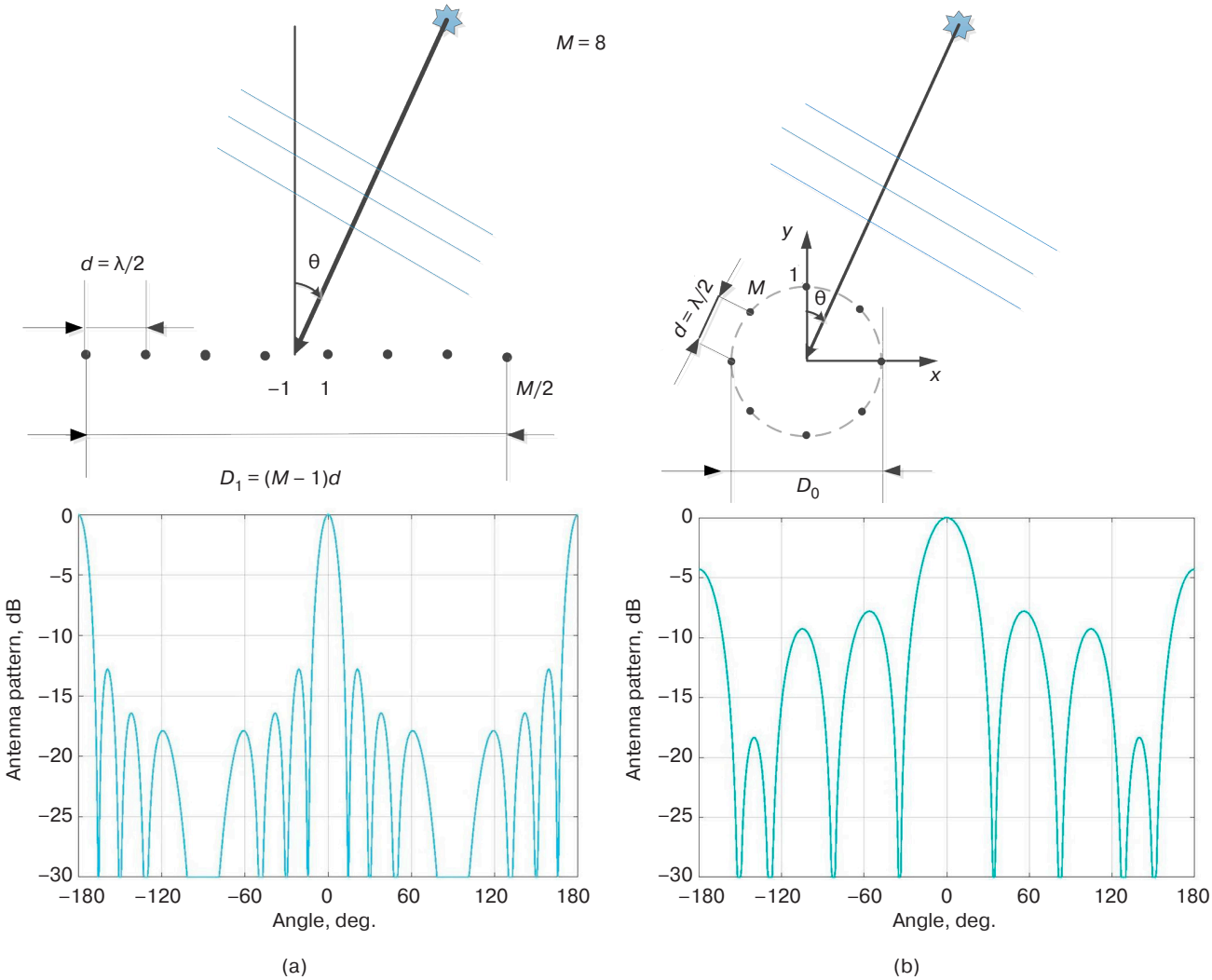

Fig. 1. Examples of signal reception schemes by M-element equidistant AAs with radiation patterns: (a) ULA with aperture D_1; (b) UCA with aperture D_0 with the same distances between elements as ULA

power $\nu = \left\langle \left| a^2[n] \right| \right\rangle$. This model adequately describes the case of estimating the AoA of a signal from a source with unknown characteristics located in the far field of the AA [11, 29].

After resolving the problem of the useful signal initial detection in the receiving M-element AA and making a decision about the presence of the signal, the next step is to resolve the problem of optimal estimation of the unknown parameters of the useful signal—in the case considered, the power and the AoA of the wavefront[1].

For both models of the useful signal (deterministic or random), the wave-front phasor vector **s** is considered as an unknown deterministic vector, depending on the initial phase of the signal, the AoA θ, and the antenna geometry. For an arbitrary AA geometry, it can be written as:

$$\mathbf{s} = \mathbf{s}(\varphi_0, \theta) = e^{j\varphi_0} \cdot \left[e^{j\varphi_1} \quad e^{j\varphi_2} \quad \cdots \quad e^{j\varphi_M} \right]^{\mathrm{T}}, \quad (2)$$

wherein φ_0 is the initial phase of the signal (on one of the AA elements or at the center of the antenna), and the phase of the signal on the mth AA element is determined as the sum of the initial phase φ_0 and the corresponding phase shift φ_m relative to the initial phase. It should be noted that this model does not account for possible fluctuations in the phase and amplitude of the signal phasor vector caused by the propagation medium, positions of antenna elements, and angular position of the remote useful signal source, which is typical, for example, in hydroacoustic channel models [7, 8].

In order to estimate the unknown parameters of the wavefront vector **s**, we will use the ML method, according to which the estimate should be taken as the value $\hat{\mathbf{s}}$ from vector **s** admissible range maximizing the likelihood function $W(\mathbf{x}[1], \ldots, \mathbf{x}[N]|\mathbf{s})$ for the observed sample vectors: $\mathbf{x}[1], \ldots, \mathbf{x}[N]$. Under the assumption of a Gaussian distribution of the observed vectors $\mathbf{x}[n]$ (1), the likelihood function can be expressed in the following form:

$$W(\mathbf{x}[1], \ldots, \mathbf{x}[N] \,|\, \mathbf{s}) = \frac{1}{\pi^{MN} \det(\mathbf{R})^N} e^{-\sum_{i=1}^{N} (\mathbf{x}[n]-\boldsymbol{\mu})^{\mathrm{H}} \mathbf{R}^{-1} (\mathbf{x}[n]-\boldsymbol{\mu})}, \quad (3)$$

wherein the symbol H denotes Hermitian transpose, $\mathbf{R} = \left\langle \mathbf{x}[n]\mathbf{x}^{\mathrm{T}}[n] \right\rangle$, $\boldsymbol{\mu}$ is the covariance matrix and the mean value vector of the Gaussian distribution of the observed vector **x**, respectively. For each of the considered useful signal models, the covariance matrix and the mean value vector included in the likelihood function (3) are easily determined:

- for a deterministic useful signal

$$\mathbf{R} = \boldsymbol{\sigma}^2 \mathbf{I}, \ \boldsymbol{\mu} = a[n]\mathbf{s}. \quad (4)$$

It is assumed that the covariance matrix of the intrinsic noise vector is identity, which is equivalent to knowledge of the intrinsic noise level (calibration). That leads to a likelihood function of the following form:

$$W(\mathbf{x} \,|\, \mathbf{s}) = \frac{1}{\pi^{MN}} e^{-\sum_{n=1}^{N} (\mathbf{x}[n]-a[n]\mathbf{s})^{\mathrm{H}} (\mathbf{x}[n]-a[n]\mathbf{s})}; \quad (5)$$

- for a random useful signal

$$\boldsymbol{\mu} = \mathbf{0}, \ \mathbf{R} = \mathbf{I} + \nu \mathbf{s}\mathbf{s}^{\mathrm{H}}, \quad (6)$$

which leads to a likelihood function of the form:

$$W(\mathbf{x} / \mathbf{s}) = \pi^{-MN} \det(\mathbf{R})^{-N} e^{-N \mathrm{tr} \mathbf{R}^{-1} (\mathbf{R}^{-1} \hat{\mathbf{R}})}, \quad (7)$$

wherein tr denotes the trace of a matrix.

For a deterministic signal, maximizing the likelihood function (5), it can easily be shown that the ML estimate of the phasor vector (without accounting for prior information about the planar wavefront of the useful signal) is given by means of the following expression:

$$\hat{\mathbf{s}} = \sum_{n=1}^{N} a^*[n]\mathbf{x}[n] = \mathbf{y}, \quad (8)$$

wherein the symbol '*' denotes complex conjugation, and the vector **y** represents the signals at the outputs of M parallel correlators (or matched filters) performing the initial optimal processing of signals from M antenna elements.

For a random signal, in the general case of an arbitrary wavefront, the ML estimate $\hat{\mathbf{s}}$ of the vector **s** is expressed through the first eigenvector $\hat{\boldsymbol{\psi}}_1$ corresponding to the largest eigenvalue $\hat{\lambda}_1$, of the sample covariance matrix of the signals at the AA elements, as follows [28]:

$$\hat{\boldsymbol{\psi}}_1 = \hat{\mathbf{s}} / \sqrt{M}. \quad (9)$$

However, when the source of the useful signal is located in the far field of the antenna, its wavefront is a plane wave with equal signal amplitudes across the

[1] According to strict statistical theory, the problem of detection and estimation of the unknown parameters of the useful signal should be resolved jointly based on the Generalized Likelihood Ratio Test (GLRT) [14]. The effectiveness of the GLRT method applied to the problem considered here has been thoroughly investigated in [28, 29, 43].

AA elements. In order to incorporate this important prior information when finding the ML estimate of the signal wavefront, we can consider two main AA configurations—linear and circular.

For a linear equidistant AA, the phase shifts φ_m relative to its geometric center can be written as:

$$\varphi_m = \Delta\varphi \cdot m = 2\pi \frac{d}{\lambda} \sin(\theta) \cdot m, \quad (10)$$

wherein d is the distance between the AA elements, λ is the wavelength, and θ is the AoA of the useful signal relative to the normal to the antenna aperture. When the phase shifts φ_m are measured from the geometric center of the AA and the numbering of the antenna elements mm is symmetric relative to this center, then for an odd number of elements, the index is $m = -\frac{M-1}{2}, ..., -1, 0, 1, ..., \frac{M-1}{2}$, and for an even number of elements, $m = -\frac{M-1}{2}, ..., -\frac{1}{2}, \frac{1}{2}, ..., \frac{M-1}{2}$.

For a circular AA, the phase shift φ_m relative to its geometric center are defined as

$$\varphi_m = 2\pi \frac{R}{\lambda} \cos\left(\theta - \frac{2\pi(m-1)}{M}\right), \quad (11)$$

wherein $m = 1, \ldots, M$; R is the radius of the circular AA.

Clearly the problem of estimating the phasor vector $\mathbf{s}$ of a plane wavefront for both AA configurations (linear and circular) is reduced to estimating only the initial phase and the AoA of the useful signal. Therefore, the ML estimate $\tilde{\mathbf{s}}$ may be found by resolving the maximization problem of the scalar product:

- for a deterministic signal, between the vector of signals y at the outputs of the matched filters and a "trial" phasor vector $\tilde{\mathbf{s}}$ of a plane wave, the phases of which are determined by expression (10) for a linear AA and (11) for a circular AA;
- for a random signal between the eigenvector $\hat{\boldsymbol{\psi}}_1 = \hat{\mathbf{s}}/\sqrt{M}$ and the "trial" phasor of a plane wave $\tilde{\mathbf{s}}$.

Various algorithms for finding the ML estimates of the parameters of a plane wave-front for a linear AA were discussed in detail in [26, 41, 42], for a known deterministic signal, and in [29, 43] for a random signal. These works proposed efficient two-stage algorithms for finding ML estimates. In the first stage, a rough estimate of the useful signal's wavefront is obtained by scanning the sector of possible AoA of the useful signal. For equidistant AAs, such scanning is typically performed using the discrete Fourier transform of the vector of signals observed at the AA elements. In the second stage, the rough estimate is refined by finding a correction to the wave vector estimate obtained in the first step. This refinement is achieved using either a regression algorithm or an iterative algorithm. The circular AA is replaced by a virtual non-equidistant linear AA [41]. For comparison, the stages of finding the ML estimates of the phasor vector of a plane wavefront for deterministic and random signals are summarized in Table 1.

2. ACCURACY OF WAVEFRONT PARAMETER ESTIMATION

The effectiveness of the algorithms developed for finding ML estimates of the plane wavefront signal was determined by comparing the variances of the estimates obtained in numerical experiments with the theoretically minimal variances as defined by the Cramér–Rao inequalities [11, 13, 14]. Furthermore, in the case of a deterministic useful signal, when investigating the question of the ultimate achievable accuracy of estimating the plane wavefront parameters, the problem of joint estimation of the initial phase and the AoA of the signal need to be considered. Therefore, let us first consider the general case of determining the Cramér–Rao lower bounds for an arbitrary number of estimated parameters. This can be conveniently written as a vector $\boldsymbol{\eta}$. Then, the variance of the ith estimated parameter η_i satisfies the following inequality:

$$\sigma^2(\hat{\eta}_i) = \left\langle \left(\hat{\eta}_i - \eta_i\right)^2 \right\rangle \geq \left[\mathbf{CRB}(\boldsymbol{\eta})\right]_{ii}, \quad (12)$$

Table 1. The stages of finding the MP estimates of the phasor vector of a plane wavefront for deterministic and random signals

Stages	Deterministic signal	Random signal
ML estimate in the case of an arbitrary wavefront	$\hat{\mathbf{s}} = \sum_{n=1}^{N} a^*[n]\mathbf{x}[n] = \mathbf{y}$	$\hat{\mathbf{s}} = \sqrt{M}\hat{\boldsymbol{\psi}}_1$
Coarse estimate in the case of a plane wavefront (discrete Fourier transform with resampling)	$\hat{\mathbf{s}} = \arg\max_{\varphi_0, \Delta\varphi} \left\lvert \tilde{\mathbf{s}}^{\mathrm{H}} \mathbf{y} \right\rvert$	$\hat{\mathbf{s}} = \arg\max_{\varphi_0, \Delta\varphi} \left\lvert \hat{\mathbf{s}}^{\mathrm{H}} \hat{\boldsymbol{\psi}}_1 \right\rvert$
Refinement of the estimate using linear regression	$\hat{\varphi}_m = \varphi_0 + \Delta\varphi(m-1)$	$\hat{\varphi}_m = \varphi_0 + \Delta\varphi(m-1)$

wherein $\boldsymbol{\eta}$ is the vector of estimated parameters, $\hat{\eta}_i$ is the estimate of the ith parameter, and $\mathbf{CRB}(\boldsymbol{\eta})$ is the covariance matrix of the parameter estimates, which is the inverse to the Fisher information matrix ($\mathbf{FIM}$), $\mathbf{CRB}(\boldsymbol{\eta}) = \mathbf{FIM}^{-1}(\boldsymbol{\eta})$.

In accordance with the general methodology for finding the Cramér–Rao bounds [11], when estimating the accuracy of multiple parameters (the parameter vector $\boldsymbol{\eta}$), an expression for the Fisher information matrix first needs to be derived in terms of the derivatives of the likelihood function. The elements of the FIM, in the general case, are expressed as:

$$\left[\mathbf{FIM}(\boldsymbol{\eta})\right]_{i,j} = -\left\langle\left\{\frac{\partial^2 \ln(W(\mathbf{y}\,|\,\boldsymbol{\eta})}{\partial\eta_i\partial\eta_j}\right\}\right\rangle. \quad (13)$$

For the observation model with additive Gaussian noise (1), the expression for the Fisher information matrix is written as [16]:

$$\left[\mathbf{FIM}(\boldsymbol{\eta})\right]_{i,j} = \\ = \mathrm{tr}\left\{\mathbf{R}^{-1}\frac{\partial\mathbf{R}}{\partial\eta_i}\mathbf{R}^{-1}\frac{\partial\mathbf{R}}{\partial\eta_j}\right\} + 2\,\mathrm{Re}\left\{\frac{\partial\boldsymbol{\mu}^{\mathrm{H}}}{\partial\eta_i}\mathbf{R}^{-1}\frac{\partial\boldsymbol{\mu}}{\partial\eta_j}\right\}. \quad (14)$$

2.1. Deterministic useful signal

When a deterministic signal with an unknown wavefront of the form (2) is observed in Gaussian noise, the noise covariance matrix $\mathbf{R}$ (4) does not depend on the estimated parameters φ_0 and θ, and therefore the first term in expression (14) will be zero. For the problem under consideration, the vector of estimated parameters is $\boldsymbol{\eta} = [\theta,\ \varphi_0]$. Taking (4) into account, the Fisher information matrix (14) can be expressed as:

$$\mathbf{FIM}(\boldsymbol{\eta})_{i,j} = \\ = 2N\cdot\mathrm{SNR}\cdot\mathrm{Re}\left\{\frac{\partial\mathbf{S}(\eta)^{\mathrm{H}}}{\partial\eta_i}\cdot\frac{\partial\mathbf{S}(\eta)}{\partial\eta_j}\right\}, \quad (15)$$

wherein $\mathrm{SNR} = \dfrac{\frac{1}{N}\sum_{n=1}^{N}|a[n]|^2}{\sigma^2}$ is the SNR at a single antenna element, defined as the ratio of the average received useful signal power at one element to the noise power.

For a linear AA, when the initial phase of the signal φ_0 is estimated at the geometric center of the antenna, the Fisher information matrix (15) becomes diagonal and takes the following form [36]:

$$\mathbf{FIM}(\boldsymbol{\eta}) = \\ = 2N\cdot\mathrm{SNR}\cdot\begin{bmatrix}\left(2\pi\dfrac{d}{\lambda}\right)^2\cos^2\theta\dfrac{M(M^2-1)}{12} & 0\\ 0 & M\end{bmatrix}. \quad (16)$$

This facilitates the finding of the correlation matrix for the estimates of the AoA θ and the initial phase φ_0 of the useful signal:

$$\mathbf{C}(\theta,\varphi_0) = \mathbf{FIM}^{-1}(\theta,\varphi_0). \quad (17)$$

For this 2 × 2 matrix, the off-diagonal elements are zero, while the diagonal elements represent the minimum possible variances of the θ and φ_0 estimates:

$$\mathrm{CRB}(\theta) = \\ = \frac{1}{(2\pi d/\lambda)^2}\cdot\frac{1}{N\cdot\mathrm{SNR}\cdot\cos^2\theta}\cdot\frac{6}{M(M^2-1)}, \quad (18)$$

$$\mathrm{CRB}(\varphi_0) = \frac{1}{2N\cdot\mathrm{SNR}}\cdot\frac{1}{M}. \quad (19)$$

For a circular AA, when the signal phase φ_0 is estimated to be at the geometric center of the antenna, the Fisher information matrix (15) also becomes diagonal and is written in the following form [41]:

$$\mathbf{FIM}(\boldsymbol{\eta}) = 2N\cdot\mathrm{SNR}\cdot\begin{bmatrix}\dfrac{2\pi^2R_0^2}{\lambda^2}M & 0\\ 0 & M\end{bmatrix}. \quad (20)$$

This facilitates the finding of its inverse, the covariance matrix of the estimates of the AoA θ and the initial phase φ_0, of the useful signal, whose diagonal elements are:

$$\mathrm{CRB}(\theta) = \frac{1}{N\cdot\mathrm{SNR}}\cdot\frac{1}{M\cdot 4\pi^2\cdot R_0^2/\lambda^2}, \quad (21)$$

$$\mathrm{CRB}(\varphi_0) = \frac{1}{2N\cdot\mathrm{SNR}}\cdot\frac{1}{M}, \quad (22)$$

with zero off-diagonal elements.

2.2. Random useful signal

When the useful signal is a random Gaussian process, the covariance matrix $\mathbf{R}$ of the observed vector $\mathbf{x}[n]$ depends on the estimated φ_0 and θ, while the mean vector $\boldsymbol{\mu}$ is zero (6). Therefore, the first term in the expression for the Fisher information matrix (14) is non-zero, while the second term is zero. Furthermore, when estimating the initial phase, φ_0 in the phasor vector

is meaningless, since the complex amplitude $a[n]$ of the random useful signal $\mathbf{s}[n] = a[n]\mathbf{s}$ at each sample has a random phase uniformly distributed in the interval $[-\pi, \pi]$. Therefore, after calculating the first term in expression (14)

$$\mathbf{FIM}(\boldsymbol{\eta})_{i,j} = \mathrm{tr}\left\{\mathbf{R}^{-1}\frac{\partial \mathbf{R}}{\partial \eta_i}\mathbf{R}^{-1}\frac{\partial \mathbf{R}}{\partial \eta_j}\right\} \quad (23)$$

all elements of the Fisher information matrix, except one, are equal to zero. Therefore, in this case, only one parameter can be estimated—AoA of the useful signal θ. Taking into account expression (6) for the covariance matrix **R**, its inverse matrix can be found:

$$\mathbf{R}^{-1} = \mathbf{I} - \frac{\nu}{1+\nu M}\mathbf{s}\mathbf{s}^{\mathrm{H}}. \quad (24)$$

Substituting (6) and (24) into the first term of formula (14) allows an expression for the desired element of the Fisher matrix to be obtained:

$$\mathrm{FIM}(\theta) == \frac{2\cdot N\cdot M\cdot \sigma_{\mathrm{s}}^4}{\sigma_{\mathrm{n}}^2\left(\sigma_{\mathrm{n}}^2 + M\sigma_{\mathrm{s}}^2\right)}\times$$
$$\times\left(\frac{\partial \mathbf{s}(\eta)^{\mathrm{H}}}{\partial\theta}\frac{\partial \mathbf{s}(\eta)}{\partial\theta} - \frac{1}{M}\frac{\partial \mathbf{s}(\eta)^{\mathrm{H}}}{\partial\theta}\mathbf{s}(\eta)\mathbf{s}(\eta)^{\mathrm{H}}\frac{\partial \mathbf{s}(\eta)}{\partial\theta}\right) = \quad (25)$$
$$= \left(2\pi\frac{d}{\lambda}\right)^2\cos^2\theta\frac{M(M^2-1)}{12},$$

wherein σ_{s}^2 and σ_{n}^2 are the signal and noise variances, respectively.

For a linear AA, substituting the phasor vector with phases defined by formula (10) into the expression for the Fisher information matrix (25), the lower bound for the variance of the AoA estimate can be easily found as:

$$\mathrm{CRB}(\theta) = \mathrm{FIM}^{-1}(\theta) = \frac{1}{\left(2\pi d/\lambda\right)^2}\times$$
$$\times\frac{1+M\cdot\mathrm{SNR}}{N\cdot\mathrm{SNR}^2\cos^2\theta}\cdot\frac{6}{M^2(M^2-1)}. \quad (26)$$

For a circular AA, the lower bound for the variance of the AoA estimate of a random signal can be found in a similar way. In order to do this, the phasor vector with phases defined by formula (11) should be substituted into the expression for the Fisher information matrix (25). As a result, we obtain the following:

$$\mathrm{CRB}(\theta) = \mathrm{FIM}^{-1}(\theta) =$$
$$= \frac{1+M\cdot\mathrm{SNR}}{N\cdot M^2\cdot\mathrm{SNR}^2\cdot 4\pi^2\cdot R_0^2/\lambda^2}. \quad (27)$$

For comparison purposes, all derived lower bounds for the variance of the signal angle of arrival estimates for linear and circular AAs are summarized in Table 2. Here CRB(θ) is denoted by the letter *L* for linear arrays and by the letter *C* for circular arrays, while the subscripts 'det' and 'rand' correspond to deterministic and random signals, respectively.

The formulas provided in Table 2 demonstrate that the ratio of the Cramér–Rao lower bounds for the variances of the AoA estimates for random and deterministic signals is the same for both linear and circular AAs and equals:

$$\frac{L_{\mathrm{rand}}}{L_{\mathrm{det}}} = \frac{1+M\cdot\mathrm{SNR}}{M\cdot\mathrm{SNR}} = \frac{C_{\mathrm{rand}}}{C_{\mathrm{det}}}. \quad (28)$$

Moreover, from expression (28), it follows that as the SNR and the number of antenna elements increase (when $M \cdot \mathrm{SNR} >> 1$), the Cramér–Rao bounds (CRLB) for the variances of the AoA estimates for random and deterministic signals become the same. For example, in the case of $M = 8$, the difference between the CRLB

Table 2. Final CRB(θ) expressions for different signal types and array configurations

Arrays	Deterministic signal	Random signal
ULA	$L_{\mathrm{det}} = \frac{1}{\left(2\pi d/\lambda\right)^2}\cdot\frac{1}{N\cdot\mathrm{SNR}\cdot\cos^2\theta}\cdot\frac{6}{M(M^2-1)}$	$L_{\mathrm{rand}} = \frac{1}{\left(2\pi d/\lambda\right)^2}\cdot\frac{1+M\cdot\mathrm{SNR}}{N\cdot\mathrm{SNR}^2\cos^2\theta}\cdot\frac{6}{M^2(M^2-1)}$
UCA	$C_{\mathrm{det}} = \frac{1}{N\cdot\mathrm{SNR}}\cdot\frac{1}{M\cdot 4\pi^2\cdot R_0^2/\lambda^2}$	$C_{\mathrm{rand}} = \frac{1+M\cdot\mathrm{SNR}}{N\cdot M^2\cdot\mathrm{SNR}^2\cdot 4\pi^2\cdot R_0^2/\lambda^2}$

Note: that the Cramér–Rao bounds in Table 2 are given for an arbitrary radius of the circular antenna. In the case where the distance between adjacent elements of the circular antenna is half the wavelength, the ratio is $R_0^2/\lambda^2 = \frac{1}{16\sin^2(\pi/M)}$.

for random and deterministic signals becomes less than 10% already at SNR > 0.8 dB, and for $M = 16$ at SNR > −2.2 dB. This is further verified by the simulation results shown in Figs. 2 and 3 in the following section.

3. NUMERICAL INVESTIGATION OF THE ALGORITHMS IMPLEMENTING ML AoA ESTIMATES

A comparative analysis of the characteristics of the above algorithms applied for estimating the AoA of the useful signal was carried out using the examples of linear and circular AAs. Different numbers of antenna elements were used under the condition of a line-of-sight channel with additive Gaussian noise (1). For all AA configurations, the distance between the antenna elements was taken to be a half wavelength ($d = \lambda/2$). A constant-amplitude pseudo-random binary phase-shift keyed signal (0, π) known at the receiver was used as the deterministic reference signal $a[n]$. For the random useful signal, a complex Gaussian sequence of independent samples of the same length N was employed.

As noted earlier, in [9] and [16], the inefficiency of ML algorithms for estimating the AoA of a random useful signal with a finite sample size N was theoretically proven. This leads to the unattainability of the Cramér–Rao bound solely by increasing the SNR for a fixed sample size. However, the detailed numerical studies of this interesting fact, performed in [29], showed that at sufficiently high SNR, the limiting values of the variances of the AoA estimates exceed the CRLB by a small relative value $\sim 1/(N-1)$. In practice, this can clearly be neglected for large N. Therefore, in the numerical experiments presented below, in order to avoid accounting for the finite sample size, the sample size N was chosen to be sufficiently large ($N = 64$) for both models of the useful signal—deterministic and random.

In order to determine the threshold SNR ratios $\mathrm{SNR}_{\mathrm{th}}$ (below which anomalously large errors occur), the following methodology was proposed. The threshold values $\mathrm{SNR}_{\mathrm{th}}$ were found as the values at which the root mean square error of the useful signal's AoA estimates exceeded the theoretical Cramér–Rao lower bounds by a specified percentage. A key advantage of this methodology is that the Cramér–Rao lower bounds can be easily calculated using the analytical formulas provided in Table 2 for linear and circular arrays. The exceedance level of theoretical values was set to 10% based on preliminary numerical experiments. This showed that on one hand, for $\mathrm{SNR} < \mathrm{SNR}_{\mathrm{th}}$, a rapid, nearly abrupt increase in estimation root mean squared error (MSE) occurs. On the other hand, measuring this 10% deviation can be achieved with a high level of accuracy (about 1%) given a reasonable number of trials (approximately 1 million).

The MSE of the ML estimates of the plane wavefront AoA obtained using the algorithms described in Section 2 and listed in Table 1 for both useful signal models were investigated. For each algorithm, AA configuration, and signal model, the MSE of the AoA estimates was determined based on $2 \cdot 10^5$ numerical experiments, each processing a signal of length N samples ($N = 64$).

For linear AAs, Fig. 2 shows the MSE ($\sigma_{\sin\theta}$) of the sine of the AoA estimates for deterministic and random signals as a function of the SNR ratio measured at a single antenna element. The AoA of the useful signal was randomly and uniformly distributed in each experiment within the range of ±60°. The dashed lines of corresponding colors represent the CRB for the deterministic signal according to formula (18) and for the random signal according to formula (26).

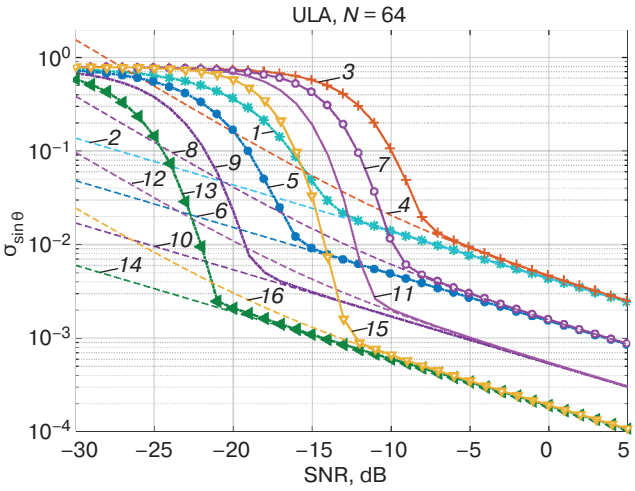

(*1*) $M = 8$, det.
(*2*) CRB $M = 8$, det.
(*3*) $M = 8$, rand.
(*4*) CRB $M = 8$, rand.
(*5*) $M = 16$, det.
(*6*) CRB $M = 16$, det.
(*7*) $M = 16$, rand.
(*8*) CRB $M = 16$, rand.
(*9*) $M = 32$, det.
(*10*) CRB $M = 32$, det.
(*11*) $M = 32$, rand.
(*12*) CRB $M = 32$, rand.
(*13*) $M = 64$, det.
(*14*) CRB $M = 64$, det.
(*15*) $M = 64$, rand.
(*16*) CRB $M = 64$, rand.

Fig. 2. MSE of the estimates of the sine of the AoA for deterministic (det) and random (rand) signals as a function of the SNR for a linear AA with different numbers of antenna elements M

From the results presented in Fig. 2, it can be seen that the MSE of the estimates for both signal models tends towards the same limiting values as the SNR increases, depending on the number of antenna elements M. Furthermore, when the number of antenna elements is doubled, the MSE of the estimates decreases by approximately a factor of 2.83. This is in good agreement with the analytical expressions provided in Table 2. It is also interesting to note that,

in order to achieve the same reduction in MSE for a fixed number of antenna elements M, the SNR must be increased by approximately 10 dB. At the same time, the threshold SNR values (SNR_{th}), above which the MSE of the estimates practically reaches the CRB, depend significantly on the type of useful signal. For deterministic signals, the SNR_{th} values are significantly lower than for random signals.

For circular AAs (UCA), Fig. 3 presents similar plots of the root mean square errors σ_θ of the angle of arrival estimates for deterministic and random signals as a function of the SNR ratio per antenna element. The angle of arrival of the useful signal was randomly uniformly distributed in the range from 0° to 180°/M (due to the radial M-symmetry of the problem. This distribution is equivalent to a uniform distribution from 0° to 360°). The dashed lines of corresponding colors depict the Cramér–Rao bounds for the deterministic signal according to formula (21) and for the random signal according to formula (27). The results presented above show that for circular arrays, as for linear arrays, the MSE of the angle estimates for both signal models approach the same limiting values as SNR increases, depending on the number of antenna elements M. The threshold SNR ratios SNR_{th}, above which the MSE of the estimates practically reach the Cramér–Rao bounds, depend significantly on the type of useful signal. Furthermore, for deterministic signals, the threshold SNR values are lower than those for random signals.

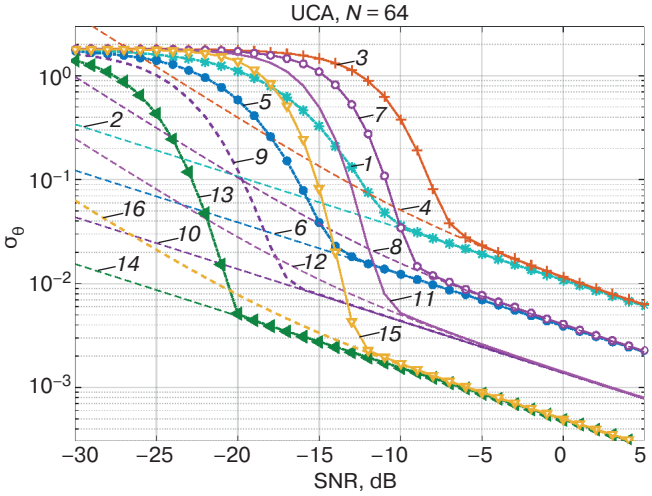

(*1*) M = 8, det.
(*2*) CRB M = 8, det.
(*3*) M = 8, rand.
(*4*) CRB M = 8, rand.
(*5*) M = 16, det.
(*6*) CRB M = 16, det.
(*7*) M = 16, rand.
(*8*) CRB M = 16, rand.
(*9*) M = 32, det.
(*10*) CRB M = 32, det.
(*11*) M = 32, rand.
(*12*) CRB M = 32, rand.
(*13*) M = 64, det.
(*14*) CRB M = 64, det.
(*15*) M = 64, rand.
(*16*) CRB M = 64, rand.

Fig. 3. MSE of the estimates of the sine of the AoA for deterministic and random signals as a function of the SNR for a circular AA with different numbers of antenna elements M

From the comparison of the two AA geometries considered, it is evident that the behavior of the MSE of the AoA estimates as a function of the number of antenna elements M and the SNR is similar in the region of high SNR (exceeding SNR_{th}). At the same time, for an equal number of antenna elements and spacing between them, the MSE of the estimates for a linear AA (in the case of a zero AoA, i.e., when the signal arrives perpendicular to the aperture of the AA) is approximately 2.5 times smaller than for a circular AA. This is obviously due to the smaller aperture size (approximately 3 times) of the circular AA when compared to the linear AA. However, it can easily be shown that this advantage of the linear AA over the circular AA in the accuracy of the AoA estimation is maintained only within a sector of ±67°. For larger angles, the circular AA provides higher estimation accuracy than the linear AA. In addition, the results obtained (both analytical and numerical) indicate that the estimation accuracy of the circular AA at high SNR ($SNR > SNR_{th}$) does not in any way depend on the AoA of the useful signal.

In the second series of numerical experiments, a more detailed investigation of the achievable accuracies of the AoA estimation was conducted for all the above considered antenna configurations and signal models in the most interesting region of threshold SNR ratio values (SNR_{th} region). For this purpose, the number of numerical experiments for each SNR near to SNR_{th} was increased to $1 \cdot 10^6$, and linear interpolation was used to determine more precisely the refined threshold values.

For the deterministic model of the useful signal, Table 3 presents the refined SNR_{th} values for ULA and UCA (given with an accuracy of 0.1 dB), the corresponding MSE of the AoA estimates $\sigma_{\sin\theta}/\sin\theta$ (given with an accuracy of 3 significant digits), and the limiting Cramér–Rao lower bounds $\left(\sqrt{L_{\text{det}}}/\sqrt{C_{\text{det}}}\right)$, calculated by using the analytical expressions provided in Table 2. The control values of the 10 percentage excess of the MSE over the Cramér–Rao bounds ($\delta_{\sigma\sin\theta}/\delta_{\sigma\theta}$) are given in the bottom row of the table (with an accuracy of 3 significant digits).

For the random model of the useful signal and linear and circular AA configurations, Table 4 similarly presents the refined SNR_{th}, values for ULA and UCA, the corresponding MSE of the AoA estimates $\sigma_{\sin\theta}/\sin\theta$ and the limiting Cramér–Rao lower bounds $\left(\sqrt{L_{\text{rand}}}/\sqrt{C_{\text{rand}}}\right)$, also calculated using the formulas provided in Table 2. The control values of the relative 10% excess of the MSE over the Cramér–Rao bounds are given in the bottom row of Table 4.

For a more visual comparison of the numerical results presented in Tables 3 and 4, Fig. 4 shows the calculated refined threshold values SNR_{th} for all AA configurations and useful signal models on a single picture.

Table 3. SNR_{th} values for linear and circular arrays for deterministic signals

M	8		16		32		64	
	ULA	UCA	ULA	UCA	ULA	UCA	ULA	UCA
SNR_{th}, dB	−13.3	−10.3	−15.5	−13.6	−17.5	−16.8	−20.0	−20.1
$\sigma_{\sin\theta}/\sin\theta$	$2.20 \cdot 10^{-2}$	$3.92 \cdot 10^{-2}$	$9.95 \cdot 10^{-3}$	$2.03 \cdot 10^{-2}$	$4.44 \cdot 10^{-3}$	$1.04 \cdot 10^{-2}$	$2.09 \cdot 10^{-3}$	$5.43 \cdot 10^{-3}$
$\sqrt{L_{rand}}/\sqrt{C_{rand}}$	$2.00 \cdot 10^{-2}$	$3.53 \cdot 10^{-2}$	$9.04 \cdot 10^{-3}$	$1.85 \cdot 10^{-2}$	$4.04 \cdot 10^{-3}$	$9.49 \cdot 10^{-3}$	$1.90 \cdot 10^{-3}$	$4.94 \cdot 10^{-3}$
$\delta_{\sigma\sin\theta}/\delta_{\sigma\theta}$	0.100	0.100	0.100	0.100	0.100	0.100	0.100	0.100

Table 4. SNR_{th} values for linear and circular arrays for random signals

M	8		16		32		64	
	ULA	UCA	ULA	UCA	ULA	UCA	ULA	UCA
SNR_{th}, dB	−7.3	−6.4	−9.1	−9.0	−10.7	−10.3	−12.2	−12.2
$\sigma_{\sin\theta}/\sin\theta$	$1.42 \cdot 10^{-2}$	$3.07 \cdot 10^{-2}$	$5.90 \cdot 10^{-3}$	$1.48 \cdot 10^{-2}$	$2.37 \cdot 10^{-3}$	$5.76 \cdot 10^{-3}$	$9.55 \cdot 10^{-4}$	$2.45 \cdot 10^{-3}$
$\sqrt{L_{rand}}/\sqrt{C_{rand}}$	$1.29 \cdot 10^{-2}$	$2.79 \cdot 10^{-2}$	$5.36 \cdot 10^{-3}$	$1.35 \cdot 10^{-2}$	$2.15 \cdot 10^{-3}$	$5.23 \cdot 10^{-3}$	$8.68 \cdot 10^{-4}$	$2.23 \cdot 10^{-3}$
$\delta_{\sigma\sin\theta}/\delta_{\sigma\theta}$	0.100	0.100	0.100	0.100	0.100	0.100	0.100	0.100

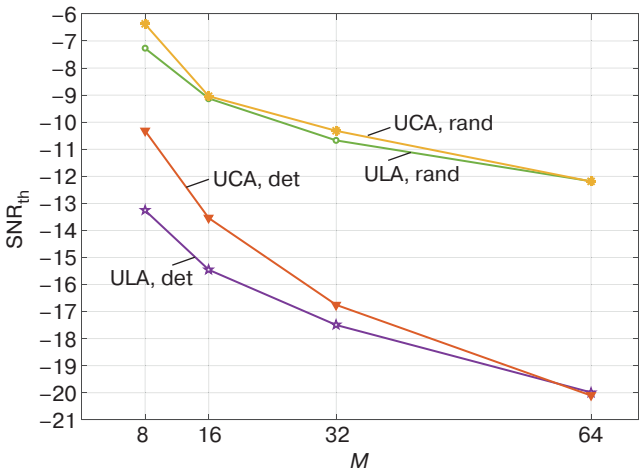

Fig. 4. Dependencies of the refined SNR_{th} on the number of antenna elements for all AA configurations and useful signal models

Important practical conclusions can be drawn from the graphs presented in Fig. 4. First, the threshold SNR ratio values strongly depend on the type of received signal. For deterministic (*a priori* known) signals, they are approximately 6–7 dB lower than for random (*a priori* unknown) signals. Second, the threshold SNR values depend very weakly on the AA configuration and, for a large number of antenna elements ($M > 16$), practically coincide for the linear and circular AAs considered in this work. Furthermore, when the number of antenna elements is doubled, SNR_{th} decreases by approximately 2 dB.

CONCLUSIONS

The paper presents a detailed numerical study of the accuracy of ML estimates of the AoA of a signal with a plane wavefront received by linear and circular AAs. Two models of the useful signal were analyzed: a deterministic signal with *a priori* known waveform; and a random signal—Gaussian noise with uncorrelated samples.

Through detailed numerical experiments, it was shown that as the SNR increases and with large sample sizes, the MSE of ML estimates for both signal models tend towards the same theoretical limiting values (Cramér–Rao bounds), depending only on the number of antenna elements M and the AA configuration.

The paper proposes a method for accurate determining the threshold values (below which anomalously large errors occur) based on a given relative excess of the MSE of ML estimates over the theoretical Cramér–Rao lower bounds, found analytically in the paper. The detailed numerical investigations conducted herein allowed such

SNR threshold values to be found for deterministic and random signal models.

Simple regularities were identified between the main characteristics of the estimation system: the geometry of the AAs; the number of antenna elements; the type of signal being processed; and the algorithm used. These regularities, based on interpolation and approximation of the results already presented in the paper (without additional numerical modeling), allow the threshold SNR values for the two basic signal models (deterministic and random) in linear and circular AAs to be determined with practically any number of antenna elements greater than four.

Thus, one of the key results of this work, in the authors' opinion, is the numerical proof that coherent and incoherent signal processing achieve identical ultimate accuracy at the same SNR ratios above threshold values ($SNR > SNR_{th}$). At the same time, the type of useful signal and its processing method significantly affect the threshold SNR_{th} values below which anomalously large errors occur.

The results obtained in this work can be used practically at the initial stage of defining the architecture of high-precision direction-finding and localization systems for sources emitting various types of signals.

REFERENCES

1. Skolnik M.I. *Radar Handbook*. 3rd ed. New York: McGraw-Hill Professional; 2008. 1328 p.
2. Shirman Ya.D., Manzhos V.N. *Teoriya i tekhnika obrabotki radiolokatsionnoi informatsii na fone pomekh* (*Theory and Technique of Radar Information Processing Against the Background of Interference*). Moscow: Radio i svyaz; 1981. 416 p. (in Russ.).
3. Richards M.A. *Fundamentals of Radar Signal Processing*. New York: McGraw-Hill; 2014. 640 p.
4. Vaughan R., Andersen J.B. *Channels, Propagation and Antennas for Mobile Communications*. London: The Institution of Engineering and Technology; 2003. 784 p. https://doi.org/10.1049/PBEW050E
5. Sand S., Dammann A., Mensing C. *Positioning in Wireless Communications Systems*. Chichester: John Wiley & Sons; 2014. 280 p.
6. Krim H., Viberg M. Two decades of array signal processing research: the parametric approach. *IEEE Signal Processing Mag*. 1996;13(4):67–94. https://doi.org/10.1109/79.526899
7. Dosso S.E., Wilmut M.J. Maximum-likelihood and other processors for incoherent and coherent matched-field localization. *J. Acoust. Soc. Am*. 2012;132(4):2273–2285. https://doi.org/10.1121/1.4730978
8. Malekhanov A.I., Smirnov A.V. Large-Array Processing of Coherence-Degraded Signals: Analytical Study, Modeling, and Estimations of Optimization Possibilities. *Radiophys. Quantum El*. 2023;66(12):988–1011. https://doi.org/10.1007/s11141-024-10346-3
   [Original Russian Text: Malekhanov A.I., Smirnov A.V. Large-Array Processing of Coherence-Degraded Signals: Analytical Study, Modeling, and Estimations of Optimization Possibilities. *Izvestiya vysshikh uchebnykh zavedenii. Radiofizika*. 2023;66(12):1094–1121 (in Russ.). https://doi.org/10.52452/00213462_2023_66_12_1094]
9. Stoica P., Nehorai A. MUSIC, maximum likelihood, and Cramér–Rao bound. *IEEE Trans. Acoust. Speech Signal Process*. 1989;37(5):720–741. https://doi.org/10.1109/29.17564
10. Li J., Compton R.T. Maximum likelihood angle estimation for signals with known waveforms. *IEEE Trans. Signal Process*. 1993;41(9):2850–2862. https://doi.org/10.1109/78.236507
11. Kay S.M. *Fundamentals of Statistical Signal Processing. Volume 1. Estimation Theory*. Upper Saddle River, NJ: Prentice Hall; 1993. 625 p.
12. Viberg M., Ottersten B., Nehorai A. Performance analysis of direction finding with large arrays and finite data. *IEEE Trans. Signal Process*. 1995;43(2):469–477. https://doi.org/10.1109/78.348129
13. Van Trees H.L. *Detection, Estimation, and Modulation Theory, Part I: Detection, Estimation, and Linear Modulation Theory*. New York, NY: Wiley; 2001. 716 p.
14. Van Trees H.L., Bell K.L. *Detection, Estimation, and Modulation Theory, Part IV: Optimum Array Processing*. Hoboken, NJ: Wiley; 2002. 1480 p.
15. Renaux A., Foster P., Chaumette E., Larzabal P. On the high-SNR conditional maximum-likelihood estimator full statistical characterization. *IEEE Trans. Signal Process.* 2006;54(12):4840–4843. https://doi.org/10.1109/TSP.2006.882072
16. Renaux A., Forster P., Boyer E., Larzabal P. Unconditional maximum likelihood performance at finite number of samples and high signal-to-noise ratio. *IEEE Trans. Signal Process*. 2007;55(5):2358–2364. https://doi.org/10.1109/TSP.2007.893205
17. Cramer H. *Mathematical Methods of Statistics*. Princeton, New Jersey: Princeton University Press; 1946. 589 p.
18. Rao C.R. *Linear Statistical Inference and Its Applications*. New York: Wiley; 1946. 660 p.
19. Tikhonov V.I. *Optimal'nyi priem signalov* (*Optimal Signal Detection*). Moscow: Radio i svyaz; 1983. 320 p. (in Russ.).
20. Trifonov A.P., Shinakov Yu.S. *Sovmestnoe razlichenie signalov i otsenka ikh parametrov na fone pomekh* (*Joint Discrimination of Signals and Estimation of Their Parameters Against the Background of Interference*). Moscow: Radio i svyaz; 1986. 264 p. (in Russ.).

21. Barankin E.W. Locally best unbiased estimates. *Ann. Math. Statist*. 1949;20(4):477–501. https://doi.org/10.1214/aoms/1177729943
22. Bhattacharyya A. On some analogues of the amount of information and their use in statistical estimation. *Sankhyā*. 1946;8(1):201–218. Available from URL: https://www.jstor.org/stable/25047921
23. Bell K.L., Ephraim Y., Van Trees H.L. Ziv-Zakai lower bounds in bearing estimation. In: *Proceedings of the 1995 International Conference on Acoustics, Speech, and Signal Processing* (*ICASSP*); 1995 May 9–12; Detroit, MI, USA. IEEE. P. 2852–2855. https://doi.org/10.1109/ICASSP.1995.479888
24. Athley F. Threshold Region Performance of Maximum Likelihood Direction of Arrival Estimators. *IEEE Trans. Signal Process*. 2005;53(4):1359–1373. https://doi.org/10.1109/TSP.2005.843717
25. Chernoyarov O.V., Rozanov A.E., Salnikova A.V. Quasi-likelihood appearance time estimate of the random pulse with free-form envelope shape and inaccurately known duration. *Radiotekhnika = Radioengineering*. 2013;10:65–70 (in Russ.).
26. Bolkhovskaya O., Maltsev A., Sergeev V. The wavefront estimation and signal detection in multi-element antenna arrays at low SNR. In: *Proceedings 2018 2nd European Conference on Electrical Engineering and Computer Science* (*EECS*); 2018 Dec 20–22; Bern, Switzerland. IEEE. P. 497–501. https://doi.org/10.1109/EECS.2018.00097
27. Trifonov A.P., Korchagin Yu.E., Titov K.D. Efficiency of the Detection of a Specific Wideband Signal under a Priori Parametric Uncertainty. *Tech. Phys.* 2018;63(8):1199–1204. https://doi.org/10.1134/S1063784218080212
[Original Russian Text: Trifonov A.P., Korchagin Yu.E., Titov K.D. Efficiency of the Detection of a Specific Wideband Signal under a Priori Parametric Uncertainty. *Zhurnal tekhnicheskoi fiziki.* 2018;88(8):1235–1240 (in Russ.). https://doi.org/10.21883/JTF.2018.08.46315.2552]
28. Bolkhovskaya O., Maltsev A., Sergeev V. Joint detection and the AoA estimation of noncoherent signals in multi-element antennas. In: *Proceedings 2019 International Symposium on Performance Evaluation of Computer and Telecommunication Systems* (*SPECTS*). 2019 Jul 22–24; Berlin, Germany. IEEE. P. 1–6. https://doi.org/10.23919/SPECTS.2019.8823557
29. Bolkhovskaya O., Maltsev A., Sergeev V., Keusgen W., Peter M. Investigation of theoretical limits for unconditional AoA estimations in multi-element antenna arrays by simulations. In: *Proceedings 2020 IEEE International Conference on Industrial Technology* (*ICIT*). 2020 Feb 26–28; Buenos Aires, Argentina. IEEE. P. 663–668. https://doi.org/10.1109/ICIT45562.2020.9067150
30. Fateev A.A., Tokarev A.B., Chernoyarov O.V., Salnikova A.V. Influence of the radiation pattern errors for the correlation interferometer. *J. Phys.: Conf. Ser*. 2021;2094(2):022054. http://doi.org/10.1088/1742-6596/2094/2/022054
31. Serbes A., Qaraqe K.A. Threshold regions in frequency estimation. *IEEE Trans. Aerosp. Electron. Syst*. 2022;58(5): 4850–4856. https://doi.org/10.1109/TAES.2022.3166063
32. Bolkhovskaya O.V., Maltsev A.A., Sergeev V.A. A passive system for source detection and distance measurement based on signal wavefront estimation. *Radiotekhnika = Radioengineering*. 2022;86(9):98–112 (in Russ.). https://doi.org/10.18127/j00338486-202209-11
33. Beshara-Flynn K., Adhikari K. Effects of signal and array parameters on MSE and CRB in DOA estimation. In: *2022 IEEE 13th Annual Ubiquitous Computing, Electronics & Mobile Communication Conference* (*UEMCON*). 2022 Oct 26–29; New York, NY, USA. IEEE. P. 373–379. https://doi.org/10.1109/UEMCON54665.2022.9965625
34. Chumankin Yu.E., Fidelman V.R., Morozov O.A. A Method for Estimating the Changes in the Directions of the Main Maxima of the Directional Pattern of a Multibeam Antenna in the Problem of Passive Direction Finding. *Radiophys. Quantum El*. 2022;65(9):689–697. https://doi.org/10.1007/s11141-023-10249-9
[Original Russian Text: Chumankin Yu.E., Fidelman V.R., Morozov O.A. A Method for Estimating the Changes in the Directions of the Main Maxima of the Directional Pattern of a Multibeam Antenna in the Problem of Passive Direction Finding. *Izvestiya vysshikh uchebnykh zavedenii. Radiofizika*. 2022;65(9):758–767 (in Russ.). https://doi.org/10.52452/00213462_2022_65_09_758]
35. Shchukin A.A., Pavlov A.E. Parameterization of user functions in digital signal processing for obtaining angular superresolution. *Russ. Technol. J*. 2022;10(4):38–43. https://doi.org/10.32362/2500-316X-2022-10-4-38-43
36. Bolkhovskaya O., Sergeev V., Maltsev A. Cramér–Rao lower bounds for the task of joint estimation of signal initial phase and AoA in multi-element antenna arrays. In: *2023 Wave Electronics and its Application in Information and Telecommunication Systems* (*WECONF*). 2023 Jun 5–9; St. Petersburg, Russian Federation. IEEE. P. 1–6. https://doi.org/10.1109/WECONF57201.2023.10148023
37. Xu Y., Cao N., Jin H., et al. Robust beamforming design for integrated sensing and communication systems. *IEEE J. Sel. Areas Sens*. 2024;1:114–123. https://doi.org/10.1109/JSAS.2024.3421391
38. Korchagin Yu.E., Titov K.D., Volovach V.I., Kondratovich P.A., Zavalishina O.N. Quasi-likelihood estimation of the arrival time of an ultra-wideband quasi-radio signal with unknown amplitude and initial phase. *Radiotekhnika = Radioengineering*. 2024;88(9):112–122 (in Russ.). https://doi.org/10.18127/j00338486-202409-10
39. Ermolaev V.T., Semenov V.Yu., Flaksman A.G. Spatiotemporal signal processing in automotive radar subject to active interference. *Radiophys. Quantum El*. 2024;67(3):261–269. https://doi.org/10.1007/s11141-025-10371-w
[Original Russian Text: Ermolaev V.T., Semenov V.Yu., Flaksman A.G. Spatiotemporal signal processing in automotive radar subject to active interference. *Izvestiya vysshikh uchebnykh zavedenii. Radiofizika*. 2024;67(3):292–301 (in Russ.). https://doi.org/10.52452/00213462_2024_67_03_292]
40. Mazor Y., Berman I.E., Routtenberg T. On the limitations of the Bayesian Cramér–Rao bound for mixed-resolution data. *IEEE Signal Process. Lett*. 2025;32:446–450. https://doi.org/10.1109/LSP.2024.3519804

41. Bolkhovskaya O.V., Sergeev V.A., Maltsev A.A. Detection and position determination of the signal source in the near-field zone of the circular antenna array. *Antenny = Antennas*. 2023;5:23–37 (in Russ.). https://doi.org/10.18127/j03209601-202305-03
42. Sergeev V.A. Optimization of the size of the circular antenna array in the problem of determining the direction to the radiation source in the far-field zone. *Antenny = Antennas*. 2023;5:13–22 (in Russ.). https://doi.org/10.18127/j03209601-202305-02
43. Bolkhovskaya O., Maltsev A., Sergeev V., Keusgen W., Peter M. Accurate iterative algorithm for detection and the signal AoA estimation in low SNR region. In: *2019 4th International Conference on Computing, Communications and Security* (*ICCCS*). 2019 Oct 10–12; Rome, Italy. IEEE. P. 89–95. https://doi.org/10.1109/CCCS.2019.8888112

СПИСОК ЛИТЕРАТУРЫ

1. Skolnik M.I. *Radar Handbook*. 3rd ed. New York: McGraw-Hill Professional; 2008. 1328 p.
2. Ширман Я.Д., Манжос В.Н. *Теория и техника обработки радиолокационной информации на фоне помех*. М.: Радио и связь; 1981. 416 с.
3. Richards M.A. *Fundamentals of Radar Signal Processing*. New York: McGraw-Hill; 2014. 640 p.
4. Vaughan R., Andersen J.B. *Channels, Propagation and Antennas for Mobile Communications*. London: The Institution of Engineering and Technology; 2003. 784 p. https://doi.org/10.1049/PBEW050E
5. Sand S., Dammann A., Mensing C. *Positioning in Wireless Communications Systems*. Chichester: John Wiley & Sons; 2014. 280 p.
6. Krim H., Viberg M. Two decades of array signal processing research: the parametric approach. *IEEE Signal Processing Mag*. 1996;13(4):67–94. https://doi.org/10.1109/79.526899
7. Dosso S.E., Wilmut M.J. Maximum-likelihood and other processors for incoherent and coherent matched-field localization. *J. Acoust. Soc. Am*. 2012;132(4):2273–2285. https://doi.org/10.1121/1.4730978
8. Малеханов А.И., Смирнов А.В. Пространственная обработка частично-когерентных сигналов в больших антенных решетках: анализ, моделирование и оценки возможностей оптимизации. *Известия вузов. Радиофизика*. 2023;66(12):1094–1121. https://doi.org/10.52452/00213462_2023_66_12_1094
9. Stoica P., Nehorai A. MUSIC, maximum likelihood, and Cramér–Rao bound. *IEEE Trans. Acoust. Speech Signal Process*. 1989;37(5):720–741. https://doi.org/10.1109/29.17564
10. Li J., Compton R.T. Maximum likelihood angle estimation for signals with known waveforms. *IEEE Trans. Signal Process*. 1993;41(9):2850–2862. https://doi.org/10.1109/78.236507
11. Kay S.M. *Fundamentals of Statistical Signal Processing. Volume 1. Estimation Theory*. Upper Saddle River, NJ: Prentice Hall; 1993. 625 p.
12. Viberg M., Ottersten B., Nehorai A. Performance analysis of direction finding with large arrays and finite data. *IEEE Trans. Signal Process*. 1995;43(2):469–477. https://doi.org/10.1109/78.348129
13. Van Trees H.L. *Detection, Estimation, and Modulation Theory, Part I: Detection, Estimation, and Linear Modulation Theory*. New York, NY: Wiley; 2001. 716 p.
14. Van Trees H.L., Bell K.L. *Detection, Estimation, and Modulation Theory, Part IV: Optimum Array Processing*. Hoboken, NJ: Wiley; 2002. 1480 p.
15. Renaux A., Foster P., Chaumette E., Larzabal P. On the high-SNR conditional maximum-likelihood estimator full statistical characterization. *IEEE Trans. Signal Process.* 2006;54(12):4840–4843. https://doi.org/10.1109/TSP.2006.882072
16. Renaux A., Forster P., Boyer E., Larzabal P. Unconditional maximum likelihood performance at finite number of samples and high signal-to-noise ratio. *IEEE Trans. Signal Process*. 2007;55(5):2358–2364. https://doi.org/10.1109/TSP.2007.893205
17. Cramer H. *Mathematical Methods of Statistics*. Princeton, New Jersey: Princeton University Press; 1946. 589 p.
18. Rao C.R. *Linear Statistical Inference and Its Applications*. New York: Wiley; 1946. 660 p.
19. Тихонов В.И. *Оптимальный прием сигналов*. М.: Радио и связь; 1983. 320 с.
20. Трифонов А.П., Шинаков Ю.С. *Совместное различение сигналов и оценка их параметров на фоне помех*. М.: Радио и связь; 1986. 264 с.
21. Barankin E.W. Locally best unbiased estimates. *Ann. Math. Statist*. 1949;20(4):477–501. https://doi.org/10.1214/aoms/1177729943
22. Bhattacharyya A. On some analogues of the amount of information and their use in statistical estimation. *Sankhyā*. 1946;8(1):201–218. URL: https://www.jstor.org/stable/25047921
23. Bell K.L., Ephraim Y., Van Trees H.L. Ziv-Zakai lower bounds in bearing estimation. In: *Proceedings of the 1995 International Conference on Acoustics, Speech, and Signal Processing* (*ICASSP*). 1995 May 9–12; Detroit, MI, USA. IEEE. P. 2852–2855. https://doi.org/10.1109/ICASSP.1995.479888
24. Athley F. Threshold Region Performance of Maximum Likelihood Direction of Arrival Estimators. *IEEE Trans. Signal Process*. 2005;53(4):1359–1373. https://doi.org/10.1109/TSP.2005.843717
25. Чернояров О.В., Розанов А.Е., Сальникова А.В. Квазиправдоподобная оценка времени прихода случайного импульса с огибающей произвольной формы и неточно известной длительностью. *Радиотехника*. 2013;10:65–70.
26. Bolkhovskaya O., Maltsev A., Sergeev V. The wavefront estimation and signal detection in multi-element antenna arrays at low SNR. In: *Proceedings 2018 2nd European Conference on Electrical Engineering and Computer Science* (*EECS*). 2018 Dec 20–22; Bern, Switzerland. IEEE. P. 497–501. https://doi.org/10.1109/EECS.2018.00097

27. Трифонов А.П., Корчагин Ю.Э., Титов К.Д. Эффективность обнаружения одного класса сверхширокополосных сигналов в условиях параметрической априорной неопределенности. *Журнал технической физики*. 2018;88(8): 1235–1240. https://doi.org/10.21883/JTF.2018.08.46315.2552
28. Bolkhovskaya O., Maltsev A., Sergeev V. Joint detection and the AoA estimation of noncoherent signals in multi-element antennas. In: *Proceedings 2019 International Symposium on Performance Evaluation of Computer and Telecommunication Systems* (*SPECTS*). 2019 Jul 22–24; Berlin, Germany. IEEE. P. 1–6. https://doi.org/10.23919/SPECTS.2019.8823557
29. Bolkhovskaya O., Maltsev A., Sergeev V., Keusgen W., Peter M. Investigation of theoretical limits for unconditional AoA estimations in multi-element antenna arrays by simulations. In: *Proceedings 2020 IEEE International Conference on Industrial Technology* (*ICIT*). 2020 Feb 26–28; Buenos Aires, Argentina. IEEE. P. 663–668. https://doi.org/10.1109/ICIT45562.2020.9067150
30. Fateev A.A., Tokarev A.B., Chernoyarov O.V., Salnikova A.V. Influence of the radiation pattern errors for the correlation interferometer. *J. Phys.: Conf. Ser*. 2021;2094(2):022054. http://doi.org/10.1088/1742-6596/2094/2/022054
31. Serbes A., Qaraqe K.A. Threshold regions in frequency estimation. *IEEE Trans. Aerosp. Electron. Syst*. 2022;58(5): 4850–4856. https://doi.org/10.1109/TAES.2022.3166063
32. Болховская О.В., Мальцев А.А., Сергеев В.А. Система пассивного обнаружения и измерения расстояния до источника на основе оценки волнового фронта сигнала. *Радиотехника*. 2022;86(9):98–112. https://doi.org/10.18127/j00338486-202209-11
33. Beshara-Flynn K., Adhikari K. Effects of signal and array parameters on MSE and CRB in DOA estimation. In: *2022 IEEE 13th Annual Ubiquitous Computing, Electronics & Mobile Communication Conference* (*UEMCON*). 2022 Oct 26–29; New York, NY, USA. IEEE. P. 373–379. https://doi.org/10.1109/UEMCON54665.2022.9965625
34. Чуманкин Ю.Е., Фидельман В.Р., Морозов О.А. Метод оценки изменения направлений главных максимумов диаграммы направленности многолучевой антенны в задаче пассивной пеленгации. *Известия вузов. Радиофизика*. 2022;65(9):689–697. https://doi.org/10.52452/00213462_2022_65_09_758
35. Щукин А.А., Павлов А.Е. Параметризация пользовательских функций в цифровой обработке сигналов для получения углового сверхразрешения. *Russ. Technol. J*. 2022;10(4):38–43. https://doi.org/10.32362/2500-316X-2022-10-4-38-43
36. Bolkhovskaya O., Sergeev V., Maltsev A. Cramér–Rao lower bounds for the task of joint estimation of signal initial phase and AoA in multi-element antenna arrays. In: *2023 Wave Electronics and its Application in Information and Telecommunication Systems* (*WECONF*). 2023 Jun 5–9; St. Petersburg, Russian Federation. IEEE. P. 1–6. https://doi.org/10.1109/WECONF57201.2023.10148023
37. Xu Y., Cao N., Jin H., et al. Robust beamforming design for integrated sensing and communication systems. *IEEE J. Sel. Areas Sens*. 2024;1:114–123. https://doi.org/10.1109/JSAS.2024.3421391
38. Корчагин Ю.Э., Титов К.Д., Воловач В.И., Кондратович П.А., Завалишина О.Н. Квазиправдоподобная оценка времени прихода сверхширокополосного квазирадиосигнала с неизвестными амплитудой и начальной фазой. *Радиотехника*. 2024;88(9):112–122. https://doi.org/10.18127/j00338486-202409-10
39. Ермолаев В.Т., Семенов В.Ю., Флаксман А.Г. Пространственно-временная обработка сигналов в автомобильном радаре в условиях активных помех. *Известия вузов. Радиофизика*. 2024;67(3):292–301. https://doi.org/10.52452/00213462_2024_67_03_292
40. Mazor Y., Berman I.E., Routtenberg T. On the limitations of the Bayesian Cramér–Rao bound for mixed-resolution data. *IEEE Signal Process. Lett*. 2025;32:446–450. https://doi.org/10.1109/LSP.2024.3519804
41. Болховская О.В., Сергеев В.А., Мальцев А.А. Обнаружение и определение положения источника сигнала в ближней зоне круговой антенной решетки. *Антенны*. 2023;5:23–37. https://doi.org/10.18127/j03209601-202305-03
42. Сергеев В.А. Оптимизация размера круговой антенной решетки в задаче определения направления на источник излучения в дальней зоне. *Антенны*. 2023;5:13–22. https://doi.org/10.18127/j03209601-202305-02
43. Bolkhovskaya O., Maltsev A., Sergeev V., Keusgen W., Peter M. Accurate iterative algorithm for detection and the signal AoA estimation in low SNR region. In: *2019 4th International Conference on Computing, Communications and Security* (*ICCCS*). 2019 Oct 10–12; Rome, Italy. IEEE. P. 89–95. https://doi.org/10.1109/CCCS.2019.8888112

About the Author

Olesya V. Bolkhovskaya, Cand. Sci. (Phys.-Math.), Associate Professor, Department of Statistical Radiophysics and Mobile Communication Systems, Faculty of Radiophysics, National Research Lobachevsky State University of Nizhny Novgorod (23, Gagarina pr., Nizhny Novgorod, 603950 Russia). E-mail: obol@rf.unn.ru. Scopus Author ID 56373874700, ResearcherID AAQ-4264-2020, RSCI SPIN-code 4240-6246, https://orcid.org/0000-0002-6679-9295

Об авторе

Болховская Олеся Викторовна, к.ф.-м.н., доцент, кафедра статистической радиофизики и мобильных систем связи, Радиофизический факультет, ФГАОУ ВО «Национальный исследовательский Нижегородский государственный университет им. Н.И. Лобачевского» (603950, Россия, Нижний Новгород, пр-т Гагарина, д. 23). E-mail: obol@rf.unn.ru. Scopus Author ID 56373874700, ResearcherID AAQ-4264-2020, SPIN-код РИНЦ 4240-6246, https://orcid.org/0000-0002-6679-9295

Translated from Russian into English by the Author
Edited for English language and spelling by Dr. David Mossop

Modern radio engineering and telecommunication systems
Современные радиотехнические и телекоммуникационные системы

UDC 629.3.066
https://doi.org/10.32362/2500-316X-2025-13-6-63-77
EDN FGTHOC

RESEARCH ARTICLE

A device for calling emergency operational services to provide voice communication between the driver of a two-wheeled vehicle and the operator of the ERA-GLONASS system

Vasily V. Nikitin [1], Saygid U. Uvaysov [2], Dmitry V. Basov [2, @]

[1] FICOM-IT, Moscow, 129128 Russia
[2] MIREA – Russian Technological University, Moscow, 119454 Russia
[@] Corresponding author, e-mail: d_basov@mail.ru

• **Submitted:** 29.01.2025 • **Revised:** 24.06.2025 • **Accepted:** 09.10.2025

Abstract

Objectives. The aim of the study is to improve road safety by developing an emergency call device for drivers of two-wheeled vehicles, as the most vulnerable road users, and improving their technical equipment.

Methods. In the course of the study, the characteristics of the acoustic signal transmission channel and the processes accompanying its propagation were analyzed. When studying the parameters of voice communication, noise reduction, echo cancellation and echo compensation methods were used, as well as algorithms for converting acoustic information implemented in the hardware and software of the device.

Results. The results of practical implementation are presented: the design of a prototype device, its integration into the dashboard of a two-wheeled vehicle. During the design of the device, the control features of a two-wheeled vehicle, the influence of external factors and climatic conditions were taken into account. An implementation of the interface of interaction between the driver of a two-wheeled vehicle and the operator of the ERA-GLONASS system is proposed, taking into account the specifics of its use. Structural schemes of an echo compensator and a dual speech signal detector using an adaptive filter are presented. The algorithms implementing these processes and the possibility of their adaptation to the tasks of the emergency call device are considered. The procedure for automatically adjusting the amplification of the acoustic signal of the speech range is described, an analytical description of the technical problem and the applied methods of digital processing are given. A structural diagram of the test stand, software for qualitative analysis of the acoustic signal, visualization of the test results of the prototype are presented, and the effectiveness of the proposed solution is evaluated.

Conclusions. The results of a study on the design of an emergency call device have shown that the use of analog and digital speech signal processing algorithms implemented in the device's codec and modem will ensure a high-quality level of voice communication between the driver and the emergency services operator.

Keywords: two-wheeled vehicle, acoustic signal, duplex voice communication, echo cancellation algorithm, noise reduction algorithm, normalized least squares algorithm, digital signal processor, LMS algorithm, NLMS

For citation: Nikitin V.V., Uvaysov S.U., Basov D.V. A device for calling emergency operational services to provide voice communication between the driver of a two-wheeled vehicle and the operator of the ERA-GLONASS system. *Russian Technological Journal.* 2025;13(6):63–77. https://doi.org/10.32362/2500-316X-2025-13-6-63-77, https://www.elibrary.ru/FGTHOC

Financial disclosure: The authors have no financial or proprietary interest in any material or method mentioned.

The authors declare no conflicts of interest.

НАУЧНАЯ СТАТЬЯ

Устройство вызова экстренных оперативных служб для обеспечения голосовой связи водителя двухколесного транспортного средства и оператора системы «ЭРА-ГЛОНАСС»

В.В. Никитин [1], С.У. Увайсов [2], Д.В. Басов [2, @]

[1] ООО «ФИКОМ-ИТ», Москва, 129128 Россия
[2] МИРЭА – Российский технологический университет, Москва, 119454 Россия
[@] Автор для переписки, e-mail: d_basov@mail.ru

• **Поступила:** 29.01.2025 • **Доработана:** 24.06.2025 • **Принята к опубликованию:** 09.10.2025

Резюме

Цели. Целью исследования является повышение безопасности дорожного движения за счет разработки устройства вызова экстренных оперативных служб для водителей двухколесных транспортных средств, как наиболее уязвимых участников дорожного движения, и улучшения их технической оснащенности.

Методы. В ходе исследования проанализированы характеристики канала передачи акустического сигнала и процессов, сопровождающих его распространение. При исследовании параметров голосовой связи применялись методы шумоподавления, эхоподавления и эхокомпенсации, а также алгоритмы преобразования акустической информации, реализованные в аппаратно-программной части устройства.

Результаты. В ходе проектирования устройства учтены особенности управления двухколесным транспортным средством, влияние внешних воздействующих факторов и климатических условий. Предложена реализация интерфейса взаимодействия водителя двухколесного транспортного средства с оператором системы «ЭРА-ГЛОНАСС», учитывающая специфику его использования. Приведены структурные схемы эхокомпенсатора и детектора двойного речевого сигнала с использованием адаптивного фильтра. Описана процедура автоматической регулировки усиления акустического сигнала речевого диапазона. Рассмотрены алгоритмы, реализующие эти процессы, и возможность их адаптации к задачам устройства вызова экстренных оперативных служб. Показаны результаты практической реализации опытного образца устройства: конструкция, его интеграция в приборную панель двухколесного транспортного средства. Приведены структурная схема тестового стенда, программное обеспечение для качественного анализа акустического сигнала, оценена эффективность предложенного решения.

Выводы. Результаты исследования по конструированию устройства вызова экстренных оперативных служб показали, что применение алгоритмов аналоговой и цифровой обработки речевого сигнала, реализуемых в кодеке и модеме устройства, позволит обеспечить качественный уровень голосовой связи водителя с оператором экстренных оперативных служб.

Ключевые слова: двухколесное транспортное средство, акустический сигнал, дуплексная голосовая связь, алгоритм эхокомпенсации, алгоритм шумоподавления, нормализованный алгоритм наименьших квадратов, цифровой сигнальный процессор, алгоритм LMS, алгоритм NLMS

Для цитирования: Никитин В.В., Увайсов С.У., Басов Д.В. Устройство вызова экстренных оперативных служб для обеспечения голосовой связи водителя двухколесного транспортного средства и оператора системы «ЭРА-ГЛОНАСС». *Russian Technological Journal*. 2025;13(6):63–77. https://doi.org/10.32362/2500-316X-2025-13-6-63-77, https://www.elibrary.ru/FGTHOC

Прозрачность финансовой деятельности: Авторы не имеют финансовой заинтересованности в представленных материалах или методах.

Авторы заявляют об отсутствии конфликта интересов.

INTRODUCTION

Ensuring road safety remains a critical and pressing concern, a challenge amplified by the evolving road network and infrastructure. This complexity is further heightened by the growing variety and number of vehicles using the roads on a daily basis. A crucial element of road safety lies in comprehending the nature of accidents, including the number of casualties and injured individuals, in order to provide the best possible aid and support for those affected. Accidents involving two-wheeled vehicles are especially high risk due to the lack of a protective structure for riders, unlike car drivers. As a consequence, eyewitness accounts and, if possible, statements from those involved offer valuable insights, beyond automatically detecting accidents. To this end, two-wheeled vehicles should be equipped with emergency communication systems (ECS) allowing for two-way communication with a designated operator.

The unique characteristics of the human-vehicle system (consisting of a driver and a two-wheeled vehicle) pose specific challenges for implementing ECS. During development, the significantly smaller size and mass of the vehicle compared to a car needs to be considered, as well as the driver's helmet which muffles speech and may be difficult to remove in an emergency. Additionally, the system must function in all weather conditions and account for variable distances between the speaker and microphone. The high noise levels inherent in traffic situations also pose a challenge.

In order to ensure a clear and reliable voice connection with emergency operators, the use of advanced analog-to-digital voice processing systems is crucial (GOST 34788-2021[1]). This includes effectively minimizing noise, eliminating echo, and dynamically adjusting microphone and speaker gain levels based on the surrounding environment (GOST 33468-2015[2]).

Due to the inherent delay in signal propagation caused by digital processing, a balance must be found between the desired processing quality and the acceptable signal transmission time [1].

Contemporary speech processing algorithms typically use digital signal processors (DSP) which are often integrated into cellular modems. Improving processing efficiency and reducing latency can be accomplished by distributing individual calculations across other circuit components, such as the codec and microcontroller.

KEY MEASURES OF EFFECTIVE TWO-WAY VOICE COMMUNICATION

The ECS employs a duplex hands-free communication method when interacting with emergency operators from the subscriber's end. In order to ensure the clarity of voice data, the terminal device must possess the following attributes [2]:

1) speaker signal level sufficient to exceed the total noise level;
2) microphone signal level sufficient to exceed the total noise level;
3) wide dynamic microphone range, in order to ensure stable operation in a noisy public road environment;
4) low in-channel noise;
5) automatic gain control;
6) noise reduction;
7) echo cancellation;
8) addition of comfortable noise to the communication channel.

Items 1 to 4 are accompanied by a circuit design which includes a speaker of suitable power, an audio amplifier, a high-sensitivity microphone featuring a broad dynamic

[1] GOST 34788-2021. Interstate Standard. *Motor vehicles. Call emergency services systems. Speakerphone quality. Technical requirements and test methods*. Moscow: Russian Institute of Standardization; 2021. 20 p. (in Russ.).

[2] GOST 33468-2015. Interstate Standard. *Global navigation satellite system. Road accident emergency response system. In-vehicle emergency call device/system. General technical requirements*. Moscow: Standartinform; 2016. 74 p. (in Russ.).

range and built-in amplification. Additionally, there is a bandpass filter which only allows the transmission of useful speech frequencies (300–3400 Hz), as well as filters to suppress narrowband interference (harmonics from electrical equipment and GSM[3]).

Items 5 to 8 are implemented using digital speech processing algorithms. The ECS specific configuration determines whether DSP is an independent component or integrated into a cellular modem.

The device is designed using a printing unit meticulously crafted with advanced computer-aided design software.

AUTOMATIC VOICE GAIN CONTROL

Automatic voice gain control is a difficult task to implement using digital signal processing. Thus, in most cases, the method involves transferring analog circuitry algorithms into a digital signal. However, modern speech processing systems use digital signal processing techniques in automatic gain control systems by calculating based on the analytic signal. Each sample of the digital analytic signal, $x(n)$, is a complex number:

$$x(n) = \mathrm{Re}\{x(n)\} + i\mathrm{Im}\{x(n)\},$$

wherein n is the sample number.

The normalized digital waveform has the following form:

$$x_{\mathrm{norm}}[n] = \frac{x(n)}{|x(n)|}. \quad (1)$$

When dealing with signals composed of harmonic oscillations and noise, or a combination of harmonic oscillations, normalization can lead to signal distortion. In order to ensure that the signal aligns with formula (1), the denominator should not represent a fixed reference point, but rather the average value of the signal envelope. This average amplitude can be determined using a finite impulse response (FIR) filter, in order to average the absolute value of the signal rather than the signal itself. Following this procedure, the normalization formula ultimately assumes the following form:

$$x_{\mathrm{norm}}(n) = \frac{x(n)}{x_{\mathrm{av}}(n)},$$

wherein $x_{\mathrm{av}}(n)$ is the average signal modulus value calculated using the moving average method:

$$\dot{x}_{\mathrm{av}}(n) = \frac{1}{N}\sum_{k=0}^{N-1} |\dot{x}(n-k)|,$$

wherein N is the length of the averaging window and k is the summation index.

Several key considerations arise when this speech processing technique is applied. Firstly, the pauses inherent in speech between words and phrases can lead to elevated noise levels in the digitized audio signal. This noise includes in-channel interference from electrical circuitry and external noise, along with quantization noise generated during the conversion process. In order to address this issue, two strategies can be implemented. One approach is to deactivate automatic gain control when the speech is absent. A speech detector is used to identify these pauses. This prevents the gain control from amplifying noise during these silent periods. The second strategy entails incorporating a DC component into the average signal envelope, with its parameter values set above the maximum noise levels observed during pauses. This guarantees that the calculated average signal remains uncontaminated by noise present in those areas. In this scenario, the equation to calculate the average signal would be:

$$x_{\mathrm{norm}}(n) = \frac{x(n)}{x_{\mathrm{av}}(n) + \mathrm{L}}.$$

The L constant is chosen empirically during the system tuning process for specific noise conditions.

NOISE REDUCTION

The ERA-GLONASS system operator frequently encounters noisy speech signals due to the vehicle's design. As a two-wheeled vehicle lacking an enclosed cabin, there is a significant level of ambient noise intrusion. Intense background noise can significantly disrupt the accuracy of speech analysis and recognition processes. Several noise reduction methods are utilized, in order to eliminate unwanted noise. While some techniques can work in real time with minimal impact on the signal's delay, a key difficulty in noise reduction lies in the fluctuating volume and character of noise over time. The most prevalent noise reduction techniques operate under the assumption that speech and noise signals are independent of each other [3]. Their widespread adoption stems from their proven ability to effectively diminish background noise and enhance speech recognition performance.

Let speech signal $x(n)$ be distorted by additive noise $v(n)$. Then, the noisy signal $y(n)$ can be expressed as follows:

$$y(n) = x(n) + v(n).$$

The general goal of noise reduction is to reconstruct the signal $\hat{x}(n)$ as close as possible to the original signal $x(n)$, based on the observed noisy signal $y(n)$. In

[3] Global System for Mobile Communication (GSM) is the second-generation mobile communication standard.

order to achieve this, adaptive algorithms have been developed which utilize noise estimation and suppression techniques.

When segmenting a signal into windows ranging from 10 to 30 ms, it can be reasonably assumed that both the speech signal and background noise become stationary. Therefore, noise reduction techniques are developed under this premise [4, 5]. Within contemporary modem digital signal processors, the Kochen–Berdugo algorithms for minima controlled recursive averaging (MCRA), quantile estimation, and its diverse variations are predominantly employed for noise estimation [6, 7]. A contemporary adaptation of Wiener filtering is employed specifically for noise reduction.

ECHO CANCELLATION

In telephony, there are two types of echo:

- acoustic echo caused by the reflection of sound waves; and
- electrical echo due to problems with the line matching (which is currently not a common issue).

For ECS, it is essential to eliminate acoustic echo. This phenomenon results from the acoustic connection between the microphone and speaker of the user interface unit (UIU) in the telecommunications operator system. It is also be a product of sound waves reflecting off surrounding objects and causing reverberation.

Echo cancellation techniques can be categorized into two types: those operating in the time domain; and those in the frequency domain [8, 9]. In the context of low-frequency signals, such as those found in telephone lines, time-domain algorithms have demonstrated superior efficiency in terms of computational resource utilization.

The adaptive echo cancellation algorithm involves the following steps [6]:

1. Echo path modeling.
   A model of the true acoustic path is created to describe the characteristics of the echo path $\boldsymbol{\theta}$. This model is a filter with adjustable coefficients $\hat{\boldsymbol{\theta}}$.
2. Estimating the echo signal.
   At each step n, an estimate of the echo $\hat{z}(n)$ is calculated by convolving a reference signal $\mathbf{x}$ with the model coefficients vector $\hat{\boldsymbol{\theta}}$ as follows:

$$\hat{z}(n) = \hat{\boldsymbol{\theta}}^{\mathrm{T}} \cdot \mathbf{x},$$

   wherein T indicates transposition, and the vector length is dictated by the digital filter length.
3. Model parameter adaptation.
   The $\hat{\boldsymbol{\theta}}$ model parameters are continuously adjusted based on the analysis of the error signal $e(n)$, which represents the difference between the actual echo signal $z(n)$, and its estimated value $\hat{z}(n)$. This adaptation mechanism employs a coefficient adjustment algorithm to effectively reduce this error.
4. Echo cancellation.
   The final output signal with echo cancellation is formed by subtracting the estimated echo $\hat{z}(n)$ from the total microphone signal $m(n)$, as follows:

$$y(n) = m(n) - \hat{z}(n),$$

   wherein $m(n) = \omega(n) + z(n)$, $\omega(n)$ is the useful near-end speech signal and $z(n)$ represents the real echo.

The operation of the echo canceller is illustrated in Fig. 1. In this figure, the far-end signal represents the voice of the operator, while the near-end signal indicates the voice of the user transmitted through the speakerphone system.

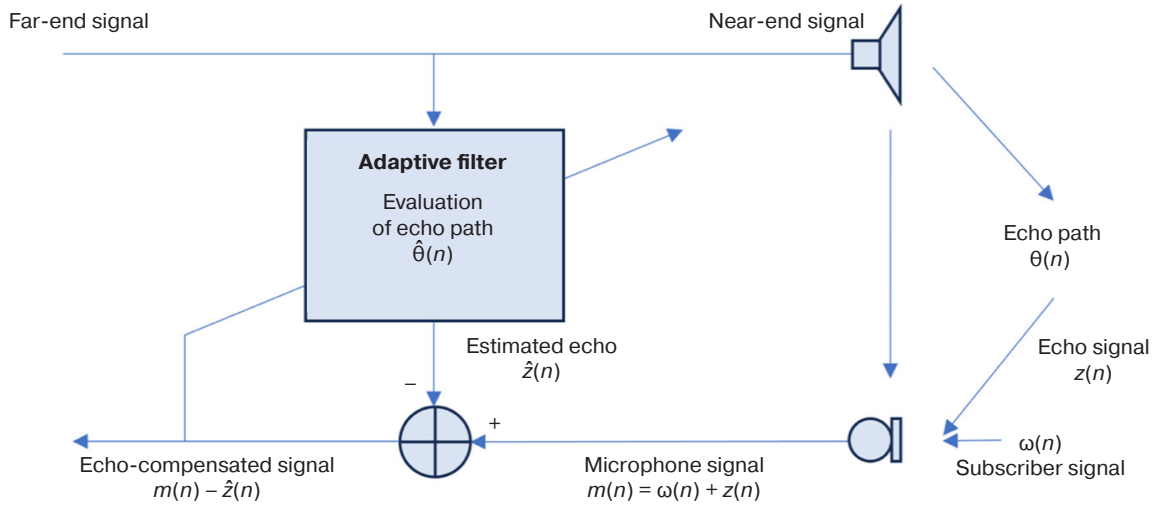

Fig. 1. Echo canceller circuit using adaptive filter

LEAST MEAN-SQUARES ALGORITHM

The Widrow–Hoff algorithm [10], also known as the Least Mean-Squares (LMS) algorithm, remains one of the most effective adaptive filtering algorithms in use today. This algorithm is widely employed in the development of echo cancellation systems, since it adjusts the filter coefficients $\hat{\boldsymbol{\theta}}$ in order to minimize the difference between the desired (target) input signal and the output of the filter. Due to its simplicity in terms of computational requirements, this algorithm has gained widespread adoption.

NORMALIZED LEAST MEAN-SQUARES ALGORITHM

The Normalized Least Mean-Squares (NLMS) algorithm [11] is derived from the LMS algorithm. The NLMS algorithm addresses the issue of the step size changing with the input power of the adaptive filter. When the input power changes over time, the step size between adjacent filter coefficients also changes which can affect the convergence rate of the algorithm. At low signal levels, the convergence rate slows down due to the small signal strength. Conversely, at high signal levels, the convergence rate increases and can cause errors. In order to address this issue, the step size needs to be adjusted based on the input signal level. This new step size is called normalized.

DOUBLE-TALK DETECTOR

Acoustic echo cancellation faces a significant challenge in addressing the double-talk (DT) effect [12] which arises when both far-end and near-end speech signals are active simultaneously. In this scenario, the signal from the remote participant becomes distorted by overlapping local speech. In order to mitigate this issue, a double talk detector is incorporated into the system. Its role is to halt the adaptation process of the filtering algorithm temporarily when a speech signal is detected at the near end, preventing inconsistencies in the performance of the adaptive algorithm.

The implementation of the Double-Talk Detector (DTD) together with the adaptive filter is shown in Fig. 2. This arrangement relies on the DTD to evaluate three critical parameters:

1) the far-end signal $x(n)$, which serves as the echo reference signal;
2) the near-end signal $m(n)$, representing a combination of the desired signal and the echo;
3) the error signal $e(n) = m(n) - \hat{z}(n)$, where $\hat{z}(n)$ is the estimated echo produced by the adaptive filter.

The error signal $e(n)$ represents an echo-compensated output generated by subtracting the simulated echo from the microphone input. This signal typically arises in two key scenarios:

- during the initial phase of operation when the adaptive filter has not yet converged;
- when there is a change in the room's acoustic properties, such as repositioning the microphone.

The DTD assesses the signal strength of $x(n)$, $m(n)$, and $e(n)$, evaluates the signal-to-echo ratio, and determines whether to update the filter coefficients. This ensures adaptation when no double talk is present or halts updates when overlapping speech is detected [13].

Various DTD algorithms exist, with the most widely used being the Geigel algorithm and those reliant on

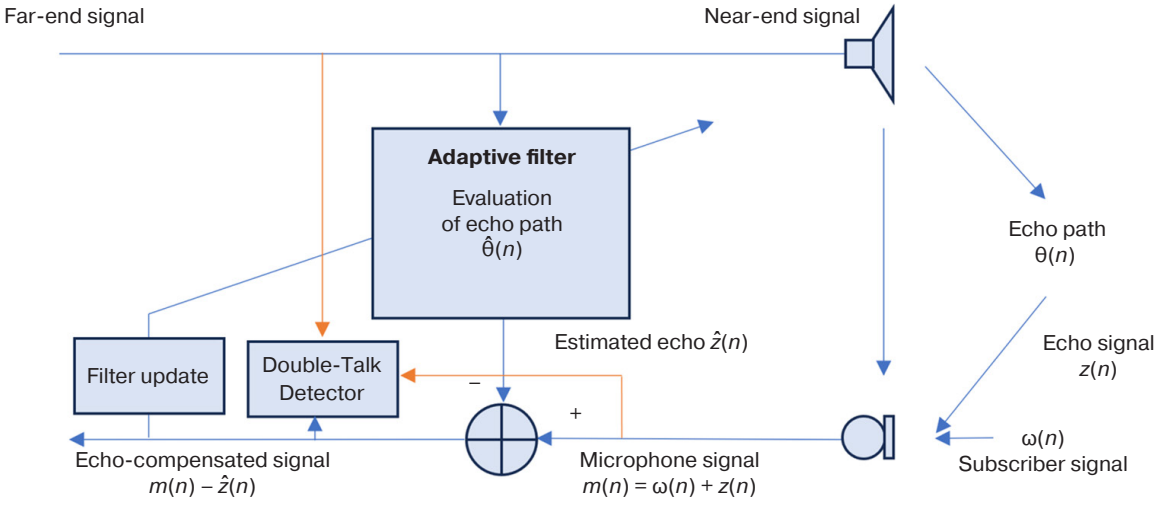

Fig. 2. Connection diagram of the double-talk detector in conjunction with an adaptive filter

cross-correlation calculations, such as Benesty and Normalized Cross-Correlation (NCC) [14].

The Geigel algorithm fundamentally works by analyzing and comparing the power levels of two signals: the microphone signal, which may include echo and/or near-end speech; and the far-end reference signal transmitted to the loudspeaker. When the microphone signal consists solely of echo without near-end speech, its power is lower than the reference signal due to attenuation along the acoustic path. However, when near-end speech is introduced alongside the echo, the overall power of the microphone signal rises substantially. This increase in signal strength enables the algorithm to identify effectively the presence of double talk.

In contrast to the Geigel energy method, the Benesty algorithm employs a normalized cross-correlation coefficient to analyze the relationship between the far-end signal (reference echo) and the microphone signal (a combination of echo and near-end speech). A higher correlation coefficient signifies that the microphone signal is predominantly influenced by echo, whereas a drop in the correlation suggests the emergence of near-end speech. This technique delivers more precise detection when compared to basic power comparison methods.

The normalized cross-correlation algorithm computes decision statistics by examining the interplay between the microphone signal and the error signal which represents deviation between the actual echo and its estimated counterpart. This approach relies on assessing the dispersion of the near-end signal (the useful signal) and evaluating the cross-correlation between the microphone and error signals. By normalizing with respect to signal power, the algorithm maintains robustness against fluctuations in signal levels, a crucial attribute in dynamic acoustic environments.

PRACTICAL IMPLEMENTATION OF THE PROTOTYPE USER INTERFACE

A prototype UIU has been designed to facilitate the modeling and testing of algorithms. The appearance of the device is shown in Fig. 3.

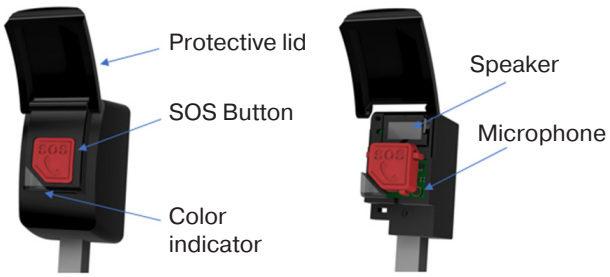

Fig. 3. Appearance of the designed UIU

The device is positioned on the steering apparatus of a two-wheeled vehicle, within easy reach of the driver. It features a microphone, speaker, an SOS button for contacting emergency services, a status indicator for the device, and a protective cover to avoid unintentional activation. The device layout and the UIU components are shown in Fig. 4.

Fig. 4. ECS placement on a two-wheeled vehicle

Since the speaker and microphone are housed within the same unit and positioned closely together, acoustic echo tends to manifest quite prominently [15]. In order to mitigate this issue, the use of a digital signal processor within the modem is suggested, while auxiliary computations can be handled by the microcontroller in the main unit. The UIU functional diagram is shown in Fig. 5.

The pathway of the acoustic speech signal as it passes through the UIU is shown in Fig. 6. Within the codec housed in the UIU, the analog signals from the microphone and speaker are transformed into digital data. The reverse process (via the I^2S interface[4]) is also performed at this stage. The signal is then transmitted via the RS-485 interface[5] to the main unit, the primary function of which is to ensure robust noise immunity. Subsequently, the main unit microcontroller transfers the signal to the I^2S interface, directing it toward the modem. Given that the I^2S interface is designed for short-range transmission, integrating the RS-485 interface proves to be a highly effective solution [16].

The ECS main unit consists of the Telit LE910 modem (manufactured by Telit Cinterion, Italy) and the NAU8810 codec (produced by Nuvoton Technology Corporation, Taiwan). The modem operates on a Qualcomm chipset and integrates a digital signal processor developed by the same company. Configuration of the digital processor parameters is managed via the user interface of the *Qualcomm QACT* software (Qualcomm, USA).

[4] I^2S (Inter-Integrated Circuit Sound) is a standardized electrical serial bus interface for connecting digital audio devices.

[5] Recommended Standard 485 is the physical layer standard for an asynchronous interface.

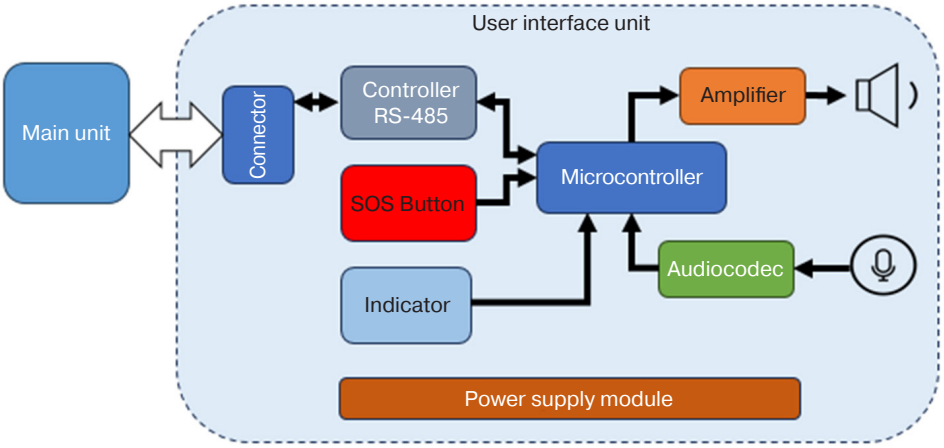

Fig. 5. UIU functional diagram

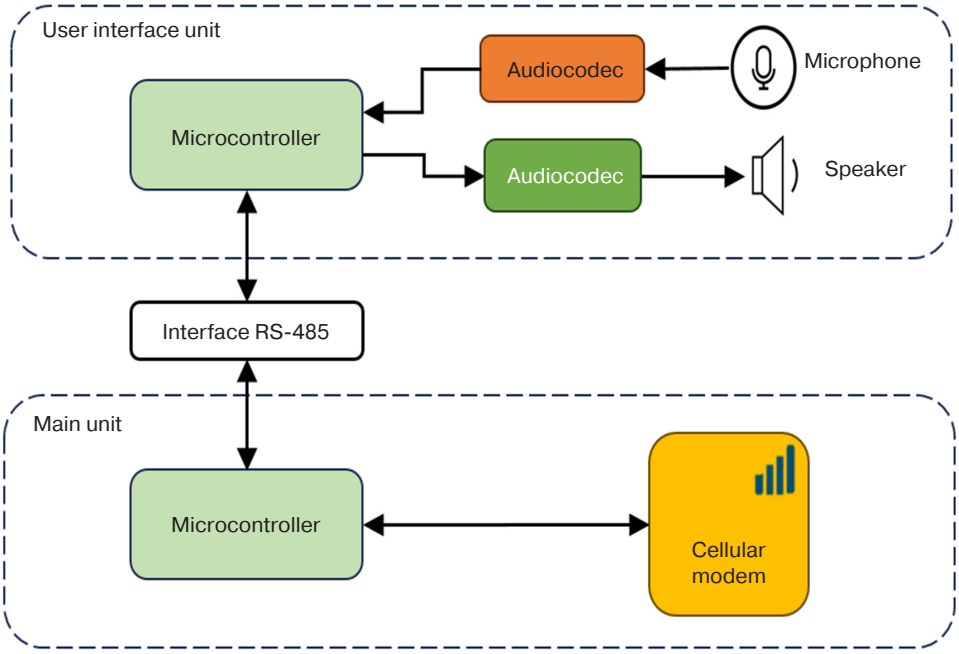

Fig. 6. Pathway of the acoustic speech signal passing through UIU

DEVICE TESTING

Figure 7 shows the block diagram of the test bench designed for evaluating and analyzing voice quality. The emergency communication system, mounted on a two-wheeled vehicle, is linked to a radio communication tester via cellular network connectivity. Additionally, the audio input of the tester is connected to a computer equipped with the *HEAD Analyzer ACQUA* software (HEAD Acoustics GmbH, Germany). This software provides a comprehensive suite of audio tests for assessing the quality of speech signals. Its operational algorithm enables voice quality testing from both the operator's perspective and the vehicle driver's viewpoint.

During operator trials, calibrated audio signals are sent to the radio communication tester, passed through the ECS modem, and routed along the speech path to the UIU speaker. From there, these signals are received by the mannequin's artificial hearing aid and analyzed using the *HEAD Analyzer ACQUA* software.

Testing on the vehicle's driver side involves transmitting calibrated audio signals from the mannequin's artificial hearing aid via the UIU microphone to the modem. These signals are then routed through the radio communication tester and analyzed using dedicated software.

To replicate street ambient noise, the noise scenarios management workplace is employed within a soundproof test chamber.

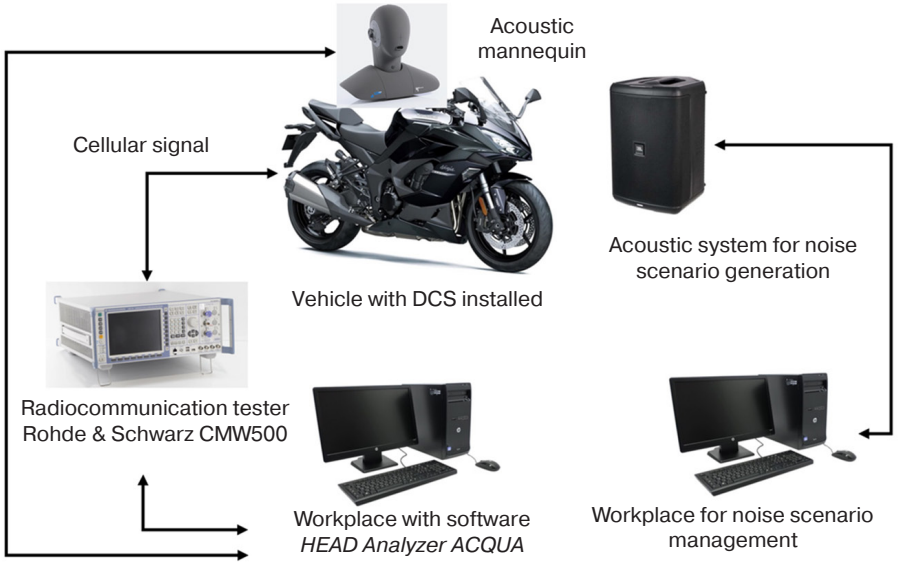

Fig. 7. Structural diagram of the DCS test bench

Table. Duplex DCS performance type parameters

Parameter	Quality class				
	1	2a	2b	2c	3
	Full duplex communication	Partial duplex communication			Half duplex communication
$A_{H,\,S,\,dt}$, dB	≤3	≤6	≤9	≤12	>12

Configuring the digital signal processor and microcontroller algorithms allows voice communication performance to be attained between the emergency operator and the vehicle driver in compliance with GOST 33464-2015[6]. Although the methods outlined in this standard are primarily designed for in-car testing, they can also be adapted for two-wheeled vehicles. Below is an overview of the tests conducted on the most critical performance indicators.

ATTENUATION IN THE TRANSMISSION CHANNEL IN DOUBLE-TALK MODE

While subscribers engage in simultaneous conversations, the maximum allowable decay $A_{H,\,S,\,dt}$ introduced by the DCS into the transmission channel S is regulated by GOST 33464-2015. This is verified using the procedures outlined in GOST 33468-2015, specifically in paragraph 7.9.2. The level of attenuation is dependent on the DCS performance type, categorized by quality class for duplex communication, and must align with the specified values detailed in the table.

The requirements must be fulfilled under both normal signal conditions, and when there is an imbalance in signal levels. The following two specific signal level scenarios should be tested:

- standard signal levels for both reception and transmission;
- a scenario where the transmission signal level is increased by 6 dB, while the reception signal level is decreased by 6 dB.

The test involves two sequences of uncorrelated composite source signals (CSS) transmitted and received simultaneously, with a partial temporal overlap to simulate the dynamics of concurrent communication.

The initial segment of each CSS period (representing a voiced sound, displayed in black in Fig. 8) moving in one direction overlaps with the concluding segment of each CSS period (characterized by pseudo noise, displayed in white) traveling in the opposite direction. The analysis is conducted during active signal instances aligned with the transmission direction.

Prior to initiating testing, the echo canceller should be configured to achieve maximum echo cancellation. This is accomplished using a training sequence on the receive channel, comprising 10-second recordings of both male and female voices.

[6] GOST 33464-2015. Interstate standard. *Global navigation satellite system. Road accident emergency response system. In-vehicle emergency call device/system. General technical requirements*. Moscow: Standartinform; 2017. 86 p. (in Russ.).

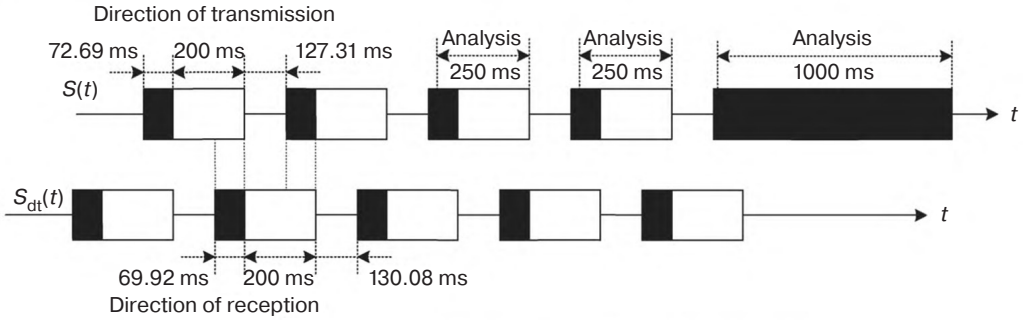

Fig. 8. Test signals used to determine the attenuation range in the transmit direction during a simultaneous conversation. The signal in the transmit direction is denoted as $S(t)$, and the signal in the receive direction is denoted as $S_{dt}(t)$

The signal strength of the transmission channel is evaluated in the time domain using an integration time constant of 5 ms. A time-based relationship for signal strength is established. Signal attenuation within the transmission channel is assessed by comparing the signal strength during simultaneous double talk or two-way conversation to that observed during one-way conversation (specifically during reception signal pauses), assuming that the transmission channel is fully active. This analysis covers the complete test sequence, beginning with the second period of the CSS signal.

Figures 9 and 10 present the measurement results. Figure 9 illustrates near-end recordings overlaid on a single timeline, both during silence and in the presence of the far-end signal emitted through the loudspeaker system. In Fig. 10, the volume level is displayed on a linear scale with values provided in volts: these readings were captured after processing through the measuring system's vocoder. This figure represents the signal ratios derived from Fig. 9, highlighting that the near-end signal, when accompanied by the far-end signal, is consistently quieter compared to its level during silence. The curve values are expressed as negative numbers.

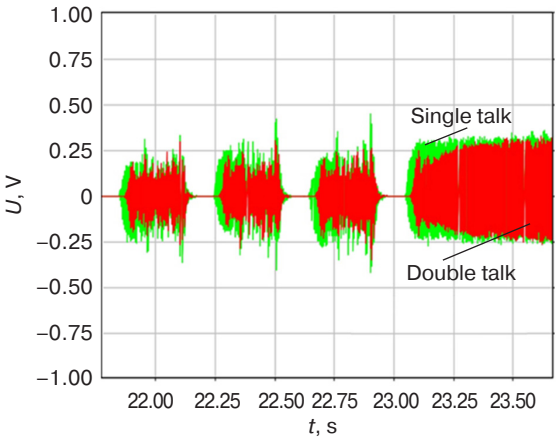

Fig. 9. Signal strength versus time for a one-way and two-way conversation in the presence of a far-end signal, integrated with a time constant of 5 ms

As a final estimate, the value of the maximum permissible attenuation is calculated in the following way:

$$A_{H,S,dt} = \frac{5}{t_{end} - t_{start}} \int_{t_{start}}^{t_{end}} |L_{dB}(t)|dt,$$

wherein $L_{dB}(t)$ is the instantaneous attenuation at time t in dB, $(t_{end} - t_{start})$ is the duration of the time interval, and 5 is the sampling step in ms.

Attenuation is defined as the average value of the area under the curve, obtained by integrating a signal with a time constant of 5 ms. This value is calculated by dividing the total area across all intervals by the number of samples used for integration, as shown in Fig. 10. In addition, the level curve is also integrated with a 5 ms time constant, in order to minimize the risk of distortion in the results caused by random short-term fluctuations.

The results obtained and analyzed using the *HEAD Analyzer ACQUA* software correspond to class 2a and meet the requirements of GOST 33464-2015.

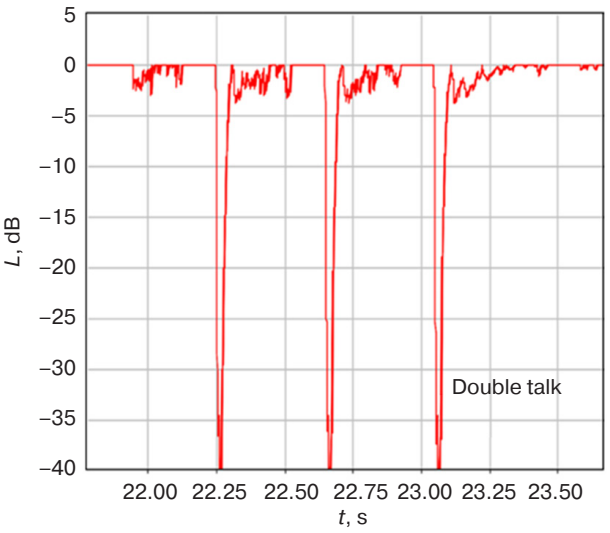

Fig. 10. Ratio of the signal transmitted during a two-way conversation scenario to that of a one-way conversation scenario over time, integrated with a time constant of 5 ms

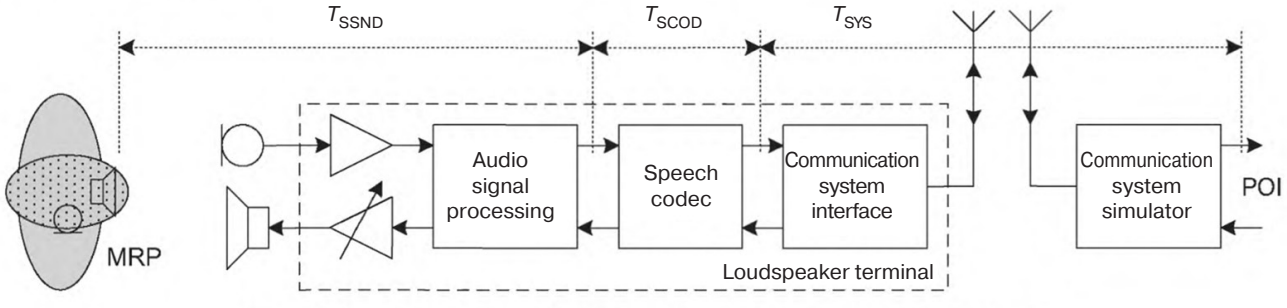

Fig. 11. Acoustic signal processing and propagation delays

Similar tests are conducted under conditions where the transmit signal level is increased by 6 dB and the receive signal level is decreased by 6 dB. In other words, this scenario corresponds to the near-end sound being 6 dB louder while the far-end sound, played through the device's speaker, is 6 dB quieter. Even at standard volume levels, the performance measurements stay within acceptable boundaries.

ECHO ATTENUATION STABILITY OVER TIME

When a test signal, combined with an artificial voice signal at a nominal level, is transmitted through the DCS reception channel, the echo signal attenuation in the DCS transmission channel should remain stable over an extended measurement period. Specifically, this attenuation should not decrease by more than 6 dB from its peak value, as outlined in the standards set forth in GOST 33464-2015, as well as the verification procedures detailed in GOST 33468-2015, paragraph 7.7.3.

The first test signal consists of a periodically repeated combined CSS signal, evaluated at two average signal levels: −5 dBm0 and −25 dBm0.

For the second test signal, a 10-second sequence is used, featuring both male and female voices, each having an average level of −16 dBm0. The analysis is conducted across the entire duration of the signals.

The echo cancellation rate is plotted against time. With an integration time constant of 35 ms, the system effectively smoothes random fluctuations and reduces the influence of short-term interference, ensuring more accurate measurement outcomes.

The CSS signal plot represents the curve of the ratio between the strength of the recorded signal in the transmit direction, while the strength of the reproduced signal in the receive direction. A key consideration is that one of these ratio signals should be time-offset to account for physical and software delays inherent in acoustic signal processing and propagation. These include: sound signal propagation delays T_{SSND} (where S stands for signal and SND signifies sound); delays stemming from the software processing of the audio signal S within the T_{SCOD} speech codec (where S stands for signal and COD signifies codec); and delays introduced by software handling during transmission over the communication system network T_{SYS} (SYS referring to system). The cumulative propagation delay across the transmission channel, $T_{SSUM} = T_{SSND} + T_{SCOD} + T_{SYS}$, is measured as the total time taken for the acoustic speech signal to travel from the sound pressure level measurement point—located 25 mm ahead of the human lips or the emission ring of an artificial mouth device (referred to as the mouth reference point, MRP)—to the point of interface (POI). The POI marks the electrical speech signal's connection and level measurement reference within the receiving and transmitting channels of a mobile communication system simulator, following decoding. This process is illustrated in Fig. 11.

For a CSS signal, the time-dependent behavior of echo cancellation is illustrated in Fig. 12. The overall curve level remains minimal because the reproduced far-end signal contains only a low-level echo component. From the perspective of assessing stability in echo cancellation over time, the system is deemed stable if the difference between the minimum and maximum values during evaluation stays within 6 dB. It is important to highlight that this evaluation focuses solely on eight active sections of the CSS signal, excluding pauses, giving the measurement mask a toothed appearance. According to the *HEAD Analyzer ACQUA*'s results, the echo attenuation stability test is successfully passed across different time intervals.

Figure 13 illustrates the time-dependent variation of the echo level for an artificial voice signal. Instead of directly comparing the artificial voice signal with the reproduced far-end signal, the focus is on evaluating the transmission signal stability (echo-opening, curve *1*) when artificial voice signals, representing male and female voices (curve *2*), are reproduced on the far-end side. The system is deemed stable, if the difference between the minimum and maximum values observed during the evaluation remains within 6 dB.

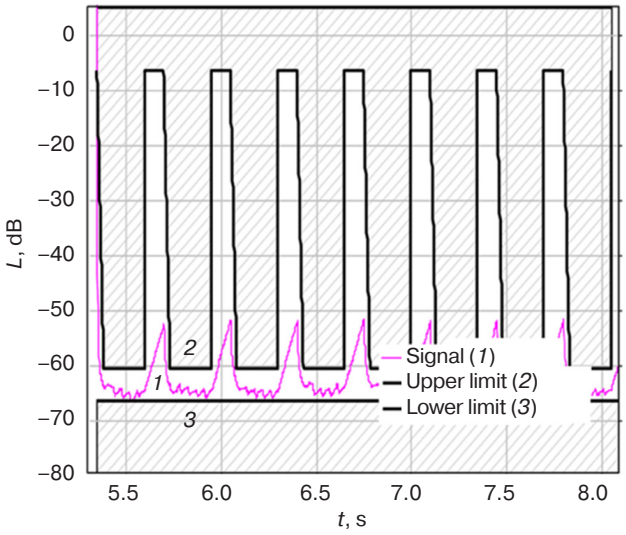

Fig. 12. CSS echo cancellation rate versus time with 35 ms integration time constant

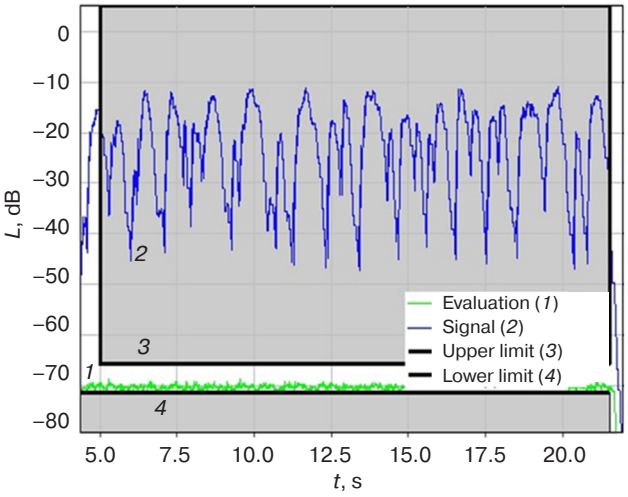

Fig. 13. Artificial voice echo level versus time with 35 ms integration time constant

OPERATION OF TRANSMISSION CHANNEL IN ACOUSTIC NOISE

For near-end speech in background acoustic noise conditions, the signal-to-noise ratio (SNR) at the output of the transmission channel should be at least 6 dB. The recommended SNR is 12 dB, as specified by GOST 33464-2015 and GOST 33468-2015, section 7.10.1.

Background acoustic noise around the two-wheeled vehicle are reproduced for both normal and worst-case noise scenarios.

When tested in noise levels greater than 50 dB (A), the output level of speech signals should increase by 3 dB for every 10 dB increase in noise, averaged over time. This reflects the effect of a person in noisy surroundings increasing the volume of their voice. The maximum increment is 8 dB.

An artificial voice serves as the input acoustic test signal, introduced through the mannequin's artificial mouth. Two sequences are employed: one representing a male voice and the other a female voice, both containing pauses.

The processed signal is extracted from the electrical output of the speech codec within the radio communication tester. In order to estimate signal and noise levels, an integration time constant of 35 ms is utilized. The signal strength envelope and pause noise are then calculated to determine SNR within the transmission channel.

The measurement outcome is represented as a graph depicting the envelope of the signal level and the noise in the transmission path. For active speech regions, an integrated assessment is performed, as follows:

$$S_s = \int_{t_{s_{start}}}^{t_{s_{end}}} L_{dB}(t)dt,$$

wherein $L_{dB}(t)$ is the signal level in decibels and $t_{s_{start}}$, $t_{s_{end}}$ are time limits for the speech segment.

This value is equal to the area under the curve in Fig. 14 that corresponds to all active speech segments.

The score value is calculated as follows:

$$S_n = \int_{t_{n_{start}}}^{t_{n_{end}}} L_{dB}(t)dt,$$

wherein $t_{n_{start}}$, $t_{n_{end}}$ are time limits for the speech pause noise. The estimate value is determined by the area under the curve shown in Fig. 14, which represents all noise segments. Both estimates incorporate an integration time constant of 35 ms, in order to filter out random

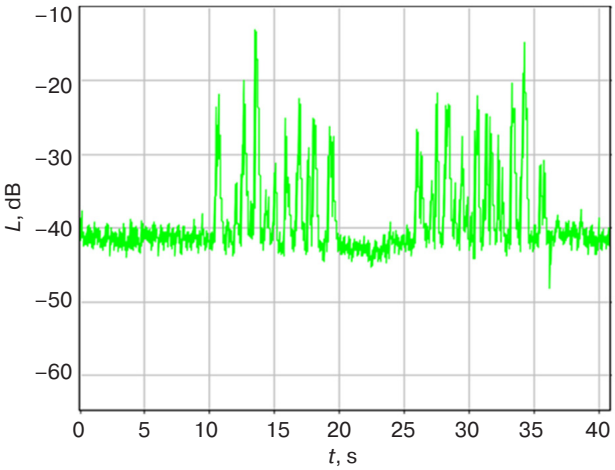

Fig. 14. The envelope level of the signal and the pause noise in the transmit direction with a 35 ms integration time constant

fluctuations in the signal. The operation of the transmission channel in acoustic noise is deemed satisfactory when the ratio of integral estimates exceeds 6 dB. In practical terms, this corresponds to a relatively soft signal, particularly when operating within the GSM standard acoustic frequency range of 300–3400 Hz. Therefore, achieving SNR of at least 12 dB is recommended. Naturally, in scenarios with more severe noise conditions, the estimate will be lower due to elevated background noise levels, which creates additional challenges for the system being tested.

The DCS data channel undergoes testing under different noise conditions derived from recorded environmental noise. For this evaluation, a street noise recording with a volume of 68 dB is utilized. Following the calibration of the microphone gain, speaker settings, and the DSP algorithms, a signal-to-noise ratio of 11 dB is achieved, thus successfully meeting the standards outlined in GOST 33464-2015.

CONCLUSIONS

As part of the project, the DCS prototype has been developed specifically for installation upon two-wheeled vehicles. Its primary function is to enable voice communication between the driver and the ERA-GLONASS system operator in cases of emergency or accidents. During the development process, the unique aspects of the "human-two-wheeled vehicle" interaction system were carefully examined, highlighting its distinctive characteristics compared to other dynamic systems within the broader road transport network. A variety of system factors, operational features, and constraints were also considered, such as weight and size requirements, installation dimensions, and optimal placement on the dashboard.

In the design of the device, significant focus was placed on addressing challenges related to acoustic signal processing, in order to ensure dependable and high-quality voice communication. Given the close proximity between the speaker and microphone within the device, a crucial element was to overcome issues such as mitigating and compensating for acoustic effects that accompany voice signals in the communication channel. In order to address these challenges, noise reduction, echo cancellation, and echo compensation algorithms were thoroughly evaluated for their applicability to the system under development. Subsequent trials and testing confirm that implementing both analog and digital speech signal processing algorithms—integrated into the codec and modem of the device—will deliver superior voice communication quality between the driver and the emergency operator.

Authors' contribution
All authors contributed equally to the research work.

REFERENCES

1. Chuchupal V.Ya., Chichagov A.S., Makovkin K.A. *Tsifrovaya fil'tratsiya zashumlennykh rechevykh signalov* (*Digital Filtering of Noisy Speech Signals*). Moscow: Vychislitel'nyi tsentr RAN; 1998; 1998. 52 p. (in Russ.).
2. Kropotov Y.U., Paramonov A. *Metody proektirovaniya algoritmov obrabotki informatsii telekommunikatsionnykh sistem audioobmena* (*Methods of Designing Algorithms for Information Processing of Telecommunication Audio Exchange Systems*). Moscow: Direct-Media; 2015. 228 p. (in Russ.). ISBN 978-5-4475-4106-4.
3. Vishnyakov I.EH., Masyagin M.M., Odintsov O.A., Slyusar V.V. Methods and algorithms for real time voise noise cleaning. *Izvestiya vysshikh uchebnykh zavedenii. Ehlektronika = Proceedings of Universities. Electronics*. 2021;26(2): 184–196 (in Russ.). https://doi.org/10.24151/1561-5405-2021-26-2-184-196
4. Lyalin S.G. Noise reduction method in speech signals using neural network. *Adv. Sci.* 2019;2:32–38 (in Russ.). https://doi.org/10.25730/VSU.0536.19.021
5. Tikhonov V.I., Kharisov V.N. *Statisticheskii analiz i sintez radiotekhnicheskikh ustroistv i sistem* (*Statistical Analysis and Synthesis of Radio Engineering Devices and Systems*). Moscow: Radio i svyaz'; 1991. 608 p. (in Russ.). ISBN 5-256-00789-0
6. Azarov I.S., Vashkevich M.I., Likhachev D.S., Petrovsky A.A. Reducting complex noises in speech using filtering in modulation domain. *Tsifrovaya obrabotka signalov = Digital Signal Processing*. 2013;4:25–31 (in Russ.). https://elibrary.ru/rvwqdz
7. Zheleznyak V.K., Rahanov K.J., Adamovskiy Y.R. Evaluation of Information Indicators of Quantization Noise Generated by Speech Signal Analogue-Digital Conversion. *Doklady BGUIR*. 2023;21(2):32–40 (in Russ.). http://doi.org/10.35596/1729-7648-2023-21-2-32-40
8. Nguyen H.N., Dowlatnia M., Sarfraz A. *Implementation of the LMS and NLMS algorithms for Acoustic Echo Cancellation in teleconference system using MATLAB.* Vaxjoe: MSI Växjo University; 2009. 69 p. Available from URL: https://www.academia.edu/94741525/Implementation_of_the_LMS_and_NLMS_algorithms_for_Acoustic_Echo_Cancellationin_teleconference_systemusing_MATLAB
9. Carline M.J., Diana D.C. An Investigation on Adaptive Algorithms for Echo Cancellation of Acoustic Signals. In: *2nd Int. Conf. Sustain. Comput. Data Commun. Syst. ICSCDS 2023 – Proc.* 2023. P. 960–966. https://doi.org/10.1109/ICSCDS56580.2023.10105081

10. Haykin S. *Adaptive Filter Theory*: 5th ed. New York: Pearson; 2014. 960 p.
11. La Rosa A.B., Pereira P.T.L., Ücker P., Paim G., da Costa E.A.C., Bampi S., Almeida S. Exploring NLMS-Based Adaptive Filter Hardware Architectures for Eliminating Power Line Interference in EEG Signals. *Circuits, Systems, and Signal Processing*. 2021;40(5):3305–3337. https://doi.org/10.1007/s00034-020-01620-6
12. Zhang H., Tan K., Wang D.L. Deep learning for joint acoustic echo and noise cancellation with nonlinear distortions. In: *Proceedings of INTERSPEECH*. 2019. P. 4255–4259. http://doi.org/10.21437/Interspeech.2019-2651
13. Zhang H., Wang D.L. Deep learning for acoustic echo cancellation in noisy and double-talk scenarios. In: *Proceedings of INTERSPEECH*. 2018. P. 3239–3243. http://doi.org/10.21437/Interspeech.2018-1484
14. Hänsler E., Schmidt G. *Acoustic Echo and Noise Control: A Practical Approach*. Wiley-IEEE Press; 2005. 472 p. ISBN 978-0-471-67839-7
15. Constantini G., Casali D. *New Advances in Audio Signal Processing.* MDPI Books; 2024. 206 p. ISBN 978-3-7258-1059-8.
16. Demidenko A.V. *Mikrokontrollery dlya nachinayushchikh: Interfeisy i upravlenie* (*Microcontrollers for Beginners: Interfaces and Control*). LitRes; 2022. 100 p. (in Russ.).

СПИСОК ЛИТЕРАТУРЫ

1. Чучупал В.Я., Чичагов А.С., Маковкин К.А. *Цифровая фильтрация зашумленных речевых сигналов*. М.: ВЦ РАН; 1998. 52 с.
2. Кропотов Ю., Парамонов А. *Методы проектирования алгоритмов обработки информации телекоммуникационных систем аудиообмена*. М.: Директ-Медиа; 2015. 228 с. ISBN 978-5-4475-4106-4
3. Вишняков И.Э., Масягин М.М., Одинцов О.А., Слюсарь В.В. Методы и алгоритмы шумоочистки звука в реальном времени. *Известия высших учебных заведений. Электроника.* 2021;26(2):184–196. https://doi.org/10.24151/1561-5405-2021-26-2-184-196
4. Лялин С.Г. Метод шумоподавления в речевых сигналах с помощью нейронной сети. *Adv. Sci*. 2019;2:32–38. https://doi.org/10.25730/VSU.0536.19.021
5. Тихонов В.И., Харисов В.Н. *Статистический анализ и синтез радиотехнических устройств и систем*. М.: Радио и связь; 1991. 608 с. ISBN 5-256-00789-0
6. Азаров И.С., Вашкевич М.И., Лихачев Д.С., Петровский А.А. Алгоритм очистки речевого сигнала от сложных помех путем фильтрации в модуляционной области. *Цифровая обработка сигналов*. 2013;4:25–31. https://elibrary.ru/rvwqdz
7. Железняк В.К., Раханов К.Я., Адамовский Е.Р. Оценка информационных показателей шума квантования аналогоцифрового преобразования речевого сигнала. *Доклады БГУИР.* 2023;21(2):32–40. http://doi.org/10.35596/1729-7648-2023-21-2-32-40
8. Nguyen H.N., Dowlatnia M., Sarfraz A. *Implementation of the LMS and NLMS algorithms for Acoustic Echo Cancellation in teleconference system using MATLAB*. Vaxjoe: MSI Växjö University; 2009. 69 p. URL: https://www.academia.edu/94741525/Implementation_of_the_LMS_and_NLMS_algorithms_for_Acoustic_Echo_Cancellationin_teleconference_systemusing_MATLAB
9. Carline M.J., Diana D.C. An Investigation on Adaptive Algorithms for Echo Cancellation of Acoustic Signals. In: *2nd Int. Conf. Sustain. Comput. Data Commun. Syst. ICSCDS 2023 – Proc.* 2023. P. 960–966. https://doi.org/10.1109/ICSCDS56580.2023.10105081
10. Haykin S. *Adaptive Filter Theory*: 5th ed. New York: Pearson; 2014. 960 p.
11. La Rosa A.B., Pereira P.T.L., Ücker P., Paim G., da Costa E.A.C., Bampi S., Almeida S. Exploring NLMS-Based Adaptive Filter Hardware Architectures for Eliminating Power Line Interference in EEG Signals. *Circuits, Systems, and Signal Processing*. 2021;40(5):3305–3337. https://doi.org/10.1007/s00034-020-01620-6
12. Zhang H., Tan K., Wang D.L. Deep learning for joint acoustic echo and noise cancellation with nonlinear distortions. In: *Proceedings of INTERSPEECH*. 2019. P. 4255–4259. http://doi.org/10.21437/Interspeech.2019-2651
13. Zhang H., Wang D.L. Deep learning for acoustic echo cancellation in noisy and double-talk scenarios. In: *Proceedings of INTERSPEECH*. 2018. P. 3239–3243. http://doi.org/10.21437/Interspeech.2018-1484
14. Hänsler E., Schmidt G. *Acoustic Echo and Noise Control: A Practical Approach*. Wiley-IEEE Press; 2005. 472 p. ISBN 978-0-471-67839-7
15. Constantini G., Casali D. *New Advances in Audio Signal Processing.* MDPI Books; 2024. 206 p. ISBN 978-3-7258-1059-8.
16. Демиденко А.В. *Микроконтроллеры для начинающих: Интерфейсы и управление*. ЛитРес; 2025. 100 с.

About the Authors

Vasily V. Nikitin, General Director, FIKOM-IT (188b/4, Mira pr., Moscow, 129128 Russia). E-mail: nvv@ficom-it.ru. https://orcid.org/0009-0009-4204-7302

Saygid U. Uvaysov, Dr. Sci. (Eng.), Professor, Head of the Department of Design and Production of Radioelectronic Devices, Institute of Radio Electronics and Informatics, MIREA – Russian Technological University (78, Vernadskogo pr., Moscow, 119454 Russia). E-mail: uvajsov@mirea.ru. Scopus Author ID 55931417100, ResearcherID H-6746-2015, RSCI SPIN-code 3801-4816, https://orcid.org/0000-0003-1943-6819

Dmitry V. Basov, Cand. Sci. (Eng.), Associate Professor, Department of Design and Production of Radioelectronic Devices, Institute of Radio Electronics and Informatics, MIREA – Russian Technological University (78, Vernadskogo pr., Moscow, 119454 Russia). E-mail: d_basov@mail.ru. https://orcid.org/0009-0003-3599-579X

Об авторах

Никитин Василий Валерьевич, генеральный директор ООО «ФИКОМ-ИТ» (129128, Россия, Москва, пр-т Мира, д. 188б, к. 4). E-mail: nvv@ficom-it.ru. https://orcid.org/0009-0009-4204-7302

Увайсов Сайгид Увайсович, д.т.н., профессор, заведующий кафедрой конструирования и производства радиоэлектронных средств, Институт радиоэлектроники и информатики, ФГБОУ ВО «МИРЭА – Российский технологический университет» (119454, Россия, Москва, пр-т Вернадского, д. 78). E-mail: uvajsov@mirea.ru. Scopus Author ID 55931417100, ResearcherID H-6746-2015, SPIN-код РИНЦ 3801-4816, https://orcid.org/0000-0003-1943-6819

Басов Дмитрий Владимирович, к.т.н., доцент, кафедра конструирования и производства радиоэлектронных средств, Институт радиоэлектроники и информатики, ФГБОУ ВО «МИРЭА – Российский технологический университет» (119454, Россия, Москва, пр-т Вернадского, д. 78). E-mail: d_basov@mail.ru. https://orcid.org/0009-0003-3599-579X

Translated from Russian into English by Kirill V. Nazarov
Edited for English language and spelling by Dr. David Mossop

Modern radio engineering and telecommunication systems

Современные радиотехнические и телекоммуникационные системы

UDC 621.391
https://doi.org/10.32362/2500-316X-2025-13-6-78-85
EDN GBSHAL

RESEARCH ARTICLE

Method of peak factor reduction with compensation signal in OFDM system using regression for parameter selection

Olga V. Tikhonova [@], **Anatoly I. Starikovskiy, Pham Thanh Tuan**

MIREA – Russian Technological University, Moscow, 119454 Russia
[@] *Corresponding author, e-mail: o_tikhonova@inbox.ru*

• **Submitted:** 17.04.2025 • **Revised:** 04.06.2025 • **Accepted:** 08.10.2025

Abstract

Objectives. The article aims to investigate the authors' developed peak-to-average power ratio (PAPR) reduction method using an additional compensation signal in orthogonal frequency-division multiplexing (OFDM) systems, employing polynomial regression for method parameter selection.

Methods. The study utilizes statistical radio technique methods and mathematical modeling to approximate the relationship between bit error rate (BER) versus clipping threshold level and number of additional signals using polynomial regression analysis.

Results. We developed an algorithm for parameter selection in the PAPR reduction method with an additional compensation signal for OFDM systems using polynomial regression. This approach enables rapid system performance evaluation without additional computational overhead for mathematical modeling. The method significantly simplifies the optimization of clipping threshold and number of additional signals, eliminating the need for complete simulation cycles for each configuration. Both simulation and analytical calculations confirm that increasing the clipping threshold reduces BER, while increasing the number of additional signals improves clipping accuracy at the cost of higher computational complexity. Optimal parameter selection achieves a compromise between PAPR reduction and signal quality preservation. Furthermore, we established that for a fixed clipping threshold, there exists an optimal number of additional signals providing the best trade-off between error probability and peak value reduction.

Conclusions. An algorithm for selecting the parameters of the clipping method with an additional compensation signal based on polynomial regression has been developed. This algorithm enables real-time evaluation of system characteristics without additional computational costs associated with repeated mathematical modeling. The proposed approach reduces calculation time by more than a factor of five, offering flexibility and adaptability in the design of OFDM systems with PAPR reduction.

Keywords: method of peak factor reduction with compensation additional signal, OFDM signal, peak-to-average power ratio, PAPR reduction method, polynomial regression

For citation: Tikhonova O.V., Starikovskiy A.I., Pham Th.T. Method of peak factor reduction with compensation signal in OFDM system using regression for parameter selection. *Russian Technological Journal.* 2025;13(6):78–85. https://doi.org/10.32362/2500-316X-2025-13-6-78-85, https://www.elibrary.ru/GBSHAL

Financial disclosure: The authors have no financial or proprietary interest in any material or method mentioned.

The authors declare no conflicts of interest.

НАУЧНАЯ СТАТЬЯ

Метод ограничения пик-фактора с дополнительным сигналом компенсации в системе с ортогональным частотным разделением каналов при применении регрессии для выбора параметров

О.В. Тихонова [@], **А.И. Стариковский**, **Фам Тхань Туан**

МИРЭА – Российский технологический университет, Москва, 119454 Россия
[@] *Автор для переписки, e-mail: o_tikhonova@inbox.ru*

• **Поступила:** 17.04.2025 • **Доработана:** 04.06.2025 • **Принята к опубликованию:** 08.10.2025

Резюме

Цели. Целью статьи является исследование разработанного авторами метода ограничения пик-фактора с дополнительным сигналом в системе связи с мультиплексированием с ортогональным частотным разделением каналов (orthogonal frequency division multiplexing, OFDM) при использовании полиномиальной регрессии для выбора параметров метода.

Методы. В работе использованы методы статистической радиотехники, математического моделирования для аппроксимации зависимости вероятности битовой ошибки от величины уровня ограничения и числа дополнительных сигналов при использовании полиномиальной регрессии.

Результаты. Разработан алгоритм выбора параметров метода ограничения пик-фактора с дополнительным сигналом в системе связи с мультиплексированием с ортогональным частотным разделением каналов на основе полиномиальной регрессии, позволяющий оперативно оценивать характеристики системы без дополнительных затрат времени на математическое моделирование. Это значительно упрощает выбор оптимального уровня ограничения и числа дополнительных сигналов без выполнения полного цикла моделирования для каждой конфигурации. Моделирование и аналитические расчеты подтвердили, что увеличение уровня ограничения способствует снижению вероятности битовой ошибки, а увеличение числа дополнительных сигналов улучшает точность ограничения, однако вызывает рост вычислительных затрат. Оптимальный выбор параметров позволяет достичь компромисса между снижением пик-фактора и сохранением качества сигнала. Также установлено, что при фиксированном уровне ограничения существует оптимальное значение числа дополнительных сигналов, обеспечивающее наилучшее соотношение между вероятностью ошибки и снижением пиковых значений.

Выводы. Предложенный подход позволяет сократить время расчетов более чем в 5 раз, обеспечивая гибкость и адаптивность при проектировании OFDM-систем с ограничением пиковых значений.

Ключевые слова: метод ограничения с дополнительным сигналом, OFDM-сигнал, пик-фактор, метод снижения пик-фактора, полиномиальная регрессия

Для цитирования: Тихонова О.В., Стариковский А.И., Фам Т.Т. Метод ограничения пик-фактора с дополнительным сигналом компенсации в системе с ортогональным частотным разделением каналов при применении регрессии для выбора параметров. *Russian Technological Journal*. 2025;13(6):78–85. https://doi.org/10.32362/2500-316X-2025-13-6-78-85, https://www.elibrary.ru/GBSHAL

Прозрачность финансовой деятельности: Авторы не имеют финансовой заинтересованности в представленных материалах или методах.

Авторы заявляют об отсутствии конфликта интересов.

INTRODUCTION

In wireless communication systems, modulation is an essential component for efficient information transmission and reduced interference effects. The orthogonal frequency division multiplexing (OFDM) is a modern and widely used modulation method that solves key problems in this area [1–5]. It provides high data transfer rates, reduces the bit error rate (BER) [6, 7], and utilizes bandwidth efficiently. However, one of the main challenges of OFDM is its high peak-to-average power ratio (PAPR), which can lead to performance issues. The development of methods to reduce PAPR is crucial for improving system performance and usability. In order to address this problem, the present authors have developed a method called MODS (modulation of the peak factor with additional signals). The effectiveness of this method, which involves limiting the peak factor of an additional signal, depends on two main parameters: the set clipping threshold C and the number of additional signals m. Since these parameters affect the ability of the method to reduce PAPR, their study and evaluation are essential for the successful application of MODS in specific situations.

The paper considers the selection of MODS parameters when using polynomial regression.

OFDM SIGNAL

A discrete OFDM signal can be mathematically expressed in the following way:

$$L_{\text{OFDM}}(v) = \frac{1}{H}\sum_{g=0}^{H-1} K(g)\mathrm{e}^{\frac{j2\pi gv}{H}},\ v = \overline{0, H-1}, \quad (1)$$

where H is the total number of subcarriers; $K(g)$ represents the information transmitted on the gth subcarrier; v is the OFDM sample number; j stands for the imaginary unit.

For a discrete-time OFDM signal, the peak factor is defined as the ratio of the maximum signal power to the average power [8–12]. This can be expressed as follows:

$$\text{PAPR}(L_{\text{OFDM}}(v)) = \frac{P_{\max}\left\{\left|L^2_{\text{OFDM}}(v)\right|\right\}}{P_{\text{avg}}\left\{\left|L^2_{\text{OFDM}}(v)\right|\right\}}, \quad (2)$$

where $P_{\max}\left\{\left|L^2_{\text{OFDM}}(v)\right|\right\}$ is the maximum power of the OFDM signal, $P_{\text{avg}}\left\{\left|L^2_{\text{OFDM}}(v)\right|\right\}$ is the average power of the OFDM signal, and $\left|L_{\text{OFDM}}(v)\right|$ represents the amplitude of the vth sample of the OFDM signal.

When using this method, the amplitude of the OFDM signal is limited to a certain threshold value while maintaining the initial phase of each sample, which can be expressed as follows:

$$L_{\text{ltd}}(v) = \begin{cases} L_{\text{int}}(v) \text{ at } \left|L_{\text{int}}(v)\right| \le C, \\ Ce^{j\phi_n} \text{ at } \left|L_{\text{int}}(v)\right| > C, \end{cases} \quad (3)$$

where C is the clipping threshold; $\left|L_{\text{int}}(v)\right|$ is the amplitude of the initial signal; ϕ_n is the phase angle of the initial sample.

For the $L_{\text{OFDM}}(v)$ signal, we search for those positions (position numbers are denoted by q) where the signal amplitude is greater than the clipping threshold C. When transmitting data with signal clipping, information is lost at some of these positions. To compensate for this loss, the transmitted L_{ltd} signal is supplemented with samples containing information about position q and the $L_{\text{add}}(q)$ signals are added, which is the difference between the initial and clipped signals [13–15]:

$$L_{\text{add}}(q) = L_{\text{int}}(q) - L_{\text{ltd}}(q). \quad (4)$$

Thus, there are no samples in the transmitted signal L_{ltd} whose amplitude exceeds the threshold value C. However, there is no information loss, as it is possible to reconstruct the original samples using their numbers q and additional data $L_{\text{add}}(q)$. The number of extra samples reserved for transmitting the position numbers q and values of $L_{\text{add}}(q)$ is denoted by m.

PARAMETER SELECTION FOR POLYNOMIAL REGRESSION

In the MODS method, BER is influenced not only by the signal-to-noise ratio (SNR) but also by specific method parameters, such as the clipping threshold C and the number of reserved additional samples m [16]. To streamline the optimization of these parameters through

mathematical modeling, the process can be simplified by approximating simulation results using polynomial curves derived from the previously obtained data.

The nth-degree polynomial regression is expressed through the following equation [17]:

$$z = b_0 + b_1 x + b_2 x^2 + \ldots + b_n x^n, \quad (5)$$

where $b_0, b_1, b_2, \ldots b_n$ are the regression coefficients that need to be determined.

The process for finding these coefficients involves several key steps:

Step 1. Generate the initial dataset by forming pairs of points $(x_1, z_1), (x_2, z_2), \ldots, (x_k, z_k)$ derived from the graph created through mathematical modeling.

Step 2. Identify the degree of the polynomial n in accordance with equation (5).

Step 3. Develop a system of equations.

The system of linear equations is created based on the initial data to find the coefficients. Each data point generates an equation in the following form:

$$\begin{cases} b_0 + b_1 x_1 + b_2 x_1^2 + \ldots + b_n x_1^n = z_1, \\ b_0 + b_1 x_2 + b_2 x_2^2 + \ldots + b_n x_2^n = z_2, \\ \ldots \\ b_0 + b_1 x_k + b_2 x_k^2 + \ldots + b_n x_k^n = z_k. \end{cases} \quad (6)$$

In matrix form, the system of equations can be written as follows:

$$\begin{pmatrix} 1 & \ldots & x_1^n \\ 1 & \ldots & x_2^n \\ \vdots & \vdots & \vdots \\ 1 & \ldots & x_k^n \end{pmatrix} \begin{pmatrix} b_0 \\ b_1 \\ \vdots \\ b_n \end{pmatrix} = \begin{pmatrix} z_1 \\ z_2 \\ \vdots \\ z_k \end{pmatrix}, \quad (7)$$

or $\mathbf{G} \cdot \mathbf{b} = \mathbf{z}$.

Step 4. Solve the system of equations to determine the coefficients $b_0, b_1, b_2, \ldots b_n$.

The solution can be found using the least squares method:

$$\mathbf{b} = (\mathbf{G}^{\mathrm{T}}\mathbf{G})^{-1}\mathbf{G}^{\mathrm{T}}\mathbf{z}. \quad (8)$$

The BER dependence on the clipping threshold C for SNR = 10 dB and m = 16 is shown in Fig. 1, based on simulation results.

The graph analysis shows a decrease in the BER value with an increase in the clipping threshold C.

The BER curve and the data obtained using the polynomial regression method are shown in Fig. 2:

$$p(C) = 0.5609 - 0.0287 \cdot C + 6.1966 \cdot 10^{-4} \cdot C^2 - \\ - 6.0957.10^{-6} \cdot C^3 + 2.2886 \cdot 10^{-8} \cdot C^4.$$

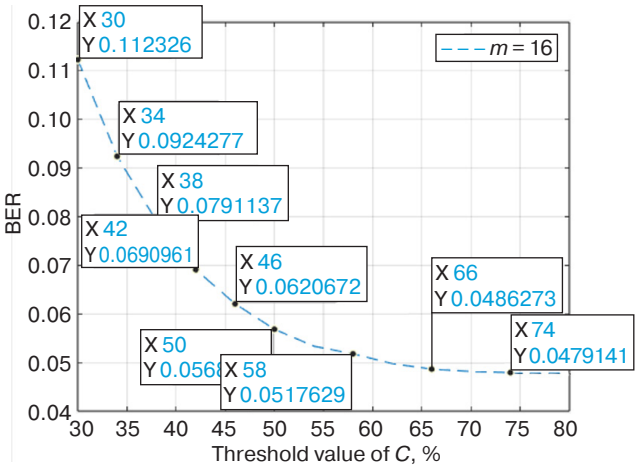

Fig. 1. Numerical values for the BER dependence on the clipping threshold C for SNR = 10 dB and m = 16 (simulation)

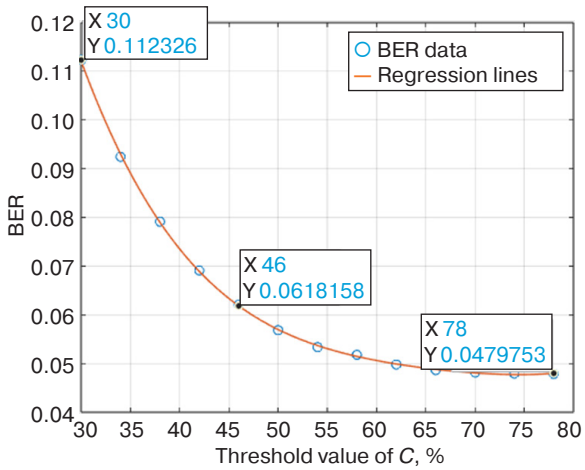

Fig. 2. Numerical values for the BER dependence on the clipping threshold C (regression)

The analysis of Figs. 1 and 2 confirms the close agreement between the simulation and approximation results. The use of pre-computed coefficients for polynomial regression significantly reduces the number of computations required for analyzing MODS parameters.

CALCULATION RESULTS

A. SNR is 5 dB

The BER dependence on the clipping threshold C at SNR = 5 dB for various m values obtained through simulation is shown in Fig. 3.

The corresponding dependencies calculated using the regression method are shown in Fig. 4.

The regression line equations for m = 4, 8, and 16 are the following:

$$p_1(C) = 0.4517 - 0.018 \cdot C + 4.2528 \cdot 10^{-4} \cdot C^2 - \\ - 4.5383 \cdot 10^{-6} \cdot C^3 + 1.8219 \cdot 10^{-8} \cdot C^4,$$

$$p_2(C) = 0.3818 - 0.0121 \cdot C + 2.543 \cdot 10^{-4} \cdot C^2 - 2.4828 \cdot 10^{-6} \cdot C^3 + 9.3811 \cdot 10^{-9} \cdot C^4,$$

$$p_3(C) = 0.4517 - 0.018 \cdot C + 4.2528 \cdot 10^{-4} \cdot C^2 - 4.5383 \cdot 10^{-6} \cdot C^3 + 1.8219 \cdot 10^{-8} \cdot C^4.$$

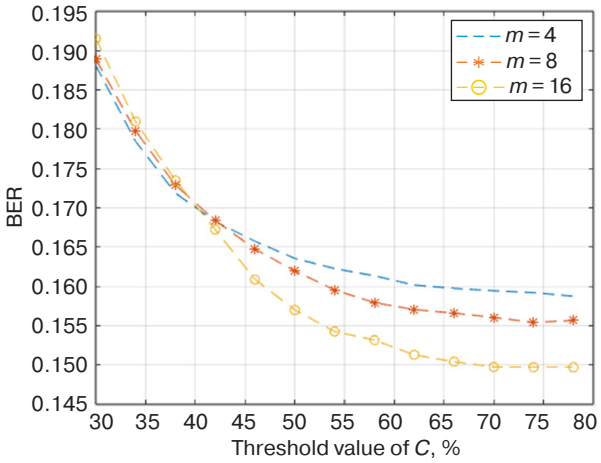

Fig. 3. BER dependence on the clipping threshold *C* (simulation)

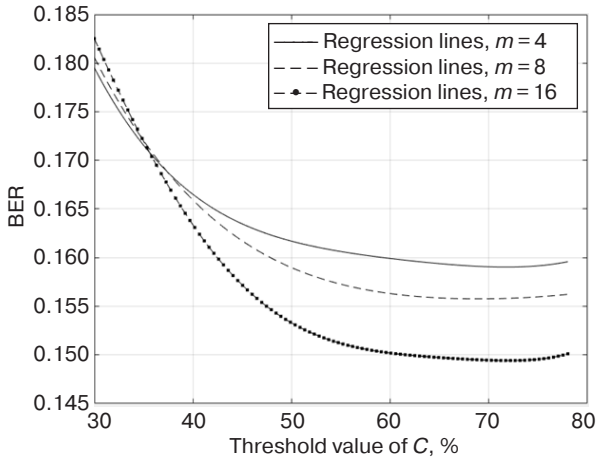

Fig. 4. BER dependence on the clipping threshold *C* (regression)

B. SNR is 10 dB

The BER dependence on the clipping threshold *C* at SNR = 10 dB for various *m* values obtained through simulation is shown in Fig. 5.

The corresponding regression lines are shown in Fig. 6.

The regression line equations for *m* = 4, 8, and 16 are the following:

$$p_1(C) = 0.741356 - 0.03974 \cdot C + 8.8787 \cdot 10^{-4} \cdot C^2 - 8.973 \cdot 10^{-6} \cdot C^3 + 3.355 \cdot 10^{-8} \cdot C^4,$$

$$p_2(C) = 0.67576 - 0.0348 \cdot C + 7.5598 \cdot 10^{-4} \cdot C^2 - 7.4855 \cdot 10^{-6} \cdot C^3 + 2.8257 \cdot 10^{-8} \cdot C^4,$$

$$p_3(C) = 0.61 - 0.0289 \cdot C + 5.701 \cdot 10^{-4} \cdot C^2 - 5.1075 \cdot 10^{-6} \cdot C^3 + 1.744 \cdot 10^{-8} \cdot C^4.$$

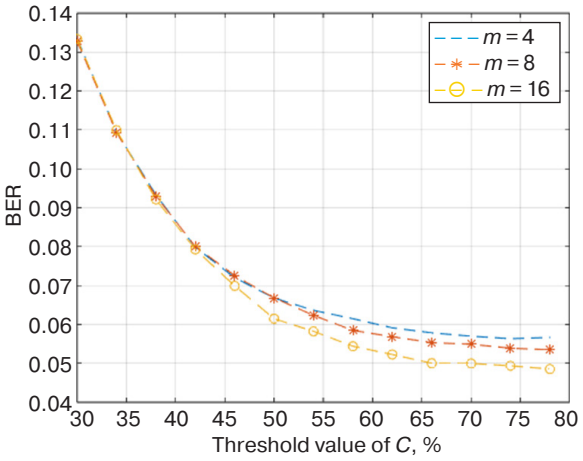

Fig. 5. BER dependence on the clipping threshold *C* (simulation)

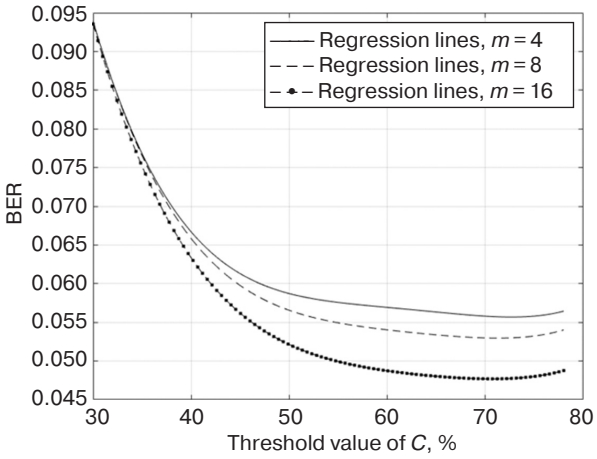

Fig. 6. BER dependence on the clipping threshold *C* (regression)

C. SNR is 15 dB

The BER dependencies for SNR = 15 dB obtained by simulation and regression are shown in Figs. 7 and 8, respectively.

Regression line equations are the following:

$$p_1(C) = 0.8899 - 0.0584 \cdot C + 0.0014 \cdot C^2 - 1.5618 \cdot 10^{-5} \cdot C^3 + 6.3155 \cdot 10^{-8} \cdot C^4,$$

$$p_2(C) = 0.859 - 0.0567 \cdot C + 0.0014 \cdot C^2 - 1.5295 \cdot 10^{-5} \cdot C^3 + 6.2075 \cdot 10^{-8} \cdot C^4,$$

$$p_3(C) = 0.8003 - 0.0533 \cdot C + 0.0013 \cdot C^2 - $$
$$- 1.4625 \cdot 10^{-5} \cdot C^3 + 5.9732 \cdot 10^{-8} \cdot C^4.$$

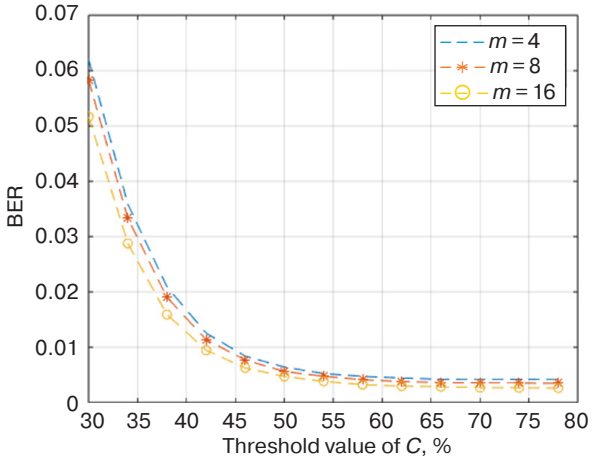

Fig. 7. BER dependence on the clipping threshold *C* (simulation)

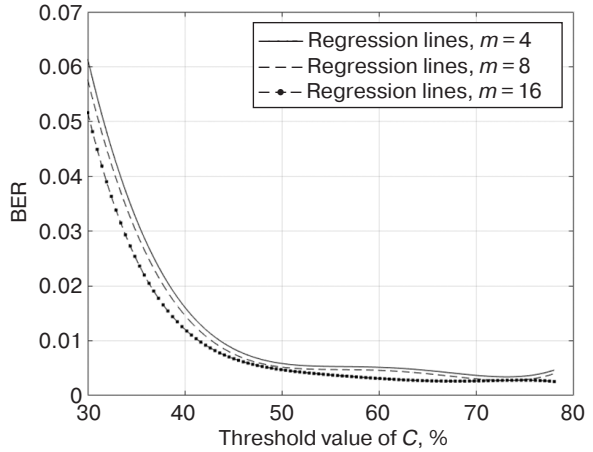

Fig. 8. BER dependence on the clipping threshold *C* (regression)

A comparative analysis of Figs. 3–8 confirms the identity of the results obtained by modeling and polynomial regression methods for different SNR values.

CONCLUSIONS

The study of the parameters for reducing the peak-to-average power ratio with an additional compensation signal in OFDM systems reveals that the effectiveness of this technique significantly depends on the optimal selection of the clipping threshold *C* and the number of additional signals *m*. These two parameters are closely interrelated.

Given a specific SNR, polynomial regression can be used to estimate and optimize the *C* and *m* parameters, allowing for the approximation of curves without the need for full-scale simulations. This method significantly reduces the time required for design and increases the flexibility of system configuration. Optimizing the *C* and *m* parameters effectively reduces the peak factor of the system.

Promising directions for future research include the development of adaptive algorithms for selecting parameters based on channel characteristics and transmission quality requirements, as well as a comparative analysis of these methods with current optimization techniques.

Authors' contributions

O.V. Tikhonova—the research idea, consultations on the issues of conducting all stages of the study.

A.I. Starikovskiy—processing the results.

Pham Thanh Tuan—conducting computer calculations.

REFERENCES

1. Kovalev V.V., Seletskaya O.Yu., Pokamestov D.A. Formation and processing of OFDM signals. *Molodoi uchenyi = Young scientist*. 2016;14(118):151–154. Available from URL: https://moluch.ru/archive/118/32800/. Accessed December 17, 2023 (in Russ.).
2. Galustov G.G., Meleshkin S.N. *Mul'tipleksirovanie s ortogonal'nym chastotnym razdeleniem signalov* (*Multiplexing with Orthogonal Frequency Division of Signals*): Textbook. Taganrog: TTI SFU Publ.; 2012. 80 p. (in Russ.).
3. Van Nee R., Prasad R. *OFDM for Wireless Multimedia Communications*. Boston; London: Artech House; 2000. 260 p.
4. Wu Y., Zou W.Y. Orthogonal frequency division multiplexing: A multi-carrier modulation scheme. *IEEE Trans. Consumer Electronics*. 1995;41(3):392–399.
5. Luferchik P.V., Konev A.N., Bogatyrev E.V., Galeev R.G. Methods for improving the energy characteristics of OFDM modems in frequency selective fading communication channels. *Sibirskii aerokosmicheskii zhurnal = Siberian Aerospace Journal*. 2022;23(2):189–196 (in Russ.). https://doi.org/10.31772/2712-8970-2022-23-2-189-196
6. Sklar B. *Tsifrovaya svyaz'. Teoreticheskie osnovy i prakticheskoe primenenie* (*Digital Communication. Theoretical Foundations and Practical Application*): transl. from Engl. Moscow: Vil'yams; 2017. 1100 p (in Russ.).
[Sklar B. *Digital Communication: Foundamentals and Applications*. Prentice-Hall PTR; 2001. 1079 p.]
7. Proakis J. *Tsifrovaya svyaz'* (*Digital Communication*): transl. from Engl. Moscow: Radio i svyaz'; 2000. 800 p. (in Russ.).
[*Proakis J. Digital Communications.* N.Y.: McGraw-Hill Publ.; 1995. 928 p.]

8. Hassan G.M., Mukred M., Gumaei A.H. Modified Method of PAPR Reduction using Clipping and Filtering for Image Transmission with OFDM. *Al-Mustansiriyah Journal of Science*. 2023;34(4):75–86. https://doi.org/10.23851/mjs.v34i4.1400
9. Shatrughna P.Y., Subhash C.B. PAPR Reduction using Clipping and Filtering Technique for Nonlinear Communication Systems. In: *International Conference on Computing, Communication and Automation*. IEEE; 2015. P. 1220–1225. https://doi.org/10.1109/CCAA.2015.7148590
10. Tripathi V., Patel P., Jain P.K., Shukla S. Peak-to-average power ratio reduction of orthogonal frequency division multiplexing signals using improved salp swarm optimization-based partial transmit sequence model. *ETRI Journal*. 2025;47(2):256–269. https://doi.org/10.4218/etrij.2023-0347
11. Puksa A.O. Reduction of peak-factor of OFDM signal by methods based on signal limitation. *Mezhdunarodnyi nauchno-issledovatel'skii zhurnal = Int. Res. J.* 2017;12(66):124–127 (in Russ.). https://doi.org/10.23670/IRJ.2017.66.145
12. Oman B.O., Majeed Y.E., Ahmad I. Peak to average power ratio reduction in spectrally efficient FDM using repeated clipping and filtering. *Indonesian J. Electric. Eng. Computer Sci*. 2023;30(2):993–1001. http://doi.org/10.11591/ijeecs.v30.i2.pp993-1001
13. Pham Th.T., Tikhonova O.V. Method for limiting the peak factor using an additional compensation signal in a system with orthogonal frequency division multiplexing for a Gaussian channel. *Russ. Technol. J.* 2024;12(5):42–49. https://doi.org/10.32362/2500-316X-2024-12-5-42-49
14. Pham Th.T., Tikhonova O.V. Limitation method with an additional signal to PAPR reduction in the system with orthogonal frequency division of channels. *Voprosy elektromekhaniki. Trudy VNIIEM = Electromechanical Matters. VNIIEM Studies.* 2023;193(2):34–38 (in Russ.).
15. Pham Th.T., Tikhonova O.V. Method for limiting the peak factor of an OFDM signal with an additional signal. In: *Actual Problems and Prospects for the Development of Radio Engineering and Infocommunication Systems.* Radioinfocom-2023: Collection of the 7th International Scientific and Practical Conference. Moscow: RTU MIREA; 2023. P. 140–142 (in Russ.).
16. Pham Th.T., Tikhonova O.V. Algorithm for selecting parameters of the limiting method with an additional signal in an orthogonal frequency division system. *Voprosy elektromekhaniki. Trudy VNIIEM = Electromechanical Matters. VNIIEM Studies.* 2024;199(2):52–55 (in Russ.).
17. Shorokhova I.S., Kislyak N.V., Mariev O.S. *Statisticheskie metody analiza* (*Statistical Methods of Analysis*). Saratov, Yekaterinburg: Profobrazovanie, Ural Federal University; 2024. 298 p. ISBN 978-5-4488-0520-2, 978-5-7996-2853-6

СПИСОК ЛИТЕРАТУРЫ

1. Ковалев В.В., Селецкая О.Ю., Покаместов Д.А. Формирование и обработка OFDM сигналов. *Молодой ученый*. 2016;14(118):151–154. URL: https://moluch.ru/archive/118/32800/. Дата обращения 17.12.2023.
2. Галустов Г.Г., Мелешкин С.Н. *Мультиплексирование с ортогональным частотным разделением сигналов: учебное пособие*. Таганрог: Изд-во ТТИ ЮФУ; 2012. 80 с.
3. Van Nee R., Prasad R. *OFDM for Wireless Multimedia Communications*. Boston; London: Artech House; 2000. 260 p.
4. Wu Y., Zou W.Y. Orthogonal frequency division multiplexing: A multi-carrier modulation scheme. *IEEE Trans. Consumer Electronics*. 1995;41(3):392–399.
5. Луферчик П.В., Конев А.Н., Богатырев Е.В., Галеев Р.Г. Методы повышения энергетической эффективности OFDM модемов в каналах связи с частотно-селективными замираниями. *Сибирский аэрокосмический журнал*. 2022;23(2):189–196. https://doi.org/10.31772/2712-8970-2022-23-2-189-196
6. Скляр Б. *Цифровая связь. Теоретические основы и практическое применение*: пер. с англ. М.: Вильямс; 2017. 1104 с.
7. Прокис Дж. *Цифровая связь*: пер. с англ.; под ред. Д.Д. Кловского. М.: Радио и связь; 2000. 800 с.
8. Hassan G.M., Mukred M., Gumaei A.H. Modified Method of PAPR Reduction using Clipping and Filtering for Image Transmission with OFDM. *Al-Mustansiriyah Journal of Science*. 2023;34(4):75–86. https://doi.org/10.23851/mjs.v34i4.1400
9. Shatrughna P.Y., Subhash C.B. PAPR Reduction using Clipping and Filtering Technique for Nonlinear Communication Systems. In: *International Conference on Computing, Communication and Automation*. IEEE; 2015. P. 1220–1225. https://doi.org/10.1109/CCAA.2015.7148590
10. Tripathi V., Patel P., Jain P.K., Shukla S. Peak-to-average power ratio reduction of orthogonal frequency division multiplexing signals using improved salp swarm optimization-based partial transmit sequence model. *ETRI Journal*. 2025;47(2):256–269. https://doi.org/10.4218/etrij.2023-0347
11. Пукса А.О. Уменьшение пик-фактора OFDM-сигнала с помощью методов, основанных на ограничении сигналов. *Международный научно-исследовательский журнал*. 2017;12(66):124–127. https://doi.org/10.23670/IRJ.2017.66.145
12. Oman B.O., Majeed Y.E., Ahmad I. Peak to average power ratio reduction in spectrally efficient FDM using repeated clipping and filtering. *Indonesian J. Electric. Eng. Computer Sci*. 2023;30(2):993–1001. http://doi.org/10.11591/ijeecs.v30.i2.pp993-1001
13. Фам Т.Т., Тихонова О.В. Метод ограничения пик-фактора с дополнительным сигналом компенсации в системе с ортогональным частотным разделением каналов для гауссовского канала. *Russ. Technol. J.* 2024;12(5):42–49. https://doi.org/10.32362/2500-316X-2024-12-5-42-49
14. Фам Т.Т., Тихонова О.В. Метод ограничения с дополнительным сигналом для уменьшения значения пик-фактора в системе с ортогональным частотным разделением каналов. *Вопросы электромеханики. Труды ВНИИЭМ*. 2023;193(2):34–38.

15. Фам Т.Т., Тихонова О.В. Метод ограничения пик-фактора сигнала OFDM с дополнительным сигналом. В сб.: *Актуальные проблемы и перспективы развития радиотехнических и инфокоммуникационных систем.* «Радиоинфоком-2023»: Сборник научных статей VII Международной научно-практической конференции. М.: РТУ МИРЭА; 2023. С. 140–142.
16. Фам Т.Т., Тихонова О.В. Алгоритм выбора параметров метода ограничения с дополнительным сигналом в системе с ортогональным частотным разделением каналов. *Вопросы электромеханики. Труды ВНИИЭМ.* 2024;199(2):52–55.
17. Шорохова И.С., Кисляк Н.В., Мариев О.С. *Статистические методы анализа*. Саратов, Екатеринбург: Изд-во Профобразование, Уральский федеральный университет; 2024. 298 с. ISBN 978-5-4488-0520-2, 978-5-7996-2853-6

About the Authors

Olga V. Tikhonova, Dr. Sci. (Eng.), Senior Researcher, Professor, Department of Radio Electronic Systems and Complexes, Institute of Radio Electronics and Informatics, MIREA – Russian Technological University (78, Vernadskogo pr., Moscow, 119454 Russia). E-mail: o_tikhonova@inbox.ru. Scopus Author ID 57208923772, RSCI SPIN-code 3362-9924, https://orcid.org/0009-0009-4013-9182

Anatoly I. Starikovskiy, Cand. Sci. (Eng.), Associate Professor, Professor, Department of Radio Electronic Systems and Complexes, Institute of Radio Electronics and Informatics, MIREA – Russian Technological University (78, Vernadskogo pr., Moscow, 119454 Russia). E-mail: starikovski@mirea.ru. Scopus Author ID 57208926243, ResearcherID AAH-2239-2020, RSCI SPIN-code 1126-4471, https://orcid.org/0000-0003-4040-3843

Pham Thanh Tuan, Postgraduate Student, Department of Radio Electronic Systems and Complexes, Institute of Radio Electronics and Informatics, MIREA – Russian Technological University (78, Vernadskogo pr., Moscow, 119454 Russia). E-mail: anhsequayve.ru@gmail.com. RSCI SPIN-code 1885-7798, https://orcid.org/0009-0000-7430-1779

Об авторах

Тихонова Ольга Вадимовна, д.т.н., старший научный сотрудник, профессор кафедры радиоэлектронных систем и комплексов, Институт радиоэлектроники и информатики, ФГБОУ ВО «МИРЭА – Российский технологический университет» (119454, Россия, Москва, пр-т Вернадского, д. 78). E-mail: o_tikhonova@inbox.ru. Scopus Author ID 57208923772, SPIN-код РИНЦ 3362-9924, https://orcid.org/0009-0009-4013-9182

Стариковский Анатолий Иванович, к.т.н., доцент, профессор кафедры радиоэлектронных систем и комплексов, Институт радиоэлектроники и информатики, ФГБОУ ВО «МИРЭА – Российский технологический университет» (119454, Россия, Москва, пр-т Вернадского, д. 78). E-mail: starikovski@mirea.ru. Scopus Author ID 57208926243, ResearcherID AAH-2239-2020, SPIN-код РИНЦ 1126-4471, https://orcid.org/0000-0003-4040-3843

Фам Тхань Туан, аспирант, кафедра радиоэлектронных систем и комплексов, Институт радиоэлектроники и информатики, ФГБОУ ВО «МИРЭА – Российский технологический университет» (119454, Россия, Москва, пр-т Вернадского, д. 78). E-mail: anhsequayve.ru@gmail.com. SPIN-код РИНЦ 1885-7798, https://orcid.org/0009-0000-7430-1779

Translated from Russian into English by K. Nazarov
Edited for English language and spelling by Thomas A. Beavitt

Micro- and nanoelectronics. Condensed matter physics

Микро- и наноэлектроника. Физика конденсированного состояния

UDC 621.382
https://doi.org/10.32362/2500-316X-2025-13-6-86-94
EDN KOATTE

RESEARCH ARTICLE

Interface traps build-up and its influence on electrostatic discharge robustness of high-power metal-oxide-semiconductor field-effect transistor

Diana M. Bakerenkova [@], **Aleksandr S. Petrov**

Research Institute of Scientific Instruments, Lytkarino, 140080 Russia
[@] *Corresponding author, e-mail: arzamasceva.diana@mail.ru*

• **Submitted:** 16.05.2025 • **Revised:** 24.06.2025 • **Accepted:** 06.10.2025

Abstract

Objectives. The aim of the study is to confirm that the robustness of high-power metal–oxide–semiconductor field-effect transistor (MOSFET) to electrostatic discharge (ESD) after gamma irradiation is determined by the concentration of built-up interface traps (IT). The reason for such dependence is the degradation of the gain of the parasitic bipolar transistor in the structure of high-power MOSFETs during accumulation of IT. As a result, higher ESD pulse voltage is required to activate the parasitic bipolar transistor and cause the subsequent catastrophic failure of MOSFET.

Methods. The study describes the physical mechanism of the influence of IT accumulation on the robustness of high-power MOSFETs to ESD. Experimental studies included determination of ESD robustness for two types of high-power MOSFETs before irradiation, ^{60}Co gamma irradiation to several levels of total ionizing dose, and subsequent determination of the ESD robustness of irradiated samples.

Results. The study developed a method for calculating IT concentration and radiation-induced charge density from subthreshold drain-gate characteristics. It was also shown that for the first type of MOSFET, when irradiated to total ionizing dose level of 3 krad, the build-up IT did not occur, nor was any change or insignificant decrease in the breakdown voltage observed when exposed to ESD. For the second type of MOSFET, build-up IT was observed when irradiated to total ionizing dose level of 2 and 4 krad and an increase in the breakdown voltage was also observed when exposed to ESD.

Conclusions. The study shows the relationship between the IT concentration and the change in the breakdown voltage when exposed to ESD. The results obtained can be used to assess the failure-free operation time of devices operating under conditions of ionizing radiation and electrostatic discharges.

Keywords: electrostatic discharge, radiation effects, interface traps, high-power MOSFETs

For citation: Bakerenkova D.M., Petrov A.S. Interface traps build-up and its influence on electrostatic discharge robustness of high-power metal-oxide-semiconductor field-effect transistor. *Russian Technological Journal.* 2025;13(6):86–94. https://doi.org/10.32362/2500-316X-2025-13-6-86-94, https://www.elibrary.ru/KOATTE

Financial disclosure: The authors have no financial or proprietary interest in any material or method mentioned.

The authors declare no conflicts of interest.

НАУЧНАЯ СТАТЬЯ

Влияние встраивания поверхностных состояний на стойкость мощных металлооксидных полупроводниковых полевых транзисторов к электростатическому разряду

Д.М. Бакеренкова [@], **А.С. Петров**

АО «Научно-исследовательский институт приборов», Лыткарино, 140080 Россия
[@] *Автор для переписки, e-mail: arzamasceva.diana@mail.ru*

• **Поступила:** 16.05.2025 • **Доработана:** 24.06.2025 • **Принята к опубликованию:** 06.10.2025

Резюме

Цели. Целью исследования является проверка гипотезы о том, что стойкость мощных металлооксидных полупроводниковых полевых транзисторов (МОПТ) к электростатическому разряду (ЭСР) после гамма-облучения определяется концентрацией встроившихся в процессе облучения поверхностных состояний (ПС). Причиной такой зависимости является деградация коэффициента усиления паразитного биполярного транзистора в структуре мощных МОПТ при накоплении ПС. Как следствие, для включения паразитного биполярного транзистора и последующего выхода из строя МОПТ требуется все большее напряжение импульса ЭСР.

Методы. Теоретическое описание физического механизма накопления ПС и его влияния на стойкость мощных МОПТ к ЭСР. Экспериментальные исследования, включающие определение стойкости к ЭСР двух типов необлученных МОПТ с помощью специально разработанного генератора ЭСР, облучение гамма-квантами ^{60}Co в активном электрическом режиме до нескольких уровней поглощенной дозы и последующее определение стойкости облученных образцов к ЭСР.

Результаты. Разработан метод, позволяющий численно рассчитать зависимости тока стока от напряжения затвор-исток для любых значений плотности накопленного радиационно-индуцированного заряда и концентрации встроившихся ПС. Показано, что для 1-го типа МОПТ при облучении до уровня поглощенной дозы в 3 крад встраивание ПС не происходило, и также не наблюдалось изменение пробивного напряжения при воздействии ЭСР или наблюдалось его незначительное снижение. Для 2-го типа МОПТ наблюдалось встраивание ПС при облучении до уровня поглощенной дозы в 2 и 4 крад, а также увеличение пробивного напряжения при воздействии ЭСР.

Выводы. Показана связь между концентрацией встроившихся ПС и изменением стойкости мощных МОПТ к ЭСР. Полученные результаты могут быть использованы при оценке времени безотказной работы устройств, работающих в условиях одновременного воздействия радиационных и импульсных электрических нагрузок.

Ключевые слова: электростатический разряд, радиационные эффекты, поверхностные состояния, мощные МОП-транзисторы

Для цитирования: Бакеренкова Д.М., Петров А.С. Влияние встраивания поверхностных состояний на стойкость мощных металлооксидных полупроводниковых полевых транзисторов к электростатическому разряду. *Russian Technological Journal*. 2025;13(6):86–94. https://doi.org/10.32362/2500-316X-2025-13-6-86-94, https://www.elibrary.ru/KOATTE

Прозрачность финансовой деятельности: Авторы не имеют финансовой заинтересованности в представленных материалах или методах.

Авторы заявляют об отсутствии конфликта интересов.

Glossary

Electrostatic discharge is a pulse transfer of the electrostatic charge between bodies with different electrostatic potentials.

Total ionizing dose is the amount of ionizing radiation energy absorbed by a substance per unit mass.

Total ionizing dose effects are effects caused by the loss of energy in a substance due to ionizing radiation for ionization.

Secondary breakdown is a sharp drop in collector-emitter voltage caused by thermal instability or avalanche injection.

Interface traps are energy states (energy levels) of conduction electrons localized near the surface of a solid.

Displacement damage is effect caused by the loss of energy due to ionizing radiation in a substance, resulting in structural damage.

Space charge region is an electrically charged layer which forms at the boundary between *n*- and *p*-areas.

Radiation-induced charge is a positive charge which accumulates in the gate dielectric of transistors under the influence of ionizing radiation.

INTRODUCTION

Research into the effect of radiation loads upon the breakdown voltage of *p-n* junctions has relatively recently been actively resumed [1–3]. Previously no critical change in the breakdown voltage of *p-n* junctions was observed after radiation exposure up to an total ionizing dose (TID) dose $4 \cdot 10^4$ rad(Si) [4, 5]. However, when a static or linearly increasing voltage is applied, the effect of electrostatic discharges (ESD) and the subsequent breakdown of *p-n* junctions manifest themselves through a more complex mechanism than breakdown.

One of the first works on this topic was published in 2017 [6] and it examines the influence of dose effects on ESD protection devices: P+/NW-diodes, Zener diodes, and gate-grounded *n*-type metal-oxide semiconductor (GGNMOS) transistors. Helium ions with an energy of 1.5 MeV were selected as the source of ionizing radiation, and the samples were exposed to ions with a fluence of 10^{14}, $2 \cdot 10^{14}$, and 10^{15} cm^{-2}. In both types of diodes, a slight increase in the breakdown voltage was observed, as well as an increase in leakage current and a decrease in failure current with an increase in the TID. In the case of GGNMOS, the behavioral characteristic of secondary breakdown disappeared after irradiation, and a decrease in failure current was also observed. However, the paper did not provide explanations or reasons for this behavior of the devices after irradiation. The question also arises with regard to the influence of displacement damage defects on the behavior of samples during the ESD pulse, since irradiation with helium ions introduces a significant number of defects into the semiconductor volume.

In [7], the effect of gamma irradiation up to a TID of 200 krad on the characteristics of low-voltage and high-voltage dual-directional silicon controlled rectifiers (DDSCR) was investigated. Unlike the trigger voltage of low-voltage DDSCRs, the trigger voltage of high-voltage DDSCRs increased significantly with increasing TID. This is mainly due to an increase in breakdown voltage, and such rectifiers failed immediately after triggering. The increase in breakdown voltage after irradiation was associated with the accumulation of traps and interface traps (IT) in the field and gate oxides. This leads to an increase in the space charge region (SCR) of the *p-n* junctions, which determines the breakdown voltage. For the same reason, leakage currents increased after irradiation, leading to weak inversion of parasitic lateral transistors. This work made assumptions about the connection between changes in behavior during the ESD pulse of irradiated devices and the accumulation of traps and IT. Nevertheless, no quantitative comparison of the concentration of accumulated IT and changes in device parameters was performed.

The aim of the current work is to identify the mechanism of change in the resistance to ESD of high-power metal oxide semiconductor field effect transistors (MOSFETs) after gamma irradiation, as well as to study the relationship between the concentration of IT build-up during irradiation and the change in breakdown voltage under the influence of ESD (V_{ESD}). In order to calculate the concentration of IT, a method needs to be developed which will enable the volt-ampere (I–V) characteristic of the transistor to be directly linked to the concentration of IT.

1. PHYSICAL MECHANISM OF IT ACCUMULATION AND ITS IMPACT ON THE STABILITY OF HIGH-POWER MOSFETS TO ESD

Previously, the authors in [8] experimentally demonstrated that irradiation of high-power MOSFETs with gamma rays leads to improved resistance to ESD, with a higher breakdown voltage corresponding to higher TIDs. This effect was associated with the activation of a “parasitic” bipolar transistor in the structure of high-power MOSFETs under the influence of ESD. However,

under the influence of gamma irradiation, the gain of parasitic bipolar transistor (h_{21e}) degrades [9]. Thus, an increasingly higher ESD voltage is required to achieve the collector current value necessary for the secondary breakdown of the bipolar transistor and the subsequent failure of the MOSFET. The degradation of h_{21e} due to the effects of ionizing radiation occurs because of an increase in the recombination rate in the SCR emitter-base junction. This is manifested as an increase in base current at a fixed emitter bias. The recombination rate increases due to two interrelated effects: an increase in the surface recombination rate; and an expansion of the SCR emitter-base junction [10]. The increase in the surface recombination rate is proportional to the density of recombination centers at the Si/SiO_2 boundary of the emitter-base junction. Interface states, as one of the recombination centers, determine this increase in rate. However, the radiation-induced positive charge accumulated at the Si/SiO_2 boundary should also be taken into account due to the complex mechanism of their interaction. Surface states physically represent a Si atom with an unpassivated broken bond, formed after the Si–H bond was broken [11].

Today, it is believed that the dominant process in the mechanism of IT accumulation is proton hopping. In the first stage of this process, radiation-induced holes formed as a result of the generation of electron-hole pairs by ionizing radiation move through the oxide and free hydrogen in the form of protons under the action of an electric field. In the second stage, the protons move by hopping, and when they reach the Si/SiO_2 boundary, they react with the Si–H bond, forming H_2 and a trivalent Si defect [12, 13].

The current methods for measuring the gain of parasitic bipolar transistor (used for high-power MOSFETs with a short-circuited substrate terminal) involve heating the samples from 25 to 300°C and measuring the dependence of the drain current on the voltage at the drain of a closed transistor [14]. Such heating after irradiation changes the dynamics of IT accumulation [15, 16]. Therefore, h_{21e} changes during the measurement process, and the application of these methods in the current case will lead to unreliable results. In order to confirm the hypothesis that the resistance of high-power MOSFETs to ESD after gamma irradiation is determined by the accumulation of IT, the IT density of unirradiated samples needs to be calculated. The samples then need to be irradiated to several TID values, and the IT density calculated after irradiation. In each case the resistance to ESD needs to be investigated.

2. EXPERIMENT

Two types of high-power MOSFETs manufactured using HEXFET (hexagonal field-effect transistor) technology were selected as test samples. Therefore, thousands of parallel-connected MOSFET cells are placed in a single crystal, forming a hexagon: IRFR4615PbF (manufactured by International Rectifier, USA); and IRFR3710ZPbF (manufactured by Infineon Technologies, Germany). Before and after irradiation, drain-gate I–V curves were measured in the subthreshold region ($V_{g.s} < V_{th}$). From this the concentration of IT was calculated.

Gamma-ray irradiation with ^{60}Co was performed in threshold voltage measurement mode: $V_{g.s} = V_{d.s}$ and I_d = 100 μA for IRFR4615PbF and $V_{g.s} = V_{d.s}$ and I_d = 250 μA for IRFR3710ZPbF. IRFR4615PbF samples were irradiated to two TID values: 1.78 krad and 3.18 krad, IRFR3710ZPbF samples were irradiated to TID values of 2 krad and 3.9 krad. An ESD generator developed by the Research Institute of Scientific Instruments (RISI[1], Russia) was used as the ESD source. Its schematic diagram is shown in Fig. 1, and its main parameters are given in Table 1.

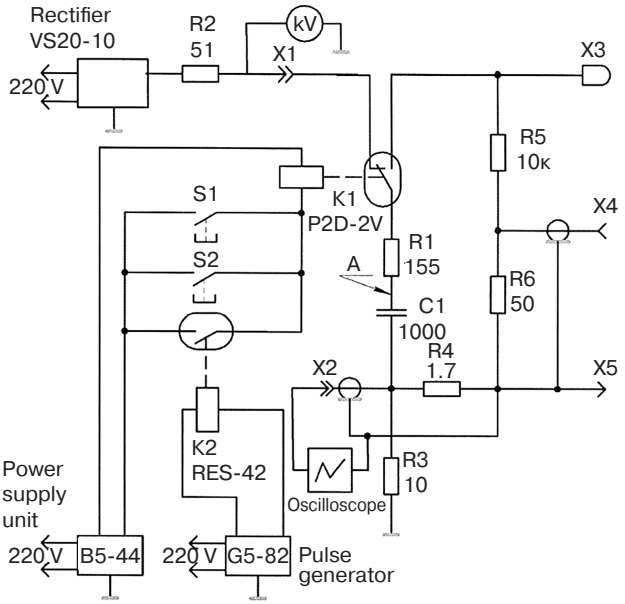

Fig. 1. Single-line diagram of the ESD generator[2]. S1 — "Start" pushbutton on the generator, S2 — remote control pushbutton for starting the generator, K1 — vacuum relay P2D-2V, K2 — intermediate relay RES-42, X1 — hook up of the high-voltage power source, X2 — current measuring connector, X3 — discharge tip, X4 — voltage measuring connector, X5 — reverse current conductor, C1 — discharge capacitor, R1 — discharge resistor, R2–R5 — resistors, B5-44 — power supply unit, G5-82 — pulse generator. The designations of the circuit elements correspond to those adopted in GOST 2.710-81[3]

[1] http://www.niipribor.ru/ (in Russ.). Accessed October 10, 2025.

[2] Figure 1 shows a diagram from the ESD generator passport.

[3] GOST 2.710-81. Interstate Standard. *Unified system for design documentation. Alpha-numerical designations in electrical diagrams*. Moscow: Izd. Standartov; 1985 (in Russ.).

Table 1. Basic parameters of the ESD generator

Parameter	Value
Output (test) continuously adjustable voltage, kV	From 1 to 20 ± 2
Output voltage polarity	Positive
Frequency of successive pulses, discharges per second	Up to 10
Peak value of discharge pulse current, A	Up to 100 ± 10
Duration of the current pulse front at the level of 0.1–0.9 amplitude, s	From $1 \cdot 10^{-9}$ to $1 \cdot 10^{-7}$
Stored energy in a storage capacitor C1, MJ	Up to 200 ± 10

The resistance of high-power MOSFET samples to ESD was determined by measuring the drain-gate I–V characteristic of the transistor after applying an ESD pulse to the drain (the source and gate are grounded at the moment of applying the pulse). The failure criterion was considered to be I–V behavior which is not typical for MOSFETs. The voltage range of the applied ESD pulse was 1–5 kV. If the sample withstood the test with one ESD pulse of the initial amplitude, the amplitude increased by 0.5 kV in the next applied pulse. The maximum withstand voltage when applying an ESD pulse (breakdown voltage value under ESD) was determined as the voltage value in the pulse after the appearance of I–V behavior not typical for MOSFETs.

3. METHOD FOR IT CONCENTRATION CALCULATION FROM SUBTHRESHOLD DRAIN-GATE CHARACTERISTICS

The subthreshold I–V characteristic is the drain-gate I–V characteristic in the weak inversion region. The surface potential in this case ranges within $\varphi_b \le \varphi_s \le 2\varphi_b$,

$$\varphi_b = \frac{kT}{q}\ln\left(\frac{N_a}{n_i}\right), \quad (1)$$

where q is the electron charge; k is the Boltzmann constant; T is the absolute temperature; N_a and n_i are the dopant concentration and the intrinsic concentration in the substrate, respectively.

In this case, the dependence of the drain current on the surface potential is described as follows [17]:

$$I_d = \frac{qDiWn_i^2}{\sqrt{2}L_{ch}N_a}\sqrt{\frac{\varepsilon_{Si}\varepsilon_0\varphi_T}{qN_a}}\left(\frac{\varphi_s}{\varphi_T}\right)^{-1/2}\exp\left(\frac{\varphi_s}{\varphi_T}\right), \quad (2)$$

wherein Di is the diffusion coefficient, L_{ch} is the channel length, W is the channel width, ε_{Si} is the permittivity of silicon, ε_0 is the electric constant, $\varphi_T = kT/q$.

If the source is connected to the substrate and grounded, then, by constructing a zone diagram (Fig. 2), $V_{g.s}$ can be expressed as the sum of the voltage drop across the oxide φ_{ox}, the voltage drop in silicon and the contact potential difference:

$$V_{g.s} = \varphi_s + \varphi_{ox} + \left[\frac{1}{q}\left(\chi_{Si} + \frac{E_g}{2}\right) + \varphi_b - \Phi_{me}\right], \quad (3)$$

wherein χ_{Si} is the electron affinity in silicon, E_g is the band gap, and Φ_{me} is the work function of the metal.

The voltage drop in the oxide can be estimated by knowing the distribution of the radiation-induced positive charge in the oxide ρ_{ox} and the electric field E_{ox} near the Si/SiO_2 boundary:

$$\varphi_{ox} = -E_{ox}d_{ox} - \frac{1}{\varepsilon_{ox}\varepsilon_0}\int_0^{d_{ox}}(d_{ox} - x)\rho_{ox}(x)dx, \quad (4)$$

wherein d_{ox} is the oxide thickness, ε_{ox} is the permittivity of SiO_2, x is the integration variable.

According to Gauss theorem for the electric displacement vector:

$$D_{ox} - D_{Si} = Q_{i.t}, \quad (5)$$

wherein D_{ox} is the electrical displacement in the oxide, D_{Si} is the electrical displacement in silicon, $Q_{i.t}$ is the IT charge.

In this case

$$\varepsilon_{ox}\varepsilon_0 E_{ox} - \varepsilon_{Si}\varepsilon_0 E_{Si} = Q_{i.t}. \quad (6)$$

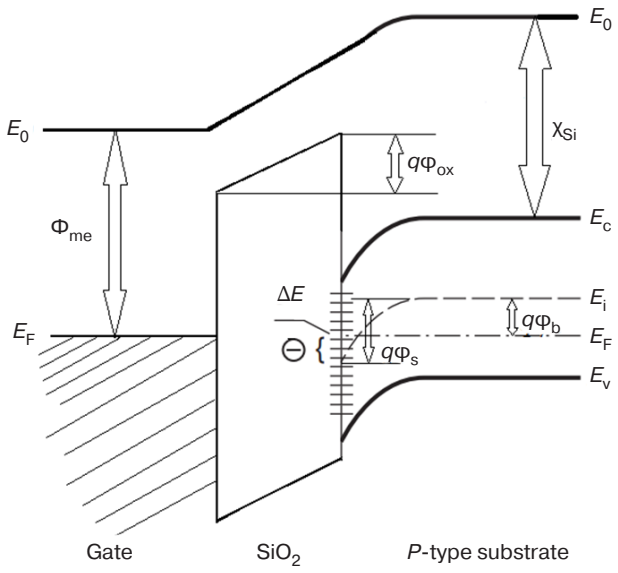

Fig. 2. Band diagram of a MOSFET structure with a *p*-type substrate: E_0 — vacuum level; E_F — Fermi level; E_v — energy corresponding to the top of the valence band; E_i — energy of the middle of the band gap; E_c — energy corresponding to the bottom of the conduction band, $\Delta E = q\Delta\varphi = q(\varphi_s - \varphi_b)$

As is known, in the upper part of the band gap ITs are acceptor-like (they can accept electrons), and in the lower part of the forbidden zone the states are donor-like (they can donate electrons [18]. ITs of the donor type are positively charged if they are located above the Fermi level and neutral if they are located below the Fermi level. ITs of the acceptor type are neutral if they are located above the Fermi level and negatively charged if they are located below the Fermi level. In the considered case of a *p*-type substrate in the weak inversion mode near the surface the Fermi level lies above the middle of the band gap, and only part of the acceptor levels in the energy range ΔE (Fig. 2).

The charged part of the levels can be expressed as follows:

$$\eta = \frac{\Delta E}{E_g}, \tag{7}$$

wherein ΔE is the distance from the middle of the band gap to the Fermi level near the Si/SiO_2 boundary.

In that case the IT is equal to:

$$Q_{i.t} = N_{i.t} q\eta = N_{i.t} q^2 \frac{\varphi_s - \varphi_b}{E_g}, \tag{8}$$

wherein $N_{i.t}$ is the IT concentration.

Applying (8) into (6), we obtain:

$$\varepsilon_{ox}\varepsilon_0 E_{ox} - \varepsilon_{Si}\varepsilon_0 E_{Si} = N_{i.t} q^2 \frac{\varphi_s - \varphi_b}{E_g}. \tag{9}$$

According to Poisson's equation:

$$\frac{d^2\varphi}{dx^2} = -\frac{\rho(x)}{\varepsilon_{Si}\varepsilon_0}, \tag{10}$$

wherein $\rho(x)$ is the total space charge density:

$$\rho(x) = q(-N_A + p(x) - n(x)), \tag{11}$$

$$p(x) = p_0 \exp\left(-\frac{\varphi(x)}{\varphi_T}\right), \tag{12}$$

$p(x)$ is the hole density distribution, p_0 is the initial hole concentration,

$$n(x) = n_0 \exp\left(-\frac{\varphi(x)}{\varphi_T}\right), \tag{13}$$

$n(x)$ is the electron density distribution, n_0 is the initial electron concentration.

Let us transform the left side of (10):

$$\frac{d^2\varphi}{dx^2} = \frac{d\frac{d\varphi}{dx}}{dx} = \frac{d\varphi}{dx}\cdot\frac{d\frac{d\varphi}{dx}}{d\varphi} = -E\frac{-d\mathrm{E}}{d\varphi} = E\frac{d\mathrm{E}}{d\varphi}. \tag{14}$$

Applying (14) into (10) and integrating over φ from φ_s to 0, we obtain:

$$\int_{E_{Si}}^{0} E\,dE = -\frac{q}{\varepsilon_{Si}\varepsilon_0}\int_{\varphi_s}^{0}\left[p_0\left(\exp\left(-\frac{\varphi_s}{\varphi_T}\right)-1\right) - n_0\exp\left(\frac{\varphi_s}{\varphi_T}\right)\right]d\varphi. \tag{15}$$

Taking into account that $p_0 = N_a$, and $n_0 = n_i^2 / N_a$, we obtain an expression for the field in silicon E_{Si}:

$$E_{Si} = \sqrt{\frac{2q\varphi_T N_a}{\varepsilon_{Si}\varepsilon_0}\left[\left(\frac{\varphi_s}{\varphi_T} + \exp\left(-\frac{\varphi_s}{\varphi_T}\right)-1\right) + \frac{n_i^2}{N_a^2}\left(\exp\left(\frac{\varphi_s}{\varphi_T}\right)-1\right)\right]}. \tag{16}$$

Thus, the system of equations (3, 4), (9), (16) directly connects the value $V_{g.s}$ with φ_s. By changing φ_s in the range φ_b from $2\varphi_b$ and using expressions (1)–(16), the dependences of I_d from $V_{g.s}$ can be numerically calculated for any values of the density of the accumulated radiation-induced charge and the concentration of the build-up ITs.

4. RESULTS AND ANALYSIS

Tables 2 and 3 present the results of calculating the concentration of IT and charge in the oxide (Q_{ox}) before and after irradiation, as well as the experimentally obtained values of the maximum voltage of the ESD pulse (V_{ESD}). The values of the breakdown voltage under ESD for non-irradiated samples were in the range of 3–4 kV for IRFR4615PbF and 4–4.5 kV for IRFR3710ZPbF.

Table 2 shows that for the IRFR4615PbF samples irradiated with a dose of 1.78 krad, ITs accumulated as a result of gamma irradiation were not built-up. Their concentration remained at the same level as before irradiation. For the samples irradiated with a dose of 3.9 krad, insignificant built-up IT already occurred, and the breakdown voltage under ESD exposure also remained virtually unchanged. For the IRFR3710ZPbF samples, the built-up ITs occurred at all values of the TID, and the concentration of the built-up ITs increased with an increase in the TID.

After irradiation, the breakdown voltage under ESD exposure increased. This is consistent with the proposed hypothesis that an increase in the concentration of built-up IT leads to degradation of the gain of the parasitic bipolar transistor. As a consequence, a higher ESD voltage is required for the collector current to reach the value necessary to initiate secondary breakdown of the bipolar transistor. It is worth noting that the initial concentration of IT in both types of samples is very high. This complicates the study, and even when irradiated to a TID close to the failure level, the number of built-up IT will be comparable to the initial concentration.

CONCLUSIONS

The study presents a theoretical description of the physical mechanism of the increase in breakdown voltage under the influence of ESD after gamma irradiation of high-power MOSFETs. The main reason for this phenomenon is the degradation of the gain of the parasitic bipolar transistor in the MOSFET structure, which, in turn, occurs due to the growth of the recombination rate in the SCR of the emitter-base junction, proportional to the density of the IT.

The resistance to ESD of two types of high-power MOSFETs was determined using a specially developed ESD generator before and after gamma irradiation. Gamma irradiation of the samples studied was carried out in the threshold voltage measurement mode on a ^{60}Co source at room temperature. Before and after irradiation, drain-gate I–V characteristics were recorded in the subthreshold region, from which the concentration of the IT was subsequently calculated. The study presents a method for calculating the dependence of the drain current on

Table 2. Experimental and calculated data for IRFR4615PbF

Sample No.	Absorbed dose, krad (Si)	Pre-irradiation		After irradiation		
		$N_{i.t}$, cm^{-2}	Q_{ox}, C	$N_{i.t}$, cm^{-2}	Q_{ox}, C	V_{ESD}, kV
1	1.78	$2.5 \cdot 10^{11}$	0	$2.5 \cdot 10^{11}$	$2.3 \cdot 10^{-8}$	2.5
2	1.78	$2.0 \cdot 10^{11}$	0	$2.0 \cdot 10^{11}$	$2.4 \cdot 10^{-8}$	3
3	3.18	$2.2 \cdot 10^{11}$	0	$2.4 \cdot 10^{11}$	$4.8 \cdot 10^{-8}$	3.5
4	3.18	$1.0 \cdot 10^{11}$	0	$1.2 \cdot 10^{11}$	$5.0 \cdot 10^{-8}$	2.5

Table 3. Experimental and calculated data for IRFR3710ZPbF

Sample No.	Absorbed dose, krad (Si)	Pre-irradiation		After irradiation		
		$N_{i.t}$, cm^{-2}	Q_{ox}, C	$N_{i.t}$, cm^{-2}	Q_{ox}, C	V_{ESD}, kV
1	2	$5.0 \cdot 10^{11}$	0	$8.0 \cdot 10^{11}$	$5.7 \cdot 10^{-8}$	5.5
2	3.9	$3.0 \cdot 10^{11}$	0	$7.0 \cdot 10^{11}$	$7.1 \cdot 10^{-8}$	5.5
3	3.9	$2.0 \cdot 10^{11}$	0	$6.0 \cdot 10^{11}$	$8 \cdot 10^{-8}$	5.5

the gate-source voltage for any values of the density of the accumulated radiation-induced charge and the concentration of built-up IT. The study also shows that with an increase in the concentration of built-up IT, the breakdown voltage of the sample under the influence of ESD increases.

Authors' contributions

D.M. Bakerenkova—hypothesis, development of a method for calculating the concentration of interface states, experimental studies, writing the text of the article.

A.S. Petrov—development of experimental methodology, validation, writing the text of the article, and editing.

REFERENCES

1. Paderov V.P., Silkin D.S., Goryachkin Yu.V., et al. Effect of proton irradiation on the breakdown voltage of a high-voltage *p–n* junction. *J. Commun. Technol. Electron*. 2017;62(6):616–620. https://doi.org/10.1134/S1064226917060158 [Original Russian Text: Paderov V.P., Silkin D.S., Goryachkin Yu.V., Khapugin A.A., Grishanin A.V. Effect of proton irradiation on the breakdown voltage of a high-voltage *p–n* junction. *Radiotekhnika i ehlektronika*. 2017;62(6):596–600 (in Russ.). https://www.elibrary.ru/ysugwj]
2. Shu L., Zhao Y.-F., Galloway K.F., Wang L., Wang X.-S., Yuan Z.-Y., Zhou X., Chen W.-P., Qiao M., Wang T.-Q. Effect of Drift Length on Shifts in 400-V SOI LDMOS Breakdown Voltage Due to TID. *IEEE Trans. Nucl. Sci*. 2020;67(11): 2392–2395. https://doi.org/10.1109/TNS.2020.2970743
3. Zhou X., Chen L., Chen C., Qiao M., Li Z., Zhang B. New Insight into Total-Ionizing-Dose Effect-Induced Breakdown Voltage Degradation for SOI LDMOS: Irradiation Charge Field Modulation. *IEEE Trans. Nucl. Sci*. 2023;70(4):659–666. https://doi.org/10.1109/TNS.2022.3231877
4. Seehra S.S., Slusark W.J. The Effect of Operating Conditions on the Radiation Resistance of VDMOS Power FETs. *IEEE Trans. Nucl. Sci*. 1982;29(6):1559–1563. https://doi.org/10.1109/TNS.1982.4336404
5. Blackburn D.L., Benedetto J.M., Galloway K.F. The Effect of Ionizing Radiation on the Breakdown Voltage of Power MOSFETS. *IEEE Trans. Nucl. Sci*. 1983;30(6):4116–4121. https://doi.org/10.1109/TNS.1983.4333092
6. Liang W., Alexandrou K., Klebanov M., Kuo C.-C., Kymissis I., Sundaram K.B., Liou J.J. Characterization of ESD protection devices under total ionizing dose irradiation. In: *IEEE 24th International Symposium on the Physical and Failure Analysis of Integrated Circuits* (*IPFA*), Chengdu, China: 2017. P. 1–4. https://doi.org/10.1109/IPFA.2017.8060225
7. Wu M., Lu W., Zhang C., Peng W., Zeng Y., Jin H., Xu J., Chen Z. The impact of radiation and temperature effects on dual-direction SCR devices for on-chip ESD protections. *Semicond. Sci. Technol*. 2020;35(4):045016. https://doi.org/10.1088/1361-6641/ab74ed
8. Arzamastseva D.M., Petrov A.S., Tapero K.I. Effect of Preliminary Gamma Irradiation on Degradation of Power *N*-MOS Transistors Influenced by Electrical Static Discharge. *Voprosy atomnoi nauki i tekhniki. Seriya: Fizika radiatsionnogo vozdeistviya na radioehlektronnuyu apparaturu*. 2023;3:19–22 (in Russ.).
9. Bakerenkov A.S., Felitsyn V.A., Chubunov P.A., Skorkin I.V. Temperature Dependence of Surface Recombination Current in Bipolar Transistors. In: *5th International Conference on Radiation Effects of Electronic Devices* (*ICREED*). Kunming, China: 2023. https://doi.org/10.1109/ICREED59404.2023.10390896
10. Kosier S.L., Schrimpf R.D., Nowlin R.N., Fleetwood D.M., DeLaus M., Pease R.L. Charge Separation for Bipolar Transistors. *IEEE Trans. Nucl. Sci*. 1993;40(6):1276–1285. https://doi.org/10.1109/23.273541
11. Lenahan P.M., Dressendorfer P.V. An Electron Spin Resonance Study of Radiation Induced Electrically Active Paramagnetic Centers at the Si/SiO_2 Interface. *J. Appl. Phys.* 1983;54(3):1457–1460. https://doi.org/10.1063/1.332171
12. McLean F.B. A Framework for Understanding Radiation-Induced Interface States in SiO_2 MOS Structures. *IEEE Trans. Nucl. Sci*. 1980;27(6):1651–1657. https://doi.org/10.1109/TNS.1980.4331084
13. Winokur P.S., McGarrity J.M., Boesch H.E. Dependence of Interface-State Buildup on Hole Generation and Transport in Irradiated MOS Capacitors. *IEEE Trans. Nucl. Sci*. 1976;23(6):1580–1585. https://doi.org/10.1109/TNS.1976.4328543
14. Reichert G., Raynaud C., Faynot O., Balestra F., Cristoloveanu S. Temperature dependence (300–600 K) of parasitic bipolar effects in SOI-MOSFETs. In: *Proceedings of the 7th European Solid-State Device Research Conference*. 1997.
15. Saks N.S., Dozier C.M., Brown D.B. Time Dependence of Interface Trap Formation in MOSFETs Following Pulsed Irradiation *IEEE Trans. Nucl. Sci*. 1988;35(6):1168–1177. https://doi.org/10.1109/23.25435
16. Winokur P.S., Boesch H.E., McGarrity J.M., McLean F.B. Field- and Time-Dependent Radiation Effects at the Si/SiO_2 Interface of Hardened MOS Capacitors. *IEEE Trans. Nucl. Sci*. 1977;24(6):2113–2118. https://doi.org/10.1109/TNS.1977.4329176
17. McWhorter P.J., Winokur P.S. Simple technique for separating the effects of interface traps and trapped-oxide charge in metal-oxide-semiconductor transistors. *Appl. Phys. Lett*. 1986;48(2):133–135. https://doi.org/10.1063/1.96974
18. Schwank J.R., Shaneyfelt M.R., Fleetwood D.M., Felix J.A., Dodd P.E., Paillet P., Ferlet-Cavrois V. Radiation Effects in MOS Oxides *IEEE Trans. Nucl. Sci*. 2008;55(4):1833–1853. https://doi.org/10.1109/TNS.2008.2001040

About the Authors

Diana M. Bakerenkova, Test Engineer, Research Institute of Scientific Instruments (8, Turaevo Industrial Area, Lytkarino, Moscow oblast, 140080 Russia). E-mail: arzamasceva.diana@mail.ru. RSCI SPIN-code 8543-8866, https://orcid.org/0009-0000-8670-812X

Aleksandr S. Petrov, Cand. Sci. (Eng.), Head of Department, Research Institute of Scientific Instruments (8, Turaevo Industrial Area, Lytkarino, Moscow oblast, 140080 Russia). E-mail: as_petrov@inbox.ru. Scopus Author ID 7401779679, RSCI SPIN-code 8304-5998, https://orcid.org/0009-0008-1198-980X

Об авторах

Бакеренкова Диана Максимовна, инженер-испытатель, Акционерное общество «Научно-исследовательский институт приборов» (140080, Россия, Московская обл., г. Лыткарино, промзона Тураево, стр. 8). E-mail: arzamasceva.diana@mail.ru. SPIN-код РИНЦ 8543-8866, https://orcid.org/0009-0000-8670-812X

Петров Александр Сергеевич, к.т.н., начальник отдела, Акционерное общество «Научно-исследовательский институт приборов» (140080, Россия, Московская обл., г. Лыткарино, промзона Тураево, стр. 8). E-mail: as_petrov@inbox.ru. Scopus Author ID 7401779679, SPIN-код РИНЦ 8304-5998, https://orcid.org/0009-0008-1198-980X

Translated from Russian into English by Lyudmila O. Bychkova
Edited for English language and spelling by Dr. David Mossop

Analytical instrument engineering and technology

Аналитическое приборостроение и технологии

UDC 550.380.8
https://doi.org/10.32362/2500-316X-2025-13-6-95-103
EDN JCFXYH

RESEARCH ARTICLE

On the working zone of a magnetometer-electromagnet measuring device when using opposing pole pieces with flat surfaces

Daria A. Sandulyak [@], Maria N. Polismakova, Daria A. Golovchenko, Alexey S. Kharin, Alexander V. Sandulyak, Anna A. Sandulyak

MIREA – Russian Technological University, Russian Federation, 119454 Moscow
[@] Corresponding author, e-mail: d.sandulyak@mail.ru

• **Submitted:** 29.01.2025 • **Revised:** 31.05.2025 • **Accepted:** 06.10.2025

Abstract

Objectives. The work set out to develop an approach for assessing the working (local) zone in magnetometer-electromagnet measuring devices designed for controlling the magnetic properties of samples in which the homogeneity of the magnetic field should be observed in terms of constancy of the field strength or induction.

Methods. The coordinate characteristics of the field strength (induction) between pole components were experimentally obtained to identify the desired working zone (in the vicinity of the minimum of each of these characteristics), taking into account the distance *b* between the poles and their diameter *D*.

Results. Data on working zones between opposing flat poles are obtained for different values *b* and *D*. With increased ratios b/D = 0.7–1.3, the size of the working zone concentrated in the middle axial part of the interpolar area is estimated at a value not exceeding 25–30% of the distance *b* such that the characteristic longitudinal size of the sample does not exceed 5–10 mm. As *D* increases and b/D decreases, the working area increases. In particular, at $b/D \cong 0.5$, the size of the working area is estimated to be up to 90% and even 100% of the distance *b*.

Conclusions. A principled approach to the assessment of the working (axial) zone between opposing flat poles is demonstrated by obtaining and analyzing the necessary coordinate (significantly dependent on *b* and *D*) characteristics of the field strength (induction) between them.

Keywords: homogeneity of the magnetic field, magnetometer-electromagnet, strength, induction, flat pole pieces

For citation: Sandulyak D.A., Polismakova M.N., Golovchenko D.A., Kharin A.S., Sandulyak A.V., Sandulyak A.A. On the working zone of a magnetometer-electromagnet measuring device when using opposing pole pieces with flat surfaces. *Russian Technological Journal.* 2025;13(6):95–103. https://doi.org/10.32362/2500-316X-2025-13-6-95-103, https://www.elibrary.ru/JCFXYH

Financial disclosure: The authors have no financial or proprietary interest in any material or method mentioned.

The authors declare no conflicts of interest.

НАУЧНАЯ СТАТЬЯ

О рабочей зоне измерительного устройства при использовании в нем противостоящих полюсов с плоскими поверхностями

Д.А. Сандуляк [@], М.Н. Полисмакова, Д.А. Головченко, А.С. Харин, А.В. Сандуляк, А.А. Сандуляк

МИРЭА – Российский технологический университет, Россия, 119454 Москва
[@] *Автор для переписки, e-mail: d.sandulyak@mail.ru*

• **Поступила:** 29.01.2025 • **Доработана:** 31.05.2025 • **Принята к опубликованию:** 06.10.2025

Резюме

Цели. Цель работы – восполнить пробел, касающийся подхода к оценке рабочей (локальной) зоны в измерительных устройствах – магнитометрах-электромагнитах, предназначенных для контроля магнитных свойств образцов с обеспечением в данной зоне условия однородности магнитного поля: постоянства напряженности поля или индукции.

Методы. В основе методологии достижения поставленной цели – экспериментальное получение координатных характеристик напряженности (индукции) поля между полюсами и идентификация искомой рабочей зоны (в окрестности экстремума, фактически – минимума каждой из таких характеристик) с учетом расстояния b между полюсами и их диаметра D.

Результаты. Приведены экспериментально аргументированные данные о рабочих зонах между противостоящими плоскими полюсами для разных величин b и D. Так, при повышенных отношениях b/D = 0.7–1.3 размер рабочей зоны, сосредоточенной в срединной приосевой части межполюсной области, оценивается величиной, не превышающей 25–30% от расстояния b. Тогда характерный продольный размер образца со сравнительно малыми поперечными размерами (при размещении образца в такой зоне) не должен превышать 5–10 мм. С увеличением диаметра D и уменьшением отношения b/D рабочая зона увеличивается. В частности, при $b/D \cong 0.5$ размер рабочей зоны оценивается величиной до 90% и даже 100% от расстояния b.

Выводы. Показан и реализован принципиальный подход к оценке рабочей (приосевой) зоны между противостоящими плоскими полюсами посредством получения и анализа необходимых для этого координатных (экстремальных по виду, существенно зависимых от расстояния между полюсами и их диаметра) характеристик напряженности (индукции) поля между ними.

Ключевые слова: однородное магнитное поле, магнитометр-электромагнит, напряженность, индукция, плоские полюсные наконечники

Для цитирования: Сандуляк Д.А., Полисмакова М.Н., Головченко Д.А., Харин А.С., Сандуляк А.В., Сандуляк А.А. О рабочей зоне измерительного устройства при использовании в нем противостоящих полюсов с плоскими поверхностями. *Russian Technological Journal*. 2025;13(6):95–103. https://doi.org/10.32362/2500-316X-2025-13-6-95-103, https://www.elibrary.ru/JCFXYH

Прозрачность финансовой деятельности: Авторы не имеют финансовой заинтересованности в представленных материалах или методах.

Авторы заявляют об отсутствии конфликта интересов.

INTRODUCTION

Measuring devices based on ballistic magnetometers, whose key component is a solenoid, are widely used in science and technology for measuring various parameters, including those characterizing the magnetic properties of various samples and their materials. In order to create the necessary magnetic field in the working zone of which (i.e., the zone of a homogeneous magnetic field) the sample under study should be placed [1–6], an electromagnet is also used. The shape of the pole tips for creating the corresponding magnetic field between opposing magnetic poles is selected depending on the problem to be solved [7–15].

In order to create the necessary homogeneous magnetic field for studying magnetic properties of samples, the opposing surfaces of pole tips (truncated cone, cylindrical disks [9], etc.) should be flat and mutually parallel. Here the working zone (in which the required field homogeneity is observed, i.e., practically constancy of this or that value of the field strength H) is not the whole interpolar area, but only its median part depending on the distance b between the pole planes and their diameter D. Otherwise it may turn out that the results of measurements carried out in different parts of the studied object will be obtained under different conditions (by H), leading to incorrect results. Thus, the relevant issue of determining the working zone of such a measuring device is considered in the present article.

From the standpoint of the mentioned question, the main characteristic of the field between opposing magnetic poles (flat or differently reversed) is the coordinate characteristic of the field. This parameter, which is important both in the operation and creation of measuring devices of this type, is defined by the induction data B (or intensity $H = B/\mu_0$, where μ_0 is a magnetic constant) obtained in the interpolar area.

EXPERIMENTAL DATA, PROCESSING AND DISCUSSION

As follows from the above, a measuring device worthy of attention (a variant of a ballistic magnetometer) is an electromagnet employing opposing pole pieces whose surfaces, facing each other, are flat and mutually parallel. The sample under study should be placed between the disk-shaped pole pieces, as shown in Fig. 1, precisely in the working zone where the generated magnetic field is practically uniform. Meanwhile, in the interpolar area of such measuring device/magnetometer, the specified condition can be ensured only with a comparatively small distance b between the poles, and only in the central part of the area between them (as b increases, the field strength H decreases at the periphery and increases at the poles).

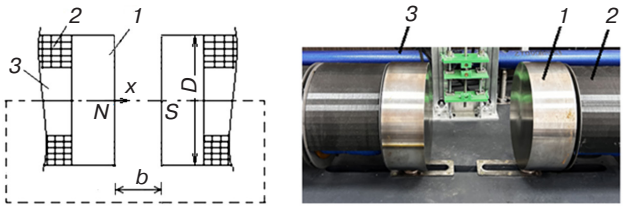

Fig. 1. Diagram and general view of a variant of the ballistic type magnetometer with pole tips-discs: (*1*) pole tip; (*2*) magnetizing coil; (*3*) magnet conductor. *N* and *S* are poles of the magnet, *x* is a direction of induction measurement

Figure 2 shows the coordinate characteristics of magnetic induction B obtained via a Hall sensor at a distance x from one of the poles along the interpolar axis [11]. For determining these characteristics, flat magnetic elements Nd–Fe–B with a diameter of D = 25 mm and a thickness of 10 mm were used. To determine characteristics analogous those depicted in Fig. 2, it is sufficient to experimentally obtain one of the symmetric branches of any of them [11]. The obtained values of b (increased compared to D) were b = 18–33 mm (b/D = 0.7–1.3).

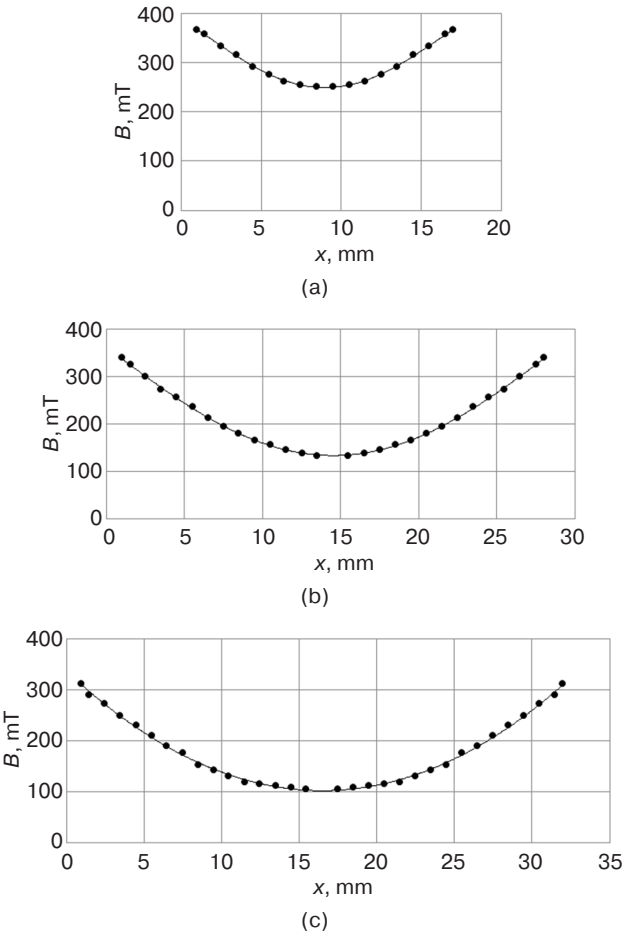

Fig. 2. Coordinate characteristics of magnetic field induction B between opposing poles with diameter D = 25 mm (for the near-axis part of the interpolar area) at different distances b between them: (a) 18 mm; (b) 29 mm; (c) 33 mm

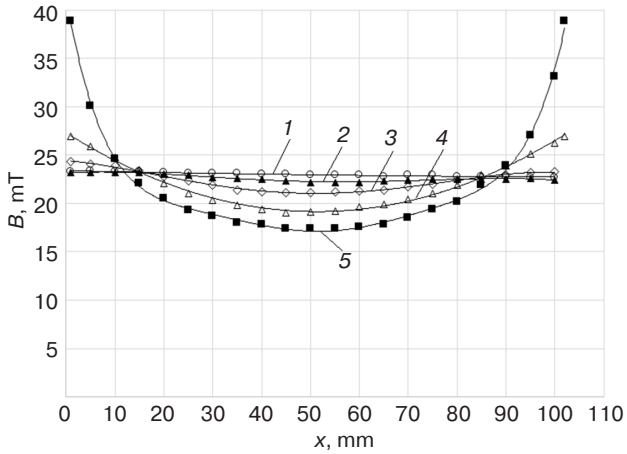

Fig. 3. Coordinate characteristics of induction *B* of the magnetic field between opposing poles with diameter *D* = 200 mm (for example, in the electromagnetic system according to Fig. 1) at the distance *b* = 102 mm between them:
1 (○) shows data for the near-axis part of the interpolar area; *2* (▲), *3* (◊), *4* (Δ), and *5* (■) shows data for the sections, which are 0.15*D*, 0.3*D*, 0.38*D*, and 0.45*D* away from the axis, respectively

According to the data given in Fig. 2, the working zone for the study of a particular sample is the median zone in the vicinity of the extremum (minimum) of the curve *B* from *x*; in terms of length, it can be estimated as no more than 25–30% of the value of *b*. For the researcher, this result means that the size of the sample under study when placed in such a zone should not exceed only 5–10 mm; moreover, this is true only for samples of relatively small transverse dimensions.

In order to achieve homogeneity of the field in it, the length of the working zone can be increased by increasing the diameter *D* of the poles (pole tips in the form of disks) and/or decreasing the distance *b* between them.

Figure 3 shows the coordinate characteristics of induction *B* between the poles with diameter *D* = 200 mm, which are remote from each other by distance *b* = 102 mm (*b*/*D* ≅ 0.5). The corresponding dependencies are given both for the near-axis part of the interpolar area and for other parts of this area at different distances from the axis: 0.15*D*, 0.3*D*, 0.38*D*, and 0.45*D* (almost at the periphery).

In this case the working zone can be considered as practically the whole interpolar near-axis area; the transverse radius with respect to the axis is not more than 0.15*D*. Here the extent of the working zone, estimated by the value 90–100% of *b* (for the near-axis part of the interpolar area) may enable the docking of the ends of the studied sample with the pole surfaces, but only when studying samples of relatively small transverse dimensions.

At the same time, it should be borne in mind that increasing the diameter *D* of poles and decreasing the distance *b* between them, although solving the problem of creating the necessary working area (with the provision of practically homogeneous magnetic field), also limits the possibility of using such a working area for conducting studies of relatively oblong samples in it.

Due to the fact that the primary coordinate characteristic in such electromagnetic systems is characteristic in the axial direction of the interpolar area, where the induction force lines are not curved, the possibility of obtaining such characteristics by superposition may become relevant. It is only necessary to possess the corresponding coordinate characteristic of induction *B* from the side of one pole in the absence of an opposing magnetic pole having a mirror characteristic, which is conditionally located at a certain distance.

Figure 4 shows the coordinate characteristic of the field induction from the side of one magnetic pole of the indicated magnetic element [11]. It can be seen that as *x* moves away from the center of its pole surface, the field induction *B* monotonically decreases, obeying a dependence close to the exponential dependence [11].

Operating with this characteristic, including its "mirror reflection" symmetrical at a distance equal to this or that interpolar distance *b* (the size of the interpolar area), we can obtain the resulting induction characteristic by adding the corresponding induction values in the axis direction (here between the actual and fictitious poles) using superposition technique.

Figure 5 shows the results of such a method used to obtain the corresponding resulting (points □) coordinate characteristics of the induction *B* [11] for different values of the (fictitious) pole-to-pole distance *b*.

Figure 6 summarizes the actual data of induction *B*, obtained between the opposing (differently reversed)

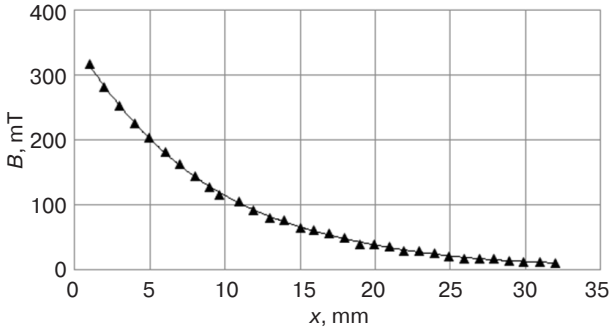

Fig. 4. Coordinate characteristic of the field induction *B* from the side of one pole of the magnetic element-disk at a distance from the center of the pole surface

magnetic poles, with the data of induction *B*, obtained by superposition.

The good agreement of the compared coordinate characteristics *B* (Fig. 6) testifies to the possibility of applying the superposition principle to this problem and obtaining a universal solution to the problem of obtaining the coordinate (i.e., near-axis) characteristics of the field induction in a system of two opposing poles with flat surfaces. Thus, it is possible to dispense with preliminary measurements of induction of a given magnetic system used in a measuring device by relying on the single coordinate characteristic obtained from the side of one magnetic pole. This confirms the possibility of practical use of the superposition principle in the creation of such systems.

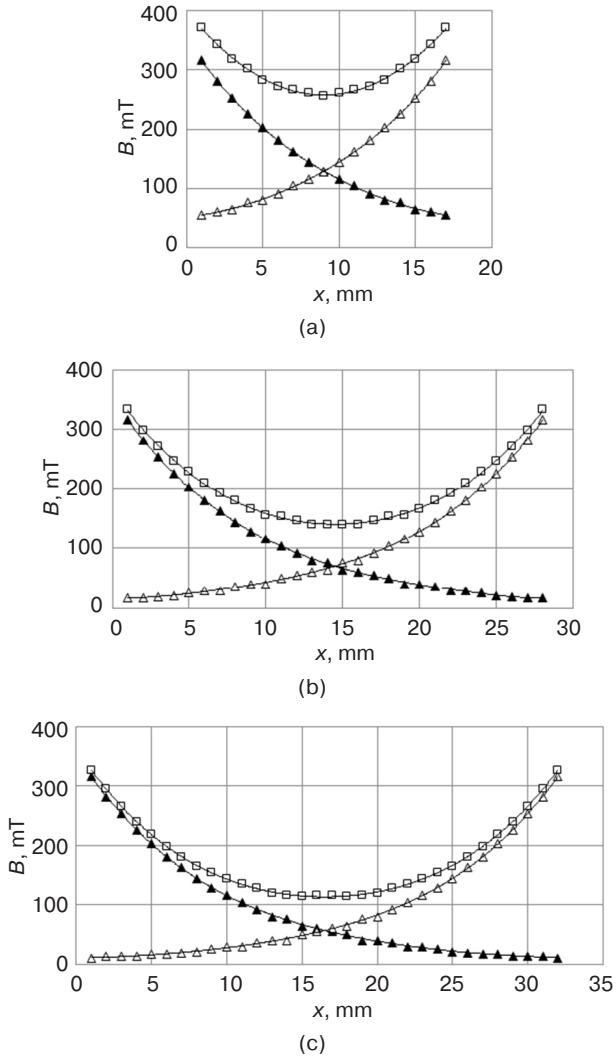

Fig. 5. Results of superposition of induction *B* (□) between the actual (data *B* are marked with the points ▲) and conditionally opposing at the distance *b* (data *B* are marked with the points Δ) magnetic poles of disk elements: (a) *b* = 18 mm; (b) *b* = 29 mm; (c) *b* = 33 mm

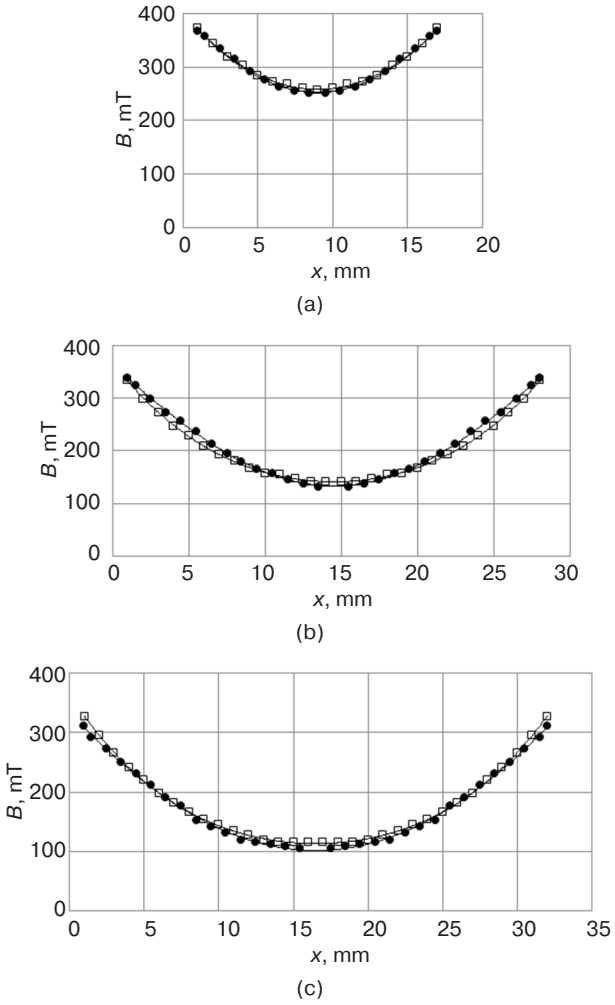

Fig. 6. Comparison of the actual coordinate characteristic of the induction data between two opposing poles separated by a distance *b* (points ● from Fig. 2) with the corresponding characteristic obtained by superposition of the induction data of each of these magnetic poles (points □ from Fig. 5): (a) *b* = 18 mm; (b) *b* = 29 mm; (c) *b* = 33 mm

CONCLUSIONS

Since different parts of a sample under study will be under different conditions (by *H* or *B*), the results of such measurements should be treated as not quite correct. The conducted study confirms the relevance of estimating the size of the working zone in which the values of field strength *H* or induction *B* are practically constant between the opposing flat poles in order to determine the reliability of determining the magnetic properties of samples placed in this zone.

Experimentally validated data on working zones when the opposing magnetic poles are in the form of flat disks are given for different distances *b* between pole planes and different diameters *D*. It is established that the size of the working zone will not exceed 25–30% of *b* at increased relative to *D* values of *b*. Thus, a sample placed in this zone for research should not exceed 5–10 mm and have a relatively small transverse dimension.

It is shown that the working area increases with increasing diameter *D* and decreasing distance *b*. In particular, at *b* = 102 mm and *D* = 200 mm (i.e., at $b/D \cong 0.5$), the size of the working zone is estimated by the value starting from 90% and up to 100% of *b* for the near-axial part of the interpolar area. This estimation applies to the permissible junction of the ends of the studied specimen with the pole surfaces, but only when studying specimens of relatively small transverse dimensions.

The possibility of estimating the working (near-axis) zone between the opposing planar magnetic poles by obtaining the necessary coordinate characteristics of the field induction (strength) between them by superposition (using the corresponding coordinate characteristics from the side of one of the magnetic poles) is confirmed.

ACKNOWLEDGMENTS

The study was financially supported by the Ministry of Science and Higher Education of the Russian Federation within the framework of the State Assignment in the field of science (project No. FSFZ-2024-0005).

Authors' contributions

D.A. Sandulyak—methodology, data verification and analysis, writing and editing the text of the article.

M.N. Polismakova—conceptualization, conducting the research, writing and editing the text of the article.

D.A. Golovchenko—collecting and analyzing materials for the study, writing the original draft.

A.S. Kharin—conducting the research, collecting materials for the study.

A.V. Sandulyak—data verification, formal analysis, supervision.

A.A. Sandulyak—methodology, editing.

REFERENCES

1. Kolesov K.A., Mashirov A.V., Koledov V.V., et al. Solenoid based on tapes of high-temperature superconductor for magnetocaloric applications. *Zhurnal radioehlektroniki = J. Radio Electronics.* 2024;11 (in Russ.). https://doi.org/10.30898/1684-1719.2024.11.31
2. Franz V.G. Superconducting solenoid from the second-generation HTSC tape. In: *Gagarin Readings – 2022:* Collection of Abstracts of the Works of the International Youth Scientific Conference 48th Gagarin Readings 2022. Moscow: 2022. P. 310 (in Russ.). https://www.elibrary.ru/zlbgea
3. Chen D.X., Pardo E., Zhu Y.-H., Xiang L.-X., Ding J.-Q. Demagnetizing correction in fluxmetric measurements of magnetization curves and hysteresis loops of ferromagnetic cylinders. *J. Magn. Magn. Mater.* 2018;449:447–454. https://doi.org/10.1016/j.jmmm.2017.10.069
4. Sandulyak D.A., Sandulyak A.A., Gorpinenko Yu.O., et al. "Pipe-layer" model of the magnetized chain of spheres: magnetic properties and assessment of the hyper-amplification field between the spheres. *Vestnik MGTU im. N.E. Baumana. Ser. Priborostroenie = Herald of the Bauman Moscow State Technical University. Series Instrument Engineering*. 2023;3(144): 49–61 (in Russ.). https://doi.org/10.18698/0236-3933-2023-3-49-61
5. Tsitsikyan G.N., Antipov M.Yu. Calculating the Inductance of Single- and Two-Layer Solenoids Taking into Account the Specific Features of Their Practical Application. *Elektrichestvo.* 2019;10:48–53 (in Russ.). https://doi.org/10.24160/0013-5380-2019-10-48-53
6. Kapitza P.L., Filimonov S.I. Solenoid producing a magnetic field up to 30 kOe in a volume of 5 liters and consuming 500 kW. *Sov. Phys. Usp*. 1968;11(3):299–303. https://doi.org/10.1070/PU1968v011n03ABEH003833
   [Original Russian Text: Kapitza P.L., Filimonov S.I. Solenoid producing a magnetic field up to 30 kOe in a volume of 5 liters and consuming 500 kW. *Uspekhi fizicheskikh nauk.* 1968;95(1):35–43 (in Russ.). https://doi.org/10.3367/UFNr.0095.196805d.0035]
7. Chechernikov V.I. *Magnitnye izmereniya* (*Magnetic Measurements*). Moscow: Moscow State University; 1963. 286 p. (in Russ.).
8. Thirumurugan A., Ramadoss A., Dhanabalan S., et al. MXene/Ferrite Magnetic Nanocomposites for Electrochemical Supercapacitor Applications. *Micromachines* (*Basel*). 2022;13(10):1792. https://doi.org/10.3390/mi13101792
9. Lopez-Dominguez V., Quesada A., Guzmán-Mínguez J.C., Moreno L., Lere M., Spottorno J., Giacomone F., Fernández J.F., Hernando A., García M.A. A simple vibrating sample magnetometer for macroscopic samples. *Rev. Sci. Instrum*. 2018;89(3):034707. https://doi.org/10.1063/1.5017708
10. Li W., Cai H., Kang Y., Ying Y., Yu J., Zheng J., Qiao L., Che S. High permeability and low loss bioinspired soft magnetic composites with nacre-like structure for high frequency applications. *Acta Materialia*. 2019;167:267–274. https://doi.org/10.1016/j.actamat.2019.01.035
11. Sandulyak A.A., Ershov D.V., Oreshkin D.V., Sandulyak A.V. Characteristics of magnetic field induction inside a module of a magnetic separator. *Vestnik MGSU*. 2013;5:103–111 (in Russ.).
12. Neiman L.A., Neiman V.Yu. *Single Coil Electromagnet*: RF Pat. RU 2791925. Publ. 14.03.2023 (in Russ.).
13. Amoskov V.M., Znamenshchikova N.S., Kukhtin V.P., Kaparkova M.V., Krylova N.A., Lamzin E.A., Larionov M.S., Mel'nikov D.D. *Method for Ensuring Magnetic Field Homogeneity in the Working Region of a Salient-Pole Magnetic Resonance Device*: RF Pat. RU 2833238. Publ. 15.01.2025 (in Russ.).
14. Sandulyak A.V., Sandulyak A.A., Polismakova M.N., Kiselev D.O., Sandulyak D.A. Faraday magnetometer with spheric pole pieces: identification zone with a stable force factor. *Russ. Technol. J*. 2017;5(6):43–54 (in Russ.). https://doi.org/10.32362/2500-316X-2017-5-6-43-54
15. Sandulyak A.A., Sandulyak A.V., Polismakova M.N., et al. The Use of Spherical Pole Pieces for Performing the Faraday Balance Method. *Instrum. Exp. Tech*. 2018;61(1)123–126. https://doi.org/10.1134/S0020441218010293
   [Original Russian Text: Sandulyak A.A., Sandulyak A.V., Polismakova M.N., Kiselev D.O., Ershova V.A., Sandulyak D.A. The Use of Spherical Pole Pieces for Performing the Faraday Balance Method. *Pribory i tekhnika eksperimenta*. 2018;1: 109–112 (in Russ.). https://doi.org/10.7868/S0032816218010342]

СПИСОК ЛИТЕРАТУРЫ

1. Колесов К.А., Маширов А.В., Коледов В.В., Петров А.О., Орлов А.П., Бычков И.В., Кузьмин Д.А., Gaida D., Кошкидько Ю.С., Шавров В.Г., Суслов Д.А. Соленоид на основе лент высокотемпературного сверхпроводника для магнитокалорических применений. *Журнал радиоэлектроники*. 2024;11. https://doi.org/10.30898/1684-1719.2024.11.31
2. Франц В.Г. Сверхпроводящий соленоид из ВТСП ленты второго поколения. В сб.: *Гагаринские чтения – 2022:* Сборник тезисов работ международной молодежной научной конференции XLVIII Гагаринские чтения 2022. М.: 2022. С. 310. https://www.elibrary.ru/zlbgea
3. Chen D.X., Pardo E., Zhu Y.-H., Xiang L.-X., Ding J.-Q. Demagnetizing correction in fluxmetric measurements of magnetization curves and hysteresis loops of ferromagnetic cylinders. *J. Magn. Magn. Mater.* 2018;449:447–454. https://doi.org/10.1016/j.jmmm.2017.10.069
4. Сандуляк Д.А., Сандуляк А.А., Горпиненко Ю.О., Сандуляк А.В., Соловьев И.А. Модель «трубок-слоев» намагничиваемой цепочки шаров: магнитные свойства, оценка гиперусиления поля между шарами. *Вестник МГТУ им. Н.Э. Баумана. Сер. Приборостроение.* 2023;3(144):49–61. https://doi.org/10.18698/0236-3933-2023-3-49-61

5. Цицикян Г.Н., Антипов М.Ю. Расчет индуктивности однослойного и двухслойного соленоида с учетом особенностей практического применения. *Электричество*. 2019;10:48–53. https://doi.org/10.24160/0013-5380-2019-10-48-53
6. Капица П.Л., Филимонов С.И. Соленоид, создающий магнитное поле до 30 кЭ в объеме 5 л и потребляющий 500 кВт. *УФН*. 1968;95(1):35–43. https://doi.org/10.3367/UFNr.0095.196805d.0035
7. Чечерников В.И. *Магнитные измерения.* М.: МГУ; 1963. 286 с.
8. Thirumurugan A., Ramadoss A., Dhanabalan S., et al. MXene/Ferrite Magnetic Nanocomposites for Electrochemical Supercapacitor Applications. *Micromachines* (*Basel*). 2022;13(10):1792. https://doi.org/10.3390/mi13101792
9. Lopez-Dominguez V., Quesada A., Guzmán-Mínguez J.C., Moreno L., Lere M., Spottorno J., Giacomone F., Fernández J.F., Hernando A., García M.A. A simple vibrating sample magnetometer for macroscopic samples. *Rev. Sci. Instrum*. 2018;89(3):034707. https://doi.org/10.1063/1.5017708
10. Li W., Cai H., Kang Y., Ying Y., Yu J., Zheng J., Qiao L., Che S. High permeability and low loss bioinspired soft magnetic composites with nacre-like structure for high frequency applications. *Acta Materialia*. 2019;167:267–274. https://doi.org/10.1016/j.actamat.2019.01.035
11. Сандуляк А.А., Ершов Д.В., Орешкин Д.В., Сандуляк А.В. Характеристики индукции поля в модуле магнитного сепаратора. *Вестник МГСУ*. 2013;5:103–111. https://www.elibrary.ru/olirce
12. Нейман Л.А., Нейман В.Ю. *Однокатушечный электромагнит*: пат. 2791925 РФ. Заявка № 2022115710; заявл. 10.06.2022; опубл. 14.03.2023. Бюл. № 8.
13. Амосков В.М., Знаменщикова Н.С., Кухтин В.П., Капаркова М.В., Крылова Н.А., Ламзин Е.А., Ларионов М.С., Мельников Д.Д. *Способ обеспечения однородности магнитного поля в рабочей области явнополюсного магниторезонансного устройства*: пат. 2833238 РФ. Заявка № 2023126377; заявл. 15.10.2023; опубл. 15.01.2025. Бюл. № 2.
14. Сандуляк А.В., Сандуляк А.А., Полисмакова М.Н., Киселев Д.О., Сандуляк Д.А. Магнетометр Фарадея с полюсными наконечниками-полусферами: идентификация зоны стабильного силового фактора. *Russ. Technol. J*. 2017;5(6):43–54. https://doi.org/10.32362/2500-316X-2017-5-6-43-54
15. Сандуляк А.А., Сандуляк А.В., Полисмакова М.Н., Киселев Д.О., Ершова В.А., Сандуляк Д.А. Использование полюсных наконечников сферической формы для реализации метода Фарадея. *Приборы и техника эксперимента*. 2018;1:109–112. https://doi.org/10.7868/S0032816218010342

About the Authors

Daria A. Sandulyak, Cand. Sci. (Eng.), Associate Professor, Department of Devices and Information-Measuring Systems, Institute for Cybersecurity and Digital Technologies, MIREA – Russian Technological University (78, Vernadskogo pr., Moscow, 119454 Russia). E-mail: sandulyak_d@mirea.ru. Scopus Author ID 36621369400, ResearcherID L-9814-2016, RSCI SPIN-code 8114-8109, https://orcid.org/0000-0003-4269-6133

Maria N. Polismakova, Cand. Sci. (Eng.), Associate Professor, Department of Devices and Information-Measuring Systems, Institute for Cybersecurity and Digital Technologies, MIREA – Russian Technological University (78, Vernadskogo pr., Moscow, 119454 Russia). E-mail: polismakova@mirea.ru. Scopus Author ID 36621096600, ResearcherID O-8796-2017, RSCI SPIN-code 3845-8391, https://orcid.org/0000-0002-4564-6206

Daria A. Golovchenko, Researcher Intern, Laboratory of Magnetic Control and Material's Separation, MIREA – Russian Technological University (78, Vernadskogo pr., Moscow, 119454 Russia). E-mail: golovchenko@mirea.ru. RSCI SPIN-code 4303-1093, https://orcid.org/0000-0002-6227-6884

Alexey S. Kharin, Engineer, Laboratory of Magnetic Control and Material's Separation, MIREA – Russian Technological University (78, Vernadskogo pr., Moscow, 119454 Russia). E-mail: linnetdar@mail.ru. RSCI SPIN-code 8435-3232, https://orcid.org/0000-0002-0922-1366

Alexander V. Sandulyak, Dr. Sci. (Eng.), Professor, Department of Devices and Information-Measuring Systems, Institute for Cybersecurity and Digital Technologies, MIREA – Russian Technological University (78, Vernadskogo pr., Moscow, 119454 Russia). E-mail: sandulyak@mirea.ru. Scopus Author ID 57194504434, ResearcherID V-6094-2018, RSCI SPIN-code 3795-5374, https://orcid.org/0000-0001-7605-2702

Anna A. Sandulyak, Dr. Sci. (Eng.), Professor, Department of Devices and Information-Measuring Systems, Institute for Cybersecurity and Digital Technologies, MIREA – Russian Technological University (78, Vernadskogo pr., Moscow, 119454 Russia). E-mail: sandulyak_a@mirea.ru. Scopus Author ID 7004032043, ResearcherID S-5187-2017, RSCI SPIN-code 8858-1720, https://orcid.org/0000-0002-5111-6092

Об авторах

Сандуляк Дарья Александровна, к.т.н., доцент, кафедра «Приборы и информационно-измерительные системы», Институт кибербезопасности и цифровых технологий, ФГБОУ ВО «МИРЭА – Российский технологический университет» (119454, Россия, Москва, пр-т Вернадского, д. 78). E-mail: sandulyak_d@mirea.ru. Scopus Author ID 36621369400, ResearcherID L-9814-2016, SPIN-код РИНЦ 8114-8109, https://orcid.org/0000-0003-4269-6133

Полисмакова Мария Николаевна, к.т.н., доцент, кафедра «Приборы и информационно-измерительные системы», Институт кибербезопасности и цифровых технологий, ФГБОУ ВО «МИРЭА – Российский технологический университет» (119454, Россия, Москва, пр-т Вернадского, д. 78). E-mail: polismakova@mirea.ru. Scopus Author ID 36621096600, ResearcherID O-8796-2017, SPIN-код РИНЦ 3845-8391, https://orcid.org/0000-0002-4564-6206

Головченко Дарья Андреевна, преподаватель-исследователь, стажер-исследователь лаборатории магнитного контроля и разделения материалов, ФГБОУ ВО «МИРЭА – Российский технологический университет» (119454, Россия, Москва, пр-т Вернадского, д. 78). E-mail: golovchenko@mirea.ru. SPIN-код РИНЦ 4303-1093, https://orcid.org/0000-0002-6227-6884

Харин Алексей Сергеевич, преподаватель-исследователь, инженер лаборатории магнитного контроля и разделения материалов, ФГБОУ ВО «МИРЭА – Российский технологический университет» (119454, Россия, Москва, пр-т Вернадского, д. 78). E-mail: linnetdar@mail.ru. SPIN-код РИНЦ 8435-3232, https://orcid.org/0000-0002-0922-1366

Сандуляк Александр Васильевич, д.т.н., профессор, кафедра «Приборы и информационно-измерительные системы», Институт кибербезопасности и цифровых технологий, ФГБОУ ВО «МИРЭА – Российский технологический университет» (119454, Россия, Москва, пр-т Вернадского, д. 78). E-mail: sandulyak@mirea.ru. Scopus Author ID 57194504434, ResearcherID V-6094-2018, SPIN-код РИНЦ 3795-5374, https://orcid.org/0000-0001-7605-2702

Сандуляк Анна Александровна, д.т.н., профессор, кафедра «Приборы и информационно-измерительные системы», Институт кибербезопасности и цифровых технологий, ФГБОУ ВО «МИРЭА – Российский технологический университет» (119454, Россия, Москва, пр-т Вернадского, д. 78). E-mail: sandulyak_a@mirea.ru. Scopus Author ID 7004032043, ResearcherID S-5187-2017, SPIN-код РИНЦ 8858-1720, https://orcid.org/0000-0002-5111-6092

Translated from Russian into English by Lyudmila O. Bychkova
Edited for English language and spelling by Dr. David Mossop

Mathematical modeling

Математическое моделирование

UDC 539.3
https://doi.org/10.32362/2500-316X-2025-13-6-104-115
EDN NGHUVB

RESEARCH ARTICLE

Method for splitting integral transformation in problems of complex heat transfer

Eduard M. Kartashov @

MIREA – Russian Technological University, Moscow, 119454 Russia
@ *Corresponding author, e-mail: professor.kartashov@gmail.com*

• **Submitted:** 11.04.2025 • **Revised:** 02.07.2025 • **Accepted:** 06.10.2025

Abstract

Objectives. This paper presents the development of a rather rare method for splitting the integral Fourier–Hankel transform when finding an exact analytical solution to the generalized third boundary value problem of complex heat transfer, where both the heat transfer coefficient and ambient temperature vary in time. The generalization lies in the simultaneous consideration of the problem in three different coordinate systems: Cartesian (a half-space bounded by a flat surface), cylindrical (a space bounded by a cylindrical cavity from the inside), and spherical (a space bounded by a spherical cavity from the inside). The aim was to develop a method for splitting the integral transformation as applied to finding an exact analytical solution to a generalized model problem of non-stationary thermal conductivity of complex heat exchange with an arbitrary dependence of the heat exchange coefficient and ambient temperature on time.

Methods. The generalized integral transformation developed for these purposes is used simultaneously in three coordinate systems, and the method for its splitting is applied to the problem of complex heat transfer.

Results. Initially, a special mathematical apparatus constituting a generalized integral Fourier–Hankel transform for three coordinate systems simultaneously was developed. For comparison, in the literature, such a transformation is formulated, as a rule, separately for each coordinate system. The availability of this mathematical apparatus made it possible to develop a method for its splitting and to obtain an exact analytical solution to the third boundary value problem for nonstationary thermal conductivity in complex heat transfer, simultaneously for all three coordinate systems. To illustrate this, a specific case in Cartesian coordinates was considered and a rapid growth of the Picard process was established.

Conclusions. Based on the developed special mathematical apparatus, an exact analytical solution to the generalized third boundary value problem of heat conductivity with time-varying heat transfer coefficient and ambient temperature, simultaneously in three coordinate systems, was obtained. These results constitute the scientific novelty of the work and represent a significant contribution to analytical thermal physics.

Keywords: generalized integral transformation, splitting method, analytical solution to the thermal problem

For citation: Kartashov E.M. Method for splitting integral transformation in problems of complex heat transfer. *Russian Technological Journal.* 2025;13(6):104–115. https://doi.org/10.32362/2500-316X-2025-13-6-104-115, https://www.elibrary.ru/NGHUVB

Financial disclosure: The author has no financial or proprietary interest in any material or method mentioned.

The author declares no conflicts of interest.

НАУЧНАЯ СТАТЬЯ

Метод расщепления интегрального преобразования в задачах сложного теплообмена

Э.М. Карташов [@]

МИРЭА – Российский технологический университет, Москва, 119454 Россия
[@] *Автор для переписки, e-mail: professor.kartashov@gmail.com*

• **Поступила:** 11.04.2025 • **Доработана:** 02.07.2025 • **Принята к опубликованию:** 06.10.2025

Резюме

Цели. Статья посвящена развитию достаточно редкого метода расщепления интегрального преобразования Фурье – Ханкеля при нахождении точного аналитического решения обобщенной третьей краевой задачи сложного теплообмена с переменным во времени коэффициентом теплообмена и переменной во времени температурой окружающей среды. Обобщение заключается в том, что исходная задача рассматривается одновременно в трех системах координат: декартовой (полупространство, ограниченное плоской поверхностью), цилиндрической (пространство, ограниченное изнутри цилиндрической полостью), сферической (пространство, ограниченное изнутри сферической полостью).

Методы. Используется развитое для этих целей обобщенное интегральное преобразование одновременно в трех системах координат и метод его расщепления применительно к задаче сложного теплообмена.

Результаты. Предварительно создан специальный математический аппарат – обобщенное интегральное преобразование Фурье – Ханкеля одновременно для трех систем координат (в литературе указанное преобразование сформулировано для каждой системы координат отдельно). Наличие указанного математического аппарата позволило развить метод его расщепления и получить точное аналитическое решение третьей краевой задачи нестационарной теплопроводности сложного теплообмена одновременно для всех трех систем координат. В качестве иллюстрации рассмотрен частный случай в декартовых координатах и установлен быстрый рост пикаровского процесса.

Выводы. На основе развитого специального математического аппарата получено точное аналитическое решение обобщенной третьей краевой задачи теплопроводности с переменными во времени коэффициентом теплообмена и температуры окружающей среды одновременно в трех системах координат. Полученные результаты составляют научную новизну работы и являются новыми в аналитической теплофизике.

Ключевые слова: интегральное преобразование обобщенного типа, метод расщепления, аналитическое решение тепловой задачи

Для цитирования: Карташов Э.М. Метод расщепления интегрального преобразования в задачах сложного теплообмена. *Russian Technological Journal*. 2025;13(6):104–115. https://doi.org/10.32362/2500-316X-2025-13-6-104-115, https://www.elibrary.ru/NGHUVB

Прозрачность финансовой деятельности: Автор не имеет финансовой заинтересованности в представленных материалах или методах.

Автор заявляет об отсутствии конфликта интересов.

INTRODUCTION

Heat and mass transfer problems with a boundary condition expressed as

$$(\partial T / \partial n)\big|_{\mathrm{B}} = h(t)\left[T_{\mathrm{B}} - T_{\mathrm{a}}(t)\right],\ t > 0$$

present considerable challenges due to the relationship $h(t) = \alpha(t)/\lambda^*$. Herein, T_{B} denotes the temperature at the boundary of the region, $\overline{n}$ represents the normal vector, T_{a} is the ambient temperature, $\alpha(t)$ is the heat transfer coefficient, λ^* is the thermal conductivity of the material, and t signifies time. Since the definition of $\alpha(t)$ can be difficult to determine, it is assumed to be a constant value in most criteria equations, α = const ($h = \alpha/\lambda^*$ = const). This allows for accurate analytical solutions to heat exchange problems. To that end, specialized calculation tables, known in heat transfer theory as Kartashov Tables No. 1 and No. 2, have been developed. These tables enable quick and efficient formulation of analytical solutions in Cartesian, cylindrical, and spherical coordinate systems. Additionally, they enhance solutions by their expression as Fourier–Hankel series, ensuring absolute and uniform convergence up to the boundary of the region when solving differential thermal conductivity equations. However, complications arise when the heat transfer coefficient h becomes time-dependent ($h = h(t)$). This variation renders the analytical resolution of model problems significantly more difficult and often infeasible. To date, this challenge has remained unresolved, since accurate analytical solutions under such dynamic conditions are yet to be obtained [2–6].

Since the 1950s, numerous publications across various disciplines—mathematics, physics, mechanics, and chemistry (physical chemistry in particular) studying diffusion processes in metals—have attempted to derive precise or approximate analytical solutions to the problem of complex heat exchange. Researchers have employed a range of classical approaches using differential equations from mathematical physics [7, 8]. Despite this diversity of methods, each approach ultimately has yielded either an approximate solution or the most effective first approximation through the Picard iteration process, which is itself an approximate technique. As of today, this problem has remained unresolved.

We consider the generalized formulation of the problem presented as follows:

$$\left.\begin{aligned}
&\frac{\partial T(x,t)}{\partial t} = a\left(\frac{\partial^2 T}{\partial x^2} + \frac{2m+1}{x}\frac{\partial T}{\partial x}\right),\ x > x_0,\ t > 0,\\
&T(x,t)\big|_{t=0} = T_0,\ x \ge x_0, \left|T(x,t)\right| < \infty,\ x \ge x_0,\ t \ge 0,\\
&\frac{\partial T(x,t)}{\partial x}\bigg|_{x=x_0} = h(t)\left[T(x,t)\big|_{x=x_0} - \varphi(t)\right],\ t > 0.
\end{aligned}\right\} \quad (1)$$

Herein, $m = -1/2$, 0, and 1/2 for Cartesian, cylindrical, and spherical coordinate systems, respectively; a is temperature transmission; and x, x_0 are model parameters. The functions $h(t)$, $\varphi(t)$ are nonnegative and absolutely integrable within the half-space $[0, +\infty)$. In this case, the conditions for the existence of a solution to the problem (1) and the unique solution are satisfied, i.e., there exists the unique solution, $T(x,t) \in L^2\left[(x_0,\infty) \times L^1(0,\infty)\right]$, where L^n is the set of continuously differentiable functions up to order n, as described in [8–10]. The primary focus of this paper is to determine this solution. A further extension of the theory discussed herein is the consideration of locally unbalanced heat exchange, in which the final rate of thermal propagation is taken into account[1] [11–16].

PROBLEM STATEMENT

The analytical solution to problem (1) is derived using the method of splitting the integral Fourier–Hankel transform of a generalized type. This transformation relies on operational calculation ratios established in [1]. Below is the final expression resulting from all the defining relations.

The generalized integral transformation of the function $T(x, t)$ for the third boundary problem takes the form:

$$\overline{T}(\lambda,t) = \int_{x_0}^{\infty} \rho^{2m+1} T(\rho,t)\Psi(\lambda,\rho)d\rho, \quad (2)$$

$$T(x,t) = \int_0^{\infty} \frac{\overline{T}(\lambda,t)\Psi(\lambda,x)}{\left[\lambda J_{m+1}(\lambda x_0) + hJ_m(\lambda x_0)\right]^2 + \left[\lambda Y_{m+1}(\lambda x_0) + hY_m(\lambda x_0)\right]^2}\lambda d\lambda, \quad (3)$$

[1] Savelyeva I.Yu. *Development and analysis of the mathematical model of thermomechanics of structurally sensitive materials.* Dr. Sci. Thesis (Phys.-Math.), Bauman Moscow State Technical University; 2023, 32 p. (in Russ.).

$$\Psi(\lambda,x)=x^{-m}\left\{\lambda\left[J_m(\lambda x)Y_{m+1}(\lambda x_0)-Y_m(\lambda x)J_{m+1}(\lambda x_0)\right]+h\left[J_m(\lambda x)Y_m(\lambda x_0)-Y_m(\lambda x)J_m(\lambda x_0)\right]\right\}. \quad (4)$$

In this scenario, the representation of the operator $\Delta T(x, t)$ is expressed as follows:

$$\int_{x_0}^{\infty}\rho^{2m+1}\Delta T(\rho,t)\Psi(\lambda,\rho)d\rho=\frac{2x_0{}^{-m}}{\pi}\left[\frac{\partial T(x,t)}{\partial x}-hT(x,t)\right]\Big|_{x=x_0}-\lambda^2\overline{T}(\lambda,t). \quad (5)$$

Here, $J_m(\cdot)$, $Y_m(\cdot)$ denotes Bessel functions.

Utilizing the generalized integral transformation provided in equations (2)–(5), it becomes straightforward to derive an exact analytical solution to problem (1) under the condition of h = const. This solution accommodates all heterogeneities present in both the equation itself caused by an internal transient heat source, as well as those in the boundary conditions stemming from initial temperature values and ambient temperature effects. From (2)–(5), corresponding transformations can be obtained at m = 0, –1/2, and 1/2 in cylindrical, Cartesian, and spherical coordinates, respectively.

CONSTRUCTION OF AN EXACT ANALYTICAL SOLUTION TO A GENERALIZED PROBLEM USING THE SPLIT INTEGRAL TRANSFORMATION METHOD

We consider problem (1) in dimensionless variables:

$$\rho=x/x_0,\ F_0=at/x_0^2,\ Bi(F_0)=\frac{\alpha(t)x_0}{\lambda^*},\ \Theta(\rho,F_0)=\frac{T(x,t)-T_0}{T_a^*-T_0},\ T_a(F_0)=\frac{\varphi(t)-T_0}{T_a^*-T_0}, \quad (6)$$

wherein T_a^* is the selected computing unit and Bi is the dimensionless heat exchange coefficient.

Problem (1) can now be reformulated as follows:

$$\left.\begin{aligned}&\frac{\partial\Theta}{\partial F_0}=\frac{\partial^2\Theta}{\partial\rho^2}+\frac{2m+1}{\rho}\frac{\partial\Theta}{\partial\rho},\ \rho>1,F_0>0,\\&\Theta(\rho,F_0)\big|_{F_0=0}=0,\ \rho\ge1,\left|\Theta(\rho,F_0)\right|<\infty,\ \rho\ge1,F_0\ge0,\\&\frac{\partial\Theta(\rho,F_0)}{\partial\rho}\Big|_{\rho=1}=Bi(F_0)\left[\Theta(\rho,F_0)\big|_{\rho=1}-T_a(F_0)\right],F_0>0.\end{aligned}\right\} \quad (7)$$

We write the generalized integral transformation (2)–(5) in the following form:

$$\overline{\Theta}(\lambda,F_0)=\int_1^{\infty}\rho^{2m+1}\Theta(\rho,F_0)K(\rho,\lambda,F_0)d\rho, \quad (8)$$

$$\begin{aligned}K(\rho,\lambda,F_0)&=\rho^{-m}\left\{\lambda\left[J_m(\lambda\rho)Y_{m+1}(\lambda)-Y_m(\lambda\rho)J_{m+1}(\lambda)\right]+Bi(F_0)\left[J_m(\lambda\rho)Y_m(\lambda)-Y_m(\lambda\rho)J_m(\lambda)\right]\right\}=\\&=\left[Bi(F_0)Y_m(\lambda)+\lambda Y_{m+1}(\lambda)\right]\left[\rho^{-m}J_m(\lambda\rho)\right]-\left[Bi(F_0)J_m(\lambda)+\lambda J_{m+1}(\lambda)\right]\left[\rho^{-m}Y_m(\lambda\rho)\right].\end{aligned} \quad (9)$$

Denote:

$$\left.\begin{aligned}\alpha(\lambda,F_0)&=Bi(F_0)Y_m(\lambda)+\lambda Y_{m+1}(\lambda),\\\beta(\lambda,F_0)&=Bi(F_0)J_m(\lambda)+\lambda J_{m+1}(\lambda).\end{aligned}\right\} \quad (10)$$

Then, the inverse formula for transformation (8) is:

$$\Theta(\rho,F_0)=\int_0^{\infty}\overline{\Theta}(\lambda,F_0)\frac{K(\rho,\lambda,F_0)}{\alpha^2(\lambda,F_0)+\beta^2(\lambda,F_0)}\lambda d\lambda. \quad (11)$$

At the same time,

$$K(\rho,\lambda,F_0)=\alpha(\lambda,F_0)\left[\rho^{-m}J_m(\lambda\rho)\right]-\beta(\lambda,F_0)\left[\rho^{-m}Y_m(\lambda\rho)\right], \tag{12}$$

$$\int_1^{\infty}\rho^{2m+1}\Delta\Theta(\rho,F_0)K(\rho,\lambda,F_0)d\rho=\frac{2}{\pi}\left[\frac{\partial\Theta(\rho,F_0)}{\partial\rho}-Bi(F_0)\Theta(\rho,F_0)\right]\Big|_{\rho=1}-\lambda^2\overline{\Theta}(\lambda,F_0). \tag{13}$$

Let us introduce some important designations:

$$\left.\begin{aligned}
\omega(\lambda,F_0)&=\alpha(\lambda,F_0)+i\beta(\lambda,F_0),\\
\overline{\omega}(\lambda,F_0)&=\alpha(\lambda,F_0)-i\beta(\lambda,F_0),\\
H_0^{(1)}(\lambda\rho)&=\left[J_m(\lambda\rho)+iY_m(\lambda\rho)\right](\rho^{-m}),\\
H_0^{(2)}(\lambda\rho)&=\left[J_m(\lambda\rho)-iY_m(\lambda\rho)\right](\rho^{-m}),\\
A(\lambda,F_0)&=\int_1^{\infty}\rho^{2m+1}\Theta(\rho,F_0)H_0^{(1)}(\lambda\rho)d\rho,\\
\overline{A}(\lambda,F_0)&=\int_1^{\infty}\rho^{2m+1}\Theta(\rho,F_0)H_0^{(2)}(\lambda\rho)d\rho.
\end{aligned}\right\} \tag{14}$$

Then, we can write:

$$\overline{\Theta}(\lambda,F_0)=\frac{1}{2}\left[\omega(\lambda,F_0)A(\lambda,F_0)+\overline{\omega}(\lambda,F_0)\overline{A}(\lambda,F_0)\right] \tag{15}$$

or

$$\overline{\Theta}(\lambda,F_0)=\mathrm{Re}\left[\omega(\lambda,F_0)A(\lambda,F_0)\right]. \tag{16}$$

The further step is to transform the original problem (7) into the image space (8). To that end, let us first write the integral transformation of the left-hand side of the equation in (7), as follows:

$$\frac{\partial\overline{\Theta}(\lambda,F_0)}{\partial F_0}=\int_1^{\infty}\rho^{2m+1}\frac{\partial\Theta(\rho,F_0)}{\partial F_0}K(\rho,\lambda,F_0)d\rho=\frac{1}{2}\left[\omega(\lambda,F_0)\frac{\partial A(\lambda,F_0)}{\partial F_0}+\overline{\omega}(\lambda,F_0)\frac{\partial\overline{A}(\lambda,F_0)}{\partial F_0}\right].$$

The image operator $\Delta\Theta(\rho, F_0)$ in (13) will be:

$$\begin{aligned}
&\int_1^{\infty}\rho^{2m+1}\Delta\Theta(\rho,F_0)K(\rho,\lambda,F_0)d\rho=\frac{2}{\pi}\left[\frac{\partial\Theta(\rho,F_0)}{\partial\rho}-Bi(F_0)\Theta(\rho,F_0)\right]\Big|_{\rho=1}-\lambda^2\overline{\Theta}(\lambda,F_0)=\\
&=-\frac{2}{\pi}Bi(F_0)T_{\mathrm{a}}(F_0)-\lambda^2\overline{\Theta}(\lambda,F_0)=-\frac{1}{2}\lambda^2\left[\omega(\lambda,F_0)A(\lambda,F_0)+\overline{\omega}(\lambda,F_0)\overline{A}(\lambda,F_0)\right]-\frac{2}{\pi}Bi(F_0)T_{\mathrm{a}}(F_0).
\end{aligned} \tag{17}$$

On this basis, the original problem (7) acquires the form:

$$\left.\begin{aligned}
&\omega(\lambda,F_0)\frac{\partial A(\lambda,F_0)}{\partial F_0}+\overline{\omega}(\lambda,F_0)\frac{\partial\overline{A}(\lambda,F_0)}{\partial F_0}+\lambda^2\left[\omega(\lambda,F_0)A(\lambda,F_0)+\overline{\omega}(\lambda,F_0)\overline{A}(\lambda,F_0)\right]=-\frac{4}{\pi}Bi(F_0)T_{\mathrm{a}}(F_0),F_0>0,\\
&A(\lambda,0)=\overline{A}(\lambda,0)=0
\end{aligned}\right\} \tag{18}$$

or

$$\left.\begin{aligned}
&\left[\omega(\lambda,F_0)\frac{\partial A(\lambda,F_0)}{\partial F_0}+\lambda^2\omega(\lambda,F_0)A(\lambda,F_0)+\frac{2}{\pi}Bi(F_0)T_{\mathrm{a}}(F_0)\right]=\\
&=-\left[\overline{\omega}(\lambda,F_0)\frac{\partial\overline{A}(\lambda,F_0)}{\partial F_0}+\lambda^2\overline{\omega}(\lambda,F_0)\overline{A}(\lambda,F_0)+\frac{2}{\pi}Bi(F_0)T_{\mathrm{a}}(F_0)\right],F_0>0,\\
&A(\lambda,0)=\overline{A}(\lambda,0)=0.
\end{aligned}\right\} \tag{19}$$

Looking at equality (18), it can be seen that after the transformations, an important relationship arises:

$$\int_1^\infty \rho^{2m+1} \frac{\partial \Theta(\rho, F_0)}{\partial F_0} K(\rho, \lambda, F_0) d\rho + \lambda^2 \int_1^\infty \rho^{2m+1} \Theta(\rho, F_0) d\rho + \\ + \frac{2}{\pi} Bi(F_0) T_a(F_0) = W(\lambda, F_0) = 0. \tag{20}$$

Expanding the left side of equation in (19), we find:

$$\left[\alpha(\lambda, F_0) + i\beta(\lambda, F_0)\right] \int_1^\infty \rho^{2m+1} \frac{\partial \Theta(\rho, F_0)}{\partial F_0} \left[(J_m(\lambda\rho) + iY_m(\lambda\rho))\rho^{-m}\right] d\rho +$$

$$+\lambda^2 \left[\alpha(\lambda, F_0) + i\beta(\lambda, F_0)\right] \int_1^\infty \rho^{2m+1} \Theta(\rho, F_0) \left[(J_m(\lambda\rho) + iY_m(\lambda\rho))\rho^{-m}\right] d\rho +$$

$$+\frac{2}{\pi} Bi(F_0) T_a(F_0) = \int_1^\infty \rho^{2m+1} \frac{\partial \Theta(\rho, F_0)}{\partial F_0} K(\rho, \lambda, F_0) d\rho + \lambda^2 \int_1^\infty \rho^{2m+1} \Theta(\rho, F_0) K(\rho, \lambda, F_0) d\rho + \frac{2}{\pi} Bi(F_0) T_a(F_0) +$$

$$+ i \left\{ \int_1^\infty \rho^{2m+1} \frac{\partial \Theta(\rho, F_0)}{\partial F_0} \left[\beta(\lambda, F_0)(J_m(\lambda\rho)\rho^{-m}) + \alpha(\lambda, F_0)(Y_m(\lambda\rho)\rho^{-m})\right] d\rho + \right.$$

$$\left. + \lambda^2 \int_1^\infty \rho^{2m+1} \Theta(\rho, F_0) \left[\beta(\lambda, F_0)(J_m(\lambda\rho)\rho^{-m}) + \alpha(\lambda, F_0)(Y_m(\lambda\rho)\rho^{-m})\right] d\rho \right\} = W(\lambda, F_0) + i\Psi(\lambda, F_0) = i\Psi(\lambda, F_0).$$

Here:

$$\Psi(\lambda, F_0) = \int_1^\infty \rho^{2m+1} \frac{\partial \Theta(\rho, F_0)}{\partial F_0} \left[\beta(\lambda, F_0)(J_m(\lambda\rho)\rho^{-m}) + \alpha(\lambda, F_0)(Y_m(\lambda\rho)\rho^{-m})\right] d\rho + \\ + \lambda^2 \int_1^\infty \rho^{2m+1} \Theta(\rho, F_0) \left[\beta(\lambda, F_0)(J_m(\lambda\rho)\rho^{-m}) + \alpha(\lambda, F_0)(Y_m(\lambda\rho)\rho^{-m})\right] d\rho. \tag{21}$$

Now, the desired problem can be reduced to the following Cauchy problem:

$$\left.\begin{array}{c} \dfrac{\partial A(\lambda, F_0)}{\partial F_0} + \lambda^2 A(\lambda, F_0) = -\dfrac{2}{\pi} \cdot \dfrac{Bi(F_0)}{\omega(\lambda, F_0)} T_a(F_0) + i \dfrac{\Psi(\lambda, F_0)}{\omega(\lambda, F_0)}, F_0 > 0, \\ A(\lambda, 0) = 0 \end{array}\right\} \tag{22}$$

with a solution in the following form:

$$A(\lambda, F_0) = -\frac{2}{\pi} \int_0^{F_0} \frac{Bi(\tau) T_a(\tau)}{\omega(\lambda, \tau)} \exp\left[-\lambda^2 (F_0 - \tau)\right] d\tau + i \int_0^{F_0} \frac{\Psi(\lambda, \tau)}{\omega(\lambda, \tau)} \exp\left[-\lambda^2 (F_0 - \tau)\right] d\tau. \tag{23}$$

At the same time,

$$\frac{1}{\omega(\lambda, \tau)} = \frac{\alpha(\lambda, \tau) - i\beta(\lambda, \tau)}{\alpha^2(\lambda, \tau) + \beta^2(\lambda, \tau)}.$$

The fundamental equality for further research is the following:

$$\overline{\Theta}(\lambda, F_0) = \mathrm{Re}\left[\omega(\lambda, F_0) A(\lambda, F_0)\right]. \tag{24}$$

We expand $\Psi(\lambda, F_0)$:

$$\begin{aligned}\Psi(\lambda,F_0)&=\int_1^\infty \rho^{2m+1}\Delta\Theta(\rho,F_0)\left[\beta(\lambda,F_0)(J_m(\lambda\rho)\rho^{-m})+\alpha(\lambda,F_0)(Y_m(\lambda\rho)\rho^{-m})\right]d\rho+\\&+\lambda^2\int_1^\infty \rho^{2m+1}\Theta(\rho,F_0)\left[\beta(\lambda,F_0)(J_m(\lambda\rho)\rho^{-m})+\alpha(\lambda,F_0)(Y_m(\lambda\rho)\rho^{-m})\right]d\rho=\\&=\int_1^\infty \frac{\partial}{\partial\rho}\left(\rho^{2m+1}\frac{\partial\Theta(\rho,F_0)}{\partial\rho}\right)\left[\beta(\lambda,F_0)(J_m(\lambda\rho)\rho^{-m})+\alpha(\lambda,F_0)(Y_m(\lambda\rho)\rho^{-m})\right]d\rho+\\&+\lambda^2\int_1^\infty \rho^{2m+1}\Theta(\rho,F_0)\left[\beta(\lambda,F_0)(J_m(\lambda\rho)\rho^{-m})+\alpha(\lambda,F_0)(Y_m(\lambda\rho)\rho^{-m})\right]d\rho.\end{aligned}\tag{25}$$

By integrating twice in parts (the first integral in (25)), and considering the equations

$$\frac{1}{\rho^{2m+1}}\frac{\partial}{\partial\rho}\left[\rho^{2m+1}\frac{\partial(J_m(\lambda\rho)\rho^{-m})}{\partial\rho}\right]=-\lambda^2(J_m(\lambda\rho)\rho^{-m}),$$

$$\frac{\partial}{\partial\rho}\left[J_m(\lambda\rho)\rho^{-m}\right]=-\lambda\left[J_{m+1}(\lambda\rho)\rho^{-m}\right],$$

which are equal to $[Y_m(\lambda\rho)\rho^{-m}]$ as well, we can establish that

$$\Psi(\lambda,F_0)=-\left\{\Theta(1,F_0)\left[\alpha^2(\lambda,F_0)+\beta^2(\lambda,F_0)\right]-Bi(F_0)T_{\text{a}}(F_0)\left[\beta(\lambda,F_0)J_m(\lambda)+\alpha(\lambda,F_0)Y_m(\lambda)\right]\right\}.\tag{26}$$

Using equation (24), we calculate by multiplying $\omega(\lambda, F_0)$ from (14) with $A(\lambda, F_0)$ from (23). After applying extensive transformations and focusing on the real part, we arrive at the desired result:

$$\begin{aligned}\overline{\Theta}(\lambda,F_0)=\left(-\frac{2}{\pi}\right)\Bigg\{&\int_0^{F_0}\left[\frac{Bi(\tau)T_{\text{a}}(\tau)\alpha(\lambda,\tau)}{\alpha^2(\lambda,\tau)+\beta^2(\lambda,\tau)}\alpha(\lambda,F_0)+\frac{Bi(\tau)T_{\text{a}}(\tau)\beta(\lambda,\tau)}{\alpha^2(\lambda,\tau)+\beta^2(\lambda,\tau)}\beta(\lambda,F_0)\right]\exp\left[-\lambda^2(F_0-\tau)\right]d\tau\Bigg\}-\\&-\int_0^{F_0}\Theta(1,\tau)\left[\alpha(\lambda,F_0)\beta(\lambda,\tau)-\beta(\lambda,F_0)\alpha(\lambda,\tau)\right]\exp\left[-\lambda^2(F_0-\tau)\right]d\tau+\\&+\int_0^{F_0}\left\{Bi(\tau)T_{\text{a}}(\tau)\left[\beta(\lambda,\tau)J_m(\lambda)+\alpha(\lambda,\tau)Y_m(\lambda)\right]\frac{\left[\beta(\lambda,\tau)\alpha(\lambda,F_0)-\alpha(\lambda,\tau)\beta(\lambda,F_0)\right]}{\alpha^2(\lambda,\tau)+\beta^2(\lambda,\tau)}\exp\left[-\lambda^2(F_0-\tau)\right]\right\}d\tau.\end{aligned}$$

Using the conversion theorem (11), the desired function $\Theta(\rho, F_0)$, which is the solution to problem (7), can be written as follows:

$$\begin{aligned}\Theta(\rho,F_0)=\int_0^\infty\overline{\Theta}(\lambda,F_0)\frac{K(\rho,\lambda,F_0)}{\alpha^2(\lambda,F_0)+\beta^2(\lambda,F_0)}\lambda d\lambda&=\left(-\frac{2}{\pi}\right)\int_0^{F_0}Bi(\tau)T_{\text{a}}(\tau)d\tau\int_0^\infty\frac{K(\rho,\lambda,F_0)}{\alpha^2(\lambda,\tau)+\beta^2(\lambda,\tau)}\times\\&\times\frac{\alpha(\lambda,F_0)\alpha(\lambda,\tau)+\beta(\lambda,F_0)\beta(\lambda,\tau)}{\alpha^2(\lambda,F_0)+\beta^2(\lambda,F_0)}\exp\left[-\lambda^2(F_0-\tau)\right]\lambda d\lambda+\\&+\int_0^{F_0}Bi(\tau)T_{\text{a}}(\tau)d\tau\int_0^\infty\frac{K(\rho,\lambda,F_0)\left[\beta(\lambda,\tau)J_m(\lambda)+\alpha(\lambda,\tau)Y_m(\lambda)\right]}{\alpha^2(\lambda,\tau)+\beta^2(\lambda,\tau)}\cdot\frac{\beta(\lambda,\tau)\alpha(\lambda,F_0)-\alpha(\lambda,\tau)\beta(\lambda,F_0)}{\alpha^2(\lambda,F_0)+\beta^2(\lambda,F_0)}\times\\&\times\exp\left[-\lambda^2(F_0-\tau)\right]\lambda d\lambda-\int_0^{F_0}\Theta(1,\tau)d\tau\int_0^\infty\frac{K(\rho,\lambda,F_0)\left[\alpha(\lambda,F_0)\beta(\lambda,\tau)-\beta(\lambda,F_0)\alpha(\lambda,\tau)\right]}{\alpha^2(\lambda,F_0)+\beta^2(\lambda,F_0)}\exp\left[-\lambda^2(F_0-\tau)\right]\lambda d\lambda.\end{aligned}\tag{27}$$

The right-hand side of equation (27) depends on the unknown value of $\Theta(1, F_0)$. Assuming $\rho = 1$ in (27), and using the relation $J_m(z)Y_{m+1}(z) - J_{m+1}(z)Y_m(z) = -2/(\pi z)$, we arrive at the Volterra integral equation of the second kind associated with $\Theta(1, F_0)$:

$$\Theta(1,F_0) = \Theta_1(F_0) + \frac{2}{\pi}\int_0^{F_0} \Theta_2(\tau,F_0)\Theta(1,\tau)d\tau, \tag{28}$$

wherein

$$\Theta_1(F_0) = \left(\frac{2}{\pi}\right)^2 \int_0^{F_0} Bi(\tau)T_a(\tau)d\tau \int_0^{\infty} \frac{\alpha(\lambda,F_0)\alpha(\lambda,\tau)+\beta(\lambda,F_0)\beta(\lambda,\tau)}{\alpha^2(\lambda,\tau)+\beta^2(\lambda,\tau)} \times$$
$$\times \frac{\exp\left[-\lambda^2(F_0-\tau)\right]}{\alpha^2(\lambda,F_0)+\beta^2(\lambda,F_0)}\lambda d\lambda - \frac{2}{\pi}\int_0^{F_0} Bi(\tau)T_a(\tau)d\tau \int_0^{\infty} \frac{\beta(\lambda,\tau)J_m(\lambda)+\alpha(\lambda,\tau)Y_m(\lambda)}{\alpha^2(\lambda,\tau)+\beta^2(\lambda,\tau)} \times \tag{29}$$
$$\times \frac{\beta(\lambda,\tau)\alpha(\lambda,F_0)-\alpha(\lambda,\tau)\beta(\lambda,F_0)}{\alpha^2(\lambda,F_0)+\beta^2(\lambda,F_0)}\exp\left[-\lambda^2(F_0-\tau)\right]\lambda d\lambda,$$

$$\Theta_2(\tau,F_0) = \int_0^{\infty} \frac{\alpha(\lambda,F_0)\beta(\lambda,\tau)-\beta(\lambda,F_0)\alpha(\lambda,\tau)}{\alpha^2(\lambda,F_0)+\beta^2(\lambda,F_0)}\exp\left[-\lambda^2(F_0-\tau)\right]\lambda d\lambda. \tag{30}$$

The solution to the integral equation in (28) can be expressed through the Picard process of successive approximations, as follows:

$$\Theta(1,F_0) = \Psi_0(F_0) + \sum_{n=1}^{\infty}\left(\frac{2}{\pi}\right)^n \Psi_n(F_0), \tag{31}$$

wherein

$$\Psi_0(F_0) = \Theta_1(F_0), \Psi_n(F_0) = \int_0^{F_0} \Theta_2(\tau,F_0)\Psi_{n-1}(\tau)d\tau. \tag{32}$$

From (31), (32) we find the desired value in the following form:

$$\Theta(1,F_0) = \Theta_1(F_0) + \sum_{n=1}^{\infty}\left(\frac{2}{\pi}\right)^n \int_0^{F_0} \Theta_2(\tau,F_0)d\tau \int_0^{\tau} \Theta_2(\tau_1,\tau)d\tau_1 \ldots \int_0^{\tau_{n-2}} \Theta_2(\tau_{n-1},\tau_{n-2})\Theta_1(\tau_{n-1})d\tau_{n-1}. \tag{33}$$

This completes the process of deriving an accurate analytical solution to the generalized complex heat exchange problem (7).

It should be noted that, in a generalized form, this solution is the first of its kind in the literature on analytical thermophysics.

CASE STUDY OF THE PROPOSED APPROACH

To illustrate the application of the advanced approach when solving problem (1), we consider the case of Cartesian coordinates: $m = -1/2$, $x_0 = 0$, $\varphi(t) = T_a$. It should be noted here that

$$J_{1/2}(z) = \sqrt{2/\pi}\sin(z/\sqrt{z}),\ J_{-1/2}(z) = \sqrt{2/\pi}\cos(z/\sqrt{z}),$$
$$Y_{1/2}(z) = -\sqrt{2/\pi}\cos(z/\sqrt{z}),\ Y_{-1/2}(z) = \sqrt{2/\pi}\sin(z/\sqrt{z}).$$

In dimensionless variables

$$z = x / l, F_0 = at / l^2, Bi(F_0) = \alpha(t) l / \lambda^*, \Theta(z, F_0) = \frac{T(x,t) - T_0}{T_a - T_0},$$

wherein l is the selected scale unit, we have the following problem:

$$\left.\begin{gathered} \frac{\partial \Theta(z, F_0)}{\partial F_0} = \frac{\partial^2 \Theta}{\partial z^2},\ z > 0,\ F_0 > 0, \\ \Theta(z, F_0)\Big|_{F_0=0} = 0,\ z \geq 0,\ \left|\Theta(z, F_0)\right| < \infty,\ z \geq 0,\ F_0 \geq 0, \\ \frac{\partial \Theta(z, F_0)}{\partial z}\Big|_{z=0} = Bi(F_0)\left[\Theta(z, F_0) - 1\right],\ F_0 > 0. \end{gathered}\right\} \quad (34)$$

By omitting extensive transformations from generalized coordinates to Cartesian coordinates, we obtain the following analytical solution to problem (34):

$$\begin{gathered} \Theta(z, F_0) = \frac{2}{\pi} \int_0^{F_0} Bi(\tau) d\tau \int_0^{\infty} \left[\cos \xi z + \frac{Bi(F_0)}{\xi} \sin \xi z \right] \frac{\xi^2}{\xi^2 + Bi^2(F_0)} \exp\left[-\xi^2 (F_0 - \tau) \right] d\xi + \\ + \frac{2}{\pi} \int_0^{F_0} \Theta(0, \tau) \left[Bi(F_0) - Bi(\tau) \right] d\tau \int_0^{\infty} \left[\cos \xi z + \frac{Bi(F_0)}{\xi} \sin \xi z \right] \frac{\xi^2}{\xi^2 + Bi^2(F_0)} \exp\left[-\xi^2 (F_0 - \tau) \right] d\xi, \end{gathered} \quad (35)$$

where

$$\Theta(0, F_0) = \Theta_1(F_0) + \sum_{n=1}^{\infty} \left(\frac{2}{\pi} \right)^n \int_0^{F_0} \Theta_2(F_0, \tau) d\tau \int_0^{\tau} \Theta_2(\tau, \tau_1) d\tau_1 \ldots \int_0^{\tau_{n-2}} \Theta_1(\tau_{n-1}) \Theta_2(\tau_{n-2}, \tau_{n-1}) d\tau_{n-1}, \quad (36)$$

$$\Theta_1(F_0) = \frac{2}{\pi} \int_0^{F_0} Bi(\tau) \Psi_0(F_0, \tau) d\tau,$$

$$\Theta_2(F_0, \tau) = \left[Bi(F_0) - Bi(\tau) \right] \Psi_0(F_0, \tau), \quad (37)$$

$$\Psi_0(F_0, \tau) = \frac{\sqrt{\pi / 2}}{\sqrt{F_0 - \tau}} - \frac{\pi Bi(F_0)}{2} \exp\left[Bi^2(F_0)(F_0 - \tau)^2 \right] \Phi^*\left[Bi(F_0)\sqrt{(F_0 - \tau)^2} \right]. \quad (38)$$

One of the ways to prove the validity of the discovered relationship (35) is by considering a specific classical case where $Bi(F_0) = Bi$ = const. In this case, relationship (35) automatically provides a classic solution:

$$\Theta(z, F_0) = \Phi^*\left(\frac{z}{2\sqrt{F_0}} \right) - \exp(Biz - Bi^2 F_0) \Phi^*\left(\frac{z}{2\sqrt{F_0}} + BiF_0 \right),$$

wherein $\Phi^*(z) = 1 - \Phi(z)$, $\Phi(z)$ is the Laplace function.

When the condition $\left|Bi(F_0)\right| \leq M / 2$ is met, the series (36) evidently converges uniformly for all $F_0 > 0$ within any finite interval F_0 and is dominated by the series:

$$\sum_{n=1}^{\infty} \frac{2^{n-1} M^{n+1} d_{n+1}}{\pi^n} (\sqrt{F_0})^{n+1},\ d_{n+1} = \begin{cases} \dfrac{\pi^{-1/2} 2^{(n+1/2)}}{(n+1)!!},\ n = 2k+1, \\ \dfrac{2^{(n+1/2)}}{(n+1)!!},\ n = 2k, \end{cases}$$

whose convergence for all $F_0 > 0$ can be easily verified using the D'Alembert criterion. As a numerical illustration, let us consider $Bi(F_0) = \exp(-F_0)$ and write a series of successive approximations for $\Theta(0, F_0)$ from (36):

$$\Theta_0(0,F_0) = \Theta_1(F_0),$$

$$\Theta_1(0,F_0) = \int_0^{F_0} \Theta_2(F_0,\tau)\Theta_1(\tau)d\tau,$$

$$\Theta_2(0,F_0) = \int_0^{F_0} \Theta_2(F_0,\tau)d\tau \int_0^{\tau} \Theta_2(\tau,\tau_1)\Theta_1(\tau_1)d\tau_1.$$

The figure illustrates the outcomes of numerical calculations for various approximations of the temperature function $\Theta(z, F_0)$: $\Psi_1 = \Theta_1(z, F_0)$, $\Psi_2 = \Theta_1(z, F_0) + \Theta_2(z, F_0)$, $\Psi_3 = \Theta_1(z, F_0) + \Theta_2(z, F_0) + \Theta_3(z, F_0)$, and etc., calculated based on the criterion F_0 for points (a) $z = 0.707$ and (b) $z = 2$. The figure demonstrates that the graphs for the first and second approximations encompass the top and bottom (or "pincer," as referred to by the author) of the graph for the third approximation. Similarly, the graphs for the second and third approximations encompass the graph for the fourth approximation from above and below, and etc. This pattern highlights the rapid convergence of the iterative process for $\Theta(z, t)$, allowing a sufficient practical accuracy to be achieved by stopping at the third approximation. With regard to spherical coordinates, this scenario can be reduced to that considered in Cartesian coordinates by making the substitution $W(z, F_0) = z\Theta(z, F_0)$.

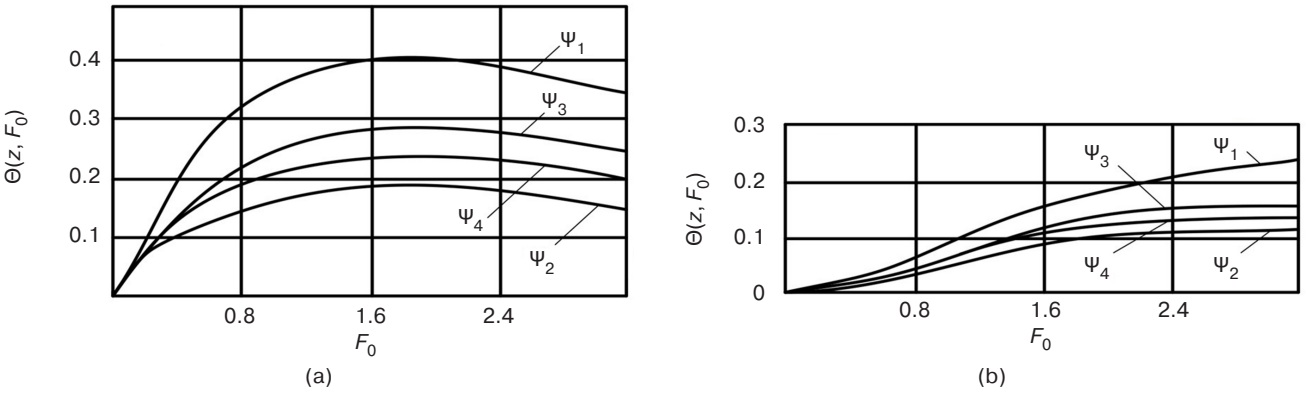

Fig. Approximations of temperature function $\Theta(z, F_0)$ versus F_0 at points: (a) $z = 0.707$; (b) $z = 2$

CONCLUSIONS

This paper introduces a method for dividing the generalized integral Fourier transform to derive precise analytical solutions to the temperature problem in complex heat exchange. The method takes into account an arbitrary time-dependent heat exchange coefficient and ambient temperature in generalized coordinates. It is further extended to Cartesian, cylindrical, and spherical coordinate systems. The results obtained represent a novel contribution to analytical thermophysics.

REFERENCES

1. Kartashov E.M. *Analiticheskie metody v teorii teploprovodnosti tverdykh tel* (*Analytical Methods in the Theory of Thermal Conductivity of Solids*). Moscow: Vysshaya shkola; 2001. 549 p. (in Russ.). ISBN 5-06-004091-7
2. Attetkov A.V., Volkov I.K. Formation of temperature fields in the region internally restricted by cylindrical hollow. *Vestnik MGTU im. Baumana. Seriya Mashinostroenie = Herald of the Bauman Moscow State Technical University. Series Mechanical Engineering.* 1999;1:49–56 (in Russ.).
3. Volkov I.K., Kanatnikov A.N. *Integral'noe preobrazovanie i operatsionnoe ischislenie* (*Integral Transformation and Operational Calculus*). Moscow: Bauman Press; 1996. 228 p. (in Russ.). ISBN 5-7938-1273-9
4. Lykov A.V. *Teoriya teploprovodnosti* (*Theory of Thermal Conductivity*). Moscow: Vysshaya shkola; 1967. 600 p. (in Russ.).

5. Podstrigach Ya.S., Kolyano Yu.M. *Termouprugost' tel pri peremennykh koehffitsientakh teploobmena* (*Thermoelasticity of Bodies with Variable Heat Transfer Coefficients*). Kiev: Naukova Dumka; 1977. 159 p. (in Russ.).
6. Carslow H.S., Jaeger J.C. *Teploprovodnost' tverdykh tel* (*Conduction of Heat in Solids*): transl. from Engl. Moscow: Nauka; 1964. 487 p. (in Russ.).
[Carslow H.S., Jaeger J.C. *Conduction of Heat in Solids.* Oxford: Clarendon Press; 1959. 520 p.]
7. Formalev V.F. *Uravneniya matematicheskoi fiziki* (*Equations of Mathematical Physics*). Moscow: URSS; 2021. 648 p. (in Russ.). ISBN 978-5-9710-8380-1
8. Novikov V.S. Analytical methods of transfer theory. *Promyshlennaya teplotekhnika = Industrial Heat Engineering*. 1989;11(5):11–54 (in Russ.).
9. Kudinov I.V., Kudinov V.A. *Analiticheskie resheniya parabolicheskikh i giperbolicheskikh uravnenii teplomassoperenosa* (*Analytical Solutions of Parabolic and Hyperbolic Heat and Mass Transfer Equations*). Moscow: Infra-M; 2013. 391 p. (in Russ.). ISBN 978-5-16-006724-7
10. Ladyzhenskaya O.A., Solonnikov V.A., Ural'tseva N.N. *Lineinye i kvazilineinye uravneniya parabolicheskogo tipa* (*Linear and Quasilinear Equations of Parabolic Type*). Moscow: Nauka; 1967. 736 p. (in Russ.).
11. Zarubin V.S., Kuvyrkin G.N. *Matematicheskie modeli termomekhaniki* (*Mathematical Models of Thermomechanics*). Moscow: Fizmatlit; 2002. 168 p. (in Russ.). ISBN 5-9221-0321-0
12. Kirsanov Yu.A. *Modelirovanie teplofizicheskikh protsessov* (*Modeling of Thermophysical Processes*). St. Petersburg: Politekhnika; 2022. 230 p. (in Russ.). ISBN 978-5-7325-1192-5. https://doi.org/10.25960/7325-1192-5
13. Kudinov I.V., Kudinov V.A. Mathematical Simulation of the Locally Nonequilibrium Heat Transfer in a Body with Account for its Nonlocality in Space and Time. *J. Eng. Phys. Thermophy.* 2015;88(2):406–422. https://doi.org/10.1007/s10891-015-1206-6
[Original Russian Text: Kudinov I.V., Kudinov V.A. Mathematical Simulation of the Locally Nonequilibrium Heat Transfer in a Body with Account for its Nonlocality in Space and Time. *Inzhenerno-Fizicheskii Zhurnal.* 2015;88(2):393–408 (in Russ.).]
14. Savelyeva Yu.I. Dual variational model of a stady-state thermal conductivity process taking into account spatial non-locality. *Vestnik MGTU im. Baumana. Estestvennye nauki = Herald of the Bauman Moscow State University. Series Natural Sciences.* 2022;5:45–61 (in Russ.). http://doi.org/10.18698/1812-3368-2022-5-45-61
15. Kartashov E.M. Development of model representations of the thermal response of viscoelastic bodies to a temperature field. *Russ. Technol. J.* 2024;12(6):80–90 (in Russ.). https://doi.org/10.32362/2500-316X-2024-12-6-80-90
16. Kudinov V.A., Eremin A.V., Kudinov I.V. The development and investigation of a strongly non-equilibrium model of heat transfer in fluid with allowance for the spatial and temporal non-locality and energy dissipation. *Thermophys. Aeromech.* 2017;24(6):901–907. https://doi.org/10.1134/S0869864317060087
[Original Russian Text: Kudinov V.A., Eremin A.V., Kudinov I.V. The development and investigation of a strongly non-equilibrium model of heat transfer in fluid with allowance for the spatial and temporal non-locality and energy dissipation. *Teplofizika i Aeromekhanika*. 2017;24(6):929–935 (in Russ.).]

СПИСОК ЛИТЕРАТУРЫ

1. Карташов Э.М. *Аналитические методы в теории теплопроводности твердых тел.* М.: Высшая школа; 2001. 549 с. ISBN 5-06-004091-7
2. Аттетков А.В., Волков И.К. Формирование температурных полей в области, ограниченной изнутри цилиндрической поверхностью. *Вестник МГТУ им. Баумана. Серия Машиностроение.* 1999;1:49–56.
3. Волков И.К., Канатников А.Н. *Интегральное преобразование и операционное исчисление.* М.: Изд-во МГТУ им. Баумана; 1996. 228 с. ISBN 5-7938-1273-9
4. Лыков А.В. *Теория теплопроводности*. М.: Высшая школа; 1967. 600 с.
5. Подстригач Я.С., Коляно Ю.М. *Термоупругость тел при переменных коэффициентах теплообмена.* Киев: Наукова Думка; 1977. 159 с.
6. Карслоу Г.С., Егер Д. *Теплопроводность твердых тел:* пер. с англ. М.: Наука; 1964. 487 с.
7. Формалев В.Ф. *Уравнения математической физики*. М.: URSS; 2021. 648 с. ISBN 978-5-9710-8380-1
8. Новиков В.С. Аналитические методы теории переноса. *Промышленная теплотехника*. 1989;11(5):11–54.
9. Кудинов И.В., Кудинов В.А. *Аналитические решения параболических и гиперболических уравнений тепломассопереноса*. М.: Инфра-М; 2013. 391 с. ISBN 978-5-16-006724-7
10. Ладыженская О.А., Солонников В.А., Уральцева Н.Н. *Линейные и квазилинейные уравнения параболического типа.* М.: Наука; 1967. 736 с.
11. Зарубин В.С., Кувыркин Г.Н. *Математические модели термомеханики*. М.: Физматлит; 2002. 168 с. ISBN 5-9221-0321-0
12. Кирсанов Ю.А. *Моделирование теплофизических процессов*. СПб.: Политехника; 2022. 229 с. ISBN 978-5-7325-1192-5. https://doi.org/10.25960/7325-1192-5
13. Кудинов И.В., Кудинов В.А. Математическая модель локально-неравновесного теплопереноса с учетом пространственно-временной нелокальности. *Инженерно-физический журнал*. 2015;88(2):393–408.

14. Савельева Ю.И. Двойственная вариационная модель процесса теплопроводности, учитывающая пространственную нелокальность. *Вестник МГТУ им. Баумана. Естественные науки.* 2022;5:45–61. http://doi.org/10.18698/1812-3368-2022-5-45-61
15. Карташов Э.М. Развитие модельных представлений термической реакции вязкоупругих тел на температурное поле. *Russ. Technol. J.* 2024;12(6):80–90. https://doi.org/10.32362/2500-316X-2024-12-6-80-90
16. Кудинов В.А., Еремин А.В., Кудинов И.В. Разработка и исследование сильно неравновесной модели теплообмена в жидкости с учетом пространственно-временной нелокальности и диссипации энергии. *Теплофизика и аэромеханика*. 2017;24(6):929–935.

About the Author

Eduard M. Kartashov, Dr. Sci. (Phys.-Math.), Honored Scientist of the Russian Federation, Honorary Worker of Higher Professional Education of the Russian Federation, Honorary Worker of Science and Technology of the Russian Federation, Honorary Professor of the Lomonosov Moscow State University of Fine Chemical Technology, Laureate of the Golden Medal of the Academy of Sciences of Belarus in Thermophysics, Professor, Department of Higher and Applied Mathematics, M.V. Lomonosov Institute of Fine Chemical Technologies, MIREA – Russian Technological University (78, Vernadskogo pr., Moscow, 119454 Russia). E-mail: professor.kartashov@gmail.com. Scopus Author ID 7004134344, ResearcherID Q-9572-2016, https://orcid.org/0000-0002-7808-4246

Об авторе

Карташов Эдуард Михайлович, д.ф.-м.н., Заслуженный деятель науки Российской Федерации, Почетный работник высшего профессионального образования Российской Федерации, Почетный работник науки и техники Российской Федерации, Почетный профессор МИТХТ им. М.В. Ломоносова, Лауреат Золотой медали Академии наук Беларуси по теплофизике, профессор кафедры высшей и прикладной математики, Институт тонких химических технологий им. М.В. Ломоносова, ФГБОУ ВО «МИРЭА – Российский технологический университет (119454, Россия, Москва, пр-т Вернадского, д. 78). E-mail: professor.kartashov@gmail.com. Scopus Author ID 7004134344, ResearcherID Q-9572-2016, https://orcid.org/0000-0002-7808-4246

Translated from Russian into English by Kirill V. Nazarov
Edited for English language and spelling by Dr. David Mossop

Mathematical modeling

Математическое моделирование

UDC 004:005.584.1:502/504
https://doi.org/10.32362/2500-316X-2025-13-6-116-126
EDN LAVZAN

RESEARCH ARTICLE

On monitoring and forecasting the dynamics of the development of the structure of tropical cyclones based on almost periodic analysis of satellite images

Alexander A. Paramonov [@], Andrew V. Kalach, Tatiana E. Saratova

MIREA – Russian Technological University, Moscow, 119454 Russia
[@] Corresponding author, e-mail: paramonov_a_a99@mail.ru

• **Submitted:** 11.03.2025 • **Revised:** 04.06.2025 • **Accepted:** 06.10.2025

Abstract

Objectives. The article sets out to identify the characteristics of tropical cyclones using almost periodic analysis of images of cloud dynamics of hurricanes in order to forecast the cyclone structure. Almost periodic analysis is applied in the processing and analysis of tropical cyclone structure images based on the obtained almost period values using a modified mathematical computational apparatus.

Methods. The main tool for processing and analyzing images of the tropical cyclone structure is almost periodic analysis, i.e., analysis of data with an ordered argument to identify dependencies that are close to periodic. By this means critical boundaries of changes in the trends of the studied data can be identified regardless of *a priori* assumptions. In the course of analysis the almost period information parameter, corresponding to the values closest to the periods, is determined. A modification of the known mathematical apparatus of almost periodic analysis is proposed for processing large and multidimensional datasets.

Results. In the course of the study, the characteristic almost periodic values of the structural zones at the moment of the beginning of the formation of the dynamics of the cyclone development were revealed on the example of the analysis of the frames of the dynamics of tropical cyclone Milton, operating from October 5, 2024 to October 10, 2024. Based on the identified values, forecast estimates of the tropical cyclone structure development were made to an accuracy of 95%.

Conclusions. Together with the results of studies published earlier, the results of this study support the conclusion that it is possible to apply almost periodic analysis to the identification of characteristic patterns of tropical cyclone structures and carry out qualitative forecast estimates of the dynamics of emergency situations caused by tropical cyclones.

Keywords: almost periodic analysis, image processing and analysis, tropical cyclone monitoring, tropical cyclone forecasting, technosphere safety, typhoons

For citation: Paramonov A.A., Kalach A.V., Saratova T.E. On monitoring and forecasting the dynamics of the development of the structure of tropical cyclones based on almost periodic analysis of satellite images.*Russian Technological Journal.* 2025;13(6):116–126. https://doi.org/10.32362/2500-316X-2025-13-6-116-126, https://www.elibrary.ru/LAVZAN

Financial disclosure: The authors have no financial or proprietary interest in any material or method mentioned.

The authors declare no conflicts of interest.

НАУЧНАЯ СТАТЬЯ

О мониторинге и прогнозировании динамики развития структуры тропических циклонов на основе почти периодического анализа спутниковых изображений

А.А. Парамонов [@], А.В. Калач, Т.Е. Саратова

МИРЭА – Российский технологический университет, Москва, 119454 Россия
[@] Автор для переписки, e-mail: paramonov_a_a99@mail.ru

• **Поступила:** 11.03.2025 • **Доработана:** 04.06.2025 • **Принята к опубликованию:** 06.10.2025

Резюме

Цели. Статья посвящена проблеме идентификации характеристик тропических циклонов с использованием почти периодического анализа изображений облачной динамики ураганов и прогнозирования структуры циклона на основе полученных значений почти периодов. Цель статьи заключается в применении почти периодического анализа с использованием модифицированного математического аппарата вычислений при обработке и анализе изображений структуры тропического циклона с возможностью осуществления прогнозных оценок.

Методы. Основным инструментом обработки и анализа изображений структуры тропического циклона является почти периодический анализ – анализ данных с упорядоченным аргументом по выявлению зависимостей, близких к периодическим. Использование аппарата почти периодического анализа позволяет проводить выявление критических рубежей изменения тенденций исследуемых данных вне зависимости от априорных предположений. В ходе проведения такого анализа определяется информационный параметр – почти период, соответствующий значениям, наиболее близким к периодам. Предложена модификация известного математического аппарата почти периодического анализа, позволяющая обрабатывать большие и многомерные данные.

Результаты. В ходе исследования на примере анализа кадров динамики тропического циклона Милтон, действующего с 5 по 10 октября 2024 г., выявлены характерные почти периодические значения структурных зон в момент начала формирования динамики развития циклона. На основе выявленных значений составлены прогнозные оценки развития структуры тропического циклона, точность которых составила 95%.

Выводы. Полученные результаты совместно с результатами исследований, опубликованными ранее, позволяют сделать вывод о возможности применения почти периодического анализа к выявлению характерных паттернов структур тропических циклонов и составлению качественных прогнозных оценок динамики развития чрезвычайных ситуаций, вызванных тропическими циклонами.

Ключевые слова: почти периодический анализ, обработка и анализ изображений, мониторинг тропических циклонов, прогнозирование тропических циклонов, техносферная безопасность, тайфуны

Для цитирования: Парамонов А.А., Калач А.В., Саратова Т.Е. О мониторинге и прогнозировании динамики развития структуры тропических циклонов на основе почти периодического анализа спутниковых изображений. *Russian Technological Journal*. 2025;13(6):116–126. https://doi.org/10.32362/2500-316X-2025-13-6-116-126, https://www.elibrary.ru/LAVZAN

Прозрачность финансовой деятельности: Авторы не имеют финансовой заинтересованности в представленных материалах или методах.

Авторы заявляют об отсутствии конфликта интересов.

INTRODUCTION

Weather forecasting is important for ensuring the safety and sustainable development of human society. Among extreme weather events associated with ongoing changes in climatic conditions, one of the most potentially dangerous are tropical cyclones, comprising powerful atmospheric vortices that occur in tropical and subtropical latitudes over warm ocean waters. According to statistics from the Russian Ministry of Emergency Situations, more than 100 dangerous natural phenomena occur annually, causing total material damage exceeding RUR 50 bn.[1]

The increasing pace of life and enormous volume of information exchange demand prompt, balanced, accurate, and well-founded decisions based on relevant forecasts. In this regard, it is important to improve the speed of effective decision-making in emergency situations by obtaining improved forecasts of the dynamics of dangerous natural phenomena, which contributes to the timely adoption of measures to ensure human safety, as well as the preparation of measures to counteract emergency situations.

Traditional numerical weather models are based on solving systems of differential equations that describe the physics of the atmosphere. However, such models have limitations in terms of accuracy and require significant computing resources. The application of artificial intelligence and machine learning technologies has the potential to significantly improve the speed and accuracy of forecasting dangerous weather events and the dynamics of emergency situations.

In this context, it seems relevant to develop an approach to forecasting the dynamics of tropical cyclones based on an almost periodic analysis of images of cyclone structures. Images are one category of data with an ordered argument. Data with an ordered argument represent a set of measurements of some experimental quantity that depends on the argument, comprising an ordered vector of values.

Time or space can serve as examples of arguments. Currently, such data is analyzed and processed using special programming languages and their built-in libraries [1, 2]. The most common approach to analysis involves the use of machine learning methods [3–9]. Methods involving the study and identification of hidden patterns in data with an ordered argument are actively used in medicine, economics, and other fields [10–16].

It should be noted that the use of spatiotemporal remote sensing data enables tracking the dynamics of natural phenomena, especially tropical cyclones [17–19].

The present study is devoted to modified analysis and forecasting of tropical cyclone dynamics based on satellite images using the almost periodic data analysis method. The described modified almost periodic analysis method aims to improve existing data analysis tools with an ordered argument.

RESEARCH METHODOLOGY

Almost periodic analysis is the analysis of data with an ordered argument to identify dependencies that are close to periodic. The use of almost periodic analysis enables the identification of critical turning points in the trends of the data under study, regardless of *a priori* assumptions. During such an analysis, the almost period information parameter is determined by obtaining values closest to the periods. In general, an almost periodic function $f(t)$ is a function that satisfies the condition: $|f(t+\tau)-f(t)|<\varepsilon$, where $\varepsilon > 0$ is the shift, τ is the almost period of this function [20].

Currently, most studies using almost periodic analysis of discrete data with an ordered argument are based on formulas whose values are determined by sequential iterative algorithms.

The algorithm for almost periodic analysis of a discrete data set conceptually consists of two stages:

1) exclusion of the trend from the vector of processed data;
2) processing of the obtained oscillations with a generalized shear function to identify almost periods.

At the first stage, the trend component must be excluded from the processed data in order to further analyze the almost periodic components of the series fluctuations. Since there is no information about the trend equation at the initial stage of data processing, an approach based on a transformation based on the theory of proportions is used to remove it from the data. This approach to removing the trend from the data is independent of any *a priori* assumptions about the behavior of the trend in the data.

Trend exclusion based on the theory of proportions is based on the assumption that trend characteristics are encoded through reference points. As an example of implementation, consider the simplest dependence of the values of a discrete data set of three points y_t, $y_{t-\Delta t}$, $y_{t+\Delta t}$, which encode the entire series under study [21]. If we take the ratio of, for example, a geometric progression as a basis, then the transformations for excluding the trend and obtaining fluctuations relative to the ordered argument t for the data y will look as follows:

$$\ln\left(\frac{y_{t-\Delta t}y_{t+\Delta t}}{y_t^2}\right)\sim t, \qquad (1)$$

[1] Ministry of the Russian Federation for Civil Defense, Emergencies, and Disaster Relief. https://mchs.gov.ru/ (in Russ.). Accessed August 10, 2025.

where y_t is the current value of the series y with the ordered argument t; $y_{t-\Delta t}$ is the previous value of the original series at a distance Δt based on the argument from the current value y_t; $y_{t+\Delta t}$ is the next value of the original series at a distance Δt based on the argument from the current value y_t.

As a result of such transformations, we obtain a series of oscillations corresponding to the shift parameter Δt. For a comprehensive analysis of all types of oscillations in the original data, it is necessary to obtain oscillations for each shift parameter by argument Δt. The range of Δt values is from 1 to $N/2$, where N is the length of the original data series.

The second step in the almost periodic analysis of a discrete data series with an ordered argument involves processing the obtained sets of oscillation vectors in order to exclude the trend using a shift function of the form:

$$a(\tau)=\frac{1}{n-\tau}\sum_{t=1}^{n-\tau}\left|\hat{y}_{\Delta t}(t+\tau)-\hat{y}_{\Delta t}(t)\right|, \qquad (2)$$

where n is the total number of oscillation readings $\hat{y}_{\Delta t}(t)$, obtained during the shift by argument Δt.

Each oscillation vector is processed by function (2). As a result of the calculations, we obtain a vector of shear function values corresponding to a series of oscillations of the initial data when shifted by the argument Δt.

To obtain almost period values τ, the result of the shift function is examined for the presence of pronounced minima. The closer the minimum is to zero, the more significant and closer to the pure period the identified almost period value turns out to be.

The result of processing all sets of vibration vectors obtained by excluding the trend using transformation type (1) with the shift function (2) will be a matrix of shift function vectors. For sequential calculation and accounting for the dependence of the shift function on the value of Δt, a generalized shift function is determined. An example of its implementation, taking into account the geometric exclusion of the trend, is presented by the following formula[2]:

$$a(\tau,\Delta t)=\frac{1}{n-\tau-2\Delta t}\times \times\sum_{t=1}^{n-\tau-2\Delta t}\left|\ln\left(\frac{y_{t-\Delta t+\tau}y_{t+\Delta t-\tau}}{y_{t+\tau}^2}\right)-\ln\left(\frac{y_{t-\Delta t}y_{t+\Delta t}}{y_t^2}\right)\right|. \qquad (3)$$

[2] Kuzmin V.I., Gadzaov A.F. *Methods for building models based on empirical data*: tutorial. Moscow: Moscow State Institute of Radio Engineering, Electronics and Automation (Technical University), 2012. 94 p. (in Russ.).

The applicability of these formulas in almost periodic analysis has been discussed in the literature [21]. However, the approach of sequential iterative calculation of discrete series values with an ordered argument is difficult to implement for large data volumes, including image processing [22].

In order to process and analyze large discrete series and matrices with ordered arguments, the authors implemented a modification of the mathematical apparatus of almost periodic analysis.

The first proposed modification comprised an algorithm for excluding trends from the data. By calculating the entire vector of fluctuations for a fixed shift value Δt, it became possible to perform trend exclusion operations:

$$\vec{P}_{\Delta t}=\ln\left(\frac{\vec{y}_{t-\Delta t}\cdot\vec{y}_{t+\Delta t}}{\vec{y}_t^2}\right), \qquad (4)$$

where $\vec{P}_{\Delta t}$ is the vector of oscillation values obtained by excluding the trend based on the theory of proportions, with dimension $N-2\Delta t$; $\vec{y}_t^2$ is the vector of the square of the values y_t; $\vec{y}_{t-\Delta t}$ is the vector of the values $y_{t-\Delta t}$; $\vec{y}_{t+\Delta t}$ is the vector of the values $y_{t+\Delta t}$.

Then, the calculation of the shear function (2) for a fixed value of Δt can also be represented in vector form (5).

$$\vec{a}(\tau)_{\Delta t}=\frac{1}{N-\tau-2\Delta t}\left|\vec{P}_{\Delta t+\tau}-\vec{P}_{\Delta t}\right|, \qquad (5)$$

where $\vec{a}(\tau)_{\Delta t}$ is the shift function vector for the vibration vector with a shift in the argument Δt; $\vec{P}_{\Delta t+\tau}$ is the excluded trend vector at the value Δt, shifted by τ; $\vec{P}_{\Delta t}$ is the excluded trend vector at the value Δt.

In (5), the modulus operation is overloaded, i.e., the result of the modulus of the difference between vectors $\vec{P}_{\Delta t+\tau}$ and $\vec{P}_{\Delta t}$ is a vector of absolute values.

As a result of such transformations, the set of vectors $\vec{a}(\tau)_{\Delta t}$ when calculating all shift values by the argument Δt becomes the result of the generalized shift function (3). The presented algorithms were implemented as a program for determining almost periods in empirical data with an ordered argument, capable of working with large volumes of data using parallel computing [23].

For the task of monitoring and forecasting the dynamics of the development of emergency situations caused by tropical cyclones, methods developed based on the almost periodic analysis of satellite images have been used to analyze tropical cyclone frames to form predictive estimates of the dynamics of the development of the structure of tropical cyclones.

Thus, for example, the method of processing and analyzing satellite images of tropical cyclones to identify almost periodic characteristics includes the following stages. At the first stage, the video sequence under study is cropped if the original data is presented in this format. The next step consists in processing and conversion of the frame to black and white format. The resulting images are a matrix of pixels that take values from 0 to 255. The size of the converted image is 500 × 500 pixels.

The next step involves determining the center of the tropical cyclone in the image and further converting the frame into polar coordinates. This transformation is chosen as a first approximation of the centric structure of tropical cyclones to enable the application of the almost periodic analysis to the obtained values of radius vector modules at fixed polar angles to identify the critical radii of cyclone structure zones.

Subsequent sequential processing of value vectors at fixed polar angles yields a set of matrices of generalized shear function results for each image slice. The almost period values of each image slice in polar coordinates obtained by analyzing the obtained minima of each generalized shear function are compared and the coinciding values are as characteristic almost periods of the entire structure of the studied tropical cyclone.

The method for forecasting the dynamics of tropical cyclones based on almost periodic analysis of satellite images enables for a predictive assessment of the dynamics of tropical cyclone structure based on identified almost periods and classified hazard zones in the early stages of tropical cyclone development.

On the basis of the almost periods identified as a result of the analysis, the original image is marked with circles having radii that are multiples of the identified almost periods. The central zone of the tropical cyclone frame, which usually occupies the areas of the first and second zonal circles, is classified as a particularly dangerous zone. Depending on the value of the almost period on which they are based, the zones of the next two or three circles occupy most of the frame of the tropical cyclone structure are classified as dangerous zones. The remaining zones in the frame of the tropical cyclone structure are zones of increased observation.

We will illustrate the described processing and analysis methods with the results of forecasts for the development of a tropical cyclone structure using the example of Hurricane Milton, which occurred from October 5 to 10, 2024. The data used for analysis consisted of photographs and video footage of the tropical cyclone taken from an open Internet source: the official website of the United States National Oceanic and Atmospheric Administration.[3]

[3] National Oceanic and Atmospheric Administration. U.S. Department of Commerce. https://www.noaa.gov/. Accessed February 08, 2025.

RESULTS AND DISCUSSION

Figure 1 shows a frame of a tropical cyclone in the infrared range converted to black and white format in Cartesian coordinates with the center of the cyclone marked, relative to which the cyclone structure is projected into polar coordinates (Fig. 2).

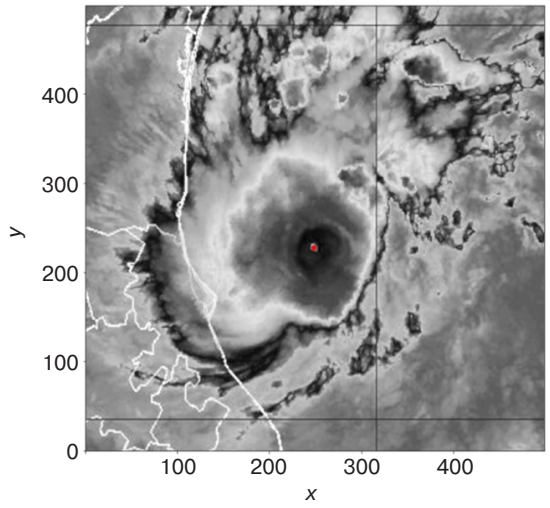

Fig. 1. Snapshot of the early development of tropical cyclone Milton at 15:00 UTC[4] on October 5, 2024, with the cyclone center marked at a size of 500 × 500 pixels

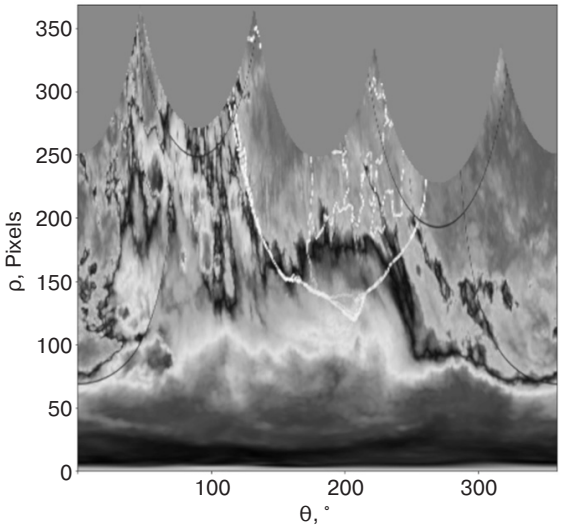

Fig. 2. Snapshot converted to polar coordinates showing the beginning of the development of tropical cyclone Milton, with a resolution of 360 × 360 pixels, where ρ are the values of the radius vectors, and θ are the values of the polar angles

Vertical sections of the obtained image (Fig. 2) at polar angles were processed using functions (4) and (5), resulting in a set of generalized shear function values for radius vector modules. Figure 3 shows an example of a slice of the generalized shear function with values

[4] Coordinated Universal Time.

similar to almost periods for a transformed cyclone frame at an angle of 50°.

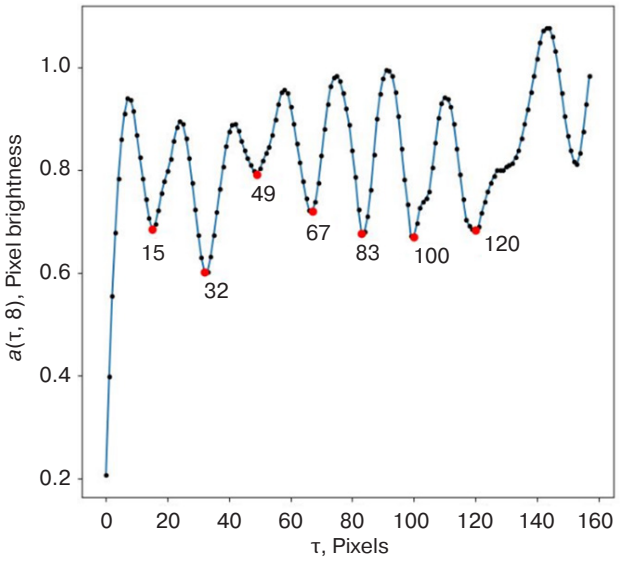

Fig. 3. Example of a generalized shear function at $\Delta t = 8$ for a vector of values at a fixed angle of 50°

The obtained results of almost periodic radius vectors (Fig. 3) are displayed on the original data. The results are presented as the snapshots of a video sequence in the form of circles with radii that are multiples of the detected almost period. The centers of the multiple circles are located in the detected center of the tropical cyclone structure (Fig. 1) with the detected almost periodic values serving as the reference radius of the first circle from the center.

Figure 4 depicts an example of determining centric zones that are multiples of the detected almost period of 83 pixels. The application of this marking will make it possible to determine the characteristic almost periodic components of the structure of the tropical cyclone under study, which will enable the application of a method for forecasting the dynamics of tropical cyclones based on almost periodic analysis of satellite images. The shading of the highlighted areas in Figure 4 should be noted. Diagonal shading indicates particularly dangerous areas affected by the tropical cyclone, while dotted shading indicates dangerous areas affected by the tropical cyclone, and grid shading indicates areas of increased observation.

As a result of studies [24–26], it was established that the almost periodic values of the structure of tropical cyclones obtained in images of the early stages of their development are manifested in the later stages of hurricane development with an error of no more than 12%, which is acceptable in the tasks of forecasting dynamic systems of technical analysis [27].

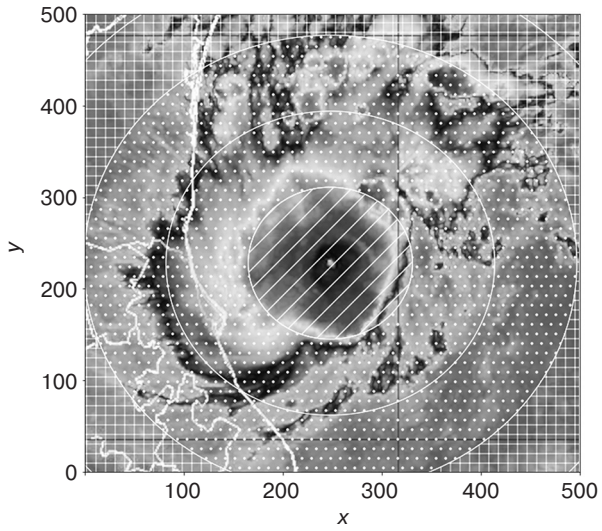

Fig. 4. Snapshot of the early development of tropical cyclone Milton at 15:00 UTC on October 5, 2024, with marked danger zones

To verify the forecast estimates based on the identified almost period of 83 pixels, a frame of tropical cyclone Milton was taken at the moment it reached its peak dynamic state at 21:35 on October 8, 2024, and zones multiple of the almost period of 83 pixels were marked (Fig. 5). It is important to note that the obtained results describe the structure of the tropical cyclone with a sufficient level of accuracy.

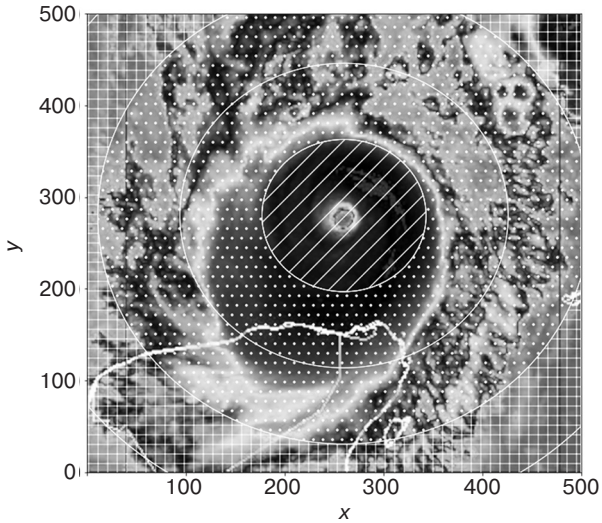

Fig. 5. Snapshot of tropical cyclone Milton at its peak on October 8, 2024, at 21:35 UTC, with danger zones marked

To obtain numerical estimates, a method is applied for processing and analyzing satellite images of tropical cyclones to identify almost periodic characteristics for the data (Fig. 5). The results of the generalized shift function cross-sections yield almost periods close to the values obtained at an early stage (Fig. 6).

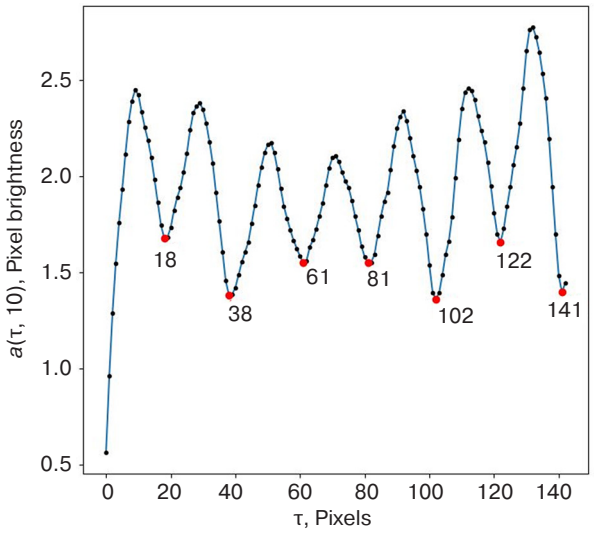

Fig. 6. Generalized shift function at Δt = 10 for a vector of values at a fixed angle of 45° for the image in Fig. 5

The accuracy of the forecast values obtained for almost periods can be estimated using the formula:

$$\sigma = \frac{\left|\tau_{\text{forecast}} - \tau_{\text{actual}}\right|}{\tau_{\text{actual}}}, \quad (6)$$

Where τ_{forecast} is the value of the forecast almost period, τ_{actual} is the value of the calculated actual almost period.

Thus, the forecast estimates with the revealed actual values of almost periods for the tropical cyclone structure in Fig. 6 have an error not exceeding 5%. This confirms the previously obtained results on the estimates of the forecasting dynamics of the tropical cyclone structure based on almost periodic analysis. The obtained results of the errors of the obtained forecast values are comparable with complex models that take into account the relationships of the physical quantities of cyclones [28].

CONCLUSIONS

The article presents a modified method of almost periodic data analysis with an ordered argument to analyze both one-dimensional data of large dimensions and data arrays on the example of tropical cyclone frames.

The method for processing and analyzing the satellite images of tropical cyclones for identifying the almost periodic characteristics was used to establish the characteristic almost periods of the tropical cyclone structure at the initial stage of formation on the example of cyclone Milton. Unlike existing approaches used in constructing forecasts, in which physical parameters of tropical cyclones are used, the proposed approach provides a simultaneous opportunity to monitor and forecast the dynamics of the development of the structure of tropical cyclones based on satellite images using the identification of the almost period, a parameter that is independent of physical quantities. Using one of the characteristic almost periods as an example, the marking of dangerous zones of the tropical cyclone structure was implemented based on circles with radii multiples of the identified almost period of 83 pixels.

The developed methodology based on the modified almost periodic analysis method was tested on the example of forecasting the dynamics of tropical cyclones development. The accuracy of the forecast estimates obtained during the study was about 95%.

The developed approach was used to identify characteristic structural changes in tropical cyclone images and predict the dynamics of a tropical cyclone with sufficient accuracy using Hurricane Milton as an example. The obtained results are of practical importance for risk assessment and the development of emergency management strategies caused by tropical cyclones.

Authors' contributions

A.A. Paramonov—processing the initial data, calculating parameters, and analysis of results.

A.V. Kalach—problem formulation, analysis of results.

T.E. Saratova—designing the research stages, analysis of results.

REFERENCES

1. Donatelli R.E., Park J.A., Matthews S.M., Lee S.D. Time series analysis. *Am. J. Orthod. Dentofacial Orthop*. 2022;161(4): 605–608. https://doi.org/10.1016/j.ajodo.2021.07.013
2. Seibert J., Gross Y., Schrott C. A systematic review of packages for time series analysis. *Eng. Proc*. 2021;5(1):22. https://doi.org/10.3390/engproc2021005022
3. Choi K., Yi J., Park K., Yoon S. Deep learning for anomaly detection in time series data: A review, analysis, and guidelines. *IEEE Access*. 2021;9:120043–120065. https://doi.org/10.1109/ACCESS.2021.3107975
4. Kumar R., Kumar P., Kumar Y. Multi-step time series analysis and forecasting strategy using ARIMA and evolutionary algorithms. *Int. J. Inf. Technol*. 2022;14(1):359–373. https://doi.org/10.1007/s41870-021-00741-8
5. Dubey A.K., Kumar A., Garcia-Diaz V., Sharma A.K., Kanhaiya K. Study and analysis SARIMA and LSTM in forecasting time series data. *Sustainable Energy Technologies and Assessments*. 2021;47:101474. https://doi.org/10.1016/j.seta.2021.101474
6. Pashshoev B., Petrusevich D.A. Neural network analysis in time series forecasting. *Russ. Technol. J*. 2024;12(4):106–116. https://doi.org/10.32362/2500-316X-2024-12-4-106-116
7. Mokhnatkina U.S., Parfenov D.V., Petrusevich D.A. Analysis of approaches to identification of trend in the structure of the time series. *Russ. Technol. J*. 2024;12(3):93–103. https://doi.org/10.32362/2500-316X-2024-12-3-93-103
8. Perova J.P., Lesko S.A., Ivanov A.A. Analyzing and forecasting the dynamics of Internet resource user sentiments based on the Fokker–Planck equation. *Russ. Technol. J*. 2024;12(3):78–92. https://doi.org/10.32362/2500-316X-2024-12-3-78-92
9. Gramovich I.V., Musatov D.Yu., Petrusevich D.A. Implementation of bagging in time series forecasting. *Russ. Technol. J*. 2024;12(1):101–110. https://doi.org/10.32362/2500-316X-2024-12-1-101-110
10. Kracalik I., Mowla S., Katz L., Cumming M., Sapiano M.R., Basavaraju S.V. Impact of the early coronavirus disease 2019 pandemic on blood utilization in the United States: A time series analysis of data submitted to the National Healthcare Safety Network Hemovigilance Module. *Transfusion*. 2021;61(Suppl. 2):S36–S43. https://doi.org/10.1111/trf.16451
11. Kumar R., Jain A., Tripathi A.K., Tyagi S. COVID-19 outbreak: An epidemic analysis using time series prediction model. In: *11th International Conference on Cloud Computing, Data Science & Engineering* (*Confluence*). 2021. IEEE. P. 1090–1094. https://doi.org/10.1109/Confluence51648.2021.9377075
12. Balli S. Data analysis of COVID-19 pandemic and short-term cumulative case forecasting using machine learning time series methods. *Chaos Solitons Fractals*. 2021;142:110512. https://doi.org/10.1016/j.chaos.2020.110512
13. Chen X., Wang X., Zhang K., Fung K.M., Thai T.C., Moore K., Mannel R.S., Liu H., Zheng B., Qiu Y. Recent advances and clinical applications of deep learning in medical image analysis. *Med. Image Anal*. 2022;79:102444. https://doi.org/10.1016/j.media.2022.102444
14. Suganyadevi S., Sithalakshmi V., Balasami K. A review on deep learning in medical image analysis. *Int. J. Multimed. Info. Retr*. 2022;11(1):19–38. https://doi.org/10.1007/s13735-021-00218-1
15. Van der Velden B.H., Kuijf H.J., Gilhuis K.G., Virgeever M.A. Explainable artificial intelligence (XAI) in deep learning-based medical image analysis. *Med. Image Anal*. 2022;79:102470. https://doi.org/10.1016/j.media.2022.102470
16. Meyer-Hein L., Reinke A., Godau P., et al. Metrics reloaded: Pitfalls and recommendations for image analysis validation. *arXiv*. 2022 Jul 7; arXiv:2206.01653. https://doi.org/10.48550/arXiv.2206.01653
17. Fu Y., Zhu Z., Liu L., Zhan W., He T., Shen H., Zhao J., Liu Y., Zhang H., Liu Z., Xue Y. Remote sensing time series analysis: A review of data and applications. *J. Remote Sens.* 2024;4:0285. https://doi.org/10.34133/remotesensing.0285
18. Richards J.A. *Remote Sensing Digital Image Analysis.* Berlin/Heidelberg, Germany: Springer; 2022. 567 p. https://doi.org/10.1007/978-3-030-82327-6
19. Krynetskiy B.A. Analysis of models of periodic structures of spatiotemporal processes. In: *Actual Problems of Applied Mathematics, Informatics, and Mechanics:* Proceedings of the International Scientific Conference. Voronezh; 2024. P. 497–501 (in Russ.). https://elibrary.ru/vbsjnl
20. Kuzmin V.I., Gadzaov A.F. Mathematical methods of analysis of periodic components of nonlinear processes and predict the dynamics of the limited growth based on them. *Vestnik MGTU MIREA = Herald of MSTU MIREA* (*Russ. Technol. J.*). 2015;4-2(9):94–104 (in Russ.). https://elibrary.ru/vhiyoz
21. Kuzmin V.I., Samokhin A.B. Almost periodic functions with trend. *Vestnik MGTU MIREA = Herald of MSTU MIREA* (*Russ. Technol. J.*). 2015;4-2(9):105–110 (in Russ.). https://elibrary.ru/vhiypj
22. Paramonov A.A., Krynetskiy B.A. Asymptotic analysis of an algorithm for searching for almost-periods in data with an ordered argument. *Zashchita informatsii. Insait.* 2023;4(112):53–57 (in Russ.).
23. Kalach A.V., Paramonov A.A., Tolstova I.S., Danilova V.A. *Program for Almost-Periodic Data Processing with Parallel Computing Option*: Computer Program RU2024688438 RF. Publ. 13.02.2025 (in Russ.).
24. Paramonov A.A. Identification of almost-periodic characteristics of satellite images of typhoons in the aspect of solving problems of technosphere safety. *Tekhnosfernaya bezopasnost' = Technosphere Safety*. 2024;44(3):71–76 (in Russ.).
25. Paramonov A.A., Kalach A.V. Simulation of emergencies using almost periodic analysis of images of typhoon structure. *Vestnik Yuzhno-Ural'skogo gosudarstvennogo universiteta. Seriya: Matematika. Mekhanika. Fizika = Bulletin of the South Ural State University. Series: Mathematics. Mechanics. Physics.* 2024;16(4):67–74 (in Russ.). http://doi.org/10.14529/10.14529/mmph240408

26. Kalach A.V., Paramonov A.A. On the possibilities of using the method of near-periodic analysis method for image processing. *Modelirovanie sistem i protsessov = Modeling of Systems and Processes*. 2024;17(3):44–52 (in Russ.). http://doi.org/10.12737/2219-0767-2024-42-50
27. Fridzon M.B., Evtushenko O.A. About requirements for exactness of meteo information. *Nauchnyi vestnik Moskovskogo gosudarstvennogo tekhnicheskogo universiteta grazhdanskoi aviatsii* (*Nauchnyi Vestnik MGTU GA*) *= Civil Aviation High Technologies*. 2014;210:142–144 (in Russ.). https://elibrary.ru/tbubqh
28. Wang X., Chen K., Liu L., Han T., Li B., Bai L. Global tropical cyclone intensity forecasting with multi-modal multi-scale causal autoregressive model. In: *ICASSP 2025–2025 IEEE International Conference on Acoustics, Speech and Signal Processing*. IEEE; 2025. P. 1–5. https://doi.org/10.1109/ICASSP49660.2025.10888556

СПИСОК ЛИТЕРАТУРЫ

1. Donatelli R.E., Park J.A., Matthews S.M., Lee S.D. Time series analysis. *Am. J. Orthod. Dentofacial Orthop*. 2022;161(4): 605–608. https://doi.org/10.1016/j.ajodo.2021.07.013
2. Seibert J., Gross Y., Schrott C. A systematic review of packages for time series analysis. *Eng. Proc*. 2021;5(1):22. https://doi.org/10.3390/engproc2021005022
3. Choi K., Yi J., Park K., Yoon S. Deep learning for anomaly detection in time series data: A review, analysis, and guidelines. *IEEE Access*. 2021;9:120043–120065. https://doi.org/10.1109/ACCESS.2021.3107975
4. Kumar R., Kumar P., Kumar Y. Multi-step time series analysis and forecasting strategy using ARIMA and evolutionary algorithms. *Int. J. Inf. Technol*. 2022;14(1):359–373. https://doi.org/10.1007/s41870-021-00741-8
5. Dubey A.K., Kumar A., Garcia-Diaz V., Sharma A.K., Kanhaiya K. Study and analysis SARIMA and LSTM in forecasting time series data. *Sustainable Energy Technologies and Assessments*. 2021;47:101474. https://doi.org/10.1016/j.seta.2021.101474
6. Пашшоев Б., Петрусевич Д.А. Анализ нейросетевых моделей для прогнозирования временных рядов. *Russ. Technol. J*. 2024;12(4):106–116. https://doi.org/10.32362/2500-316X-2024-12-4-106-116
7. Мохнаткина У.С., Парфенов Д.В., Петрусевич Д.А. Анализ подходов к определению тренда в структуре временных рядов. *Russ. Technol. J*. 2024;12(3):93–103. https://doi.org/10.32362/2500-316X-2024-12-3-93-103
8. Перова Ю.П., Леско С.А., Иванов А.А. Анализ и прогнозирование динамики настроений пользователей интернет-ресурсов на основе уравнения Фоккера – Планка. *Russ. Technol. J*. 2024;12(3):78–92. https://doi.org/10.32362/2500-316X-2024-12-3-78-92
9. Грамович Ю.В., Мусатов Д.Ю., Петрусевич Д.А. Применение бэггинга в прогнозировании временных рядов. *Russ. Technol. J*. 2024;12(1):101–110. https://doi.org/10.32362/2500-316X-2024-12-1-101-110
10. Kracalik I., Mowla S., Katz L., Cumming M., Sapiano M.R., Basavaraju S.V. Impact of the early coronavirus disease 2019 pandemic on blood utilization in the United States: A time series analysis of data submitted to the National Healthcare Safety Network Hemovigilance Module. *Transfusion*. 2021;61(Suppl. 2):S36–S43. https://doi.org/10.1111/trf.16451
11. Kumar R., Jain A., Tripathi A.K., Tyagi S. COVID-19 outbreak: An epidemic analysis using time series prediction model. In: *11th International Conference on Cloud Computing, Data Science & Engineering* (*Confluence*). 2021. IEEE. P. 1090–1094. https://doi.org/10.1109/Confluence51648.2021.9377075
12. Balli S. Data analysis of COVID-19 pandemic and short-term cumulative case forecasting using machine learning time series methods. *Chaos Solitons Fractals*. 2021;142:110512. https://doi.org/10.1016/j.chaos.2020.110512
13. Chen X., Wang X., Zhang K., Fung K.M., Thai T.C., Moore K., Mannel R.S., Liu H., Zheng B., Qiu Y. Recent advances and clinical applications of deep learning in medical image analysis. *Med. Image Anal*. 2022;79:102444. https://doi.org/10.1016/j.media.2022.102444
14. Suganyadevi S., Sithalakshmi V., Balasami K. A review on deep learning in medical image analysis. *Int. J. Multimed. Info. Retr*. 2022;11(1):19–38. https://doi.org/10.1007/s13735-021-00218-1
15. Van der Velden B.H., Kuijf H.J., Gilhuis K.G., Virgeever M.A. Explainable artificial intelligence (XAI) in deep learning-based medical image analysis. *Med. Image Anal*. 2022;79:102470. https://doi.org/10.1016/j.media.2022.102470
16. Meyer-Hein L., Reinke A., Godau P., et al. Metrics reloaded: Pitfalls and recommendations for image analysis validation. *arXiv*. 2022 Jul 7; arXiv:2206.01653. https://doi.org/10.48550/arXiv.2206.01653
17. Fu Y., Zhu Z., Liu L., Zhan W., He T., Shen H., Zhao J., Liu Y., Zhang H., Liu Z., Xue Y. Remote sensing time series analysis: A review of data and applications. *J. Remote Sens.* 2024;4:0285. https://doi.org/10.34133/remotesensing.0285
18. Richards J.A. *Remote Sensing Digital Image Analysis.* Berlin/Heidelberg, Germany: Springer; 2022. 567 p. https://doi.org/10.1007/978-3-030-82327-6
19. Крынецкий Б.А. Анализ моделей периодических структур пространственно-временных процессов. В сб.: *Актуальные проблемы прикладной математики, информатики и механики:* Труды Международной научной конференции. Воронеж; 2024. С. 497–501. https://elibrary.ru/vbsjnl
20. Кузьмин В.И., Гадзаов А.Ф. Математические методы анализа периодических компонент нелинейных процессов и прогнозирование на их основе динамики ограниченного роста. *Вестник МГТУ МИРЭА*. 2015;4-2(9):94–104. https://elibrary.ru/vhiyoz
21. Кузьмин В.И., Самохин А.Б. Почти периодические функции с трендом. *Вестник МГТУ МИРЭА.* 2015;4-2(9): 105–110. https://elibrary.ru/vhiypj

22. Парамонов А.А., Крынецкий Б.А. Асимптотический анализ алгоритма поиска почти-периодов в данных с упорядоченным аргументом. *Защита информации. Инсайт*. 2023;4(112):53–57.
23. Калач А.В., Парамонов А.А., Толстова И.С., Данилова В.А. *Программа почти периодической обработки данных с возможностью выбора параллельных вычислений*: Свидетельство о государственной регистрации программы для ЭВМ № 2024688438 РФ. Заявка № 2024686766; Заявл. 08.11.2024; опубл. 27.11.2024. Бюл. № 12.
24. Парамонов А.А. Выявление почти-периодических характеристик спутниковых изображений тайфунов в аспекте решения проблем техносферной безопасности. *Техносферная безопасность*. 2024;44(3):71–76.
25. Парамонов А.А., Калач А.В. Моделирование чрезвычайных ситуаций с использованием почти-периодического анализа изображений структуры тайфунов. *Вестник Южно-Уральского государственного университета. Серия: Математика. Механика. Физика*. 2024;16(4):67–74. https://doi.org/10.14529/mmph240408
26. Калач А.В., Парамонов А.А. О возможностях применения метода почти-периодического анализа для обработки изображений. *Моделирование систем и процессов*. 2024;17(3):44–52. https://doi.org/10.12737/2219-0767-2024-42-50
27. Фридзон М.Б., Евтушенко О.А. О требованиях к точности метеорологической информации. *Научный вестник Московского государственного технического университета гражданской авиации* (*Научный Вестник МГТУ ГА*). 2014;210:142–144. https://elibrary.ru/tbubqh
28. Wang X., Chen K., Liu L., Han T., Li B., Bai L. Global tropical cyclone intensity forecasting with multi-modal multi-scale causal autoregressive model. In: *ICASSP 2025-2025 IEEE International Conference on Acoustics, Speech and Signal Processing*. IEEE; 2025. P. 1–5. https://doi.org/10.1109/ICASSP49660.2025.10888556

About the Authors

Alexander A. Paramonov, Postgraduate Student, Senior Lecturer, Department of Applied Mathematics, Institute of Information Technologies, MIREA – Russian Technological University (78, Vernadskogo pr., Moscow, 119454 Russia). E-mail: paramonov_a_a99@mail.ru. RSCI SPIN-code 7885-7510, https://orcid.org/0000-0002-8504-2108

Andrew V. Kalach, Dr. Sci. (Chem.), Professor, Department of Applied Mathematics, Institute of Information Technologies, MIREA – Russian Technological University (78, Vernadskogo pr., Moscow, 119454 Russia). E-mail: a_kalach@mail.ru. Scopus Author ID 57201667604, RSCI SPIN-code 2584-7456

Tatiana E. Saratova, Dr. Sci. (Eng.), Head of the Department of Applied Mathematics, Institute of Information Technologies, MIREA – Russian Technological University (78, Vernadskogo pr., Moscow, 119454 Russia). E-mail: smolenceva@mirea.ru. Scopus Author ID 57201668525, RSCI SPIN-code 2383-6811, https://orcid.org/0000-0003-4810-8734

Об авторах

Парамонов Александр Александрович, аспирант, старший преподаватель, кафедра прикладной математики, Институт информационных технологий, ФГБОУ ВО «МИРЭА – Российский технологический университет» (119454, Россия, Москва, пр-т Вернадского, д. 78). E-mail: paramonov_a_a99@mail.ru. SPIN-код РИНЦ 7885-7510, https://orcid.org/0000-0002-8504-2108

Калач Андрей Владимирович, д.х.н., профессор, кафедра прикладной математики, Институт информационных технологий, ФГБОУ ВО «МИРЭА – Российский технологический университет» (119454, Россия, Москва, пр-т Вернадского, д. 78). E-mail: a_kalach@mail.ru. Scopus Author ID 57201667604, SPIN-код РИНЦ 2584-7456

Смоленцева Татьяна Евгеньевна, д.т.н., заведующий кафедрой прикладной математики, Институт информационных технологий, ФГБОУ ВО «МИРЭА – Российский технологический университет» (119454, Россия, Москва, пр-т Вернадского, д. 78). E-mail: smolenceva@mirea.ru. Scopus Author ID 57201668525, SPIN-код РИНЦ 2383-6811, https://orcid.org/0000-0003-4810-8734

Translated from Russian into English by Lyudmila O. Bychkova
Edited for English language and spelling by Thomas A. Beavitt

Mathematical modeling

Математическое моделирование

UDC 51-74:621.791.92
https://doi.org/10.32362/2500-316X-2025-13-6-127-138
EDN ORZKBC

RESEARCH ARTICLE

Unsteady heat transfer problem during single-pass spraying on a half-space

Mikhail E. Soloviev [1, @], Sergey S. Kokarev [2], Sergey L. Baldaev [3], Lev Kh. Baldaev [3], Denis V. Malyshev [1]

[1] *Yaroslavl State Technical University, Yaroslavl, 150023 Russia*
[2] *Regional Scientific and Educational Center "Logos," Yaroslavl, 150000 Russia*
[3] *Technological Systems for Protective Coatings, Moscow, Shcherbinka, 108851 Russia*
[@] *Corresponding author, e-mail: me_s@mail.ru*

• **Submitted:** 26.03.2025 • **Revised:** 18.05.2025 • **Accepted:** 06.10.2025

Abstract

Objectives. Thermal spraying and powder laser cladding are promising technologies widely used in various industries, including aerospace, energy, and mechanical engineering. The efficiency of these technologies depends on the management of thermal processes occurring during coating application, which directly affect the quality and durability of the resulting materials and products. This article considers a nonstationary problem of heat transfer during single-pass spraying on a half-space. The research aim was to simulate the temperature distribution in a material half-space upon the action of a moving heat source on its boundary.

Methods. A theoretical study of the temperature distribution on the surface and in the bulk of the processed material during movement of the spray head was carried out by solving the equation of nonstationary thermal conductivity in Cartesian coordinates. This equation employs a special type of the heat source power density function in the form of a thermal strip, simulating the process of heat transfer from the spray path to the material half-space of the part base.

Results. The obtained solution representing the evolution of temperature in time at different points of the medium shows that at a certain point of time after the passage of the heating pulse, the temperature inside the medium reaches its maximum value rapidly followed by its relatively slow relaxation to the equilibrium temperature of the environment. Penetrating deeper into the bulk of the medium, the thermal pulse is spreading out while decreasing its amplitude and increasing its width, accompanied by a monotonic increase in the time to reach the maximum. The transverse temperature distribution has the form of symmetrical peaks, less pronounced in depth.

Conclusions. The obtained solution can be used when describing the general temperature field at some distance from the spray head area, where specific heating details are lacking. In particular, the work shows that significant temperature gradients arise in the vicinity of the primary spray area, which will cause noticeable nonstationary temperature stresses.

Keywords: gas-thermal spraying, powder laser cladding, nonstationary heat conduction equation, temperature field, temperature wave, Newton–Richmann boundary conditions, Green's function for the heat equation

For citation: Soloviev M.E., Kokarev S.S., Baldaev S.L., Baldaev L.Kh., Malyshev D.V. Unsteady heat transfer problem during single-pass spraying on a half-space. *Russian Technological Journal.* 2025;13(6):127–138. https://doi.org/10.32362/2500-316X-2025-13-6-127-138, https://www.elibrary.ru/ORZKBC

Financial disclosure: The authors have no financial or proprietary interest in any material or method mentioned.

The authors declare no conflicts of interest.

НАУЧНАЯ СТАТЬЯ

Нестационарная задача теплопроводности в технологии газотермического напыления защитных покрытий

М.Е. Соловьев [1, @], С.С. Кокарев [2], С.Л. Балдаев [3], Л.Х. Балдаев [3], Д.В. Малышев [1]

[1] *Ярославский государственный технический университет, Ярославль, 150023 Россия*
[2] *Региональный научно-образовательный центр «Логос», Ярославль, 150000 Россия*
[3] *ООО «Технологические системы защитных покрытий», Москва, Щербинка, 108851 Россия*
[@] *Автор для переписки, e-mail: me_s@mail.ru*

• **Поступила:** 26.03.2025 • **Доработана:** 18.05.2025 • **Принята к опубликованию:** 06.10.2025

Резюме

Цели. Газотермическое напыление и порошковая лазерная наплавка – перспективные технологии, широко применяемые в различных отраслях промышленности, включая аэрокосмическую, энергетическую и машиностроительную отрасли. Одним из ключевых аспектов данных технологий является управление тепловыми процессами, возникающими при нанесении покрытий, т.к. они напрямую влияют на качество и долговечность получаемых материалов и изделий. В данной статье рассматривается нестационарная задача теплопереноса при однопроходном напылении на полупространство. Целью работы является моделирование распределения температуры в материальном полупространстве, на границе которого действует движущийся источник тепла.

Методы. Теоретическое исследование распределения температуры на поверхности и в толще обрабатываемого материала в процессе движения головки распылителя осуществлялось путем решения уравнения нестационарной теплопроводности в декартовых координатах. Особенностью уравнения является специальный вид функции плотности мощности источника тепла в виде тепловой полосы, моделирующей процесс теплопередачи от дорожки напыления в материальное полупространство основы детали.

Результаты. В результате исследования полученного решения, представляющего эволюцию во времени температуры в различных точках среды, установлено, что через некоторое время после прохождения импульса нагревания температура внутри среды довольно быстро достигает максимального значения, а затем она относительно медленно релаксирует к равновесной температуре окружающей среды. По мере углубления в толщу среды тепловой импульс расплывается, уменьшается его амплитуда и увеличивается ширина, а время достижения максимума монотонно увеличивается. Поперечное распределение температуры имеет вид симметричных пиков, менее выраженных в глубине.

Выводы. Полученное решение может быть полезным при описании общего температурного поля на некотором удалении от области действия головки распылителя, где конкретные детали нагрева не проявляются. В частности, в работе показано, что в окрестности действия первичной области напыления возникают значительные градиенты температур, которые вызывают заметные нестационарные температурные напряжения.

Ключевые слова: газотермическое напыление, порошковая лазерная наплавка, нестационарное уравнение теплопроводности, температурное поле, температурная волна, граничные условия Ньютона – Рихмана, функция Грина для уравнения теплопроводности

Для цитирования: Соловьев М.Е., Кокарев С.С., Балдаев С.Л., Балдаев Л.Х., Малышев Д.В. Нестационарная задача теплопроводности в технологии газотермического напыления защитных покрытий. *Russian Technological Journal*. 2025;13(6):127–138. https://doi.org/10.32362/2500-316X-2025-13-6-127-138, https://www.elibrary.ru/ORZKBC

Прозрачность финансовой деятельности: Авторы не имеют финансовой заинтересованности в представленных материалах или методах.

Авторы заявляют об отсутствии конфликта интересов.

INTRODUCTION

In modern mechanical engineering, powder coating technologies using gas-thermal spraying [1, 2] and laser cladding [3, 4] are widely used. These methods enable not only the effective restoration of worn parts surfaces, but also the creation of specialized coatings with a unique set of characteristics, including increased heat, wear, and chemical resistance [5, 6]. Laser cladding has also become a fundamental technology in the field of additive manufacturing of metal products, where parts are produced by applying powder material layer by layer [7, 8].

These technologies involve heating powdered materials to temperatures exceeding their melting point, followed by application to the surface of the part using a high-speed gas flow. A distinctive feature of laser cladding is the use of an infrared laser as a source of particle heating. The laser beam is focused on the surface of the part or in its close proximity, which provides for a more accurate control of the temperature of the deposited material and precise positioning of the deposition path. In the case of conventional gas-thermal spraying, the material is heated directly in the spray head. The basic technological operation of these processes is a single pass of the plasma torch along the surface being treated, resulting in the appearance of a single thin molten track on this surface at a speed equal to that of the plasma torch. In this work, we focus on this basic operation due to its determining effect on the quality of the coating.

Optimization of the technologies under consideration with the purpose of enhancing the quality of the coatings and products obtained requires elucidation of those thermophysical processes that occur when molten material interacts with the surface being treated [9–11]. In particular, the temperature distribution across the substrate material during and after the passage of the spray head is of particular interest [12]. The importance of precise heat input control for obtaining the desired coating microstructure was also underscored in [13, 14].

Mathematical modeling methods are widely used to optimize spraying technologies and predict the properties of the coatings being formed [15–17]. Numerical methods, such as the finite element method [13, 18, 19], are used to model the temperature distribution in the spray path. The authors of [20] used the finite volume method to investigate the influence of temperature distribution during laser cladding on the melting process of powdered metal in the cladding path and the influence of the Marangoni effect on the size of the melting zone. This method was also used in [21] for numerical simulation of heat and mass transfer processes in a three-dimensional problem setting when simulating powder laser cladding of stainless steel. It was shown that the temperature distribution in the cladding track is a critical factor determining the shape of its cross-section profile. In addition to the power of the radiation source, the temperature distribution in the deposition track is influenced by the speed of the deposition head relative to the sample surface and the powder flow rate [22, 23].

Along with numerical methods, analytical methods can also be used to describe a moving heat source, predict the cooling rate [13, 24], and estimate the shape of the molten metal pool [25].

When the focus is heat transfer processes during spraying, rather than a detailed distribution of thermal quantities in the track volume and their dynamics over time, simplified models can be applied. In these models, spraying generates a localized source of heat along the plasma jet line of action and localized in time. In further research, such a model can be taken as a zero (main) approximation, and all other details of the process can be taken into account in the form of corrections, in which the parameter of smallness will be the ratio of the track width to the characteristic size of the treated surface.

In this article, we consider the problem of nonstationary temperature distribution in an infinite homogeneous half-space, the boundary of which features a time-growing "heat line." This line is a heat source localized on a geometric ray, the origin of which moves along a flat boundary at a constant speed. In such a formulation, the problem is somewhat non-standard, since its initial conditions are

replaced by an asymptotic condition for the temperature field: as $t \to -\infty$, the temperature field of the half-space tends to a constant value—the ambient temperature.

TASK STATEMENT

Abstracting from the size and shape of the sprayed surface, let us consider this surface as the boundary of an infinite half-space filled with a heat-conducting substance with constant thermal conductivity α and specific volumetric heat capacity c. On this surface, let us consider a continuously growing thermal strip with a velocity $\vec{v}$ consisting of point instantaneous heat sources with a heat energy output $q_0(t)$ as a certain decreasing function of time (Fig. 1).

The axes of the fixed coordinate system are oriented as shown in Fig. 1. In the selected coordinate system, the power density of heat sources of the type under consideration is described by the ratio

$$q(t, x, y, z) = q_0(t, x)\delta(z)\delta(y)\delta(x - vt), \quad (1)$$

wherein δ is the Dirac delta function. The conditional moment $t = 0$ is shown in Fig. 1. The conditional moment $t = 0$ does not correspond to any initial conditions, since the thermal band begins to form at $t \to -\infty$

In the model under consideration, the function $q_0(t, x)$ is defined externally. Thus, it simulates the process of heat transfer from the thermal strip to the material of the half-space and depends on many physical parameters in the spraying process. In this article, we use the simplest model of "stepwise thermal illumination," in which

$$q_0(t, x) = \mathrm{k}(\theta(t - x/v) - \theta(t - x/v - \tau)), \quad (2)$$

wherein k is the constant effective thermal power of illumination; τ is the effective thermal illumination time (the effective values represent a simplified model of heat exchange along a line of heat sources, in which the heat source moves along the line at the speed of light and transfers heat to the material of the half-space with a constant power k during a finite time interval τ at each point along the line of sources); θ(x) is the standard Heaviside step function.

The heat conduction equation for the problem under consideration will take the form

$$\dot{T} - \alpha\Delta T = \\ = p\delta(y)\delta(z)\delta(x - vt)(\theta(t - x/v) - \theta(t - x/v - \tau)), \quad (3)$$

wherein T is the temperature in the region under consideration, α is the thermal conductivity coefficient, $p = \mathrm{k}/c$, and the range of the variables changing is $(x, y) \in \mathbb{R}^2$, $z \in (-\infty, 0)$, $t \in \mathbb{R}$.

Equation (3) must be supplemented with Newton–Richman boundary conditions, specified at the boundary of the half-space in the form

$$\left.\frac{-\partial T}{\partial z}\right|_{z=0} = \beta\left(T\big|_{z=0} - T_0\right), \quad (4)$$

wherein β is the reduced heat transfer coefficient, equal to the ratio of the heat transfer coefficient at the material-air interface to the thermal conductivity of the material; T_0 is the ambient (air) temperature, which coincides with the temperature in the asymptotic initial condition; the minus sign on the left side corresponds to cooling

$$T\big|_{t\to\infty} = T_0 = \mathrm{const}, \quad (5)$$

playing the role of the initial condition in the formulation of the problem under consideration and necessary for its correct formulation.

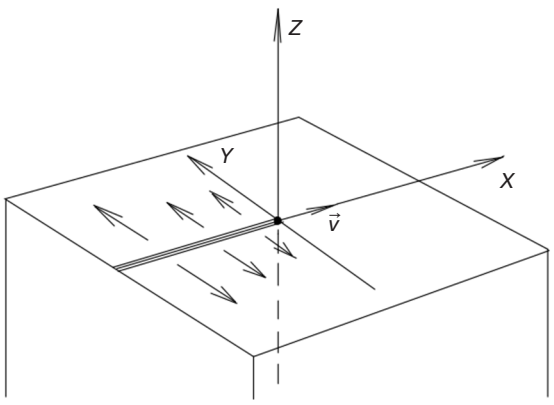

Fig. 1. Thermal strip on the surface of a semi-infinite material half-space

SOLUTION OF A NON-HOMOGENEOUS EQUATION

We will seek a particular solution to the inhomogeneous equation (3) using Green's function G for the heat conductivity operator

$$\left(\frac{\partial}{\partial t'}-\alpha\Delta'\right)G(t-t',\vec{r}-\vec{r}')=\delta(t-t')\delta^3(\vec{r}-\vec{r}'), \tag{6}$$

which, with arbitrary precision, is determined by the formula for solving a homogeneous equation

$$G(t-t',\vec{r}-\vec{r}')=\frac{1}{(2\sqrt{\alpha\pi(t-t')})^3}e^{-|\vec{r}-\vec{r}'|^2/4\alpha(t-t')}\theta(t-t'), \tag{7}$$

wherein $\vec{r}$ corresponds to the current point (x, y, z).

The particular solution $\overline{T}(t,\vec{r})$ of the equation (3) corresponding to (7) takes the form

$$\overline{T}(t,\vec{r})=\int_{-\infty}^{t}dt'\int_{\mathbb{R}^3}d^3\vec{r}'\frac{1}{\left(2\sqrt{\alpha\pi(t-t')}\right)^3}e^{-((x-x')^2+(y-y')^2+(z-z')^2)/4\alpha(t-t')}\times \\ \times p\delta(y')\delta(z')\delta(x'-vt')(\theta(t'-x'/v)-\theta(t'-x'/v-\tau)). \tag{8}$$

Integrating over y',z' leads to the following intermediate formula for the particular solution:

$$\overline{T}(t,\vec{r})=\frac{p}{\left(2\sqrt{\alpha\pi}\right)^{3/2}}\int_{-\infty}^{t}dt'\int_{-\infty}^{+\infty}dx'\frac{e^{-((x-x')^2+y^2+z^2)/4\alpha(t-t')}}{(t-t')^{3/2}}\times \\ \times\delta(x'-vt')(\theta(t'-x'/v)-\theta(t'-x'/v-\tau)). \tag{9}$$

For correct integration over variables (x, t), we will proceed to lagging and leading combinations of the initial variables:

$$r=x'-vt',\ s=x'+vt'\Leftrightarrow t'=\frac{s-r}{2v},\ x'=\frac{s+r}{2}. \tag{10}$$

The volume element will be replaced according to the rule $dt'dx'=ds\,dr/2v$, the integration region (in coordinates x', t' representing a half-plane $t'\le t$) will become a half-plane $s-r-2vt\le 0$.

In the new variables, integral (9) will take the form

$$\overline{T}(t,\vec{r})=\frac{p}{2v\left(2\sqrt{\alpha\pi}\right)^{3/2}}\int_{-\infty}^{+\infty}ds\int_{s-2vt}^{+\infty}dr\frac{e^{-((x-(s+r)/2)^2+y^2+z^2)/4\alpha(t-(s-r)/2v)}}{(t-(s-r)/2v)^{3/2}}\times \\ \times\delta(r)(\theta(-r/v)-\theta(-r/v-\tau)). \tag{11}$$

Integrating over variable r instead of function δ gives 0 if $s-2vt>0$ and 1 if the opposite additional equality holds when substituting $r=0$ into all occurrences of variable r This situation is universally described by the factor $\theta(2vt-s)$, which ultimately leads to the integral

$$\overline{T}(t,\vec{r})= \\ =\frac{p}{2v\left(2\sqrt{\alpha\pi}\right)^{3/2}}\int_{-\infty}^{+\infty}ds\frac{e^{-((x-s/2)^2+y^2+z^2)/4\alpha(t-s/2v)}}{(t-s/2v)^{3/2}}\theta(2vt-s)=\frac{p}{2v\left(2\sqrt{\alpha\pi}\right)^{3/2}}\int_{-\infty}^{2vt}ds\frac{e^{-((x-s/2)^2+y^2+z^2)/4\alpha(t-s/2v)}}{(t-s/2v)^{3/2}}. \tag{12}$$

Let us introduce a new variable $u = t - s/2v$, for which the integral will take the form

$$\overline{T}(t,\vec{r}) = \frac{p}{\left(2\sqrt{\alpha\pi}\right)^{3/2}} \int_0^{+\infty} du \frac{e^{-((x-v(t-u))^2 + y^2 + z^2)/4\alpha u}}{u^{3/2}}. \quad (13)$$

Integral (13) is calculated in elementary functions, and the final result is as follows:

$$\overline{T}(t,\vec{r}) = \frac{p}{4\alpha\pi} \cdot \frac{e^{-\left(\sqrt{(x-vt)^2 + y^2 + z^2} + x - vt\right)v/2\alpha}}{\sqrt{(x-vt)^2 + y^2 + z^2}}. \quad (14)$$

In fact, solution (14) describes an axially symmetric thermal wave whose center moves at a speed v along the x axis. In the accompanying inertial reference frame $x = vt$ formula (14) takes the form of a cylindrical wave

$$\overline{T}'(t,\vec{r}) = \frac{p}{4\alpha\pi} \cdot \frac{e^{-\rho v/2\alpha}}{\rho}, \quad (15)$$

wherein $\rho = \sqrt{y^2 + z^2}$, with an axis coinciding with the line of heat sources.

When $t \to \pm\infty$ solution (13) tends to zero for various reasons. When $t \to -\infty$, the heat has not yet been released. However, when $t \to +\infty$, the infinite heat released along the entire thermal line has time to relax over an infinite volume, which, as a result, returns to a state of zero temperature. At a typical point at a certain distance ρ from the thermal axis, the evolution of temperature over time is shown in Fig. 2. It has the form of a thermal pulse that increases rapidly immediately after the passage of the thermal pulse activation wave on the thermal line (the moment when the laser beam passes the observation point at coordinate $x = 0$) and relatively slowly (according to the law of inverse proportionality) relaxes to a state of equilibrium with zero temperature. The solution obtained does not have any physical meaning yet relevant to the task at hand: this solution must be supplemented with a general solution of the homogeneous equation, with the help of which the boundary conditions (4) can be implemented (4).

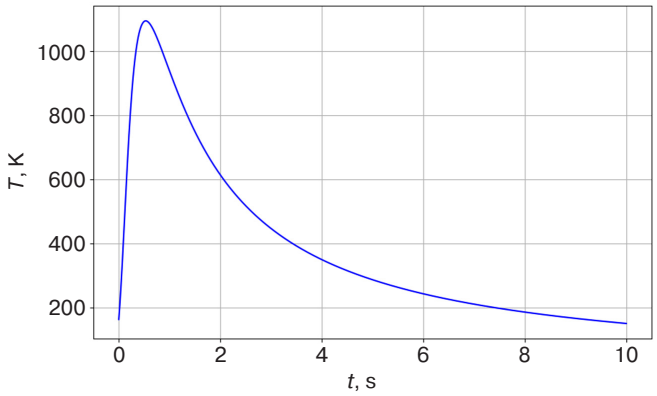

Fig. 2. Dependence $T(t)$ at parameter values: $x = 0$, $y = 1$, $z = 1$ (in mm), $v = 5$ mm/s, $\alpha = 1$ mm^2/s, $p = 1.0 \cdot 10^5$ mm^3·K/s

SOLUTION OF A HOMOGENEOUS EQUATION AND COMPLETE SOLUTION

Due to the linearity of heat conduction equation (3), its general solution can be written as the sum of a particular solution of a non-homogeneous equation and the general solution of a homogeneous equation T_h:

$$T(t,x,y,z) = \overline{T}(t,x,y,z) + T_h(t,x,y,z), \quad (16)$$

wherein $\overline{T}$ is the particular solution (14) already found in the previous section. In this section, we will find a suitable T_h. In essence, it is reduced to implementing the selected boundary condition (4) using T_h. Substituting expression (16) therein, after regrouping the summands, we find

$$\left(\beta T_{\text{h}} + \frac{\partial T_{\text{h}}}{\partial z}\right)\Bigg|_{z=0} = \beta\left(T_0 - \overline{T}\right)\Big|_{z=0}, \tag{17}$$

wherein the right-hand side is the already known function. In addition, it was taken into account that, due to the evenness of $\overline{T}$ by z, the following equality holds: $\left.\frac{\partial T_{\text{h}}}{\partial z}\right|_{z=0} = 0.$

We will seek a common solution T_{h} using the method of separation of variables:

$$T_{\text{h}} = \Theta(t)X(x)Y(y)Z(z). \tag{18}$$

Substituting (18) into equation (3) at $p = 0$ and dividing it by T_{h}, we obtain the heat conduction equation in a separated form:

$$\frac{\Theta'}{\Theta} - \alpha\left(\frac{X''}{X} + \frac{Y''}{Y} + \frac{Z''}{Z}\right) = 0, \tag{19}$$

wherein the stroke denotes differentiation with respect to the argument. The condition for separating variables takes the form of constancy of individual terms in (19); hence, this equation expresses the relationship between the separation constants

$$k_t - \alpha\left(-k_x^2 - k_y^2 + k_z^2\right) = 0, \tag{20}$$

which we will understand as an expression for the wave number k_z:

$$k_z = \pm\sqrt{\frac{k_t}{\alpha} + k_x^2 + k_y^2}. \tag{21}$$

In (20)

$$k_t = \frac{\Theta'}{\Theta},\ \frac{X''}{X} = -k_x^2\ \frac{Y''}{Y} = k_y^2,\ \frac{Z''}{Z} = k_z^2. \tag{22}$$

The general solution T_{h} has the following decomposition (a linear combination of different solutions with constant coefficients):

$$T_{\text{h}} = \sum_{k,\varepsilon} C_{k,\varepsilon} \mathrm{e}^{k_t t + i(k_x x + k_y y) + \varepsilon\sqrt{k_t/\alpha + k_x^2 + k_y^2}\, z}, \tag{23}$$

wherein $k = \{k_t, k_x, k_y\}$, and the parameter $\varepsilon = \pm 1$ distinguishes the roots for k_z в (21).

In order to find the Fourier coefficients $C_{k,\,\varepsilon}$ we substitute expression (23) into boundary condition (17), in which we also transform the right-hand side into a Fourier integral. All Fourier transforms will be greatly simplified when noting that in the right side of (17), the particular solution $\overline{T}$ depends, according to (14), only on the lagging combination $\xi = x - vt$. In order for the same combination to appear in the left side of (17), it is necessary and sufficient to require that $k_t = -ivk_x$. Only in this case will the desired combination $ik_x(x - vt) = ik_\xi\xi$ be formed in the exponent on the left, relative to which the Fourier transform will be calculated. This leads to a correct dependence on the right-hand side. Let us find the Fourier image of the right side of (17). We have a chain of equalities $\left(a + v/2\alpha,\ K = \sqrt{k_y^2 + k_\xi^2}\right)$:

$$\begin{aligned}
&\frac{1}{(2\pi)^2}\int\limits_{\mathbb{R}^2} d\xi\, dy\, \beta\left(T_0 - \frac{p}{4\pi\alpha}\cdot\frac{\mathrm{e}^{-\left(\sqrt{\xi^2+y^2}+\xi\right)v/2\alpha}}{\sqrt{\xi^2+y^2}}\right)\mathrm{e}^{-i\left(k_\xi\xi + k_y y\right)} \overset{\{\xi=\rho\cos\varphi,\ y=\rho\sin\varphi\}}{=} \\
&= \beta T_0\delta(k_\xi)\delta(k_y) - \frac{\beta p}{16\pi^3\alpha}\int\limits_0^{2\pi} d\varphi\int\limits_0^{\infty}\rho d\rho\cdot\frac{\mathrm{e}^{-a(\rho+\rho\cos\varphi)}}{\rho}\mathrm{e}^{-iK\rho\cos(\psi-\varphi)} = \\
&= \beta T_0\delta(k_\xi)\delta(k_y) - \frac{\beta p}{16\pi^3\alpha}\int\limits_0^{2\pi}\frac{d\varphi}{a(1+\cos\varphi) + iK\cos(\psi-\varphi)} \equiv F(k_y, k_\xi).
\end{aligned} \tag{24}$$

The integral in the latter expression is calculated using the analytical continuation of the real formula

$$\int_0^{2\pi} \frac{d\varphi}{a + b\cos\varphi + c\cos\varphi} = \frac{2\pi}{\sqrt{a^2 - b^2 - c^2}} \tag{25}$$

into a complex domain, which, in our case, gives the equality

$$\int_0^{2\pi} \frac{d\varphi}{a(1+\cos\varphi) + iK\cos(\psi - \varphi)} = \frac{2\pi}{\sqrt{K^2 - 2iak_\xi}} \tag{26}$$

with the choice of the root branch that gives $\sqrt{K^2} = k_y$ when $k_\xi = 0$.

Finally, for the Fourier image of the right side (17), we obtain:

$$F(k_y, k_\xi) = \beta T_0 \delta(k_\xi)\delta(k_y) - \frac{\beta p}{8\pi^2\alpha\sqrt{K^2 - 2aik_\xi}}, \tag{27}$$

wherein $K = \sqrt{k_y^2 + k_\xi^2}$, $a = v/2\alpha$. Now, substituting (23) and (28) into (17), we find the Fourier coefficients for the homogeneous solution, as follows:

$$C_k = \frac{F(k_y, k_\xi)}{\beta + \sqrt{K^2 - 2iak_\xi}}. \tag{28}$$

A homogeneous solution with correct boundary conditions can be written as the following integral (δ-functions in F are explicitly integrated):

$$T_h(\xi, y, z) = T_0 - \frac{\beta p}{8\pi^2\alpha}\int_{-\infty}^{+\infty}\int_{-\infty}^{+\infty} dk_y dk_\xi \frac{e^{i(k_\xi\xi + k_y y) + \sqrt{K^2 - 2iak_\xi}\, z}}{\sqrt{K^2 - 2iak_\xi}\left(\beta + \sqrt{K^2 - 2iak_\xi}\right)}. \tag{29}$$

As further analysis shows, formula (29) does not enable any transformation that would enable the result to be presented in an analytical form, either partially or completely free of quadratures. Therefore, all further illustrations will be obtained using numerical Fourier transformation for specific values of the model parameters.

First, let us write down the complete solution with the correct boundary conditions using formula (16):

$$\begin{aligned} T(\xi, y, z) = T_0 - \frac{\beta p}{8\pi^2\alpha}\int_{-\infty}^{+\infty}\int_{-\infty}^{+\infty} dk_y dk_\xi \frac{e^{i(k_\xi\xi + k_y y) + \sqrt{K^2 - 2iak_\xi}\, z}}{\sqrt{K^2 - 2iak_\xi}\left(\beta + \sqrt{K^2 - 2iak_\xi}\right)} + \\ + \frac{p}{4\pi\alpha} \cdot \frac{e^{-\left(\sqrt{\xi^2 + y^2 + z^2} + \xi\right)v/2\alpha}}{\sqrt{\xi^2 + y^2 + z^2}}, \end{aligned} \tag{30}$$

wherein $\xi = x - vt$.

Let us assume the following average values for the model parameters (in the SI system):

$$T_0 = 300,\ a = 40,\ \frac{p}{4\pi a} = 10^3,\ \beta = 2\pi \cdot 10^{-2},\ v = 10^{-3}.$$

Next, we note that the parameter β (which has the dimension of a wave number, i.e., the reciprocal of the wavelength) in formula (30) can be considered small. In this case, the solution will differ significantly for the region $k \to 0$, which corresponds to the long-wave modes of the solution describing regions of medium distance from the source. Thus, a simplified form of formula (30) is obtained by neglecting β in the denominator under the integral—this corresponds to the preservation of first-order terms in the expansion of the solution with respect to

parameter β (even in this case, the integrals are not calculated analytically). As a result, switching to the real form of the Fourier transform for convenience of calculation, we find

$$T(\xi,y,z)=300-100\int\limits_{-\infty}^{+\infty}\int\limits_{-\infty}^{+\infty}dk_y dk_\xi\frac{2e^{Q_+ z/\sqrt{2}}}{K^4+6400k_\xi^2}\times$$
$$\times\left(K^2\cos(k_\xi\xi+k_y y-c\,\mathrm{sgn}(k_\xi)Q_- z)-80k_\xi\sin(k_\xi\xi+k_y y-c\,\mathrm{sgn}(k_\xi)Q_- z)\right)+10000\frac{e^{-40\left(\sqrt{\xi^2+y^2+z^2}+\xi\right)}}{\sqrt{\xi^2+y^2+z^2}}, \quad (31)$$

wherein

$$Q_\pm=\sqrt{\sqrt{K^4+6400k_\xi^2}\pm K^2},\ \xi=x-10^{-3}t.$$

Let us move on to illustrations of dependence (31). Figures 3 and 4 show families of one-dimensional graphs obtained from the complete dependence (31). The family of curves in Fig. 3 represents the evolution of temperature over time at points in the medium located at different depths in the thickness of the medium below the origin of the coordinate system. The graphs show that sometime after passing the heating pulse, the temperature inside the medium reaches its maximum value rapidly, and then it slowly relaxes to the ambient temperature. At the same time, along with its penetration deeper into the medium, the thermal pulse is spreading out. As a result, its amplitude decreases and its width increases, and the time it takes to reach its maximum value increases monotonically. Overall, this picture corresponds to all physically reasonable expectations of the model under consideration.

Figure 4 shows the spatial distribution of temperature at time $t = 0$ in the bulk of the substance under the heat line—the straight trajectory of the candle flame—depending on the longitudinal coordinate x at the same depths z, similar to that in Fig. 3. At the moment in question, the candle passes over the point $x = 0$. It can be seen that the thermal impulse (which is more pronounced the closer the point in question is to the surface) has accumulated in the previous section $x < 0$ and will continue to move to the right in accordance with the dependencies in Fig. 3.

The transverse temperature distribution relative to the thermal line is represented by a family of graphs in Fig. 5. It has the expected appearance of symmetrical peaks, which become less sharp the deeper the observation point is located.

The obtained solution (16) can be used when describing the temperature field some distance away from the action area of the candle, where specific heating details (e.g., temperature distribution at the initial spray spot) are not apparent. In particular, the graphs in Fig. 4 show that significant temperature gradients arise in the vicinity of the action area of the candle, which will cause noticeable nonstationary temperature stresses. Their relaxation in the vicinity of the passed sections of the thermal line will, in one way or another, affect the quality of the coating, which can probably be controlled technologically by means of special spraying timing, coordinated with the dynamics of the temperature wave in the layer.

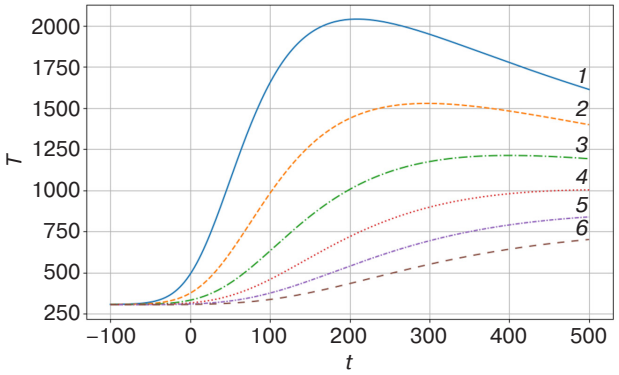

Fig. 3. Temporal evolution of temperature at points with the coordinates $x = y = 0$: (*1*) $z = -0.1$ mm, (*2*) $z = -0.2$ mm, (*3*) $z = -0.3$ mm, (*4*) $z = -0.4$ mm, (*5*) $z = -0.5$ mm, (*6*) $z = -0.6$ mm. The negative time corresponds to the accepted asymptotic initial condition (5); in a moving coordinate system, the moment $t = 0$ is conditional

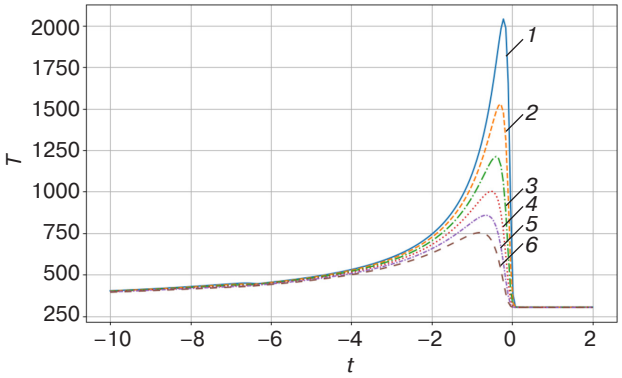

Fig. 4. Spatial profile of the temperature wave at $y = 0$, $t = 0$ as a function of coordinate x at the same depths in the layer as in Fig. 3: (*1*) $z = -0.1$ mm, (*2*) $z = -0.2$ mm, (*3*) $z = -0.3$ mm, (*4*) $z = -0.4$ mm, (*5*) $z = -0.5$ mm, (*6*) $z = -0.6$ mm

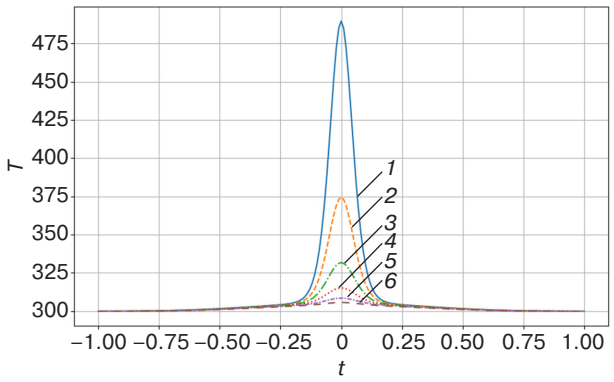

Fig. 5. Transverse spatial profile of the temperature wave at $x = 0$, $t = 0$ as a function of the y coordinate at the same depths in the layer as in Fig. 3:
(*1*) $z = -0.1$ mm, (*2*) $z = -0.2$ mm,
(*3*) $z = -0.3$ mm, (*4*) $z = -0.4$ mm,
(*5*) $z = -0.5$ mm, (*6*) $z = -0.6$ mm

CONCLUSIONS

This article addresses a nonstationary heat conduction problem simulating the technology of gas-thermal spraying of a thin strip forming part of a protective coating. An exact analytical solution describing the temperature field in the substrate material during the movement of a plasma torch creating a heat strip is obtained.

Our calculations showed that:

- after passing the heating pulse, the temperature inside the medium reaches rapidly its maximum value and then relaxes slowly to the ambient temperature;
- when penetrating deeper into the material, the thermal pulse spreads out, reducing its amplitude and increasing its width, while the time it takes to reach the maximum temperature increases;
- significant temperature gradients occur in the vicinity of the heat source, which can lead to nonstationary thermal stresses.

These facts are fully consistent with the general laws of thermophysical processes and, taken together, demonstrate the correctness of the selected physical model and the validity of the approximations made.

An accurate formula for the temperature field of a nonstationary heat strip was derived, enabling a detailed theoretical investigation of all essential characteristics of the heat pulse and their use in calculating experimentally and practically significant parameters of the spraying technology. It should be noted that the experimental possibilities for investigating the characteristics of the heat pulse under the conditions considered are rather limited and resource-intensive.

The resulting solution can be useful for describing the general temperature field at a certain distance from the spray head, where the details of the thermal band structure are not apparent. The results can be used to optimize the technological parameters of spraying, such as spraying timing, in order to control the quality of the coating obtained.

Authors' contribution
All authors contributed equally to the research work.

REFERENCES

1. Davis J.R. *Handbook of Thermal Spray Technology*. ASM International; 2004. 338 p.
2. *Gazotermicheskoe napylenie* (*Gas Thermal Spraying*). Baldaev L.H. (Ed.). Moscow: Market DS; 2007. 344 p. (in Russ.).
3. Ghasempour-Mouziraji M., Lagarinhos J., Afonso D., de Sousa R.A. A review study on metal powder materials and processing parameters in Laser Metal Deposition. *Opt. Laser Technol*. 2024;170:110226. https://doi.org/10.1016/j.optlastec.2023.110226
4. Cheng J., Xing Y., Dong E., Zhao L., Liu H., Chang T., Chen M., Wang J., Lu J., Wan J. An Overview of Laser Metal Deposition for Cladding: Defect Formation Mechanisms, Defect Suppression Methods and Performance Improvements of Laser-Cladded Layers. *Materials*. 2022;15(16):5522. https://doi.org/10.3390/ma15165522
5. Chen H.F., Zhang C., Liu Y.C., Song P., Li W.-X., Yang G., Liu B. Recent progress in thermal/environmental barrier coatings and their corrosion resistance. *Rare Met*. 2020;39(5):498–512. https://doi.org/10.1007/s12598-019-01307-1
6. Hardwicke C.U., Lau Y.C. Advances in Thermal Spray Coatings for Gas Turbines and Energy Generation: A Review. *J. Therm. Spray Technol*. 2013;22(5):564–576. https://doi.org/10.1007/s11666-013-9904-0
7. Bernhard R., Neef P., Wiche H., Wesling V., Hoff C., Hermsdorf J., Kaierle S. Laser Cladding – Additive Manufacturing. In: Cavaliere P. (Ed.) *Laser Cladding of Metals*. Springer, Cham; 2021. P. 1–8. https://doi.org/10.1007/978-3-030-53195-9_1
8. Lim W.Y.S., Cao J., Suwardi A., Meng T.L., Tan C.K.I., Liu H. Recent advances in laser-cladding of metal alloys for protective coating and additive manufacturing. *J. Adhes. Sci. Technol*. 2022;36(23–24):2482–2504. https://doi.org/10.1080/01694243.2022.2085499
9. Zhuravskiy A.V. Mathematical Modeling of Heat Transfer During Chemical Vapor Deposition. *Izvestiya vysshikh uchebnykh zavedenii. Mashinostroenie = BMSTU Journal of Mechanical Engineering*. 2017;11(692):10–17 (in Russ.). https://doi.org/10.18698/0536-1044-2017-11-10-17

10. Ravichandran K.S., An K., Dutton R.E., Semiatin S.L. Thermal conductivity of plasma-sprayed monolithic and multilayer coatings of alumina and yttria-stabilized zirconia. *J. Am. Ceram. Soc*. 2004;82(3):673–682. https://doi.org/10.1111/j.1151-2916.1999.tb01816.x
11. Ma K., Cheng Y., Jeyaprakash N., Zhou J., Wan Y., Yang W. Temperature gradient and solidification rate simulation model of the microstructure of laser-cladded 27SiMn. *Metals*. 2023;13(10):1682. https://doi.org/10.3390/met13101682
12. Moritz S., Schwanekamp T., Reuber M., Lentz J., Boes J., Weber S. Impact of *in situ* heat treatment effects during laser-based powder bed fusion of 1.3343 high-speed steel with preheating temperatures up to 700 °C. *Steel Research Int*. 2023;94(6):2200775. https://doi.org/10.1002/srin.202200775
13. Yamashita Y., Ilman K.A., Kunimine T., Sato Y. Temperature evaluation of cladding beads and the surrounding area during the laser metal deposition process. *J. Manuf. Mater. Process*. 2023;7(6):192. https://doi.org/10.3390/jmmp7060192
14. Chen C., Sun G., Ren B., Wang H., Zhang Y., Zhao X. A novel heterogeneous particle addition method based on laser cladding hybrid wire arc additive manufacturing: improvement performance of stainless steel components. *Virtual Phys. Prototyp*. 2024;19(1):e2397815 https://doi.org/10.1080/17452759.2024.2397815
15. Li C., Han X., Zhang D., Gao X., Jia T. Quantitative analysis and experimental study of the influence of process parameters on the evolution of laser cladding. *J. Adhes. Sci. Technol*. 2021;36(17):1894–1920. https://doi.org/10.1080/01694243.2021.1991142
16. Li C., Jia T., Han X., Jiang X. Study on parameter optimization of laser cladding Fe60 based on GA-BP neural network. *J. Adhes. Sci. Technol*. 2022;37(18):2556–2586. https://doi.org/10.1080/01694243.2022.2159298
17. Huang H., Wu M., Luo S., Chen Z. Optimization of process parameters in laser cladding multi channel forming using MVBM-NSGA-II method. *Mater. Manuf. Processes*. 2024;39(15):2226–2235. https://doi.org/10.1080/10426914.2024.2395002
18. Hu Z., Li C., Tian D., Li X., Wang J., Xu Z., Sun X. Numerical simulation analysis of temperature distribution of NbC-reinforced Ti-based composite coating by laser cladding. *Metals*. 2023;13(8):1348. https://doi.org/10.3390/met13081348
19. Deng C., Zhu Y., Chen W. Numerical Investigation of the Effects of Process Parameters on Temperature Distribution and Cladding-Layer Height in Laser Cladding. *Coatings*. 2024;14(8):1020. https://doi.org/10.3390/coatings14081020
20. Jiang Y., Cheng Y., Zhang X., Yang J., Yang X., Cheng Z. Simulation and experimental investigations on the effect of Marangoni convection on thermal field during laser cladding process. *Optik.* 2020;203:164044. https://doi.org/10.1016/j.ijleo.2019.164044
21. Sun Z., Guo W., Li L. Numerical modelling of heat transfer, mass transport and microstructure formation in a high deposition rate laser directed energy deposition process. *Addit. Manuf.* 2020;33:101175. https://doi.org/10.1016/j.addma.2020.101175
22. Wang C., Zhou J., Zhang T., Meng X., Li P., Huang S. Numerical simulation and solidification characteristics for laser cladding of Inconel 718. *Opt. Laser Technol*. 2022;149:107843. https://doi.org/10.1016/j.optlastec.2021.107843
23. Chai Q., Zhang H., Fang C., Qiu X., Xing Y. Numerical and experimental investigation into temperature field and profile of Stellite6 formed by ultrasonic vibration-assisted laser cladding. *J. Manuf. Process.* 2023;85:80–89. https://doi.org/10.1016/j.jmapro.2022.11.035
24. de La Batut B., Fergani O., Brotan V., Bambach M., Mansouri M.E. Analytical and numerical temperature prediction in direct metal deposition of Ti6Al4V. *J. Manuf. Mater. Process*. 2017;1(1):3. https://doi.org/10.3390/jmmp1010003
25. Gao Y., Jiang S., Tong Y., Bai S., Lu P. Temperature field simulation and experimental confirmation of laser cladding high-entropy alloy coating on Cr12MoV. *Processes*. 2024;12(2):257. https://doi.org/10.3390/pr12020257

About the Authors

Mikhail E. Soloviev, Dr. Sci. (Phys.-Math.), Professor, Department of Information Systems and Technologies, Institute of Digital Systems, Yaroslavl State Technical University (88, Moskovskii pr., Yaroslavl, 150023 Russia). E-mail: me_s@mail.ru. Scopus Author ID 57190224257, ResearcherID A-4328-2014, RSCI SPIN-code 7444-3564, https://orcid.org/0000-0002-8840-248X

Sergey S. Kokarev, Cand. Sci. (Phys.-Math.), Director of the Regional Scientific and Educational Center "Logos" (80, Respublikanskaya ul., Yaroslavl, 150000 Russia). E-mail: logos-center@mail.ru. https://orcid.org/0000-0001-6944-1400

Sergey L. Baldaev, Cand. Sci. (Eng.), Deputy General Director, Technological Systems for Protective Coatings (9A, Yuzhnaya ul., Shcherbinka, Moscow, 108851 Russia). E-mail: s.baldaev@tspc.ru. ResearcherID B-8056-2018, RSCI SPIN-code 6954-6407, https://orcid.org/0000-0002-1917-7979

Lev Kh. Baldaev, Dr. Sci. (Eng.), General Director, Technological Systems for Protective Coatings (9A, Yuzhnaya ul., Shcherbinka, Moscow, 108851 Russia). E-mail: l.baldaev@tspc.ru. RSCI SPIN-code 8991-5015, https://orcid.org/0000-0002-9084-8771

Denis V. Malyshev, Assistant, Department of Information Systems and Technologies, Institute of Digital Systems, Yaroslavl State Technical University (88, Moskovskii pr., Yaroslavl, 150023 Russia). E-mail: deniscs49@gmail.com. https://orcid.org/0009-0009-9861-1531

Об авторах

Соловьев Михаил Евгеньевич, д.ф.-м.н., профессор, кафедра информационных систем и технологий, Институт цифровых систем, ФГБОУ «Ярославский государственный технический университет» (150023, Россия, Ярославль, Московский пр-т, д. 88). E-mail: me_s@mail.ru. Scopus Author ID 57190224257, ResearcherID A-4328-2014, SPIN-код РИНЦ 7444-3564, https://orcid.org/0000-0002-8840-248X

Кокарев Сергей Сергеевич, к.ф.-м.н., директор регионального научно-образовательного центра «Логос» (150000, Россия, Ярославль, ул. Республиканская, д. 80). E-mail: logos-center@mail.ru. https://orcid.org/0000-0001-6944-1400

Балдаев Сергей Львович, к.т.н., заместитель генерального директора по технологиям, ООО «Технологические системы защитных покрытий» (108851, Россия, Москва, г. Щербинка, ул. Южная, д. 9А). E-mail: s.baldaev@tspc.ru. ResearcherID B-8056-2018, SPIN-код РИНЦ 6954-6407, https://orcid.org/0000-0002-1917-7979

Балдаев Лев Христофорович, д.т.н., генеральный директор ООО «Технологические системы защитных покрытий» (108851, Россия, Москва, г. Щербинка, ул. Южная, д. 9А). E-mail: l.baldaev@tspc.ru. SPIN-код РИНЦ 8991-5015, https://orcid.org/0000-0002-9084-8771

Малышев Денис Владимирович, ассистент, кафедра информационных систем и технологий, Институт цифровых систем, ФГБОУ «Ярославский государственный технический университет» (150023, Россия, Ярославль, Московский пр-т, д. 88). E-mail: deniscs49@gmail.com. https://orcid.org/0009-0009-9861-1531

Translated from Russian into English by Lyudmila O. Bychkova
Edited for English language and spelling by Dr. David Mossop

Mathematical modeling

Математическое моделирование

UDC 621.391:53.08
https://doi.org/10.32362/2500-316X-2025-13-6-139-147
EDN OVEHAM

RESEARCH ARTICLE

Estimation of the Gaussian blur parameter by comparing histograms of gradients with a standard image

Victor B. Fedorov [@], **Sergey G. Kharlamov**

MIREA – Russian Technological University, Moscow, 119454 Russia
[@] *Corresponding author, e-mail: feodorov@mirea.ru*

• **Submitted:** 28.05.2025 • **Revised:** 11.06.2025 • **Accepted:** 09.10.2025

Abstract

Objectives. The aim of this study is to develop a method for automatic quantitative estimation of the Gaussian blur parameter in digital images, which typically arises due to defocus of the optical system, various optical and camera-induced aberrations, as well as the influence of the propagation medium. This task is highly relevant for a wide range of applied fields, including remote sensing, forensic analysis, photogrammetry, medical imaging, automated inspection, and preprocessing of visual data prior to solving restoration, classification, or recognition problems.

Methods. The proposed method is based on comparing the two-dimensional histogram of gradients of the analyzed image with reference histograms precomputed for a high-sharpness image with similar texture and scale. The reference image is artificially blurred using convolution with a Gaussian kernel at various blur levels. For each level of blur, a two-dimensional gradient histogram is constructed, representing the distribution of directions and magnitudes of local intensity changes. The comparison with the corresponding histogram of the target image is performed after applying a logarithmic transformation and computing the Euclidean norm. This approach provides high sensitivity, interpretability, and numerical stability. The method does not require edge detection, neural network training, or labeled data, and can be implemented with minimal computational cost.

Results. Tests on synthetic data demonstrate that the proposed approach achieves high accuracy: the relative error in estimating the Gaussian blur parameter within the range of 0.7 to 2.0 pixels is less than 5%, and in most cases does not exceed 2–3%. The method is robust to noise, compression, local artifacts, and texture inhomogeneities.

Conclusions. The developed approach can be applied in automated image analysis systems as well as in blind deconvolution preprocessing tasks. It offers high accuracy, implementation simplicity, and reproducibility, providing reliable blur estimation under minimal data assumptions.

Keywords: image blur, Gaussian blur, blur parameter, gradient histogram, distribution comparison, distortion estimation, reference image, blind deconvolution, sharpness measurement, histogram distance metric

For citation: Fedorov V.B., Kharlamov S.G Estimation of the Gaussian blur parameter by comparing histograms of gradients with a standard image. *Russian Technological Journal.* 2025;13(6):139–147. https://doi.org/10.32362/2500-316X-2025-13-6-139-147, https://www.elibrary.ru/OVEHAM

Financial disclosure: The authors have no financial or proprietary interest in any material or method mentioned.

The authors declare no conflicts of interest.

НАУЧНАЯ СТАТЬЯ

Оценка параметра гауссовского размытия методом сопоставления гистограмм градиентов с эталонным изображением

В.Б. Федоров [@], **С.Г. Харламов**

МИРЭА – Российский технологический университет, Москва, 119454 Россия
[@] *Автор для переписки, e-mail: feodorov@mirea.ru*

• **Поступила:** 28.05.2025 • **Доработана:** 11.06.2025 • **Принята к опубликованию:** 09.10.2025

Резюме

Цели. Целью настоящего исследования является разработка метода автоматической количественной оценки параметра гауссовского размытия цифрового изображения, возникающего, как правило, вследствие дефокусировки оптической системы, некоторых других погрешностей вносимых оптической системой и камерой, а также вследствие влияния среды распространения света. Данная задача актуальна для множества прикладных областей, включая дистанционное зондирование, техническую экспертизу, фотограмметрию, медицинскую визуализацию, автоматическую инспекцию и предварительную обработку изображений перед решением задач их восстановления, классификации или распознавания.

Методы. Предложенный метод основан на сравнении двумерной гистограммы градиентов анализируемого изображения с эталонными гистограммами, заранее вычисленными для изображения высокой четкости, обладающего сходной текстурой и масштабом. Эталонное изображение искусственно размывается с различными значениями параметра размытия путем вычисления свертки с гауссовским ядром. Для каждого уровня размытия строится двумерная гистограмма градиентов, отражающая распределение направлений и величин локальных изменений яркости. Сравнение с аналогичной гистограммой обрабатываемого изображения выполняется после логарифмирования по евклидовой норме. Это дает высокую чувствительность, интерпретируемость и численную устойчивость. Метод не требует выделения резких границ, обучения нейросетей или наличия размеченных данных и может быть реализован с минимальными вычислительными затратами.

Результаты. На синтетических данных показано, что предложенный подход обеспечивает высокую точность: относительная ошибка оценки параметра размытия в диапазоне его значений 0.7–2.0 пикселя составляет менее 5%, а в большинстве случаев не превышает 2–3%. Метод устойчив к шуму, сжатию, локальным артефактам и текстурным неоднородностям.

Выводы. Разработанный подход может применяться в системах автоматического анализа изображений, а также в качестве предварительного этапа в задачах слепой деконволюции. Он отличается высокой точностью, простотой реализации и воспроизводимостью, обеспечивая надежную оценку степени размытия при минимальных требованиях к исходным данным.

Ключевые слова: размытие изображения, гауссовское размытие, параметр размытия, гистограмма градиентов, сравнение распределений, оценка искажений, эталонное изображение, слепая деконволюция, измерение резкости, метрика расстояния между гистограммами

Для цитирования: Федоров В.Б., Харламов С.Г. Оценка параметра гауссовского размытия методом сопоставления гистограмм градиентов с эталонным изображением. *Russian Technological Journal*. 2025;13(6):139–147. https://doi.org/10.32362/2500-316X-2025-13-6-139-147, https://www.elibrary.ru/OVEHAM

Прозрачность финансовой деятельности: Авторы не имеют финансовой заинтересованности в представленных материалах или методах.

Авторы заявляют об отсутствии конфликта интересов.

INTRODUCTION

Estimating image blur parameters is an important task in image processing and analysis. It plays a key role in improving sharpness, diagnosing data quality, and preprocessing images in satellite monitoring, medicine, industrial control, and other fields. The task of estimating the blur parameter σ in the case of Gaussian blur is particularly relevant. It is widely used as a model of spatial image degradation caused by defocusing or other forms of optical degradation. A highly accurate method for estimating the image blur parameter is important for the successful solution of the blind deconvolution problem.

Existing methods for evaluating blur parameters can be divided into several classes. The first class includes methods based on sharp edge analysis. They require accurate extraction and approximation of the transition profile, making them sensitive to noise, compression, and complex scene structure. The second class consists of frequency-based approaches, including methods based on the evaluation of the Modulation Transfer Function (MTF). These methods are also susceptible to global texture and can produce systematically overestimated values in heterogeneous image regions. The third class consists of methods based on machine learning, in particular convolutional neural networks [1, 2]. They demonstrate a high level of accuracy but require a large amount of labeled data for training and may not transfer well to new domains different from the training sample [1–7]. There are also individual studies in the literature devoted to the direct identification of the Gaussian blur parameter [8].

The method proposed in this paper aims to overcome these limitations. It does not require the localization of sharp boundaries and is resistant to noise and compression artifacts. It is based on comparing the two-dimensional histogram of gradients of the analyzed image with similar histograms obtained in advance from a reference image of a similar texture, artificially blurred with different values of σ. This allows for the degree of blurring to be estimated using the nearest neighbor principle in the histogram space. The method is easy to implement, requires no training, and demonstrates a high level of accuracy (the relative error, depending on the blur parameter value, ranges from 2% to 5%). In order to implement it, only one sufficiently arbitrary high-quality image is required as a reference.

The objective of this article is to describe formally the proposed method, experimentally evaluate its accuracy on synthetically blurred images, and compare its effectiveness with existing methods for estimating blur parameters.

1. IMAGE BLURRING MODEL

Let us consider the Cartesian coordinate system Oxy associated with the matrix of light-sensitive image elements. Let $q[x, y]$ be the discrete image of the scene—the reflected light signal coming from the object being photographed before passing through the propagation medium and the optical system. Let us assume that the camera pixel size Δ meets the condition $\Delta < 1/F_{\max}$, where $F_{\max}$ is the highest significant spatial frequency contained in the frequency spectrum of the image $q[x, y]$, which in this case, according to the sampling theorem, is represented as:

$$q[x,y] = \sum_{x',y' \in \mathbb{Z}} q[x',y']\mathrm{sinc}(x-x')\mathrm{sinc}(y-y'), \quad (1)$$

wherein, for convenience, $\Delta = 1$ is assumed.

Taking into account distortions when the signal passes through the optical channel and the camera's optical system, a Gaussian blurred image is projected onto the camera's touch panel:

$$q'(x,y) = \int_{\mathbb{R}^2} q(x',y')g_\sigma(x-x',y-y')dx'dy', \quad (2)$$

wherein

$$g_\sigma[x,y] = g_\sigma(x)g_\sigma(y), \;\; g_\sigma(x) = \frac{1}{\sqrt{2\pi}\sigma}\mathrm{e}^{-\frac{x^2}{2\sigma^2}}.$$

Here, it is assumed that the Gaussian blur parameter σ, which models the properties of the optical channel and certain design and manufacturing errors in the optical system, is sufficiently large (σ > 0.7 pixels) and therefore dominates over the effect caused by diffraction.

During the exposure time τ a charge equal to $p[x,y]=\tau\Delta^2 q'(x,y)=q'[x,y]$ accumulates on the sensor with the indices *x, y*, where τ = 1 and Δ = 1 are assumed.

From (2), taking into account (1), it follows that

$$p[x,y]= \\ =\sum_{x',y'\in\mathbb{Z}} q[x',y'](\mathrm{sinc}*h_\sigma)(x-x')(\mathrm{sinc}*h_\sigma)(y-y'), \quad (3)$$

wherein $(\mathrm{sinc}*h_\sigma)(x)=\int_{\mathbb{R}}\mathrm{sinc}(x')g_\sigma(x-x')dx$, '*' is the convolution operation, defined by Eq. (2).

In [9], it is shown that for values of the blur parameter σ > 0.7 pixels can be considered with high accuracy as $(\mathrm{sinc}*h_\sigma)(x)=g_\sigma(x)$. Taking this into account, Eq. (3) can be written as:

$$p[x,y]=\sum_{x',y'\in\mathbb{Z}} q[x',y']h_\sigma[x-x',y-y'],$$

wherein $h_\sigma[x,y]=g_\sigma(x)g_\sigma(y)$ is the two-dimensional isotropic Gaussian model of the discrete point blur function (PBF) with the blur parameter σ > 0 that we accept.

The accepted model is typical of satellite imaging of the Earth in cases where directional distortions (related to camera movement, object movement, or platform instability) are compensated. This work assumes that such directional blurring has been preliminarily eliminated by hardware or software and therefore, in a first approximation, the image can be considered isotropically blurred, without any predominant direction in the blurring.

2. THEORETICAL ASSUMPTIONS OF THE METHOD

The proposed method for estimating linear blur parameters is based on the assumption that, given the known nature of the image texture and a specified shooting scale (the ratio of the linear size of the terrain to the pixel size), the two-dimensional histogram of image gradients contains sufficient information to restore the blur parameters. In other words, it is assumed that the distribution of pixel brightness gradients, considered as a realization of a two-dimensional random variable, depends primarily on the properties of the scene texture, image scale, and blur parameters, while not depending on the content of the scene as a whole. This means that images with similar textures and the same scale, but different degrees of blur, will have different gradient statistics. This dependence can be used to estimate the distortion parameters.

It is assumed that there are broad classes of images for which the distribution of gradients can be described by a parametric family depending only on blur parameters. Such assumptions are typical for statistical models of natural scenes (natural scene statistics [1, 3, 4]) used in a number of works on distortion estimation [10–12].

It ca be presumed that such classes are determined primarily by texture characteristics: large or small details; contrasting or homogeneous structures; and linear scale. As will be shown in Section 3, this assumption is confirmed in practice: histograms of gradients of images with similar textures but different blur parameters demonstrate a stable dependence on distortion parameters.

The main idea of the method is to use a reference image belonging to the same class (i.e., with similar texture and scale) as the one being analyzed. The reference is synthetically subjected to Gaussian blurring with a blurring parameter which varies across a regular grid. For each blurred image obtained in this way, a two-dimensional gradient histogram (reference histogram) is calculated. The gradient histogram of the image being analyzed is then compared with the pre-calculated reference histograms. The following measures were considered:

- l_p-norms ($p=1,2,\infty$) from the difference of logarithms of histograms;
- Kullback–Leibler and Jensen–Shannon divergences.

This corresponds to standard practice in image quality assessment tasks [13]. However, significantly better results were obtained using logarithmic transformation and the l_2-norms.

Thus, the task is narrowed down to finding the nearest neighbor in the space of reference histograms. Each node of the parameter grid corresponds to one reference histogram and, therefore, to a uniquely defined vector of the blur parameters.

2.1. Plotting a two-dimensional histogram of image gradients

For each pixel of the input image $p[y, x]$, the discrete gradient is calculated in the following way:

$$\nabla p[y,x]=(p_x[y,x],\ p_y[y,x]),$$

wherein the gradient components are defined as the convolution of the image with the Sobel operator *D*:

$$p_x[y,x]=(p*D_x)[y,x], \quad p_y[y,x]=(p*D_y)[y,x],$$

and the operators themselves have the form

$$\begin{bmatrix} -1 & 0 & 1 \\ -2 & 0 & 2 \\ -1 & 0 & 1 \end{bmatrix}, \quad D_y = D_x^{\mathrm{T}}.$$

Each gradient vector $\nabla p[y,x]$ is further interpreted as the realization of a two-dimensional random variable observed in independent "tests" across the entire image area. Based on the set of these values, a two-dimensional histogram of gradient distribution is constructed:

$$H_{\nabla p}[i,j],\ i,j=\overline{1,N},$$

wherein N is the number of histogram cells for each measurement (p_x and p_y axes).

Let us assume that the gradient values fall within a fixed limited window (e.g., $[-G_{\max}, G_{\max}]\times[-G_{\max}, G_{\max}]$, which is evenly divided into $N \times N$ cells.

Choosing the N parameter requires a compromise between smoothing and discretization. If N is too small, the histogram becomes excessively smooth and loses important features of the distribution. If N is too large, the number of observations in each cell drops sharply, and the histogram becomes noisy. Thus, choosing the number of cells is part of the method configuration and should correspond to the sampling density and the nature of the gradients.

2.2. Reference histograms generation

A set of synthetically blurred images $\{p_{\sigma_k}\}$ is generated from the selected reference image $p^{\text{etalon}}[y,x]$ using a fairly fine two-dimensional grid of the blur parameter σ_k. For each grid value σ_k, the reference image is blurred:

$$p^{\text{etalon}}_{\sigma_k} = \left(p^{\text{etalon}} * h_{\sigma_k}\right)[y,x],$$

wherein the blur kernel $h_{\sigma_k}[y,x]$ is calculated via formula (3).

Then, for each variant of the reference image blur $p^{\text{etalon}}_{\sigma_k}[y,x]$ a separate histogram of gradients $H_{\nabla p^{\text{etalon}}_{\sigma_k}}$ как is plotted, as indicated in section 2.1.

2.3. Procedure for evaluating the blur parameter based on comparison with reference values

An appropriate metric should be used to evaluate the distances between the gradient histogram of the analyzed image and variants of similar reference histograms. Experiments have shown that the best results are obtained using the following metric:

$$\mathrm{dist}_{\log}(H_{\nabla p}, H_{\nabla p^{\text{etalon}}_{\sigma_k}}) = \sum_{i,j}\left|\log H_{\nabla p}[i,j] - \log H_{\nabla p^{\text{etalon}}_{\sigma_k}}[i,j]\right|^2.$$

In order to improve numerical stability under the logarithm sign, a regularization procedure should be used which consists of replacing the values of zero cells with the smallest of all obtained cell values before logarithmization. In such a situation, the expression of the type $\log(x)$ is often replaced by $\log(x + \varepsilon)$, where, for example, $\varepsilon = 10^{-6}$. However, as the experiment has shown, such a solution, compared to the one proposed above, often leads to a multiple increase in the relative error of the blur parameter estimation.

Thus, the evaluation of the blur parameters present in the analyzed image is carried out according to the following rule:

$$\hat{\sigma} = \arg\min_k \mathrm{dist}_{\log}(H_{\nabla p}, H_{\nabla p^{\text{etalon}}_{\sigma_k}}).$$

3. MODELING RESULTS

Figure 1 shows two high-quality images. The first, blurred to different degrees, is considered as the processed image, the degree of blurring of which needs to be evaluated (at different blurring values). The second is used as a reference (standard) image.

The modeling results are presented in Table 1.

Table 2 presents the results of modeling when changing the roles of the images under consideration—the image that was previously evaluated became the reference image, and *vice versa*.

As can be seen from the tables above, when the evaluated image is artificially blurred by the values $\sigma \in [0.7, 2.0]$, the relative accuracy of the estimates in most cases does not exceed 5%. In fact, in most cases it is significantly lower. Individual outliers in the estimate values are associated with the high sensitivity of the method to the choice of histogram cell boundaries. The estimates given in Tables 1 and 2 were obtained with histogram cell boundaries taken in the range from −2.1 to 2.1 with a step of 0.02126.

Figure 2 shows a typical one-dimensional logarithmic histogram (natural logarithm of the histogram). The corresponding one-dimensional histograms are obtained by averaging the two-dimensional histogram in each of the two directions.

Figure 3 shows typical graphs of the dependence of the $\mathrm{dist}_{\log}$ metric value on the σ_k parameter (at a fixed σ). The minima on these curves correspond to the estimation of the blur parameters. The graphs compare the results for two values of the grid step along σ: 0.01 and 0.001 pixels. As can be seen, the step of 0.01 is already small enough, and further reduction does not lead to a significant increase in accuracy.

(a) (b)

Fig. 1. Two high-quality images:
(a) the image being processed; (b) the image used as a reference

Table 1. Modeling results

True value σ	Estimation σ	Error value	Relative error, %
0.7	0.69	+0.01	4.3
0.8	0.79	+0.01	1.3
0.9	0.88	+0.02	1.1
1.0	0.99	+0.01	1.0
1.1	1.07	+0.03	1.8
1.2	1.24	−0.04	2.5
1.3	1.35	−0.05	2.3
1.4	1.42	−0.02	3.6
1.5	1.54	−0.04	7.3
1.6	1.61	−0.01	3.1
1.7	1.74	−0.04	5.9
1.8	1.82	−0.02	1.7
1.9	2.00	−0.10	7.9
2.0	2.10	−0.10	6.5
2.1	2.20	−0.10	6.7
2.2	2.30	−0.10	6.8
2.3	2.40	−0.10	7.8
2.4	2.50	−0.10	3.8
2.5	2.60	−0.10	10.0

Table 2. Modeling results when changing the roles of the images under consideration

True value σ	Estimation σ	Error value	Relative error, %
0.7	0.69	+0.01	4.3
0.8	0.80	0.00	5.0
0.9	0.93	−0.03	2.2
1.0	1.02	−0.02	1.0
1.1	1.12	−0.02	0.9
1.2	1.13	+0.07	2.5
1.3	1.24	+0.06	3.1
1.4	1.34	+0.06	3.6
1.5	1.44	+0.06	0.7
1.6	1.56	+0.04	1.3
1.7	1.64	+0.06	1.8
1.8	1.77	+0.03	3.9
1.9	1.80	+0.10	3.2
2.0	1.90	+0.10	6.0
2.1	2.00	+0.10	8.1
2.2	2.11	+0.09	1.4
2.3	2.20	+0.10	5.7
2.4	2.30	+0.10	5.4
2.5	2.40	+0.10	9.2

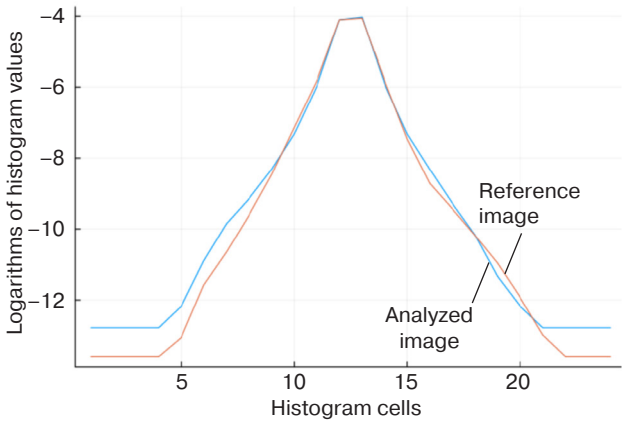

Fig. 2. A typical view of one-dimensional logarithmic histograms

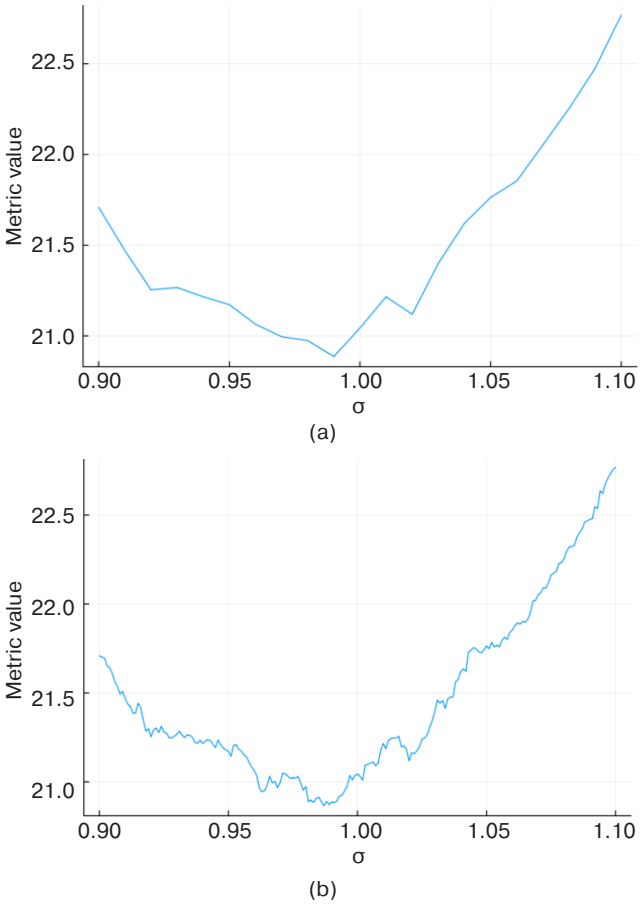

Fig. 3. A typical view of the dependence of the metric determining the similarity of the compared images on the value of the estimated blur parameter σ at grid step: (a) 0.01; (b) 0.001

4. COMPARISON WITH OTHER METHODS

This work proposes a method for estimating the Gaussian blur parameter of an image based on comparing a two-dimensional gradient histogram with pre-calculated reference histograms obtained from an image of similar texture and scale which has been artificially blurred. The method does not require boundary localization and works well even in the presence of compression and noise.

The simulation showed that the method demonstrates high accuracy in the range of blur parameter values $\sigma \in [0.7, 2.0]$, achieving a relative error that in the vast majority of cases does not exceed 5% and is often lower. At the same time, one of the key factors affecting the accuracy of the estimate is the choice of cell boundaries when constructing the gradient histogram.

The minimum grid step for the blur parameter σ_k sufficient for high accuracy is 0.01 pixels. Further reduction does not provide any significant gain which makes the method efficient in terms of computational costs.

Thus, the proposed approach is simple to implement, noise-resistant, and easily adaptable to different blur ranges. It has the potential to be applied in automatic image analysis tasks in technical, medical, and remote applications, as well as used as a preliminary stage for subsequent image restoration.

Table 3 presents a brief comparison of the proposed method with a number of known approaches to estimating Gaussian or linear blur parameters.

Thus, comparison with existing methods shows that the approach proposed achieves accuracy comparable to the best modern methods based on trainable neural network models (2–5%), while requiring no prior training, labeled data, or complex infrastructure.

It should be noted that the proposed method essentially implements the simplest version of regression in feature space, similar to how convolutional neural networks work. Two-dimensional gradient histograms serve as features, and a set of reference images artificially blurred with known values of the parameter σ serves as the training sample. Instead of training the model parameters, an explicit comparison is made using a metric, making the method interpretable and robust. Thus, the approach proposed can be considered an effective and interpretable alternative to neural network methods for blur estimation [4, 5–7, 14, 15].

Table 3. Comparative table of different methods for evaluating image blur parameters

Method	Requires a reference?	Requires a boundary?	Noise resistance	Automation	Accuracy at $\sigma \in [1.0, 2.0]$	Comments
Proposed method	Yes (similar structure)	No	High	Full	2–5% (in most cases)	High accuracy, highly scalable
Sharp boundary method	No	Yes (locally)	Low	Limited	5–15%	Requires a clear sharp boundary and may be sensitive to noise and edge line direction
Frequency method (MTF-fit)[1]	No	No	Average	Yes	5–10%	Requires correct window selection, depends on texture
Gradient statistics without a reference	No	No	Average	Yes	10–20%	Easy to implement, low accuracy
Methods based on convolutional neural networks	Not always	No	High	Requires training	2–5%	Good results on the trained sample, but difficult to apply

[1] Modulation Transfer Function is an experimental fitting of the modulation transfer function.

CONCLUSIONS

This work used a single reference image with texture characteristics similar to those of the image being analyzed. However, in order to increase the stability and versatility of the method in practice, it is reasonable to use not just one reference, but a representative set of references. This approach involves the preliminary formation of a basic set of high-quality images, their clustering by characteristics (for example, by gradient histograms at $\sigma = 0$), and the subsequent selection of the closest reference for each image under analysis. This can enable the method to be adapted to a variety of scene structures and textures, increasing the accuracy and expanding the applicability of the approach.

The method could be further developed in the direction of automatically selecting image areas with high textural informativeness, potentially reducing the requirements for selecting a reference image.

Authors' contribution
All authors contributed equally to the research work.

REFERENCES

1. Flusser J., Lebl M., Sroubek F., Pedone M., Kostkova J. Blur Invariants for Image Recognition. *Int. J. Computer Vision*. 2023;131(9):2298–2315. https://doi.org/10.1007/s11263-023-01798-7
2. Bergstrom A.C., Conran D., Messinger D.W. Gaussian Blur and Relative Edge Response. *arXiv.* arXiv:2301.00856. 2023. https://doi.org/10.48550/arXiv.2301.00856
3. Varela L.G., Boucheron L.E., Sandoval S., Voelz D., Siddik A.B. Estimation of Motion Blur Kernel Parameters Using Regression Convolutional Neural Networks. *arXiv.* arXiv:2308.01381. 2023. http://doi.org/10.48550/arXiv.2308.01381
4. Zhang K., Ren W., Luo W., Lai W.-S., Stenger B., Yang M.-H., Li H. Deep Image Deblurring: A Survey. *arXiv.* arXiv:2201.10700. 2022. https://doi.org/10.48550/arXiv.2201.10700
5. Levin A., Weiss Y., Durand F., Freeman W.T Understanding and Evaluating Blind Deconvolution Algorithms. In: *Proceedings of the IEEE Conference on Computer Vision and Pattern Recognition* (*CVPR*). 2009. P. 1964–1971. https://doi.org/10.1109/CVPR.2009.5206815
6. Ren D., Zhang K., Wang Q., Hu Q., Zuo W. Neural Blind Deconvolution Using Deep Priors. *arXiv.* arXiv:1908.02197. 2019. https://doi.org/10.48550/arXiv.1908.02197
7. Yu J., Chang Z., Xiao C. Edge-Based Blur Kernel Estimation Using Sparse Representation and Self-Similarity. *arXiv.* arXiv:1811.07161. 2018. https://doi.org/10.48550/arXiv.1811.07161

8. Chen F., Ma J. An Empirical Identification Method of Gaussian Blur Parameter for Image Deblurring. *IEEE Trans. Signal Proces*. 2009;57(7):2467–2478. https://doi.org/10.1109/TSP.2009.2018358
9. Fedorov V.B., Kharlamov S.G., Fedorov A.V. Image restoration using a discrete point spread function with consideration of finite pixel size. *Russ. Technol. J.* 2025;13(2):143–154. https://doi.org/10.32362/2500-316X-2025-13-2-143-154, https://elibrary.ru/GXAGAW
10. Pawanikar N.K., Strivaramangai R. Review of Single Blind Image Deblurring Techniques. *Int. J. Computer Sci. Trends Technol.* 2023;11(3):26–40. Available from URL: https://www.ijcstjournal.org/volume-11/issue-3/IJCST-V11I3P7.pdf
11. Yu H., Li D., Chen Y. A State-of-the-Art Review of Image Motion Deblurring Techniques in Remote Sensing. *Heliyon*. 2023;9(6):e17332. https://doi.org/10.1016/j.heliyon.2023.e17332
12. Huang Y., Chouzenoux E., Pesquet J.-C. Unrolled Variational Bayesian Algorithm for Image Blind Deconvolution. *arXiv.* arXiv:2110.07202. 2021. https://doi.org/10.48550/arXiv.2110.07202
13. Tiwari S., Shukla V.P., Singh A.K., Biradar S.R. Review of Motion Blur Estimation Techniques. *J. Image Graphics*. 2013;1(4):176–184. https://doi.org/10.12720/JOIG.1.4.176-184
14. Couzinie-Devy F., Sun J., Alahari K., Ponce J. Learning to Estimate and Remove Non-uniform Image Blur. In: *Proceedings of the IEEE Conference on Computer Vision and Pattern Recognition* (*CVPR*). 2013. P. 1075–1082. https://doi.org/10.1109/CVPR.2013.143
15. Yan R., Shao L. Blind Image Blur Estimation via Deep Learning. In: *Proceedings of the IEEE Transactions on Image Processing*. 2016;25(4):1910–1921. Available from URL: https://core.ac.uk/download/pdf/79609188.pdf

About the Authors

Victor B. Fedorov, Cand. Sci. (Eng.), Associate Professor, Higher Mathematics Department, Institute of Artificial Intelligence, MIREA – Russian Technological University (78, Vernadskogo pr., Moscow, 119454 Russia). E-mail: feodorov@mirea.ru, fdorov@mail.ru. Scopus Author ID 57208924592, RSCI SPIN-code 2622-7666, https://orcid.org/0000-0003-1011-5453

Sergey G. Kharlamov, Postgraduate Student, Higher Mathematics Department, Institute of Artificial Intelligence, MIREA – Russian Technological University (78, Vernadskogo pr., Moscow, 119454 Russia). E-mail: serhar2000@mail.ru. https://orcid.org/0000-0003-4470-6323

Об авторах

Федоров Виктор Борисович, к.т.н., доцент, кафедра высшей математики, Институт искусственного интеллекта, ФГБОУ ВО «МИРЭА – Российский технологический университет» (119454, Россия, Москва, пр-т Вернадского, д. 78). E-mail: feodorov@mirea.ru, fdorov@mail.ru. Scopus Author ID 57208924592, SPIN-код РИНЦ 2622-7666, https://orcid.org/0000-0003-1011-5453

Харламов Сергей Григорьевич, аспирант, кафедра высшей математики, Институт искусственного интеллекта, ФГБОУ ВО «МИРЭА – Российский технологический университет» (119454, Россия, Москва, пр-т Вернадского, д. 78). E-mail: serhar2000@mail.ru. https://orcid.org/0000-0003-4470-6323

Translated from Russian into English by Lyudmila O. Bychkova
Edited for English language and spelling by Dr. David Mossop

MIREA – Russian Technological University.
78, Vernadskogo pr., Moscow, 119454 Russian Federation.
Publication date November 28, 2025.
Not for sale.

МИРЭА – Российский технологический университет.
119454, РФ, г. Москва, пр-т Вернадского, д. 78.
Дата опубликования 28.11.2025 г.
Не для продажи.

https://www.rtj-mirea.ru